DESIGN OF TWO-DIMENSIONAL FUNCTIONAL MATERIALS AND NANODEVICES

EDITED BY: Guangzhao Wang, Xiaotian Wang, Yee Sin Ang, Junjie He and
Zhaofu Zhang

PUBLISHED IN: Frontiers in Chemistry and Frontiers in Materials

frontiers Research Topics

ISSN 1664-8714
ISBN 978-2-88976-611-6
DOI 10.3389/978-2-88976-611-6

About Frontiers

Frontiers is more than just an open-access publisher of scholarly articles: it is a pioneering approach to the world of academia, radically improving the way scholarly research is managed. The grand vision of Frontiers is a world where all people have an equal opportunity to seek, share and generate knowledge. Frontiers provides immediate and permanent online open access to all its publications, but this alone is not enough to realize our grand goals.

Frontiers Journal Series

The Frontiers Journal Series is a multi-tier and interdisciplinary set of open-access, online journals, promising a paradigm shift from the current review, selection and dissemination processes in academic publishing. All Frontiers journals are driven by researchers for researchers; therefore, they constitute a service to the scholarly community. At the same time, the Frontiers Journal Series operates on a revolutionary invention, the tiered publishing system, initially addressing specific communities of scholars, and gradually climbing up to broader public understanding, thus serving the interests of the lay society, too.

Dedication to Quality

Each Frontiers article is a landmark of the highest quality, thanks to genuinely collaborative interactions between authors and review editors, who include some of the world's best academicians. Research must be certified by peers before entering a stream of knowledge that may eventually reach the public - and shape society; therefore, Frontiers only applies the most rigorous and unbiased reviews.
Frontiers revolutionizes research publishing by freely delivering the most outstanding research, evaluated with no bias from both the academic and social point of view. By applying the most advanced information technologies, Frontiers is catapulting scholarly publishing into a new generation.

What are Frontiers Research Topics?

Frontiers Research Topics are very popular trademarks of the Frontiers Journals Series: they are collections of at least ten articles, all centered on a particular subject. With their unique mix of varied contributions from Original Research to Review Articles, Frontiers Research Topics unify the most influential researchers, the latest key findings and historical advances in a hot research area! Find out more on how to host your own Frontiers Research Topic or contribute to one as an author by contacting the Frontiers Editorial Office: frontiersin.org/about/contact

DESIGN OF TWO-DIMENSIONAL FUNCTIONAL MATERIALS AND NANODEVICES

Topic Editors:
Guangzhao Wang, Yangtze Normal University, China
Xiaotian Wang, Southwest University, China
Yee Sin Ang, Singapore University of Technology and Design, Singapore
Junjie He, Charles University, Czechia
Zhaofu Zhang, University of Cambridge, United Kingdom

Citation: Wang, G., Wang, X., Ang, Y. S., He, J., Zhang, Z., eds. (2022). Design of Two-Dimensional Functional Materials and Nanodevices.
Lausanne: Frontiers Media SA. doi: 10.3389/978-2-88976-611-6

Table of Contents

frontiers | Frontiers in Materials

TYPE Editorial
PUBLISHED 30 August 2022
DOI 10.3389/fmats.2022.976642

Editorial: Design of two-dimensional functional materials and nanodevices

Guangzhao Wang[1]*†, Junjie He[2,3]†, Xiaotian Wang[4], Zhaofu Zhang[5,6]* and Yee Sin Ang[7]*

[1]Key Laboratory of Extraordinary Bond Engineering and Advanced Materials Technology of Chongqing, School of Electronic Information Engineering, Yangtze Normal University, Chongqing, China, [2]Department of Physical and Macromolecular Chemistry, Faculty of Science, Charles University in Prague, Prague, Czechia, [3]Bremen Center for Computational Materials Science, University of Bremen, Bremen, Germany, [4]School of Physical Science and Technology, Southwest University, Chongqing, China, [5]The Institute of Technological Sciences, Wuhan University, Wuhan, China, [6]Department of Engineering, Cambridge University, Cambridge, United Kingdom, [7]Science, Mathematics, and Technology, Singapore University of Technology and Design, Singapore, Singapore

KEYWORDS

2D materials, 2D heterostructures, nanodevices, functional materials, first principles calculation

OPEN ACCESS

EDITED BY
Simone Taioli,
European Centre for Theoretical Studies in Nuclear Physics and Related Areas (ECT*), Italy

REVIEWED BY
Andrea Pedrielli,
Bruno Kessler Foundation (FBK), Italy
Tommaso Morresi,
European Centre for Theoretical Studies in Nuclear Physics and Related Areas (ECT*), Italy

*CORRESPONDENCE
Guangzhao Wang,
wangyan6930@yznu.edu.cn
Zhaofu Zhang,
zhaofuzhang@whu.edu.cn
Yee Sin Ang,
yeesin_ang@sutd.edu.sg

†These authors have contributed equally to this work

SPECIALTY SECTION
This article was submitted to Computational Materials Science, a section of the journal Frontiers in Materials

RECEIVED 23 June 2022
ACCEPTED 08 August 2022
PUBLISHED 30 August 2022

CITATION
Wang G, He J, Wang X, Zhang Z and Ang YS (2022), Editorial: Design of two-dimensional functional materials and nanodevices.
Front. Mater. 9:976642.
doi: 10.3389/fmats.2022.976642

Editorial on the Research Topic
Design of two-dimensional functional materials and nanodevices

Two-dimensional (2D) materials and their heterostructures have attracted much attention in the fields of sensors, spintronic devices, thermoelectricity, battery, catalysis, photocatalysis, and optoelectronic devices due to their outstanding physical and chemical properties. In this Research Topic, entitled *Design of two-dimensional functional materials and nanodevices*, we collected a total of 17 articles reporting on the recent advances of 2D materials, heterostructures and materials with exotic topological and spintronic properties. Below, we provide a summary and research highlights on these exciting works.

Novel 2D sensing materials

Li et al. presented a recent research progress of gas sensing performance of 2D h-WO_3. The characteristics and the effects of microstructure, oxygen vacancy, and doping modification on the gas sensing performance of 2D h-WO_3 are summarized. The application of 2D h-WO_3 gas sensor and the challenges are discussed. Yong et al. investigated the N_2 and O_2 gas sensing properties of pristine and defective PtS_2 via first principles calculations, they found that the $PtSe_2$ with Pt@Se anti-site defect is a sensitive electrical and optical sensor for N_2 gas detection and the $PtSe_2$ with Pt vacancy, Se vacancy, Pt@Se anti-site defect are promising electrical and optical sensors for O_2 gas detection.

Novel 2D energy and environmental materials

Combining first-principles calculations and Boltzmann transport equations, Hu et al. explored the thermoelectric property of boron singlelayer. The boron layer possesses a low lattice thermal conductivity of 20.2 W/mK at 300 K. The boron singlelayer is a potential *p*-type thermoelectric material as its p-type the thermoelectric figure of merit is up to 0.96 at 300 K. By use of first principles calculations, Zhang et al. revealed the MoS_2-based Li- and Na-ions batteries show better cycle and rate performance than that of Mg- and Zn-ions batteries may be caused by the lower ions migration energy barrier, higher storage capability, and the phase transformation from 2H to 1T of Li- and Na-ions batteries. Sun used first principles calculations to explore the catalytic mechanism and activity of 11 types N-doped graphene. Among them, the zigzag pyridinic N- and zigzag graphitic N-doped graphene show excellent catalytic activity for CO_2 electrochemical reduction reaction in producing HCOOH.

Novel 2D van der waals heterostructures for photocatalytic water-splitting, optoelectronics and nanoelectronics

Combining different 2D materials to form van der Waals heterostructures (HS) provides a novel route to expand the application scope of 2D materials. Several HS with exceptional physical properties are predicted by first principles calculations. Ren et al. predicted that the CdO/As HS with a direct bandgap is a promising Z-type photocatalyst with the solar-to-hydrogen efficiency of 11.67%. Shao et al. found that $PtS_2/MoTe_2$ HS is a potential type-II photocatalyst for water-splitting with a novel light absorption, desirable band edge positions, and a proper potential drop. Shen et al. proposed that the lateral MoSSe/WSSe HS with type-II band alignment could be potentially applied in photocatalytic water-splitting. Besides, the heat flow transport is restricted by the natural bending caused by the asymmetric interface of the Janus MoSSe/WSSe HS. Ren et al. reported that AlN/Zr_2CO_2 HS with a type-I band alignment possesses potential application in light emitting devices. Xiao et al. effectively modulated the Schottky barrier height of graphene/ZnS HS by using horizontal and vertical strains.

Novel topological and spintronics materials

Yang et al. systematically evaluated the structural, magnetic, and electronic properties of Nd_2N and Nd_2NT_2 (T = OH, O, S, F, Cl, and Br), and the results showed that Nd_2NT_2 (T = OH, O, S, F, Cl, and Br) are all half-metals. Besides, the effects of strains and varied functional group proportions on their magnetic and electronic properties were also explored. Beyond 2D materials, this Research Topic also collects several articles reporting on the computational discovery of topological and other spintronic materials. Lin et al. proposed that pristine P63/mmc type TiTe is topological semimetal with type-I, type-II, and hybrid nodal lines. Chang et al. found that the hexagonal BaAgBi possesses two Weyl nodal ring states (or two Dirac nodal lines) with the absence (or presence) of spin–orbit coupling (SOC) effect. Zhang et al. reported that the NaCl with Fmm type structure possesses the triple point, quadratic contact triple point, linear and quadratic nodal lines in its phonon dispersion. Ding et al. developed the potential parameters for the Ti–Cr binary and the Ti–Cr–N ternary systems based on the second nearest-neighbor modified embedded-atom method. Hao et al. investigated the mechanical and thermodynamic effects caused by the interstitial and substitutional dopants of Ge, B, and He atoms to explore their effects on diamond wear. Dai et al. subtly modulated the growth temperature, duration time, and growth pressure to successfully achieve the controlled growth of γ-InSe and α-In_2Se_3 crystals with completely different stoichiometries and stacking manner of atomic layers.

We hope that this Research Topic can provide theoretical insights that are useful for the development and design of novel 2D functional material and heterostructure devices. We would like to thank all the authors, reviewers, and editors who contributed to the Research Topic.

Author contributions

All authors listed have made a substantial, direct, and intellectual contribution to the work and approved it for publication.

Funding

This work was supported by the Science and Technology Research Program of Chongqing Municipal Education Commission, China under grant No. KJQN202001402.

Conflict of interest

The authors declare that the research was conducted in the absence of any commercial or financial relationships that could be construed as a potential conflict of interest.

Publisher's note

frontiers in Chemistry

ORIGINAL RESEARCH
published: 10 May 2021
doi: 10.3389/fchem.2021.677620

Metal-Ions Intercalation Mechanism in Layered Anode From First-Principles Calculation

Junbo Zhang[1,2], Xiaodong Lu[1], Jingjing Zhang[1], Han Li[3], Bowen Huang[3], Bingbing Chen[1*], Jianqiu Zhou[1,3] and Suming Jing[1]

[1] Department of Energy Science and Engineering, Nanjing Tech University, Nanjing, China, [2] Department of Electric Power Engineering, Nanjing Normal University Taizhou College, Taizhou, China, [3] Department of Mechanical and Power Engineering, Nanjing Tech University, Nanjing, China

Layered structure (MoS_2) has the potential use as an anode in metal-ions (M-ions) batteries. Here, first-principles calculations are used to systematically investigate the diffusion mechanisms and structural changes of MoS_2 as anode in lithium (Li)-, sodium (Na)-, magnesium (Mg)- and Zinc (Zn)-ions batteries. Li and Na ions are shown to be stored in the MoS_2 anode material due to the strong adsorption energies (~ -2.25 eV), in contrast to a relatively weak adsorption of Mg and Zn ions for the pristine MoS_2. To rationalize the results, we evaluate the charge transfer from the M-ions to the MoS_2 anode, and find a significant hybridization between the adsorbed atoms and S atoms in the MoS_2 anode. Furthermore, the migration energy barriers of M ions are explored using first-principles with the climbing image nudged elastic band (CINEB) method, and the migration energy barrier is in the order of Zn > Mg > Li > Na ions. Our results combined with the electrochemical performance experiments show that Li- and Na-ions batteries have good cycle and rate performance due to low ions migration energy barrier and high storage capability. However, the MoS_2 anode shows poor electrochemical performance in Zn- and Mg-ions batteries, especially Zn-ion batteries. Further analysis reveals that the MoS_2 structure undergoes the phase transformation from 2H to 1T during the intercalation of Li and Na ions, leading to strong interaction between M ions and the anode, and thus higher electrochemical performance, which, however, is difficult to occur in Mg- and Zn-ions batteries. This work focuses on the theoretical aspects of M-ions intercalation, and our findings may stimulate the experimental work for the intercalation of multi-ions to maximize the capacity of anode in M-ions batteries.

Keywords: layer structure, first-principles, metal-ions battery, structural evolution, MoS_2

Edited by:
Guangzhao Wang,
Yangtze Normal University, China

Reviewed by:
Hu Junping,
Nanchang Institute of Technology, China
Shan Guan,
Institute of Semiconductors (CAS), China

***Correspondence:**
Bingbing Chen
chenbb@njtech.edu.cn

Specialty section:
This article was submitted to Theoretical and Computational Chemistry,
a section of the journal Frontiers in Chemistry

Received: 08 March 2021
Accepted: 08 April 2021
Published: 10 May 2021

Citation:
Zhang J, Lu X, Zhang J, Li H, Huang B, Chen B, Zhou J and Jing S (2021) Metal-Ions Intercalation Mechanism in Layered Anode From First-Principles Calculation. Front. Chem. 9:677620. doi: 10.3389/fchem.2021.677620

INTRODUCTION

The rapid development of eco-friendly batteries will bring huge benefits to electrical vehicles and capacity devices (Manoj et al., 2018), and the rechargeable batteries with high energy density and long cycle life have attracted considerable attention in terms of improving the energy storage efficiency. Lithium (Li)-ions batteries represent a highly attractive and challenging alternative to rechargeable batteries. While many important achievements have been achieved for these batteries (Ju et al., 2019; Wang et al., 2020), the content of Li is limited in the Earth's crust, which will affect the extensive applications of Li-ions batteries (Schmuch et al., 2018; Sun et al., 2019), suggesting the necessity of the research of multivalent metal-ions (M-ions) batteries.

M (Li, Na, Mg, and Zn)-ions batteries have been demonstrated as very promising rechargeable batteries (Forsyth et al., 2019), and in order to enhance their capacity, many research efforts have been devoted to designing electrodes and solid electrolytes, including the nanostructured Si, transition metal oxides, and layered structure (Hu et al., 2019, 2020a). However, the ability to maintain high capacity and long cycle remains a bottleneck for M-ions batteries, especially anode materials, with a stable anode as the key component in M-ions batteries (Hu et al., 2020a). Therefore, it should be noted that finding an anode with fast ion and electron conduction is the biggest challenge in improving the performance of M-ions batteries.

Interestingly, due to their large surface-to-volume ratios, two-dimensional materials have currently become the research focus in nanostructured anode materials and have been successfully applied in M-ions batteries based on theoretical and experimental studies (Wang et al., 2018; Mohanapriya and Jha, 2019; Hu et al., 2020b). For example, layer anode materials, such as MoS_2, WS_2, borophene and graphene, were investigated for Li-ions batteries, and they exhibited good electrochemical performance as the anodes of Li (Na)-ions batteries (Xie et al., 2015). In particular, MoS_2 nanoplate anodes in Li-ions batteries have been demonstrated to possess a capacity of 1,062 mAh g^{-1} (Cui et al., 2018). Previous investigations have attributed the high performance of the MoS_2 anode behavior to its unique structural characteristics, such as the layered structure, which can provide more ions channels and storage compartments (Hu et al., 2014; Wang et al., 2017). However, the electrochemical performance of MoS_2 is poor in divalent-ions (Mg, Zn) batteries. Thus far, few studies have been performed on the diffusion mechanisms and structural changes of the layer anode in M (Li, Na, Mg and Zn)-ions batteries to describe its different electrochemical behavior.

In this work, the adsorption and diffusion mechanisms of Li, Na, Mg, and Zn ions on the ordinary MoS_2 (2H) structure were explored based on the density functional theory (DFT) and experimental analysis. In addition, the storage capability of Li, Na, Mg, and Zn ions in the MoS_2 material were predicted and verified by experiments. Moreover, the structural deformation and electronic properties of MoS_2 during ions intercalation were also investigated. Our theoretical and experimental results show that when used as the anode material of M-ions (Li and Na) batteries, MoS_2 had significantly less variation in volume during

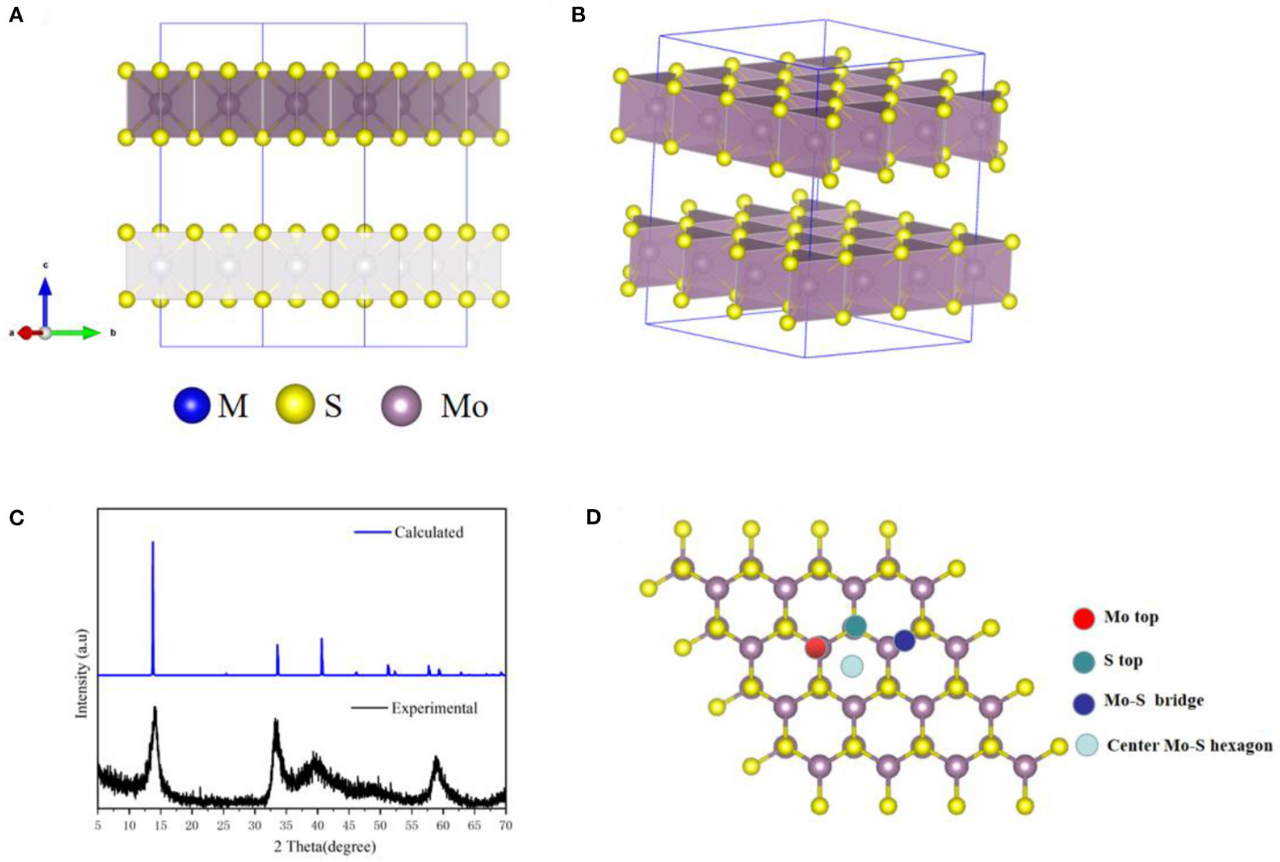

FIGURE 1 | The MoS_2 structure drawings viewed along **(A)** c-axis and **(B)** the stereo perspective. **(C)** The XRD pattern of the MoS_2 sample. **(D)** Adsorption site of M-ions.

the cycling process, while in Mg and Zn-ions batteries, MoS_2 exhibited poor electrochemical performance due to the high migration energy barrier and low adsorption energy caused by changes in the structural properties based on first-principles. Furthermore, the MoS_2 anode was found to undergo a phase transition from 2H to 1T during the intercalation of Li and Na ions, which was difficult to occur during the intercalation of Mg and Zn ions. This phase transition contributes to improving the performance of the MoS_2 anode in M-ions batteries. Our results facilitate the understanding of the mechanisms of ions diffusion and structural changes of layer materials and provide useful information for designing high-performance anode materials, especially multivalent M-ions batteries.

COMPUTATIONAL AND EXPERIMENTAL METHODS

Computational Methods

First-principles were used to describe the ions behavior in the anode based on density functional theory (DFT) with the Vienna ab initio simulation package (VASP) code (Kresse and Furthmüller, 1996). In addition, Perdewe-Burkee-Ernzerhof (PBE) generalized gradient approximation and the projected augmented wave (PAW) method were used to describe the ion-electron interactions in our systems (Perdew and Yue, 1986; Filippi et al., 1996). In this study, the plane-wave cutoff energy was set to 450 eV, and van der Waals corrections (optPBE-vdW) were adopted during structural optimization for the layer materials, and the vdWs interactions were described exactly by using DFT-D3 correction method of Grimme's scheme (Grimme et al., 2011). During the optimization, the Brillouin zone was represented by Monkhorst-Pack (MP), and the k-point mesh of 8 × 8 × 2 was used. Finally, the ion migration energies were acquired using the climbing-image nudged elastic band (CINEB) method (Henkelman et al., 2000; Yao et al., 2017). In our calculation, the structural optimization was considered complete when the force convergence criterion was <0.03 eV $Å^{-1}$ and the total energy per unit cell was within 10^{-5} eV. CI-NEB calculations were performed with linear interpolating 5 images between the initial and final states of the diffusion paths, and spring constants is set as -5. The geometry and energy of the images were then relaxed until the largest norm of the force orthogonal to the path was <0.03 eV $Å^{-1}$. To estimate the adsorption energy of M-ions on the MoS_2 anode material, the adsorption energy was calculated by the equation: $E_b = (E_{total} - E_{MoS_2} - nE_M)/n$, where E_{total} is the ground energy of M-ions adsorbed on MoS_2; E_{MoS_2}, the ground energy of MoS_2; E_M, the chemical potential of M (Li, Na, Mg, or Zn) atoms; n, the number of M atoms (Tian et al., 2020).

Experimental Methods

In a typical synthesis, 1.0 mmol ammonium molybdate [(NH4)6Mo7O24] and 28 mmol thiourea (CH4N2S) were mixed with 60 mL deionized water containing 1.0 g PVP, followed by stirring for 2 h and transferring the solution into a 100 mL Teflon-lined stainless-steel autoclave at 200°C for 24 h. After cooling down to room temperature, the black precipitate was obtained by centrifugation, washed several times with water and ethanol, dried at 80°C overnight, and collected as the MoS_2 material (Li and Peng, 2018).

For the electrochemical measurement, CR2032 cells were assembled in an argon-filled glove box by mixing the active samples, super-P and polyvinylidene fluoride at a weight ratio of 7: 2: 1. Next, the slurry was coated on Cu foil and dried at 60°C under vacuum for 10 h. After cutting into 12 mm discs, the working electrodes were obtained. Meanwhile, lithium (Li) metal or metal sodium (Na) was used as the anode, and the separators were commercial polypropylene (Celgard 2500 membrane) for Li-ions batteries and glass fiber (Whatman) for Na-ions batteries. For Li-ions batteries, the electrolyte was obtained by dissolving 1 M LiPF6 in ethylene carbonate (EC) and dimethyl carbonate (DMC) with 1:1 vol %. For Na-ions batteries, the electrolyte was prepared by dissolving 1 M NaClO4 and 5% fluoroethylene carbonate (FEC) in EC and DMC with 1:1 vol %. The electrochemical performances were recorded on Land cell test station (CT2001A) within the potential range of 0–3 V (vs Li/Li+).

RESULTS AND DISCUSSIONS

Our structures calculated have been fully relaxed using first-principles calculation. **Figure 1** shows the optimized crystal structure of MoS_2 (supercell), and the optimized lattice constants are a = b = 3.18 Å and c = 15.12 Å for unit-cells. In addition, the theoretical XRD pattern was calculated based on DFT, which was consistent with the experimental results shown in **Figure 1C**. In **Figure 1D**, it can be seen that there are four possible sites in the MoS_2 crystal structure. The large adsorption energy of ions in anode plays a fundamental role in providing a high ion storage energy in M-ions batteries, and the determination of suitable adsorption sites is a premise for the first-principles prediction of adsorption energies based on DFT. Therefore, the adsorption of M ions (Li, Na, Mg, and Zn) on MoS_2 was investigated in our work.

The greater the negative adsorption energy, the better the thermodynamics and the more favorable for the adsorption thermodynamically. In our calculation, the 3 × 3 × 1 supercell for MoS_2 was used to characterize the adsorption energy, corresponding to M_xMoS_2. Herein, as shown in **Figure 1D**, the different adsorption sites of metal on the MoS_2 had been considered, including top site where metal atom sits directly above Mo (Mo top), hollow site above the center of Mo-S hexagon (center Mo-S hexagon), bridge site at the middle of

TABLE 1 | The adsorption energies (eV) with different sites in MoS_2 structure.

Sites	Li	Na	Mg	Zn
Mo top	−1.24	−0.61	−0.31	−0.28
S top	−1.08	−0.29	−0.17	−0.12
Mo-S bridge	−1.16	−0.55	−0.28	−0.26
Center Mo-S hexagon	−2.54	−2.02	−0.97	−0.71

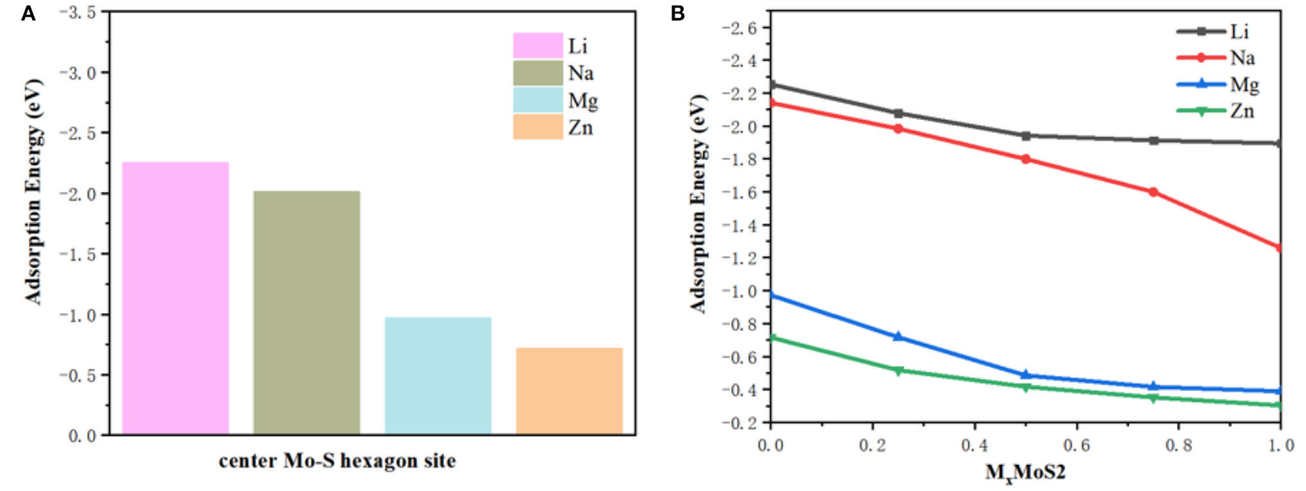

FIGURE 2 | (A) The adsorption energies center Mo-S hexagon sites and **(B)** the adsorption energies with M-ions concentration.

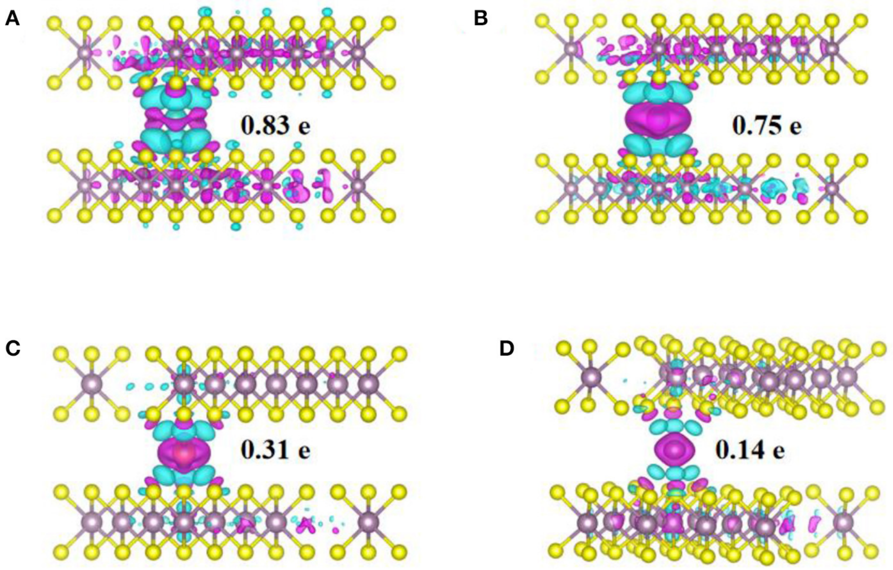

FIGURE 3 | The charge density difference and bader charge transfer of M-ions in MoS_2 structure. **(A)** Li-ion, **(B)** Na-ion, **(C)** Mg-ion, **(D)** Zn-ion.

Mo-S bond (Mo-S bridge) and the site directly above S atom (S top). And the adsorption energy had been shown in **Table 1**. Furthermore, the adsorption energy of Li and Na ions was found to be lower than that of Mg and Zn ions, implying the storage of Li and Na ions in the MoS_2 anode material, thus resulting in higher specific capacity for Li- and Na- ions batteries in **Figure 2A**. In **Figure 2B**, the adsorption energies of M ions (Li, Na, Mg and Zn) were seen to increase gradually with the increase of M-ions concentration, and the large coulomb repulsion became increasingly apparent in the adjacent positively charged M-ions due to the high metal adsorption concentration. It noted that the Na curve decreases the fastest among others with higher adsorption concentration. And it may caused by the strong coulomb repulsion between Na neighboring positively charged, the large Na ion radius and adsorption energy. In addition, the adsorption energy of M-ions was lower than the cohesive energy of metal, such as Li metals (−2.01 eV), in a real battery system to ensure a positive discharge potential. When the number of atom adsorption increases, the adsorption energy of M-ions was larger than the cohesive energy of metal, which may form clusters. In **Figure 2B**, the adsorption energy of Zn-ions was shown to be larger than that of the other ions, suggesting that a small amount of Zn-ions can be stored in the MoS_2 structure, leading to the low voltage and capacity of Zn-ions batteries. As a typical Li-ions batteries, we predict the capacity of MoS_2 for Li batteries theoretically.

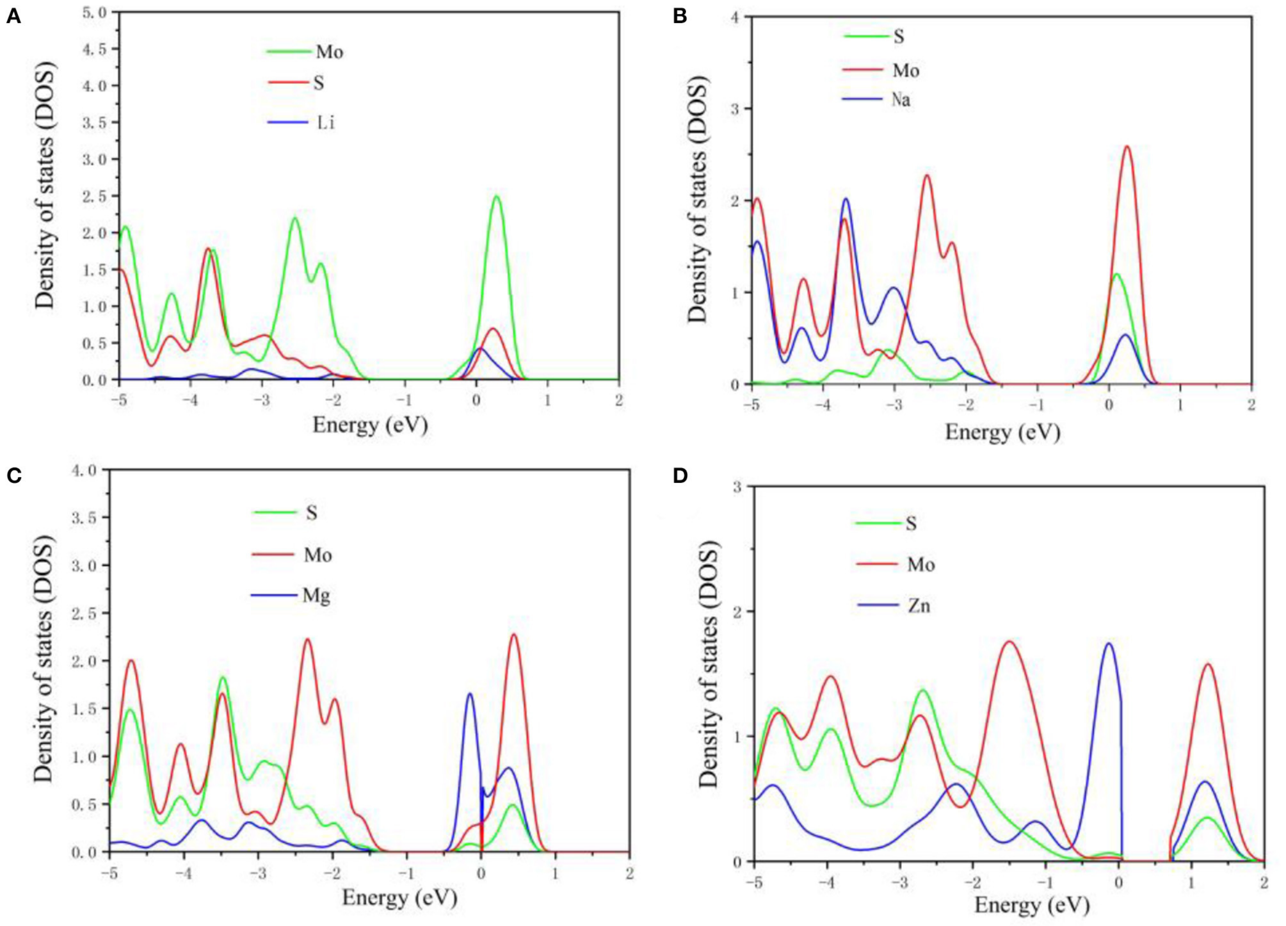

FIGURE 4 | The projected density of states in MoS_2 structure during Li **(A)**, Na **(B)**, Mg **(C)**, and Zn **(D)** intercalation.

From the **Figure 2B**, it is found that one Li atom adsorbed on a unit cell of MoS_2, corresponding to storage capacity of ∼687 mAh g^{-1}, the adsorption energy becomes smaller than the chemical potential.

To study the physical origin of ions adsorption and anode performance, the charge density differences and density of states (DOS) of the adsorption structures were calculated and shown in **Figures 3**, **4**. **Figure 3** shows the charge density differences obtained by subtracting the total electron densities of MoS_2 and isolated metal (Li, Na, Mg, and Zn) atom in center of Mo-S hexagon sites from that of the M_xMoS_2 structure. The isovalue was set as 0.03 eÅ^{-3}, charge depletion was in green and accumulation in red. the distribution was similar in the charge density difference between Li ions and Na ions. Additionally, the charge rehybridization during the intercalation of Mg and Zn ions was obviously greater than that of Li and Na ions. Furthermore, a considerable alteration can be observed in the charge accumulation region between Li/Mg ions and S atoms, because these atoms are closer to one layer of sulfurs in the MoS_2 structure. However, in **Figure 3B**, the transferred electrons were shown to be largely localized for Na ions, thus reducing the energy consumption during Na-ions diffusion.

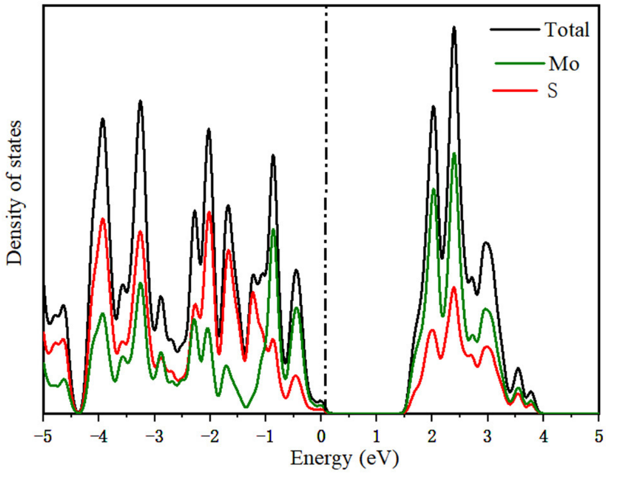

FIGURE 5 | The projected density of states in MoS_2 structure.

To further study the electronic structure of MoS_2 during the intercalation of M-ions, the DOS was investigated (**Figure 4**), with the Fermi level set to zero. In **Figures 4A,B**, the band

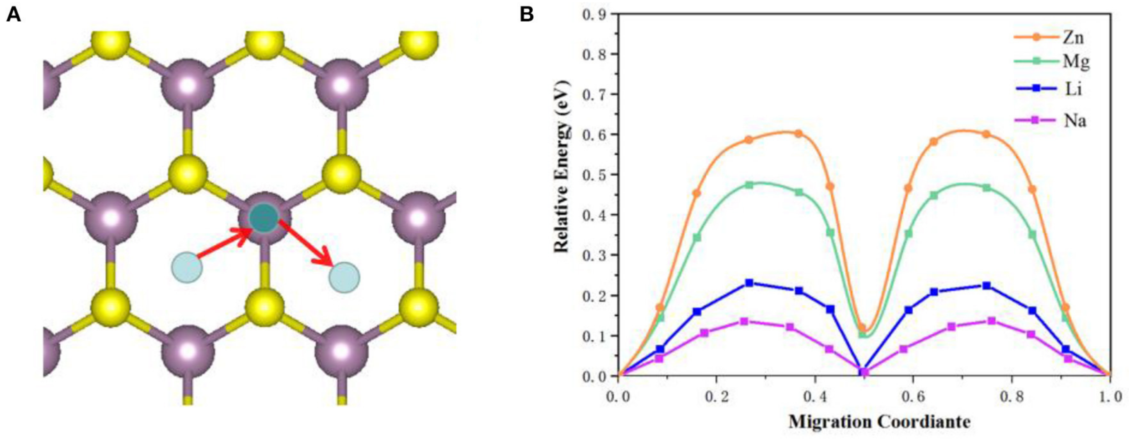

FIGURE 6 | The M-ions migration pathways **(A)** and corresponding migration energy **(B)** in MoS_2 structure.

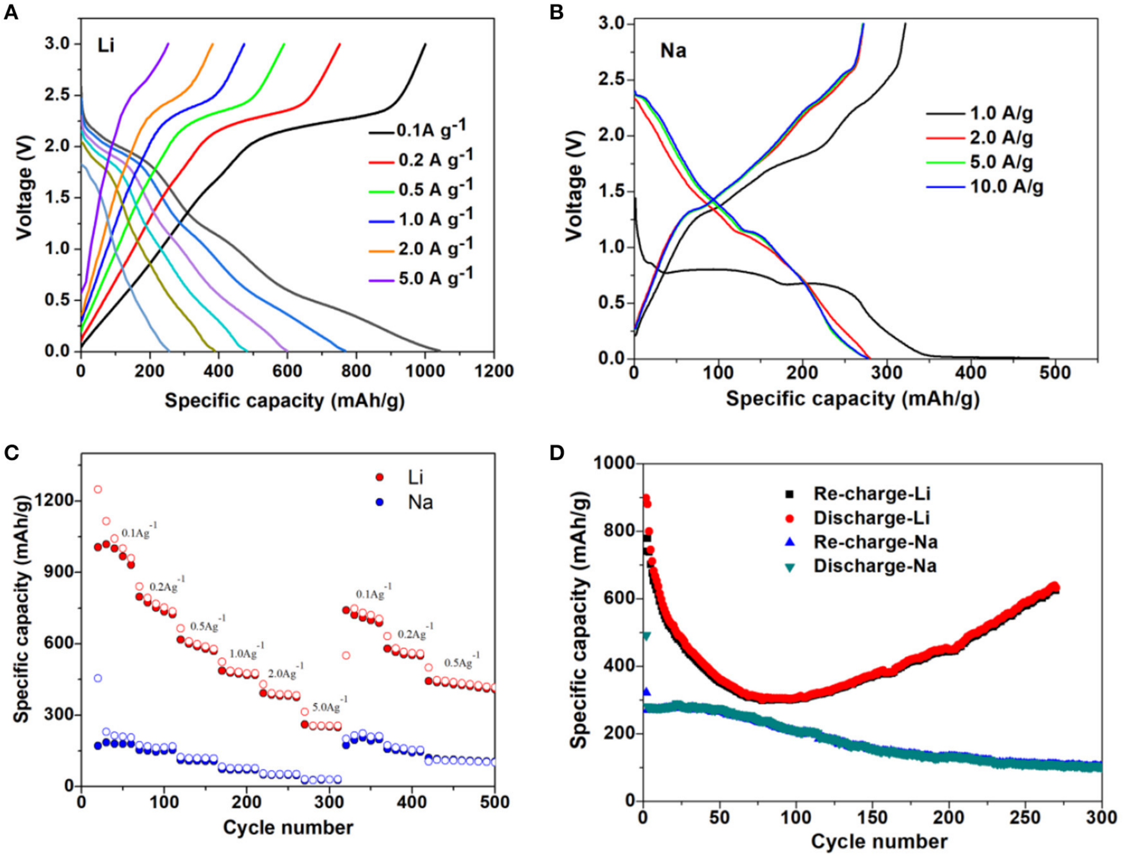

FIGURE 7 | Galvanostatic charge-discharge curves of MoS_2 at varied current density for **(A)** Li-ions battery anode and **(B)** Na-ions battery anode. **(C)** Rate properties of the MoS_2 anode for Li- and Na-ions battery. **(D)** Cycling properties of MoS_2 anode for Li- and Na-ions battery.

gap of MoS_2 was seen to vanish during the adsorption of Li and Na-ions in contrast to the existence of the band gap in the adsorption of Mg and Zn-ions on MoS_2. For comparison, the DOS of pure MoS_2 had be repeated (**Figure 5**), which was in accordance with the reported previously (Hao et al., 2018; Chen et al., 2020). These results indicated that the semiconductor MoS_2 may be transformed into metal during the insertion of Li and Na ions, while the properties of

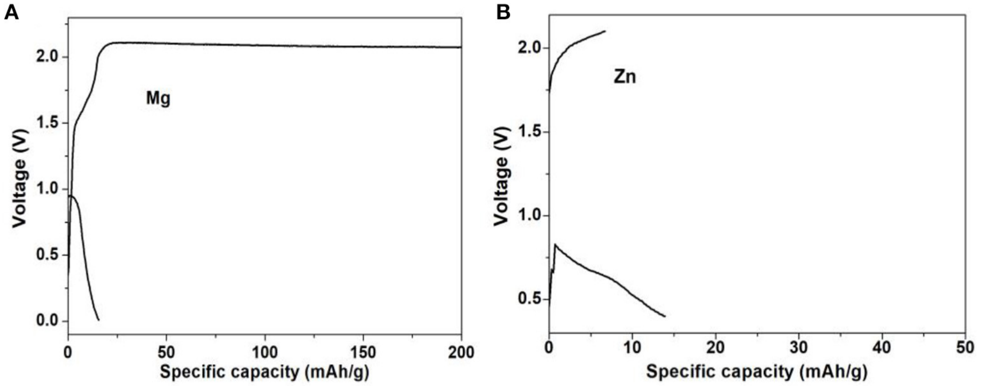

FIGURE 8 | Galvanostatic charge-discharge curves of MoS_2 for **(A)** Mg and **(B)** Zn-ions battery.

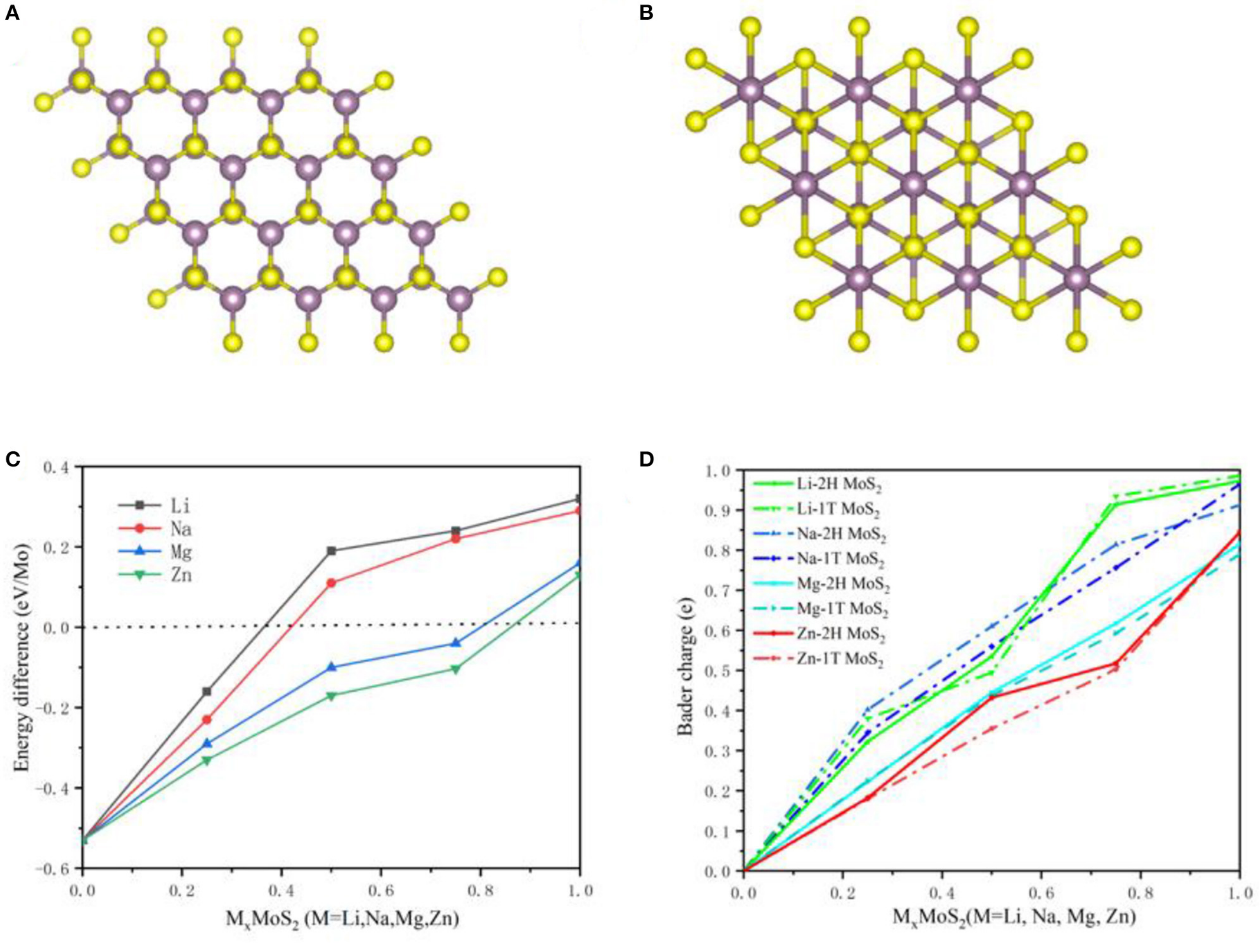

FIGURE 9 | The 2H **(A)** and 1T **(B)** for MoS_2 anodes structure. **(C)** Energy difference between the 2H and 1T structure of MoS_2 with Metal ions concentration and **(D)** Charge transfer with M-ions concentration in 2H and 1T MoS_2 structure.

the MoS_2 semiconductor remained unchanged during the insertion of Mg and Zn ions (**Figure 4D**), resulting in low electronic conductivity in divalent-ions batteries. Additionally, the conduction bands (CBM) were dominated by the Mo orbitals based on the DOS results. Meanwhile, the adsorbed ions (Li and Na) showed a discernible common peak between

-3 and -1.5 eV with the S orbitals of MoS_2, suggesting the hybridization between the adsorbed atoms and the MoS_2 anode. However, the atoms adsorbed by Zn ions did not exhibit such characteristics. This is consistent with charge transfer analysis, where Li and Na loses electrons while MoS_2 gains electrons with an itinerant feature. The electronic structures of MoS_2 adsorbed by Li and Na ions were metallic, which can ensure a good electrical conduction, while the MoS_2 adsorbed by Zn ions was shown to have semi-conductivity according to the electronic structure, leading to poor electrical conduction in Zn-ions batteries.

For the MoS_2 structure, the migration pathways of M-ions and the corresponding migration energy barriers were calculated using the CINEB method and shown in **Figure 6**. In **Figure 6A** the migration pathways of M-ions (Li, Na, Mg and Zn) were seen to move from the center Mo-S hexagon site to the adjacent Mo top site. Based on our DFT results, the migration energy barriers of M-ions were estimated and shown in **Figure 6B**, which were 0.22, 0.13, 0.47, and 0.61 eV for Li, Na, Mg and Zn ions, respectively. The energy barrier of Na ions was lower than that of the other ions and in the order of Zn>Mg>Li>Na, which was consistent with previous reports (Shu et al., 2016; Sun et al., 2018). It is worth noting that the migration barrier was lower than that of Li-ions in Na-ions, possibly due to the distribution of charge density differences. Besides, the divalent nature significantly induced charge rehybridization during the intercalation of Mg or Zn-ions, leading to sluggish mobility. These results agreed with the electronic structure analysis. Generally, the migration of ions inside the anode can directly describe the charging and discharging rates (C rate) for M-ions batteries, and thus the migration barrier of ions is always considered as a desirable design parameter.

Furthermore, the electrochemical experiments were performed for M-ions batteries, and the electrochemical performances of Li- and Na-ions batteries with the MoS_2 anode at different current densities were shown in **Figures 7A–C**. Even at the high current density of $2\,A\ g^{-1}$ for Li-ions batteries and $10\,A\ g^{-1}$ for Na-ions batteries, the discharge platform was still in good condition and could ensure effective ion/electron transmission. In **Figure 7C**, the capacity of the MoS_2 electrode was seen to remain at a high value when the current density returned to $0.1\,A\ g^{-1}$ for both Li- and Na-ions batteries, indicating the good rate capability. The long cycle performance of Li- and Na-ions batteries is shown in **Figure 7D**, with a good coincidence observed for the charge capacity and discharge capacity. In **Figure 8**, it can be seen that, compared with Li- and Na-ions batteries with MoS_2, Mg- and Zn-ions batteries with the MoS_2 anode, especially for the Zn-ions batteries, had very poor electrochemical performance. All these results were consistent with the theoretical calculation results.

Structural Transformation

Undoubtedly, the MoS_2 anode underwent a phase transition from 2H to 1T during Li ions intercalation, which has been confirmed by theoretical calculations and experimental analysis (Wang et al., 2013; Du et al., 2016; Zhu et al., 2019). **Figures 9A,B** shows the 2H and 1T structures of MoS_2, with a trigonal prism shape for 2H and an octahedron for 1T in the Mo coordination structure. In order to describe the phase transition in the MoS_2 anode during M-ions intercalation, the energy difference between the 2H and 1T structures of MoS_2 was calculated under different M-ions concentrations based on first-principles, and shown in **Figure 9C**. The energy of 2H was lower than that of the 1T structure at the early intercalation stage of M-ions, while the 1T structure obtained relatively more energy at a higher M-ions concentration, suggesting the occurrence of the transition from 2H to 1T. For Li-ions batteries, Li ions were adsorbed in the tetrahedral coordination center of the S-S, leading to the charge transfer from Li ions, which was confirmed by the above electronic structure analysis (**Figures 3**, **4**). In addition, the Mo atom was found to be surrounded by six S atoms after lithiation, implying that the Mo coordination structure may be transformed from 2H to 1T due to the intercalation of Li ions and the transfer of electrons. The 1T-type MoS_2 possessed a higher conductivity than the 2H-type MoS_2 due to its disordered octahedral structure. Therefore, this conversion of MoS_2 can improve the electronic conductivity. Moreover, the 1T structure of MoS_2 was more stable in energy when intercalating Li ions. In **Figure 9**, the phase conversion of 2H to 1T was also shown to be faster in Na ions than in the other M-ions, corresponding to a relatively lower concentration of Na-ions, which was caused by the larger ionic radius and electron transfer in Na-ions batteries. Therefore, the total charge transfer from M-ions to MoS_2 was calculated and shown in **Figure 9D**. However, in the case of a high concentration of Zn-ions and an abundant intercalation of Zn^{2+}, the energy was still higher in 2H than in the 1T structure, indicating that it is difficult to convert 2H to 1T in the MoS_2 structure. In **Figure 9D**, the Mo coordination structure showed no significant change during the intercalation of Zn-ions, with a small amount of charge transfer from Zn-ions to MoS_2. The aforementioned results suggest that the phase conversion from 2H to 1T is beneficial to improve the performance of the MoS_2 anode.

CONCLUSION

In summary, the intercalation mechanism of metal ions (Li, Na, Mg, and Zn) and the intrinsic properties of MoS_2 as an anode material in M-ions batteries were investigated by experiments and first-principles calculations, and the ground state properties, geometrical and electronic structures, as well as the intercalation mechanism of M-ions in MoS_2 were explored by DFT. Based on the calculation of adsorption energies, the Li and Na ions were stored in the MoS_2 anode material due to the low adsorption energies, which may result in higher specific capacity for Li- and Na-ions batteries, in contrast to a weak adsorption strength of MoS_2 for Mg and Zn ions, which is not conducive to the storage of anode. These results were also confirmed by the electrochemical performance experiments. Moreover, the density of states and charge density differences were investigated to explore the intercalation mechanism of M-ions. Our results suggest the hybridization between the Li/Mg-ions and the MoS$_2$ anode and a considerable alteration in the charge accumulation region due to the amount of charge transfer. However, such characteristics were not observed in the atoms adsorbed by Zn ions. Furthermore, the migration of M-ions was used to describe the charging and discharging rates (C rate) for M-ions batteries, and the energy barrier was shown to be in the order of Zn>Mg>Li>Na. Mg and Zn-ions had poor electrochemical performance due to weak adsorption and high energy barrier of ions, which also was confirmed by the electrochemical performance experiments. Interestingly, the phase conversion from 2H to 1T was found to occur during the intercalation of Li and Na ions, which may induce the high adsorption capacity and electron transfer, resulting in the high performance of the anode. However, the phase transformation failed to occur in Mg and Zn-ions batteries. In the future, we may improve the performance of multivalent-ions batteries by regulating the phase transformation of MoS$_2$. For example, the intercalation of molecules between the layers can increase the interlayer spacing and facilitate the intercalation of ions and the transfer of electrons, thereby making it more prone to phase change. Overall, the intercalation mechanism of M-ions can help optimize the design of layered structure for the high performance of M-ion batteries, and shed light on more efficient battery technologies.

DATA AVAILABILITY STATEMENT

The original contributions generated for the study are included in the article/supplementary material, further inquiries can be directed to the Corresponding author.

AUTHOR CONTRIBUTIONS

BBC developed the idea for the study. JBZ did the analyses and wrote the paper. XDL, JJZ, HL, BWH, JQZ, and SMJ conceived of the study, designed the study, and collected the data. All authors analyzed the data and were involved in writing the manuscript.

FUNDING

This work was supported by the National Natural Science Foundation of China (11902144); the Natural Science Foundation of the Jiangsu Higher Education Institutions of China (19KJB430022); and Postgraduate Research & Practice Innovation Program of Jiangsu Province (KYCX20_1074).

ACKNOWLEDGMENTS

We are grateful to the High Performance Computing Center of Nanjing Tech University for supporting the computational resources.

REFERENCES

Chen, J., Cao, J., Zhou, J., Wang, W., Zhang, Y., and Liu, X. (2020). Computational screening for enhanced hydrogen sensing by doped-2H and pristine,-1T., MoS. *Chem. Phys. Lett.* 16:137450. doi: 10.1016/j.cplett.2020.137450

Cui, C. Y., Wei, Z. X., Xu, J. T., Zhang, Y. Q., Liu, S. H., Liu, H. K., et al. (2018). Three-dimensional carbon frameworks enabling MoS2 as anode for dual ion batteries with superior sodium storage properties. *Energy Storage Mater.* 15, 22–30. doi: 10.1016/j.ensm.2018.03.011

Du, H., Guo, H. L., Liu, Y. N., Xie, X., Liang, K., Zhou, X., et al. (2016). Metallic 1T-LixMoS2 cocatalyst significantly enhanced the photocatalytic H-2 evolution over Cd0.5Zn0.5S nanocrystals under visible light irradiation. *ACS Appl. Mater. Interfaces* 8, 4023–4030. doi: 10.1021/acsami.5b11377

Filippi, C., Gonze, X., and Umrigar, C. J. (1996). "Generalized gradient approximations to density functional theory: comparison with exact results," in *Theoretical and Computational Chemistry,* ed J. M. Seminario (Amsterdam: Elsevier), 295–326. doi: 10.1016/S1380-7323(96)80090-2

Forsyth, M., Porcarelli, L., Wang, X. E., Goujon, N., and Mecerreyes, D. (2019). Innovative electrolytes based on ionic liquids and polymers for next-generation solid -state batteries. *Acc. Chem. Res.* 52, 686–694. doi: 10.1021/acs.accounts.8b00566

Grimme, S., Ehrlich, S., and Goerigk, L. (2011). Effect of the damping function in dispersion corrected density functional theory. *J. Comput. Chem.* 32, 1456–1465. doi: 10.1002/jcc.21759

Hao, J., Zheng, J., Ling, F., Chen, Y., Jing, H., Zhou, T., et al. (2018). Strain-engineered two-dimensional MoS$_2$ as anode material for performance enhancement of Li/Na-ion batteries. *Sci. Rep.* 8:2079. doi: 10.1038/s41598-018-20334-z,

Henkelman, G., Uberuaga, B. P., and Jonsson, H. (2000). A climbing image nudged elastic band method for finding saddle points and minimum energy paths. *J. Chem. Phys.* 113, 9901–9904. doi: 10.1063/1.1329672

Hu, J., Liu, Y., Liu, N., Lia, J., and Ouyang, C. (2020a). Theoretical prediction of T-graphene as a promising alkali-ion battery anode offering ultrahigh capacity. *Phys. Chem. Chem. Phys.* 22, 3281–3289. doi: 10.1039/C9CP06099E

Hu, J., Ouyang, C., Yang, S. A., and Yang, H. Y. (2019). Germagraphene as a promising anode material for lithium-ion batteries predicted from first-principles calculations. *Nanoscale Horiz.* 4, 457–463. doi: 10.1039/C8NH00333E

Hu, J., Zhong, C., Wu, W., Liu, N., Liu, Y., and Yang, S. A. (2020b). 2D honeycomb borophene oxide: a promising anode material offering super high capacity for Li/Na-ion batteries. *J. Phys.* 32:065001. doi: 10.1088/1361-648X/ab4f4d

Hu, L. R., Ren, Y. M., Yang, H. X., and Xu, Q. (2014). Fabrication of 3D Hierarchical MoS2/Polyaniline and MoS2/C architectures for lithium-ion battery applications. *ACS Appl. Mater. Interfaces* 6, 14644–14652. doi: 10.1021/am503995s

Ju, J., Ma, J., Wang, Y., Cui, Y., Han, P., and Cui, G. (2019). Solid-state energy storage devices based on two-dimensional nano-materials. *Energy Storage Mater.* 20, 269–290 doi: 10.1016/j.ensm.2018.11.025

Kresse, G., and Furthmüller, J. (1996). Efficiency of ab-initio total energy calculations for metals and semiconductors using a plane-wave basis set. *Comput. Mater. Sci.* 6, 15–50. doi: 10.1016/0927-0256(96)00008-0

Li, X. Y., and Peng, K. (2018). Hydrothermal synthesis of MoS2 nanosheet/palygorskite nanofiber hybrid nanostructures for enhanced catalytic activity. *Appl. Clay Sci.* 162, 175–181. doi: 10.1016/j.clay.2018.06.015

Manoj, M., Jasna, M., Anilkumar, K. M., Abhilash, A., Jinisha, B., Pradeep, V. S., et al. (2018). Sulfur-polyaniline coated mesoporous carbon composite in combination with carbon nanotubes interlayer as a superior cathode assembly for high capacity lithium-sulfur cells. *Appl. Surf. Sci.* 458, 751–761. doi: 10.1016/j.apsusc.2018.07.113

Mohanapriya, K., and Jha, N. (2019). Hierarchically hybrid nanostructure of carbon nanoparticles decorated graphene sheets as an efficient electrode material for supercapacitors, aqueous Al-ion battery and capacitive deionization. *Electrochim. Acta* 324:134870. doi: 10.1016/j.electacta.2019.134870

Perdew, J. P., and Yue, W. (1986). Accurate and simple density functional for the electronic exchange energy - generalized gradient approximation. *Phys. Rev. B* 33, 8800–8802. doi: 10.1103/PhysRevB.33.8800

Schmuch, R., Wagner, R., Horpel, G., Placke, T., and Winter, M. (2018). Performance and cost of materials for lithium-based rechargeable automotive batteries. *Nat. Energy* 3, 267–278. doi: 10.1038/s41560-018-0107-2

Shu, H. B., Li, F., Hu, C. L., Liang, P., Cao, D., and Chen, X. S. (2016). The capacity fading mechanism and improvement of cycling stability in MoS2-based anode materials for lithium-ion batteries. *Nanoscale* 8, 2918–2926. doi: 10.1039/C5NR07909H

Sun, D., Ye, D. L., Liu, P., Tang, Y. G., Guo, J., Wang, L. Z., et al. (2018). MoS2/graphene nanosheets from commercial bulky MoS2 and graphite as anode materials for high rate sodium-ion batteries. *Adv. Energy Mater.* 8:1702383. doi: 10.1002/aenm.201702383

Sun, Y., Guo, S. H., and Zhou, H. S. (2019). Exploration of advanced electrode materials for rechargeable sodium-ion batteries. *Adv. Energy Mater.* 9:1800212. doi: 10.1002/aenm.201800212

Tian, B., Du, W., Chen, L., Guo, J., Shu, H., Wang, Y., et al. (2020). Probing pristine and defective NiB6 monolayer as promising anode materials for Li/Na/K ion batteries. *Appl. Surf. Sci.* 527:146580. doi: 10.1016/j.apsusc.2020.146580

Wang, B. B., Zhang, Y., Zhang, J., Xia, R. Y., Chu, Y. L., Zhou, J. C., et al. (2017). Facile synthesis of a MoS2 and functionalized graphene heterostructure for enhanced lithium-storage performance. *ACS Appl. Mater. Interfaces* 9, 12907–12913. doi: 10.1021/acsami.7b00248

Wang, H. T., Lu, Z. Y., Xu, S. C., Kong, D. S., Cha, J. J., Zheng, G. Y., et al. (2013). Electrochemical tuning of vertically aligned MoS2 nanofilms and its application in improving hydrogen evolution reaction. *Proc. Natl. Acad. Sci. U. S. A.* 110, 19701–19706. doi: 10.1073/pnas.1316792110

Wang, S. W., Yang, B. C., Chen, H. Y., and Ruckenstein, E. (2018). Popgraphene: a new 2D planar carbon allotrope composed of 5-8-5 carbon rings for high-performance lithium-ion battery anodes from bottom-up programming. *J. Mater. Chem. A* 6, 6815–6821. doi: 10.1039/C8TA00438B

Wang, Y., Zheng, Y., Zhao, J., and Li, Y. (2020). Assembling free-standing and aligned tungstate/MXene fiber for flexible lithium and sodium-ion batteries with efficient pseudocapacitive energy storage. *Energy Storage Mater.* 33, 82–87. doi: 10.1016/j.ensm.2020.06.018

Xie, X. Q., Ao, Z. M., Su, D. W., Zhang, J. Q., and Wang, G. X. (2015). MoS2/graphene composite anodes with enhanced performance for sodium-ion batteries: the role of the two-dimensional heterointerface. *Adv. Funct. Mater.* 25, 1393–1403. doi: 10.1002/adfm.201404078

Yao, S. S., Cui, J., Lu, Z. H., Xu, Z. L., Qin, L., Huang, J. Q., et al. (2017). Unveiling the unique phase transformation behavior and sodiation kinetics of 1D van der Waals Sb2S3 anodes for sodium ion batteries. *Adv. Energy Mater.* 7:1602149. doi: 10.1002/aenm.201602149

Zhu, X. J., Li, D., Liang, X. G., and Lu, W. D. (2019). Ionic modulation and ionic coupling effects in MoS2 devices for neuromorphic computing. *Nat. Mater.* 18:141. doi: 10.1038/s41563-018-0248-5

Conflict of Interest: The authors declare that the research was conducted in the absence of any commercial or financial relationships that could be construed as a potential conflict of interest.

frontiers in Chemistry

ORIGINAL RESEARCH
published: 24 May 2021
doi: 10.3389/fchem.2021.676438

Efficient N_2- and O_2-Sensing Properties of $PtSe_2$ With Proper Intrinsic Defects

Xin Yong, Jianqi Zhang, Xiangchao Ma and Weiming He*

School of Physics and Optoelectronic Engineering, Xidian University, Xi'an, China

Developing efficient N_2 and O_2 gas sensors is of great importance to our daily life and industrial technology. In this work, first-principles calculations are performed to study the N_2 and O_2 gas-sensing properties of pure and defected $PtSe_2$. It is found that both N_2 and O_2 adsorb weakly on pure $PtSe_2$, and adsorption of the molecules induces negligible changes in the electrical and optical properties. Whereas the Pt@Se anti-site defect significantly improves the N_2 adsorption capacity of $PtSe_2$ and induces notable changes in the electrical property. Similar results are also observed for the Pt and Se vacancies and Pt@Se anti-site defects when examining O_2 adsorption. In addition, notable changes in the optical absorption spectra of the $PtSe_2$ with Pt@Se defect are induced upon N_2 adsorption, which also occurs for $PtSe_2$ with Pt and Se vacancies and Pt@Se anti-site defects upon O_2 adsorption. These results demonstrate that $PtSe_2$ with the corresponding defects can be both excellent electrical and optical sensors for detecting N_2 and O_2 gases. Our work offers a new avenue for preparing efficient gas sensors.

Keywords: gas sensing, electronic structures, optical properties, first-principles calculations, intrinsic defects

Edited by:
Guangzhao Wang,
Yangtze Normal University, China

Reviewed by:
Dongwei Ma,
Anyang Normal University, China
Yanan Tang,
Zhengzhou Normal University, China

****Correspondence:***
Xiangchao Ma
xcma@xidian.edu.cn

Specialty section:
This article was submitted to Theoretical and Computational Chemistry,
a section of the journal Frontiers in Chemistry

Received: *05 March 2021*
Accepted: *05 May 2021*
Published: *24 May 2021*

Citation:
Yong X, Zhang J, Ma X and He W (2021) Efficient N_2- and O_2-Sensing Properties of $PtSe_2$ With Proper Intrinsic Defects.
Front. Chem. 9:676438.
doi: 10.3389/fchem.2021.676438

INTRODUCTION

Oxygen is not only essential to the lives of humans and animals but also the key to the combustion-dependent processes such as power generation, chemical compound production, and heating. Controlling the air-to-fuel ratio during the combustion process at the critical point of excess oxygen is beneficial for improving the combustion efficiency, product generation, and safe combustion (Shuk and Jantz, 2015; Zhang et al., 2017). Because the presence of O_2 corrodes gas storage and transportation systems, monitoring O_2 in biomethane is also a necessary part (Urriza-Arsuaga et al., 2019). In the medical and food processing and waste management industries, sometimes it is also necessary to measure the oxygen content (Hong et al., 2018; Wang et al., 2019). Therefore, an efficient sensor for detecting O_2 molecules plays an important role in modern technology. On the other hand, biogas is believed to be a promising substitute for natural gas due to its high methane content. However, the presence of impurity gas like N_2 leads to a lower heating value. In addition, fuel dilution with N_2 gas is generally used to reduce heat radiation, which is one of the main factors limiting the efficiency of gas turbines and internal combustion engines. Therefore, in order to meet the quality specifications, it is also necessary to detect and control N_2 gas (Yi et al., 2013).

The generally used O_2 and N_2 gas sensors can be classified as electrical sensors and optical sensors according to the sensing principles: First, each kind of sensor requires efficient adsorption of the targeting gas molecules on the sensing material. For an electrical sensor, prominent charge transfer between the gas molecules and sensing material or charge trapping upon molecule adsorption

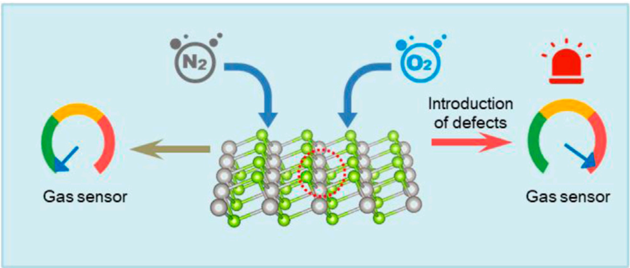

GRAPHICAL ABSTRACT |

converts the adsorption of gas molecules into electrical signal for detection. For an optical sensor, the adsorption of gas molecules notably alters the optical absorption spectrum of the sensing material. Traditionally, gas-sensing materials are metal–oxide–semiconductors, such as TiO_2, SnO_2, and ZnO (Kumar et al., 2014; Ibrahim et al., 2016; Xia et al., 2016). Recently, because of the theoretically infinite volume-to-surface ratio, which can provide enough active gas adsorption sites, intense studies on the gas-sensing properties of two-dimensional monolayer materials are reported (Yue et al., 2013; Bui et al., 2015; Ma et al., 2016a; Ma et al., 2016b; Sajjad et al., 2017; Klement et al., 2018; Ma X. et al., 2018; Ma D. et al., 2018; Jin et al., 2019; Ma D. et al., 2019; Ma et al., 2021). In particular, the intrinsic excellent sensing properties of Pt element render the monolayer $PtSe_2$ as one of the mostly examined 2D gas-sensing material (Zhao et al., 2020). For example, Muhammad Sajjad et. al. studied the gas sensitivity of monolayer $PtSe_2$ to the toxic NO_2, NO, NH_3, and CO gases (Sajjad et al., 2017); Dachang Chen et. al. studied the potential of $PtSe_2$ as a gas sensor to detect SF_6 decompositions (Chen et al., 2018).

On the other hand, the intrinsic defects, which can significantly affect the chemical, electrical, optical, and magnetic properties of $PtSe_2$, are also extensively investigated. For example, Junfeng Gao et. al. studied the atomic structures and thermodynamic stability of vacancy defects. The study of Husong Zheng et. al. shows that the intrinsic Pt vacancy, Se vacancy, and Se@Pt anti-site defects can widely exist in ultrathin layered $PtSe_2$ (Zheng et al., 2019); Ahmet Avsar et. al. found that Pt vacancy is responsible for the layer-dependent magnetism of $PtSe_2$ (Avsar et al., 2019). In 2020, Jun Ge et. al. also reported the existence of magnetic moments induced by Pt vacancy defects in $PtSe_2$ flakes (Ge et al., 2020).

Considering the ubiquity and easy introduction of intrinsic defects in $PtSe_2$, in this work, we explore the N_2 and O_2 gas-sensing properties of both pure $PtSe_2$ and $PtSe_2$ with intrinsic defects, including Pt and Se vacancy defects (hereafter denoted as Pt-v and Se-v), Pt@Se and Se@Pt anti-site defects, and Pt and Se interstitial defects (hereafter denoted as Pt-inter and Se-inter), by first-principles calculations. It is found that $PtSe_2$ with the Pt@Se anti-site defect has strong N_2 adsorption capacity and exhibits significant change in the electrical properties upon N_2 adsorption. Similar results are also observed for $PtSe_2$ with Pt-v, Se-v, and Pt@Se defects when examining O_2 adsorption. In addition, notable changes in the optical absorption spectra of the $PtSe_2$ with Pt@Se defect are induced upon N_2 adsorption, which also occurs for $PtSe_2$ with Pt-v, Se-v, and Pt@Se upon O_2 adsorption. These results demonstrate that $PtSe_2$ with the corresponding defects can sensitively detect N_2 and O_2 molecules.

COMPUTATIONAL METHODS

The first-principles calculations are conducted using the Vienna *Ab initio* Simulation Package (VASP) (Kresse and Furthmüller, 1996). A cutoff energy of 400 eV is used for plane wave expansion, and the accuracy for self-consistent iteration is set to 10^{-5} eV. 4 × 4 supercells of pure $PtSe_2$ are used for modeling the defected and molecules adsorbed on $PtSe_2$, and the Brillouin zones for them are sampled with 3 × 3 × 1 gamma-centered k-points (Monkhorst and Pack, 1976). A vacuum layer larger than 30 Å is used for separating the atoms from their periodic images. For geometric optimization, the generalized gradient approximation (GGA) functional of Perdew–Burke–Ernzerhof is used (Perdew et al., 1996), and the atomic structures are fully relaxed until the residual forces on each atom are smaller than 0.02 eV/Å. To describe the interaction between the molecule and surface, DFT-D2 correction is used in the calculation. The more accurate HSE06 functional is used for calculating the electronic structures of pure and defected $PtSe_2$ (Heyd et al., 2003). In order to quantify the electron charge redistribution between the adsorbed gas molecule and $PtSe_2$, the Bader charge is analyzed based on the method of Henkelman (Henkelman et al., 2006; Sanville et al., 2007).

RESULTS AND DISCUSSION

Adsorption Structures of Gas Molecules on Pure and Defected $PtSe_2$

Adsorption of gas molecules on $PtSe_2$ is an important parameter determining its gas-sensing properties. To establish the most stable adsorption structures of gas molecules on the monolayer, we first set many different configurations of gas molecules on the basal plane of $PtSe_2$, which are then geometrically optimized. In this article, the Pt-v (Se-v) defect is formed by removing one Pt

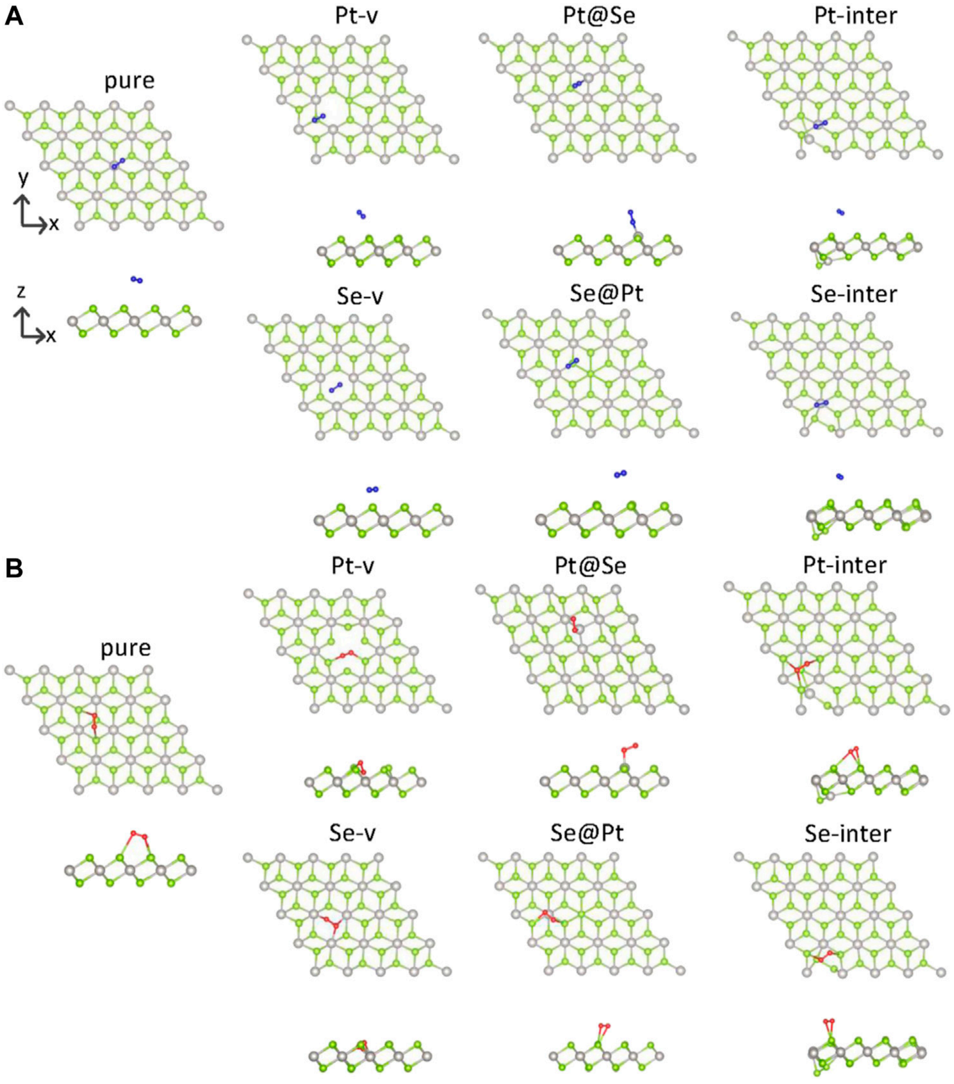

FIGURE 1 | Top and side views of the adsorption structures of N_2 **(A)** and O_2 **(B)** on pure and defected $PtSe_2$. The green and gray balls indicate Se and Pt atoms, respectively.

TABLE 1 | Adsorption distance *L* (in Å), the absorption energy *Ea* (in eV), the change in the molecular bond length *Δ* (in Å) upon adsorption, and the values of Bader charges on molecules for the various adsorption structures.

	N_2				O_2			
	***L*(Å)**	**E_a (eV)**	**Δ(Å)**	**Bader(*e*)**	**L(Å)**	**E_a (eV)**	**Δ(Å)**	**Bader(*e*)**
Pure	3.47	0.08	0.0004	0.02	2.85	0.51	0.0206	0.20
Pt-v	3.68	1.83	0.0002	0.02	1.86	2.36	0.2458	0.89
Se-v	3.58	0.19	0.0003	0.04	2.05	3.20	0.1693	0.80
Pt@Se	1.98	0.61	0.0142	0.14	1.92	1.98	0.0784	0.44
Se@Pt	3.55	0.08	0.0005	0.02	2.60	0.61	0.0297	0.28
Pt-inter	3.52	0.11	0.0005	0.02	2.73	0.59	0.0329	0.29
Se-inter	3.57	0.10	0.0005	0.02	2.91	0.52	0.0195	0.20

(Se) atom from a 4 × 4 supercell of pure $PtSe_2$; the Pt@Se (Se@Pt) defect is formed by substituting Pt (Se) for Se (Pt), and the Pt-inter and Se-inter defects are formed by inserting Pt and Se atoms into the pure $PtSe_2$. The structures with the largest adsorption energies are regarded as the most possible ones. The adsorption energy is defined as follows:

$$E_a = E_{\text{molecule}} + E_{\text{monolayer}} - E_{\text{total}},$$

where E_{molecule} is the energy of an isolated gas molecule, $E_{\text{monolayer}}$ is the energy of pure and defected $PtSe_2$, and E_{total} is that of the molecule adsorbed system. The obtained most possible structures of nitrogen and oxygen adsorbed on pure and defected $PtSe_2$ are shown in **Figure 1**. **Figure 1A** shows the adsorption structures of N_2 on pure $PtSe_2$ and $PtSe_2$ with six kinds of intrinsic defects. **Figure 1** shows the adsorption structures of O_2 on pure $PtSe_2$ and $PtSe_2$ with the six kinds of intrinsic defects. In **Table 1**, we list the detailed adsorption energy, related bond lengths, and Bader charges on molecules for the adsorption structures shown in **Figure 1**. It is necessary to point out that the reason why the Pt-v defects in **Figures 1A,B** are different is that the atomic structures around the Pt-v defect change significantly upon adsorption of N_2, whereas the changes in atomic structures are minor upon adsorption of O_2.

To describe the bonding length of the molecules on the $PtSe_2$ surface, we define the adsorption distance L as the closest distance between the atoms of gas molecules and the surface atoms. As shown in **Figure 1**; **Table 1**, it is observed that the N_2 molecule bonds with the surface Se atom of pure $PtSe_2$ and the adsorption distance and absorption energy is, respectively, 3.47 Å and 0.08 eV, which is similar to the vdW interaction length between Se and N atoms. This indicates that N_2 adsorbs on the surface by very weak vdW force. For the $PtSe_2$ with Pt-v defect, N_2 still bonds with the surface Se atom and the absorption energy becomes about 1.83 eV, which is much larger than that on pure $PtSe_2$. This is because the atomic structures around the Pt-v defect change significantly upon adsorption of N_2, which releases a significant amount of energy as will be discussed in later section. However, the adsorption distance is as long as 3.68 Å. For $PtSe_2$ with Pt@Se anti-site defect, N_2 adsorbs on the surface by forming N–Pt bond, and the bond length and absorption energy are, respectively, 1.98 Å and 0.61 eV, which is within the sum of atomic radii of N and Pt (2.33 Å), indicating chemical interaction between them. For $PtSe_2$ with Se-v, Se@Pt, Pt-inter, and Se-inter defects, the N_2 molecule still bonds with the surface Se atom and the adsorption energies are only slightly larger than those on pure $PtSe_2$, and the adsorption distances are between 3.5 and 3.6 Å. Therefore, the interaction between these defected structures and N_2 molecule is of the vdW nature.

As shown in **Figure 1B**; **Table 1**, O_2 bonds with the surface Se atoms of pure $PtSe_2$, and the corresponding adsorption distance and adsorption energy are, respectively, 2.85 Å and 0.51 eV, which is larger than the lengths of any chemical bonds between O and Se. This indicates that O_2 adsorbs on the surface mainly by vdW force. For $PtSe_2$ with Pt-v defect, the adsorption distance becomes 1.86 Å, which is similar to the sum of covalent radii of O and Se (1.89 Å), and the absorption energy is as large as 2.36 eV. This indicates that O_2 is chemically bonded to the surface. For $PtSe_2$ with Se-v and Pt@Se defects, the O_2 molecule is bonded to the surface by forming one or more Pt–O chemical bonds, and the adsorption energies are, respectively, 3.20 and 1.98 eV, and the bond lengths are, respectively, 2.05 and 1.92 Å, which is smaller than the sum of atomic radii of O and Pt (2.25 Å). Notably, as shown in **Figure 1B**, the O_2 molecule is deeply embedded in the vacancy sites of $PtSe_2$ with Pt-v and Se-v defects, indicating strong adsorption of O_2 on the surfaces. For $PtSe_2$ with Se@Pt, Pt-inter, and Se-inter defects, O_2 still bonds with the surface Se atom, and the adsorption energies are only slightly larger than those on the pure surface and the adsorption distances are between 2.60 and 2.91 Å. Therefore, the interaction between these defect structures and O_2 molecules is of vdW nature.

From the above results, it is noted that O_2 and N_2 molecules only weakly adsorb on the pure $PtSe_2$, while all the intrinsic defects enhance more or less the interaction between the gas molecules and $PtSe_2$. In particular, the Pt@Se anti-site defect transforms the initially weak vdW interaction into a strong chemical interaction between the molecules and $PtSe_2$, and the Pt-v and Se-v defects also result in strong chemical interactions between O_2 and $PtSe_2$. In addition, O_2 adsorbs more strongly than N_2 on both the pure and defected $PtSe_2$. These results are also supported by the changes in the molecular bond lengths and the Bader charges on the molecules, as listed in **Table 1**.

Charge Transfer and Electronic Structures of Gas Molecules on Pure and Defected $PtSe_2$

Prominent charge transfer between the gas molecules and $PtSe_2$ upon molecule adsorption is a fundamental prerequisite for transforming the existence of a gas molecule into electrical signal during gas-sensing application. To investigate the charge transfer between them, the Bader charge on molecules and charge density difference (CDD) for the molecule adsorbed on pure and defected $PtSe_2$ are calculated and shown in **Figure 2**. The CCD is calculated according to the following equation:

$$\Delta_\rho = \rho_{\text{total}} - \rho_{\text{monolayer}} - \rho_{\text{molecule}},$$

where ρ_{total}, $\rho_{\text{monolayer}}$, and ρ_{molecule} are the charge densities of the molecule-adsorbed system, pure or defected $PtSe_2$ without molecule adsorption, and the isolated gas molecule, respectively. From **Figure 2**, it is noted that there is always charge transfer from $PtSe_2$ to N_2 and O_2 upon molecule adsorption, except that the charge transfer between N_2 and pure $PtSe_2$ is very weak, with a Bader charge of 0.02 *e*. For $PtSe_2$ with Pt-v, Se-v, Se@Pt, Pt-inter, and Se-inter defects, the charge transfer between N_2 and them is almost the same as that between N_2 and pure $PtSe_2$, whereas the Pt@Se anti-site defect significantly promotes charge transfer from $PtSe_2$ to N_2, with a Bader charge of 0.14 *e*. Moreover, the results of CDD show that significant charge redistribution around the Pt@Se anti-site defect also occurs upon adsorption of N_2, suggesting additional charge trapping effect of the defect. For O_2 on pure $PtSe_2$ (**Figure 2B**), the amount of charge transfer is relatively large (about 0.20 *e*), and the introduction of Pt-v, Se-v, and Pt@Se defects further increases the amount of charge transfer, with Bader charges being up to 0.89 *e*, 0.80 *e*, and 0.44 *e*, respectively. For $PtSe_2$ with Se@Pt, Pt-inter, and Se-inter defects, the charge transfer is only slightly larger than that on pure $PtSe_2$, with Bader charges between 0.20 *e* and 0.29 *e*. Similarly, the results of CDD in **Figure 2** show that significant charge redistribution around the various intrinsic defects occurs upon adsorption of O_2, suggesting additional charge trapping effects of the defects.

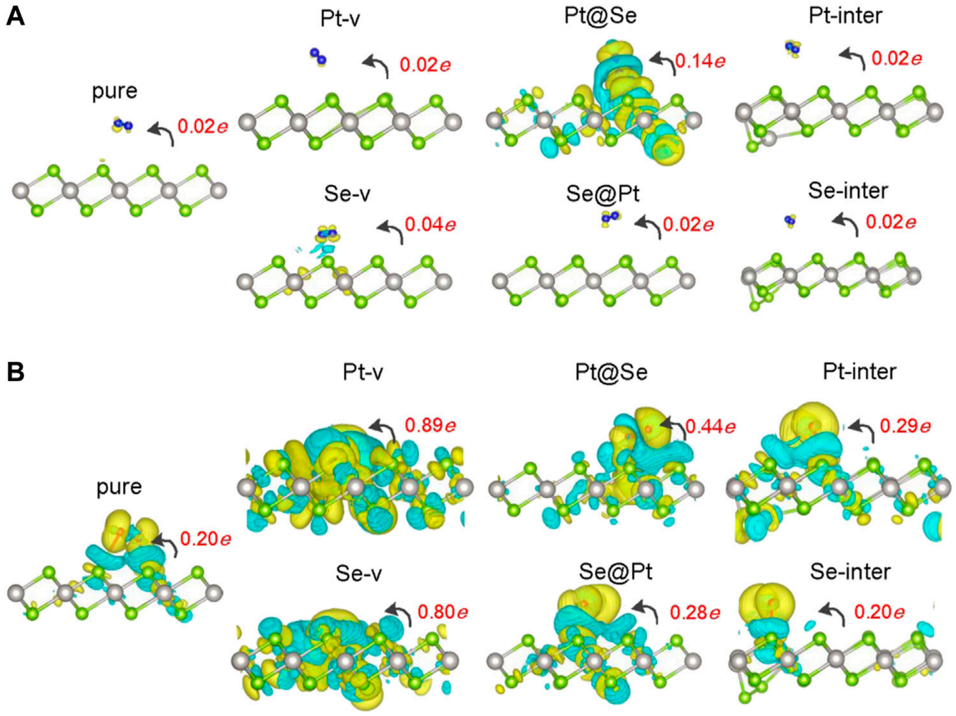

FIGURE 2 | Charge density difference (CDD) for N_2 **(A)** and O_2 **(B)** adsorbed pure and defected $PtSe_2$. The yellow (cyan) region represents charge accumulation (depletion), and the values of isosurfaces for all the structures are set to 0.0003 $e/Å^{-3}$. The red numbers indicate the values of Bader charges on the molecules, and the black curved arrows indicate the orientation of charge transfer.

In order to understand the adsorption structures, charge transfer between molecules and $PtSe_2$, and the charge trapping effects of the intrinsic defects shown above, we investigate the density of states (DOS) for pure and defected $PtSe_2$ with the adsorption of gas molecules, the DOS of isolated N_2 and O_2 molecules, and the DOS of pure and defected $PtSe_2$. As shown in **Figure 3**, the DOS of isolated N_2 molecules shows that the 2π bonding orbital just lies under the Fermi level and has a lower height than 5σ orbital near −1 eV. The DOS of N_2 basically still retains the characteristics of isolated N_2 after adsorption on pure $PtSe_2$ and $PtSe_2$ with Pt-v, Se-v, Se@Pt, Pt-inter, and Se-inter defects, which is consistent with the weak interaction between N_2 and pure and the defected $PtSe_2$, whereas the DOS of N_2 changes significantly upon the adsorption on $PtSe_2$ with the Pt@Se anti-site defect. For example, the antibonding orbital of N_2 near 4 eV splits into three peaks with lower height, and the relative values of the two bonding orbitals near −7.5 eV reverse, and they are in resonance with electronic states from $PtSe_2$, indicating strong chemical interaction between N_2 and $PtSe_2$. In addition, because N_2 bonds with the $PtSe_2$ surface by forming Pt–N chemical bonds, the large electronegativity of N results in notable electron gain from Pt, which leads to the large value of Bader charge on N_2. On the other hand, as shown in **Figure 4**, the electronic states near the valence band maximum (VBM) and conduction band minimum (CBM) are almost unchanged upon adsorption of N_2 on pure $PtSe_2$ and $PtSe_2$ with Se-v, Se@Pt, Pt-inter, and Se-inter defects, whereas small gap states near both CBM and VBM appear upon adsorption of N_2 on the $PtSe_2$ with Pt@Se defect, which may additionally trap electrons and holes. These are consistent with the results of CDD shown above. For the $PtSe_2$ with Pt-v defect, the atomic structures around the defect significantly change upon adsorption of N_2, which introduces many gap states, as will be discussed in the following section.

As shown in **Figure 3B**, the DOS of isolated O_2 shows five peaks lower than the Fermi level, and the $2\pi^*$ antibonding orbital is the highest occupied orbital. The DOS of O_2 hybridizes notably and to different extent with the DOS of $PtSe_2$ upon adsorption on pure $PtSe_2$ and defected $PtSe_2$, and the hybridization is especially significant on $PtSe_2$ with Pt-v, Se-v, and Pt@Se defects. These are consistent with the strong and different interactions between O_2 and pure and defected $PtSe_2$. Moreover, because O_2 bonds with the $PtSe_2$ surface by forming Pt (Se)–O vdW or chemical bonds, the large electronegativity of O results in notable electron gain, which leads to the large values of Bader charges on O_2. On the other hand, as shown in **Figure 4B**, new electronic states near the VBM and CBM are introduced upon adsorption of O_2 on pure $PtSe_2$ and all the defected $PtSe_2$, which may additionally trap electrons and holes. Therefore, significant redistribution of charge density around the defects occurs, as shown in the CDD of **Figure 2B**.

From the results above, it is noted that for N_2, it is mainly the Pt@Se anti-site defect that can notably enhance the charge transfer between the gas molecules and $PtSe_2$ and charge trapping states, while the other defects show negligible effects. For O_2, all the defects, except Se-inter, enhance the charge transfer between the molecule and $PtSe_2$, and the effects of Pt-v, Se-v, and Pt@Se defects are the most significant. In addition,

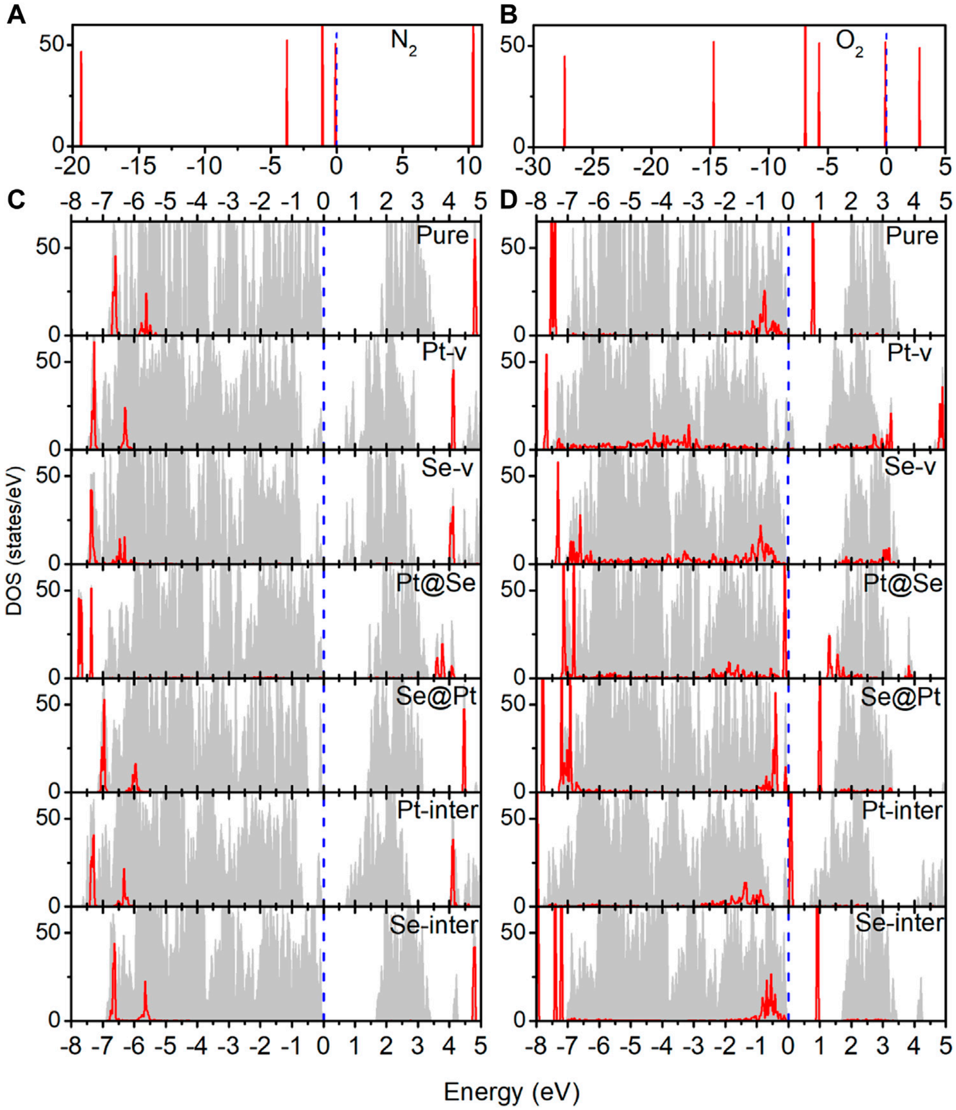

FIGURE 3 | (A) Density of states (DOS) of the isolated N_2 molecule. **(B)** DOS of the isolated O_2 molecule. **(C)** DOS of pure and defected $PtSe_2$ with the adsorption of N_2. **(D)** DOS of pure and defected $PtSe_2$ with the adsorption of O_2. The gray areas indicate total DOS of the corresponding structures, and the red lines indicate projected DOS of the absorbed molecule. The values of DOS for adsorbed N_2 and O_2 on $PtSe_2$ are set to 1.5 and 4 times for clear comparison. The Fermi levels (blue-dashed lines) for all the structures are set to 0 eV.

the intrinsic defects introduce new electron and/or hole trapping states near the VBM and/or CBM. The charge transfer and charge trapping effects can result in significant electric signal when the defected $PtSe_2$ is used as electrical sensors.

OPTICAL ABSORPTION PROPERTIES OF PURE AND DEFECTED PTSE2 WITH MOLECULE ADSORPTION

The intrinsic defects and molecule adsorption not only affect the electronic structure and electrical properties of $PtSe_2$ but may also affect its optical absorption properties. In order to study how they affect the optical properties of $PtSe_2$, we calculated the optical absorption coefficients of pure and defected $PtSe_2$ absorbed with N_2 and O_2. The specific calculation procedure is the same as one of our previous works (Ma X. et al., 2018; Ma X. et al., 2019; Yong et al., 2020; Jian et al., 2021). **Figure 5** shows the optical absorption coefficients for polarization of E field along the in-plane x direction of pure and defected $PtSe_2$ with and without the adsorption of N_2 and O_2. Note that the results for the polarization of E field along the in-plane y direction are almost the same as those along the in-plane x direction. As shown in **Figure 5**, for adsorption of N_2, the optical absorption coefficients of pure $PtSe_2$ and $PtSe_2$ with Se-v,

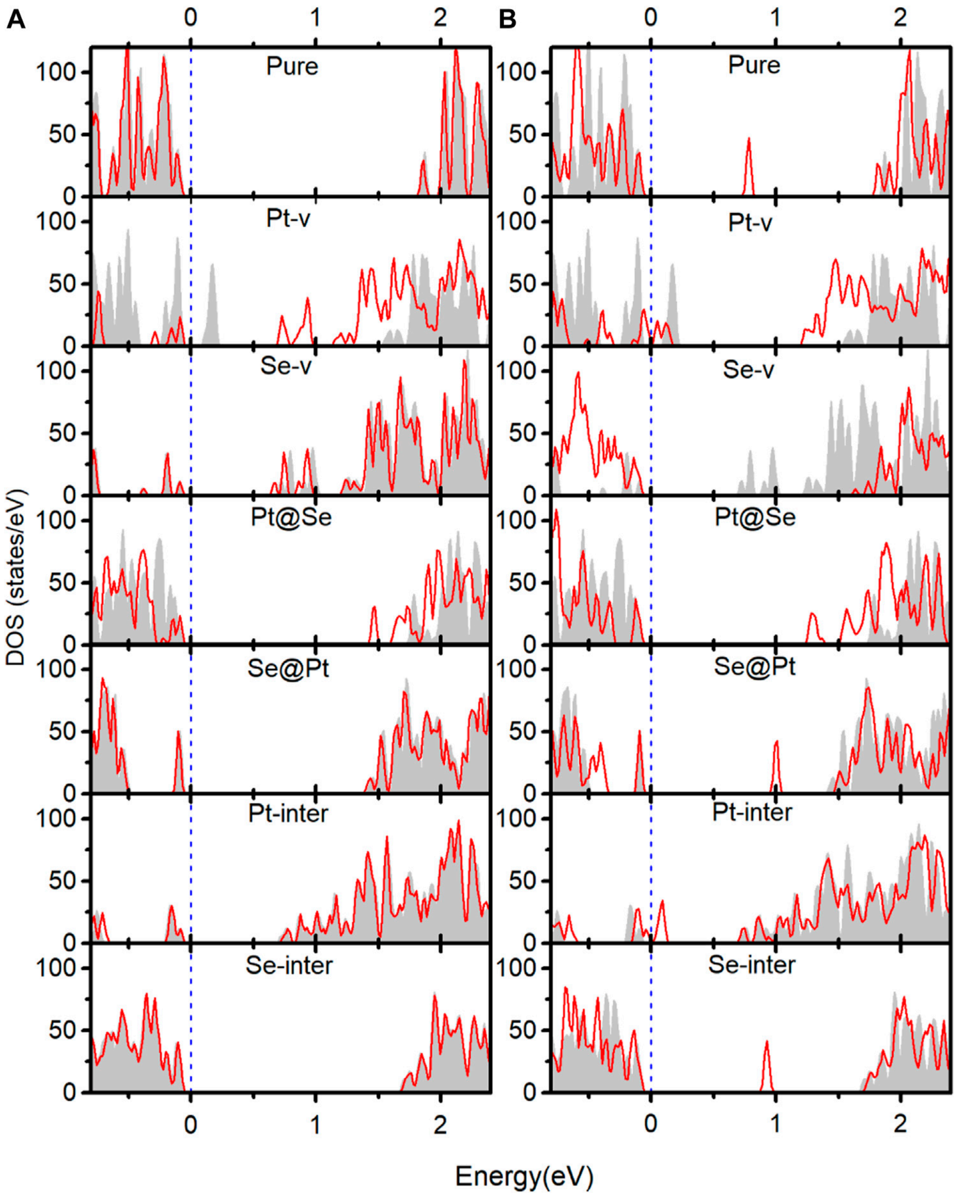

FIGURE 4 | Red lines indicate the DOS near the band edges of pure and defected $PtSe_2$ with the adsorption of N_2 **(A)** and O_2 **(B)**. The gray areas indicate the DOS near band edges of pure and defected $PtSe_2$.

Se@Pt, Pt-inter, and Se-inter defects are basically the same as those of the structures without N_2 adsorption. For the $PtSe_2$ with Pt-v defect, there are two absorption peaks around 0.33 and 0.72 eV, whereas the adsorption of N_2 eliminates these two absorption peaks and introduces a new and prominent absorption peak around 1.07 eV. For the $PtSe_2$ with Pt@Se defect, the optical absorption edges are slightly extended to lower energy.

On the other hand, for adsorption of O_2, the optical absorption coefficients of pure $PtSe_2$ and $PtSe_2$ with Pt-inter and Se-inter defects are roughly the same as those of the corresponding structures without adsorption. For the $PtSe_2$ with Pt-v defect, the initial two absorption peaks around 0.33 and 0.72 eV are weakened and the absorption valley at 1.3 eV is filled upon the adsorption of O_2. For the $PtSe_2$ with Se-v defect, the notable absorption peak around 1.0 eV is quenched, and the optical absorption edge blue shifts significantly upon O_2 adsorption. For $PtSe_2$ with Pt@Se and Se@Pt defects, the optical absorption edges, mainly red shift slightly upon O_2 adsorption. The notable changes in the absorption coefficients of defected $PtSe_2$ upon N_2 and O_2 adsorption further verify the significant interactions between them and suggest that the characteristic changes in

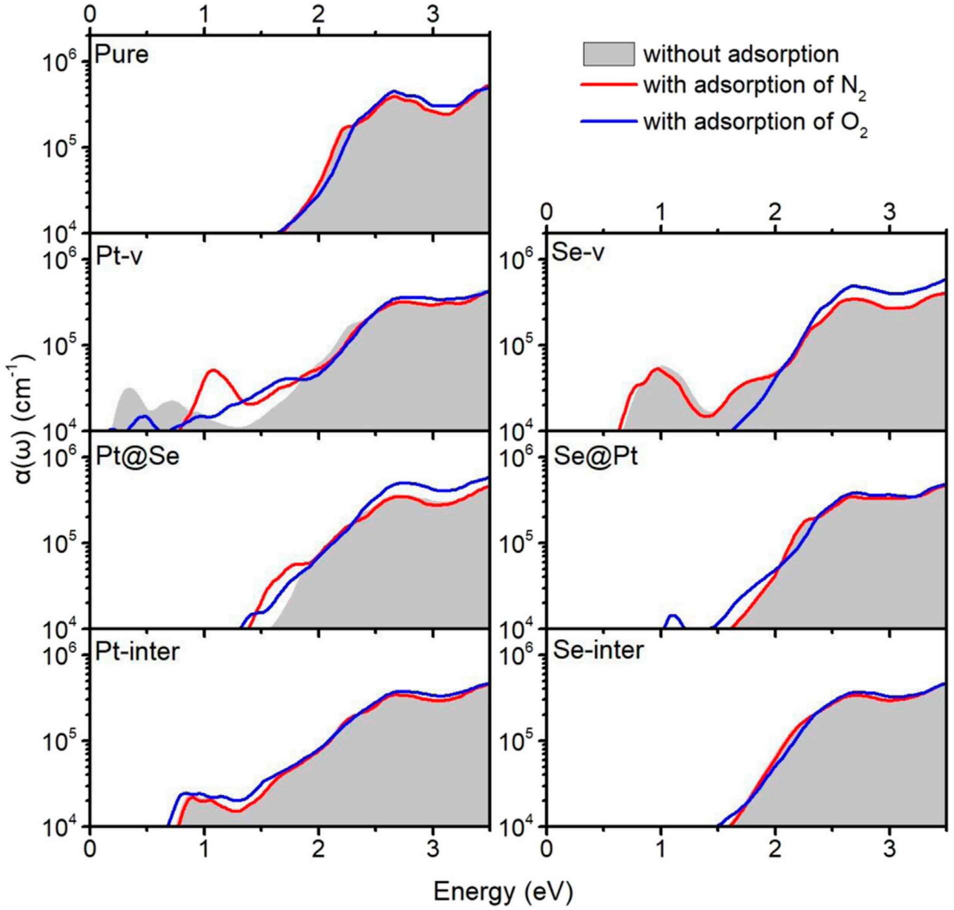

FIGURE 5 | Optical absorption coefficients α(ω) of pure $PtSe_2$ and defected $PtSe_2$ with adsorption of N_2 (red line) and O_2 (blue line). The gray areas indicate the optical absorption coefficients of pure $PtSe_2$ and defected $PtSe_2$.

the optical spectra may be utilized for making high-performance and sensitive optical N_2 and O_2 gas detectors.

SPECIAL RESULTS OF PT-V DEFECT INTRODUCED BY N_2 ADSORPTION

Figure 6A shows the initial structures of the $PtSe_2$ with Pt-v defect, which is formed by removing one of the Pt atoms in the supercell model and first-principles optimization. Upon N_2 adsorption, the surrounding atomic structures of the Pt-v vacancy site change significantly, and these changes are retained when removing the adsorbed N_2 molecule. As shown in **Figure 6B**, the upper Se atom closest to the defect site moves to the original position of Pt vacancy and bonds with the surrounding Se atoms. To characterize the differences in the properties of the two structures, the electronic structure and optical properties of them are calculated and shown in **Figures 6C,D**. As can be seen, the introduced gap states and the DOS near the valence band edge are very different for the two structures. The initial Pt-v structure introduces both occupied and unoccupied gap states near the valence band edge, whereas the new Pt-v structure introduces occupied gap states near the valence band edge and unoccupied gap states near the conduction band edge, thus exhibiting very different electrical properties. Because of this, the optical absorptions of them also show different characteristics. As shown in **Figure 6D**, the gray area shows that there are two absorption peaks around 0.33 and 0.72 eV, resulting from the gap states near the Fermi level, and there is an absorption valley at 1.3 eV. For the new Pt-v structure, there is mainly a characteristic absorption peak at 1.1 eV, resulting from the transition between gap states. The different optical absorption properties of the two structures may be used to differentiate the specific atomic structures of the Pt-v defect. The recent studies have shown that in few-layer $PtSe_2$ flakes, the Pt vacancy defect on the surface and inside can produce localized magnetic moments. The versatile properties of Pt-v and easy tunability of Pt-v with the adsorption of N_2 revealed here may be used to understand and tune the magnetic properties of $PtSe_2$.

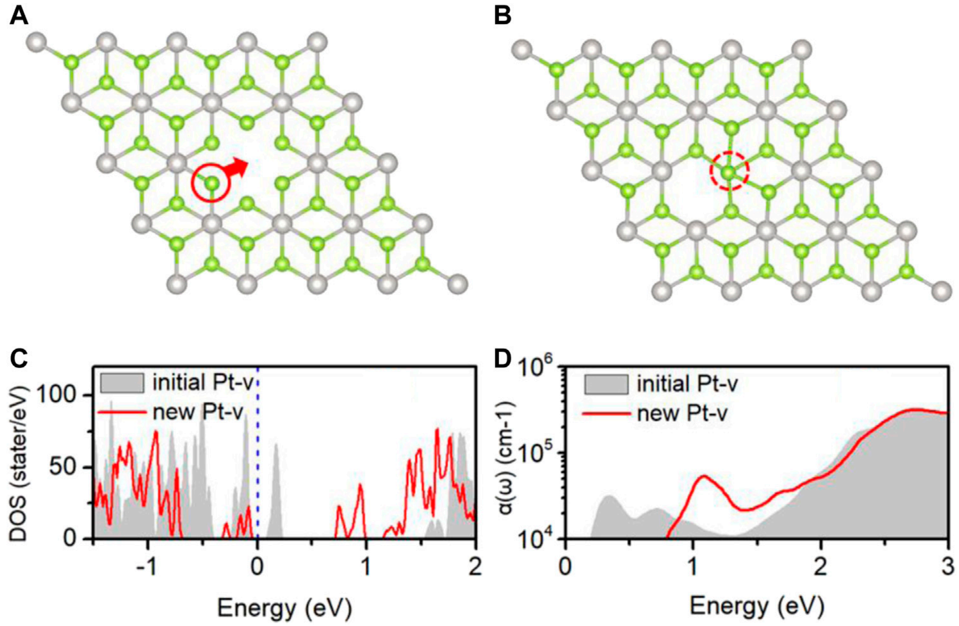

FIGURE 6 | (A) Local atomic structures of the initial **(A)** and new **(B)** Pt-v defects; the DOS **(C)** and optical absorption coefficient **(D)** of $PtSe_2$ with the initial Pt-v defect (gray areas) and new Pt-v defect (red lines). The Fermi levels (blue dashed line) are set to 0 eV.

CONCLUSION

In conclusion, we have studied the N_2 and O_2 gas-sensing properties of monolayer $PtSe_2$ by characterizing the geometric structures, charge transfer, electronic structures, and the optical absorption of pure and defected $PtSe_2$ with and without the adsorption of N_2 and O_2 molecules. It is found that both N_2 and O_2 adsorb weakly on pure $PtSe_2$, whereas the Pt@Se anti-site defect significantly improves the N_2 adsorption capacity of $PtSe_2$ by converting the initial weak vdW interaction on pure $PtSe_2$ into strong chemical interaction. Moreover, the defect not only promotes charge transfer from $PtSe_2$ to N_2 but also introduces charge trapping states around the defect, which leads to a significant change in the electrical properties of the structure. Similar results are also observed for the Pt-v, Se-v, and Pt@Se defects when examining O_2 adsorption. In addition, a notable change in the optical absorption spectra of the $PtSe_2$ with Pt@Se defect is induced upon N_2 adsorption, and this also occurs for $PtSe_2$ with Pt-v, Se-v, and Pt@Se upon O_2 adsorption. Therefore, $PtSe_2$ with the corresponding defects are promising materials for preparing sensitive electrical and optical sensors for detecting N_2 and O_2 molecules. Our work demonstrates the important role of intrinsic defects in improving and extending the sensing performance of $PtSe_2$, which may be generalized to other materials.

Surprisingly, it is also found that significant changes in the atomic structures around Pt vacancy defect are induced upon adsorption of N_2, which results in very different electronic and optical properties. The versatile properties of Pt vacancy and easy tunability with N_2 molecules revealed here may have potential application for understanding and tuning the recently reported magnetic properties of $PtSe_2$.

DATA AVAILABILITY STATEMENT

The original contributions presented in the study are included in the article/Supplementary Material, and further inquiries can be directed to the corresponding author.

AUTHOR CONTRIBUTIONS

XM conceived the basic idea. XY and WH did the implementation and ran the simulations. XY, XM, and JZ analyzed the results and wrote the manuscript.

FUNDING

This work is supported by the National Natural Science Foundation of China (11704298), the Postdoctoral Science Foundation of China (2019M653549), and the 2018 Postdoctoral Innovation Talent Support Program of China (BX20180233).

REFERENCES

Avsar, A., Ciarrocchi, A., Pizzochero, M., Unuchek, D., Yazyev, O. V., and Kis, A. (2019). Defect Induced, Layer-Modulated Magnetism in Ultrathin Metallic PtSe2. *Nat. Nanotechnol.* 14, 674–678. doi:10.1038/s41565-019-0467-1

Bui, V. Q., Pham, T.-T., Le, D. A., Thi, C. M., and Le, H. M. (2015). A First-Principles Investigation of Various Gas (CO, H_2O, NO, and O_2) Absorptions on a WS_2 Monolayer: Stability and Electronic Properties. *J. Phys. Condens. Matter.* 27, 305005. doi:10.1088/0953-8984/27/30/305005

Chen, D., Zhang, X., Tang, J., Cui, Z., Cui, H., and Pi, S. (2018). Theoretical Study of Monolayer $PtSe_2$ as Outstanding Gas Sensor to Detect SF6 Decompositions. *IEEE Electron. Device Lett.* 39, 1405–1408. doi:10.1109/LED.2018.2859258

Ge, J., Luo, T., Lin, Z., Shi, J., Liu, Y., Wang, P., et al. (2020). Magnetic Moments Induced by Atomic Vacancies in Transition Metal Dichalcogenide Flakes. *Adv. Mater.* 33, 2005465. doi:10.1002/adma.202005465

Henkelman, G., Arnaldsson, A., and Jónsson, H. (2006). A Fast and Robust Algorithm for Bader Decomposition of Charge Density. *Comput. Mater. Sci.* 36, 354–360. doi:10.1016/j.commatsci.2005.04.010

Heyd, J., Scuseria, G. E., and Ernzerhof, M. (2003). Hybrid Functionals Based on a Screened Coulomb Potential. *J. Chem. Phys.* 118, 8207–8215. doi:10.1063/1.1564060

Hong, S., Shin, J., Hong, Y., Wu, M., Jang, D., Jeong, Y., et al. (2018). Observation of Physisorption in a High-Performance FET-type Oxygen Gas Sensor Operating at Room Temperature. *Nanoscale* 10, 18019–18027. doi:10.1039/C8NR04472D

Ibrahim, A. A., Umar, A., Kumar, R., Kim, S. H., Bumajdad, A., and Baskoutas, S. (2016). Sm2O3-doped ZnO Beech Fern Hierarchical Structures for Nitroaniline Chemical Sensor. *Ceramics Int.* 42, 16505–16511. doi:10.1016/j.ceramint.2016.07.061

Jian, C.-c., Zhang, J., He, W., and Ma, X. (2021). Au-Al Intermetallic Compounds: A Series of More Efficient LSPR Materials for Hot Carriers-Based Applications Than Noble Metal Au. *Nano Energy* 82, 105763. doi:10.1016/j.nanoen.2021.105763

Jin, C., Tang, X., Tan, X., Smith, S. C., Dai, Y., and Kou, L. (2019). A Janus MoSSe Monolayer: a Superior and Strain-Sensitive Gas Sensing Material. *J. Mater. Chem. A.* 7, 1099–1106. doi:10.1039/C8TA08407F

Klement, P., Steinke, C., Chatterjee, S., Wehling, T. O., and Eickhoff, M. (2018). Effects of the Fermi Level Energy on the Adsorption of O 2 to Monolayer MoS 2. *2d Mater.* 5, 045025. doi:10.1088/2053-1583/aadc24

Kresse, G., and Furthmüller, J. (1996). Efficient Iterative Schemes Forab Initiototal-Energy Calculations Using a Plane-Wave Basis Set. *Phys. Rev. B.* 54, 11169–11186. doi:10.1103/PhysRevB.54.11169

Kumar, M., Kumar, A., and Abhyankar, A. C. (2014). SnO2 Based Sensors with Improved Sensitivity and Response-recovery Time. *Ceramics Int.* 40, 8411–8418. doi:10.1016/j.ceramint.2014.01.050

Ma, X., Yong, X., Jian, C.-c., and Zhang, J. (2019). Transition Metal-Functionalized Janus MoSSe Monolayer: A Magnetic and Efficient Single-Atom Photocatalyst for Water-Splitting Applications. *J. Phys. Chem. C.* 123, 18347–18354. doi:10.1021/acs.jpcc.9b03003

Ma, D., Zhang, J., Li, X., He, C., Lu, Z., Lu, Z., et al. (2018). C3N Monolayers as Promising Candidates for NO2 Sensors. *Sensors Actuators B: Chem.* 266, 664–673. doi:10.1016/j.snb.2018.03.159

Ma, D., Zeng, Z., Liu, L., Huang, X., and Jia, Y. (2019). Computational Evaluation of Electrocatalytic Nitrogen Reduction on TM Single-, Double-, and Triple-Atom Catalysts (TM = Mn, Fe, Co, Ni) Based on Graphdiyne Monolayers. *J. Phys. Chem. C.* 123, 19066–19076. doi:10.1021/acs.jpcc.9b05250

Ma, D., Ju, W., Li, T., Zhang, X., He, C., Ma, B., et al. (2016a). Modulating Electronic, Magnetic and Chemical Properties of MoS2 Monolayer Sheets by Substitutional Doping with Transition Metals. *Appl. Surf. Sci.* 364, 181–189. doi:10.1016/j.apsusc.2015.12.142

Ma, D., Wang, Q., Li, T., He, C., Ma, B., Tang, Y., et al. (2016b). Repairing Sulfur Vacancies in the MoS2 Monolayer by Using CO, NO and NO2 Molecules. *J. Mater. Chem. C.* 4, 7093–7101. doi:10.1039/C6TC01746K

Ma, D., Zeng, Z., Liu, L., and Jia, Y. (2021). Theoretical Screening of the Transition Metal Heteronuclear Dimer Anchored Graphdiyne for Electrocatalytic Nitrogen Reduction. *J. Energ. Chem.* 54, 501–509. doi:10.1016/j.jechem.2020.06.032

Ma, X., Wu, X., Wang, H., and Wang, Y. (2018). A Janus MoSSe Monolayer: a Potential Wide Solar-Spectrum Water-Splitting Photocatalyst with a Low Carrier Recombination Rate. *J. Mater. Chem. A.* 6, 2295–2301. doi:10.1039/C7TA10015A

Monkhorst, H. J., and Pack, J. D. (1976). Special Points for Brillouin-Zone Integrations. *Phys. Rev. B.* 13, 5188–5192. doi:10.1103/PhysRevB.13.5188

Perdew, J. P., Burke, K., and Ernzerhof, M. (1996). Generalized Gradient Approximation Made Simple. *Phys. Rev. Lett.* 77, 3865–3868. doi:10.1103/PhysRevLett.77.3865

Sajjad, M., Montes, E., Singh, N., and Schwingenschlögl, U. (2017). Superior Gas Sensing Properties of Monolayer PtSe2. *Adv. Mater. Inter.* 4, 1600911. doi:10.1002/admi.201600911

Sanville, E., Kenny, S. D., Smith, R., and Henkelman, G. (2007). Improved Grid-Based Algorithm for Bader Charge Allocation. *J. Comput. Chem.* 28, 899–908. doi:10.1002/jcc.20575

Shuk, P., and Jantz, R. (2015). *Oxygen Gas Sensing Technologies: A Comprehensive Review9th International Conference on Sensing Technology (ICST)*. Auckland, New Zealand: IEEE, 12–17.

Urriza-Arsuaga, I., Bedoya, M., and Orellana, G. (2019). Luminescent Sensor for O_2 Detection in Biomethane Streams. *Sensors Actuators B: Chem.* 279, 458–465. doi:10.1016/j.snb.2018.09.108

Wang, Y., Lai, X., Liu, B., Chen, Y., Lu, Y., Wang, F., et al. (2019). UV-induced Desorption of Oxygen at the TiO_2 Surface for Highly Sensitive Room Temperature O_2 Sensing. *J. Alloys Compd.* 793, 583–589. doi:10.1016/j.jallcom.2019.04.231

Xia, X., Wu, W., Wang, Z., Bao, Y., Huang, Z., and Gao, Y. (2016). A Hydrogen Sensor Based on Orientation Aligned TiO_2 Thin Films with Low Concentration Detecting Limit and Short Response Time. *Sensors Actuators B: Chem.* 234, 192–200. doi:10.1016/j.snb.2016.04.110

Yi, H., Li, F., Ning, P., Tang, X., Peng, J., Li, Y., et al. (2013). Adsorption Separation of CO_2, CH_4, and N_2 on Microwave Activated Carbon. *Chem. Eng. J.* 215-216, 635–642. doi:10.1016/j.cej.2012.11.050

Yong, X., Zhang, J., and Ma, X. (2020). Effects of Intrinsic Defects on the Photocatalytic Water-Splitting Activities of $PtSe_2$. *Int. J. Hydrogen Energ.* 45, 8549–8557. doi:10.1016/j.ijhydene.2020.01.066

Yue, Q., Shao, Z., Chang, S., and Li, J. (2013). Adsorption of Gas Molecules on Monolayer MoS_2 and Effect of Applied Electric Field. *Nanoscale Res. Lett.* 8, 425. doi:10.1186/1556-276X-8-425

Zhang, M., Xue, T., Xu, S., Li, Z., Yan, Y., and Huang, Y. (2017). Adverse Effect of Substrate Surface Impurities on O_2 Sensing Properties of TiO_2 Gas Sensor Operating at High Temperature. *Ceramics Int.* 43, 5842–5846. doi:10.1016/j.ceramint.2017.01.130

Zhao, X., Huang, R., Wang, T., Dai, X., Wei, S., and Ma, Y. (2020). Steady Semiconducting Properties of Monolayer $PtSe_2$ with Non-metal Atom and Transition Metal Atom Doping. *Phys. Chem. Chem. Phys.* 22, 5765–5773. doi:10.1039/C9CP06249A

Zheng, H., Choi, Y., Baniasadi, F., Hu, D., Jiao, L., Park, K., et al. (2019). Visualization of Point Defects in Ultrathin Layered 1T-$PtSe_2$. *2d Mater.* 6, 041005. doi:10.1088/2053-1583/ab3beb

Conflict of Interest: The authors declare that the research was conducted in the absence of any commercial or financial relationships that could be construed as a potential conflict of interest.

frontiers in Chemistry

ORIGINAL RESEARCH
published: 19 August 2021
doi: 10.3389/fchem.2021.734460

Achieving Selective and Efficient Electrocatalytic Activity for CO_2 Reduction on N-Doped Graphene

*Xiaoxu Sun**

Jiangsu Key Laboratory of New Power Batteries, School of Chemistry and Materials Science, Nanjing Normal University, Nanjing, China

The CO_2 electrochemical reduction reaction (CO_2RR) has been a promising conversion method for CO_2 utilization. Currently, the lack of electrocatalysts with favorable stability and high efficiency hindered the development of CO_2RR. Nitrogen-doped graphene nanocarbons have great promise in replacing metal catalysts for catalyzing CO_2RR. By using the density functional theory (DFT) method, the catalytic mechanism and activity of CO_2RR on 11 types of nitrogen-doped graphene have been explored. The free energy analysis reveals that the zigzag pyridinic N- and zigzag graphitic N-doped graphene possess outstanding catalytic activity and selectivity for HCOOH production with an energy barrier of 0.38 and 0.39 eV, respectively. CO is a competitive product since its free energy lies only about 0.20 eV above HCOOH. The minor product is CH_3OH and CH_4 for the zigzag pyridinic N-doped graphene and HCHO for zigzag graphitic N-doped graphene, respectively. However, for Z-pyN, CO_2RR is passivated by too strong HER. Meanwhile, by modifying the pH value of the electrolyte, Z-GN could be selected as a promising nonmetal electrocatalyst for CO_2RR in generating HCOOH.

Keywords: density functional theory, N-doped graphene, CO_2 reduction reaction, catalytic activity, Gibbs free energy

OPEN ACCESS

Edited by:
Zhaofu Zhang,
University of Cambridge,
United Kingdom

Reviewed by:
Liu Xuefei,
Guizhou Normal University, China
Ziheng Lu,
University of Cambridge,
United Kingdom

Correspondence:
Xiaoxu Sun
xxsun@ciac.ac.cn

Specialty section:
This article was submitted to Theoretical and Computational Chemistry,
a section of the journal Frontiers in Chemistry

Received: *01 July 2021*
Accepted: *12 July 2021*
Published: *19 August 2021*

Citation:
Sun X (2021) Achieving Selective and Efficient Electrocatalytic Activity for CO_2 Reduction on N-Doped Graphene.
Front. Chem. 9:734460.
doi: 10.3389/fchem.2021.734460

INTRODUCTION

As one of the greenhouse gases, the continual accumulation of CO_2 causes global warming, which significantly hinders the sustainable development of human society (Thomas et al., 2004; Lewis et al., 2006; Cook et al., 2010). The unbalanced CO_2 emission and consumption is becoming a pressing issue (Kondratenko et al., 2013; Appel et al., 2013). In this aspect, CO_2 electrochemical reduction reaction (CO_2RR) by using the renewable energy sources (Yi et al., 2019; Wang et al., 2020; Lu et al., 2021) offers a promising way to produce fuels and value-added chemicals. Up to now, the major obstacle for CO_2RR is the lack of electrocatalysts with high stability and efficiency. Particularly, the cathode electrocatalyst materials play a key role in the complicated product distribution of CO_2RR (Lim et al., 2014; Zhu et al., 2016). Therefore, searching for suitable electrocatalysts for CO_2RR is one of the hot topics in recent years. Till now, a lot of electrocatalysts for CO_2RR have been studied, including noble metals (Zhu et al., 2013; Kang et al., 2014; Gao et al., 2015; Kim et al., 2015), base metals (Hori et al., 1985; Hori et al., 1986; Nie et al., 2013; Zhang et al., 2014a), alloys (Kim et al., 2014; Bai et al., 2017), and metal oxides (Lee et al., 2015; Ren et al., 2015). It is well known that Ag and Au are prone to produce CO *via* the two-electron reaction pathway (Zhu et al., 2013; Kim et al., 2015). In addition, Cu is recognized as a state-of-the-art CO_2RR catalyst for generating multi-electron products, such as CO, HCOOH, CH_3OH, and CH_4 (Hori et al., 1985; Hori et al., 1986; Nie et al., 2013). However, the high cost, low efficiency due to the competitive hydrogen evolution reaction (HER), and high overpotential restrict their practical implementation and industrial-scale development in CO_2RR (Lim et al., 2014).

To solve the above issues, metal-free electrocatalysts based on carbon materials have been studied, owing to their low cost, high stability, outstanding mechanical flexibility, and superior structural durability. The introduction of heteroatoms (such as N, B, and S) could not only modify the electronic structure of carbon materials but also contribute to take advantage of the existing defects appropriately (Wang X. et al., 2014). For N-doped carbon nanofibers (NCNFs), it shows negligible overpotential (0.17 V) and 13 times higher current density than bulk Ag catalyst for CO_2RR (Kumar et al., 2013). In addition, N-doped carbon nanotubes (NCNTs) (Sharma et al., 2015), N-doped nanoporous carbon–carbon nanotube composite membrane (HNCM/CNT) (Wang et al., 2017), and polyethylenimine functionalized NCNTs have been proven to be highly active and stable electrocatalysts for CO_2RR (Zhang et al., 2014b). Remarkably, N-doped graphene possesses excellent durability in the CO_2RR process, achieving a maximum faradaic efficiency (FE) of 73% for formate with overpotential of 0.84 V (Wang et al., 2016). N-doped graphene quantum dots (NGQDs) could catalyze carbon dioxide into multicarbon hydrocarbons and oxygenates at high FE (up to 90%), with excellent selectivity (45% for ethylene and ethanol conversions) (Wu et al., 2016).

With respect to the active sites of nitrogen-doped carbon materials for CO_2RR, it is a controversial issue among the pyridinic N, pyrrolic N, graphitic N, and the C adjacent to N. Generally, these potential active sites coexist in the carbon materials, which adds to the difficulty in identifying the active site. A theoretical study indicates that for CO_2 electroreduction to CO on NCNTs, the optimal active site is pyridinic N, followed by pyrrolic N and graphitic N (Wu et al., 2015). Another study about CO_2RR on NCNTs emphasizes that the presence of graphitic and pyridinic N defects remarkably increases the selectivity toward CO formation and decreases the absolute overpotential (Sharma et al., 2015). For N-doped graphene-like material/carbon paper electrodes (NGM/CP), the FE is as high as 93.5% in producing CH_4, which is ascribed to the reactive pyridinic and pyrrolic N sites (Sun et al., 2016). A theoretical study suggested that COOH production on pyrrolic N3 is downhill by −0.21 eV, while it is uphill for pyridinic and graphitic N (Liu et al., 2016). Overall, both the experimental and theoretical studies indicate that N-doped carbon materials show significant catalytic performance of CO_2RR.

Inspired by these studies, we studied CO_2RR on N-doped graphene from the perspective of theoretical calculation in this work. To make a systematic comparison, N was doped into graphene at in-plane, zigzag edge, armchair edge, and pyrrolic edge sites, respectively. It would contribute to identifying the most dominant structure and providing a valuable design strategy for further activity enhancement in the experiment. In this study, the first-principle calculation has been performed to uncover the CO_2RR reaction pathways and electrocatalytic activity on different edges of N-doped (zigzag edge, armchair edge, and pyrrolic edge) graphene structures within a unified thermodynamic reaction scheme.

COMPUTATIONAL METHODS AND MODELS

Methods

The geometry optimization and energy calculations were performed within the density functional theory (DFT) framework (Kohn and Sham, 1965) by using the Vienna *ab initio* simulation package (VASP) (Kresse and Furthmüller, 1996a). The ion–electron interaction was described by the projector-augmented wave (PAW) potentials (Blöchl, 1994). The generalized gradient approximation parameterized by Perdew, Burke, and Ernzerhof was utilized as the exchange-correlation functional (Perdew et al., 1996). The kinetic energy cutoff of 400 eV was adopted for the plane-wave expansion. The armchair-edged ribbon, zigzag-edged ribbon, and periodic graphene slab were sampled with 4 × 1 × 1, 1 × 4×1, and 4 × 4 × 1 Monkhorst–Pack k-point grids (Delley, 2000), respectively. During the geometry optimization, all atoms were relaxed until the total energy was converged to 1.0×10^{-5} eV/atom, and the force was converged to 0.01 eV/Å. In addition, we considered the van der Waals (vdW) interactions by employing the semiempirical DFT-D2 forcefield approach (Grimme, 2006).

Models

The lattice parameters of 8.52 Å × 24.6 Å and 25.6 Å × 9.84 Å were set to model the armchair-edged graphene nanoribbon (including pyrrolic edge) and zigzag-edged graphene nanoribbon, respectively. The lattice parameters of 9.84 × 9.84Å were adopted to model the periodic graphene slab. Perpendicular to all graphene structures, a vacuum layer of 15 Å was set, which was sufficiently large to minimize the image interactions.

The adsorption energy(ΔE_{ads})of adsorbates was defined as follows:

$$\Delta E_{ads} = E_{substrate+adsorbate} - (E_{substrate} + E_{adsorbate}), \tag{1}$$

where $E_{substrate+adsorbate}$ is the total energy of the substrate with adsorbed molecules. $E_{substrate}$ and $E_{adsorbate}$ are the energy of the isolated substrate and free molecule, respectively.

Reaction Free Energy

The computational hydrogen electrode (CHE) model (Norskov et al., 2004) was adopted to evaluate the free energy change during the CO_2RR process. In the CHE model, the hydrogen atom is in equilibrium with the proton/electron pair at 298.15 K and 1 atm of pressure. In other words, the half chemical potential of gas-phase H_2 is equal to that of a proton/electron pair at 0 V in an aqueous solution.

The Gibbs free energy change (ΔG) for each elementary CO_2RR step involving proton/electron pair transfer was calculated by the expression (Norskov et al., 2004; Zuluaga and Stolbov, 2011):

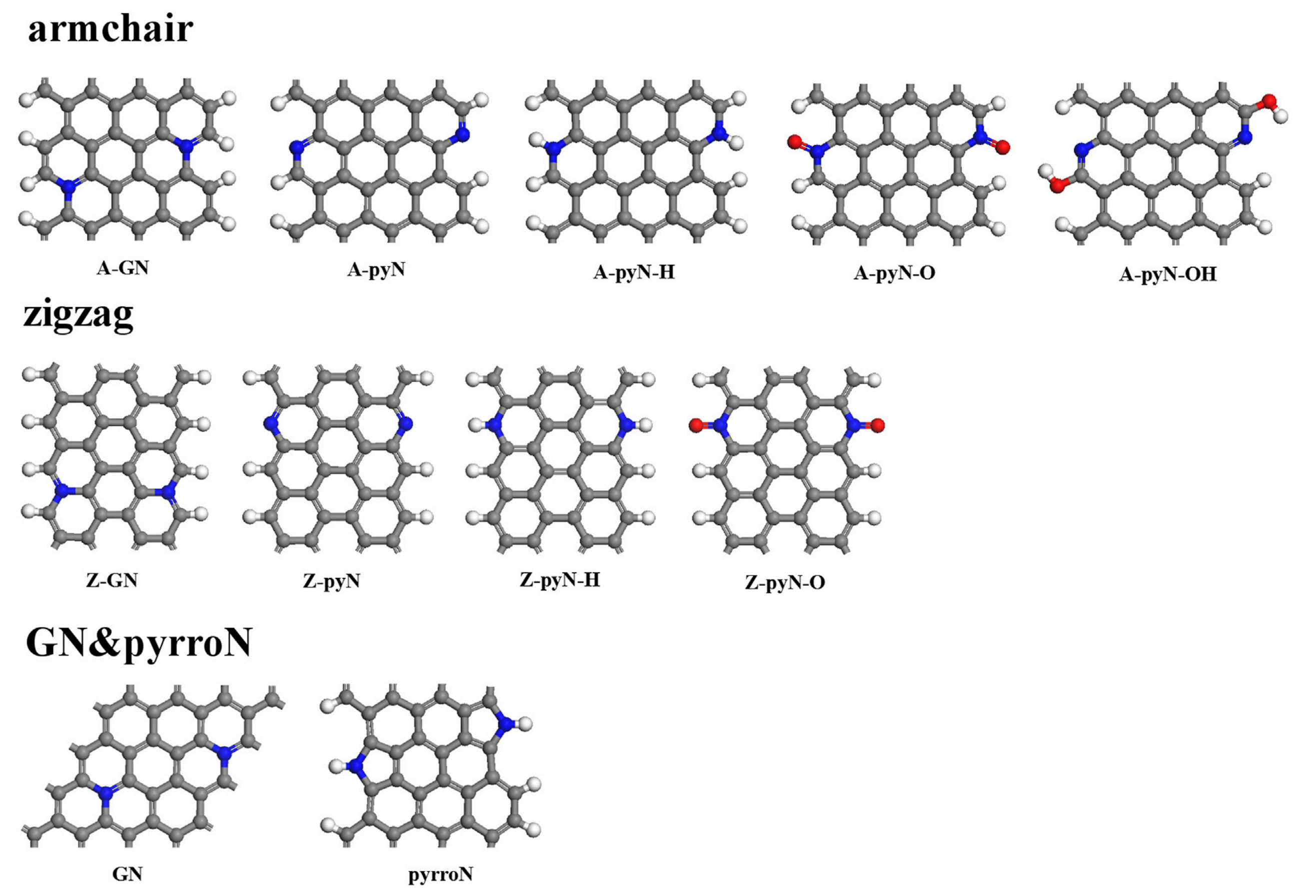

FIGURE 1 | The structures of N-doped graphene. The gray, blue, white, and red balls represent C, N, H, and O atoms, respectively.

$$\Delta G = \Delta E + \Delta ZPE - T\Delta S + \Delta G\mathrm{u} + \Delta G_{\mathrm{pH}}, \qquad (2)$$

where ΔE is the change of reaction energy based on DFT calculations. ΔZPE and ΔS are the change of zero-point energy and entropy, respectively. T refers to the temperature (298.15 K). The zero-point energy (*ZPE*) of adsorbates has been calculated from the vibrational frequencies. For the free molecules (CO_2, CO, HCOOH, CH_4, CH_3OH, *etc.*) the vibrational frequencies and entropies are obtained from the NIST database (http://webbook.nist.gov/chemistry/). ΔG_{U} = -neU, where n is the number of transferred electrons, e is the elementary charge of an electron, and U is the electrode potential vs. RHE. $\Delta G_{pH=}$ 2.303 k_{B}T *pH, k_{B} is the Boltzmann constant. In this work, the value of pH was set as 0 for the acid medium (Faccio et al., 2010; Shang et al., 2010). Approximate solvation corrections with a dielectric constant of ε = 80 are applied for the simulation of an aqueous environment (Mathew et al., 2019).

RESULT AND DISCUSSION

Adsorption of the Key Intermediates

In previous reports, the N-doped graphene materials have been widely studied as ORR electrocatalysts, which showed better stability and tolerance to methanol crossover effect than commercial Pt/C catalyst (Geng et al., 2011; Lin et al., 2013; Gong et al., 2009; Qu et al., 2010). Under different temperatures, the synthesizability of each type of the N-doped graphene materials is different. It is relatively easy to synthesize different types of N-doped graphene by controlling the temperature (Lin et al., 2013). The studied structures include five N-doped armchair graphene types, four N-doped zigzag graphene types, in-plane graphitic N (GN), and pyrrolic edge N (PyrroN)-doped graphene. For N-doped armchair graphene, it includes graphitic N (A-GN), pyridinic N (A-pyN), hydrogenated pyridinic N (A-pyN-H), oxidized pyridinic N (A-pyN-O), and pyridinic N hydroxide (A-pyN-OH), as shown in **Figure 1**. For N-doped zigzag graphene, four structures are considered, i.e., graphitic N (Z-GN), pyridinic N (Z-pyN), hydrogenated pyridinic N (Z-pyN-H), and oxidized pyridinic N (Z-pyN-O). These doped structures could be generated at high temperatures in the pyrolysis process of N-containing compounds (Wu et al., 2011; Li et al., 2012; Wang Q. et al., 2014; Holby et al., 2014).

During the CO$_2$RR process on the studied compounds, the intermediates mainly include CO_2, COOH, HCOO, HCOOH, CO + H_2O, COHOH, H_2COO, and COH + H_2O. By exploring different adsorption sites (N and its adjacent carbon atoms),

TABLE 1 | The calculated adsorption energies (E_{ads}, eV) and the shortest distances (d, Å) between the intermediate and N-doped graphene.

	*CO_2		*COOH		*HCOO		*HCOOH		*CO	
	E_{ads}	D	E_{ads}	d	E_{ads}	d	E_{ads}	d	E_{ads}	d
A-GN	−0.13	3.14	−1.26	1.57	—	—	−0.12	2.23	−0.13	3.12
A-pyN	−0.10	3.08	−1.51	1.42	−0.92	1.52	−0.33	1.73	−0.04	3.22
A-pyN-H	−0.10	3.10	−0.20	1.53	—	—	−0.05	1.92	−0.03	3.17
A-pyN-O	−0.11	3.32	−0.95	1.56	−1.29	1.50	−0.40	1.62	−0.08	3.26
A-pyN-OH	−0.11	3.12	−0.96	1.40	−0.84	1.54	−0.24	1.63	−0.07	3.19
Z-GN	−0.10	3.25	−1.99	1.58	−1.87	1.50	−0.16	2.02	−0.10	3.14
Z-pyN	−0.09	3.36	−2.48	1.41	—	—	−0.43	1.64	−0.26	1.37
Z-pyN-H	−0.09	3.19	−0.43	1.58	—	—	−0.13	2.00	−0.09	3.17
Z-pyN-O	−0.08	3.19	−0.59	1.55	—	—	−0.06	2.39	−0.10	3.20
GN	−0.06	3.11	0.34	1.61	—	—	−0.10	2.22	−0.12	3.14
PyrroN	−0.10	3.03	—	—	—	—	—	—	—	—

The "" denotes the adsorption state of the species.*

the most favorable adsorption configurations and sites are obtained (**Supplementary Figures 1–8**). Since the two main reactions on various N-doped graphene are HCOOH and CO generation pathways, we focus on the adsorption energies of CO_2, COOH, HCOO, HCOOH, and CO as listed in **Table 1**, together with the bond distance between the adsorbed intermediates and catalyst surface. It is seen that the adsorption of CO_2 molecule is weak all the time (-0.06 eV~ -0.13 eV), and linear structure is maintained above the surface. To achieve high selectivity for HCOOH or CO, COOH (or HCOO) should be adsorbed strongly, but HCOOH or CO should be adsorbed weakly for desorption. Therefore, strong COOH (HCOO) binding but weak HCOOH (CO) adsorption is essential for the formation of HCOOH or (CO) (Sharma et al., 2015; Wu et al., 2015).

As shown in **Supplementary Figures 2, 3**, COOH could not be absorbed on GN and PyrroN, and is weakly adsorbed on A-pyN-H (-0.20 eV), Z-pyN-H (-0.43 eV), and Z-pyN-O (−0.59 eV) (**Table 1**). For the remaining structures, the adsorption of COOH is relatively strong, with the adsorption energy ranging from −0.95 to −2.48 eV. However, HCOO exists only on four N-doped graphene structures, that is, A-pyN, A-pyN-O, A-pyN-OH, and Z-GN. The adsorption energies for the four structures are in the range of −1.87 eV~ −0.84 eV (**Table 1**).

For HCOOH, the adsorption energies for the studied compounds are in the range of −0.43 ~ −0.06 eV, which are relatively weak and facilitate its desorption from the catalyst surface. Similar to the HCOOH molecule, the adsorption energies of CO are in the range of −0.26 ~ −0.03 eV (**Table 1**).

Reaction Mechanism

The possible reaction pathways for the studied compounds are summarized in **Figure 2**. Based on the computational hydrogen electrode (CHE) model (Norskov et al., 2004), the limiting potential is obtained by $U_L = -\Delta G_{MAX/}e$, where ΔG_{MAX} denotes the maximum free energy difference between the two successive reaction steps. The reduction step corresponding to the limiting potential is defined as the potential determining step (PDS).

N-Doped Armchair Graphene Nanoribbons

As shown in **Figures 2A–E**, the energy of CO_2 increases by 0.25–0.37 eV from the free molecule to the adsorbed state. After CO_2 is adsorbed on the catalyst surface, it would be hydrogenated by ($H^+ + e^-$) pair. The formation of an O-H bond would produce COOH, while the formation of the C-H bond would generate the HCOO intermediate.

The reaction of $CO_2+H^++e^-\rightarrow$*COOH on A-GN, A-pyN, A-pyN-H, A-pyN-O, and A-pyN-OH is uphill by 1.16, 0.84, 2.14, 1.38, and 1.41 eV, respectively. For $CO_2+ H^++e^-\rightarrow$*HCOO, the energy increases by 1.73, 1.38, and 1.81 eV for A-pyN, A-pyN-O, and A-pyN-OH, respectively.

The hydrogenation of COOH would generate COHOH, HCOOH, and CO + H_2O. Due to the large energy increase for producing COHOH, that is, 1.55, 0.96, and 1.26 eV for A-GN, A-pyN, and A-pyN-OH, respectively, further discussion is omitted. In COOH, if the OH moiety binds (H^++e^-), it would produce CO + H_2O. If the carbon atom in COOH binds (H^++e^-), it would produce HCOOH. The production of HCOOH and CO is all thermodynamically downhill.

Similarly, the hydrogenation of HCOO may produce H_2COO and HCOOH. As *HCOO→*H_2COO step is endothermic with a large free energy increase (0.88 eV for A-pyN, 0.93 eV for A-pyN-O, and 1.86 eV for A-pyN-OH), further discussion is not provided. Thus, the final product from HCOO is HCOOH.

As illustrated in **Figures 2A–E**, the COOH intermediate has better performance in producing HCOOH than HCOO. For $CO_2\rightarrow$ *$CO_2\rightarrow$*COOH→*HCOOH/*CO, the PDS is *$CO_2\rightarrow$*COOH (**Table 2**), which is in agreement with the previous study (Wu et al., 2015). According to the free energy barrier (**Figures 2A–E**), A-pyN exhibits the highest catalytic activity toward HCOOH with a free energy barrier of 0.84 eV (**Figure 2B**). The order of catalytic activity for COOH to HCOOH/CO is A-pyN > A-GN > A-pyN-O > A-pyN-OH > A-pyN-H. In addition, $CO_2\rightarrow$ *$CO_2\rightarrow$*COOH→*CO+*H_2O is the secondary pathway with slightly larger endothermic energy than $CO_2\rightarrow$ *$CO_2\rightarrow$*COOH→*HCOOH.

N-Doped Zigzag Graphene Nanoribbons

The reaction pathways on N-doped zigzag graphene nanoribbons (**Figures 2F–I**) are similar to those on N-doped armchair

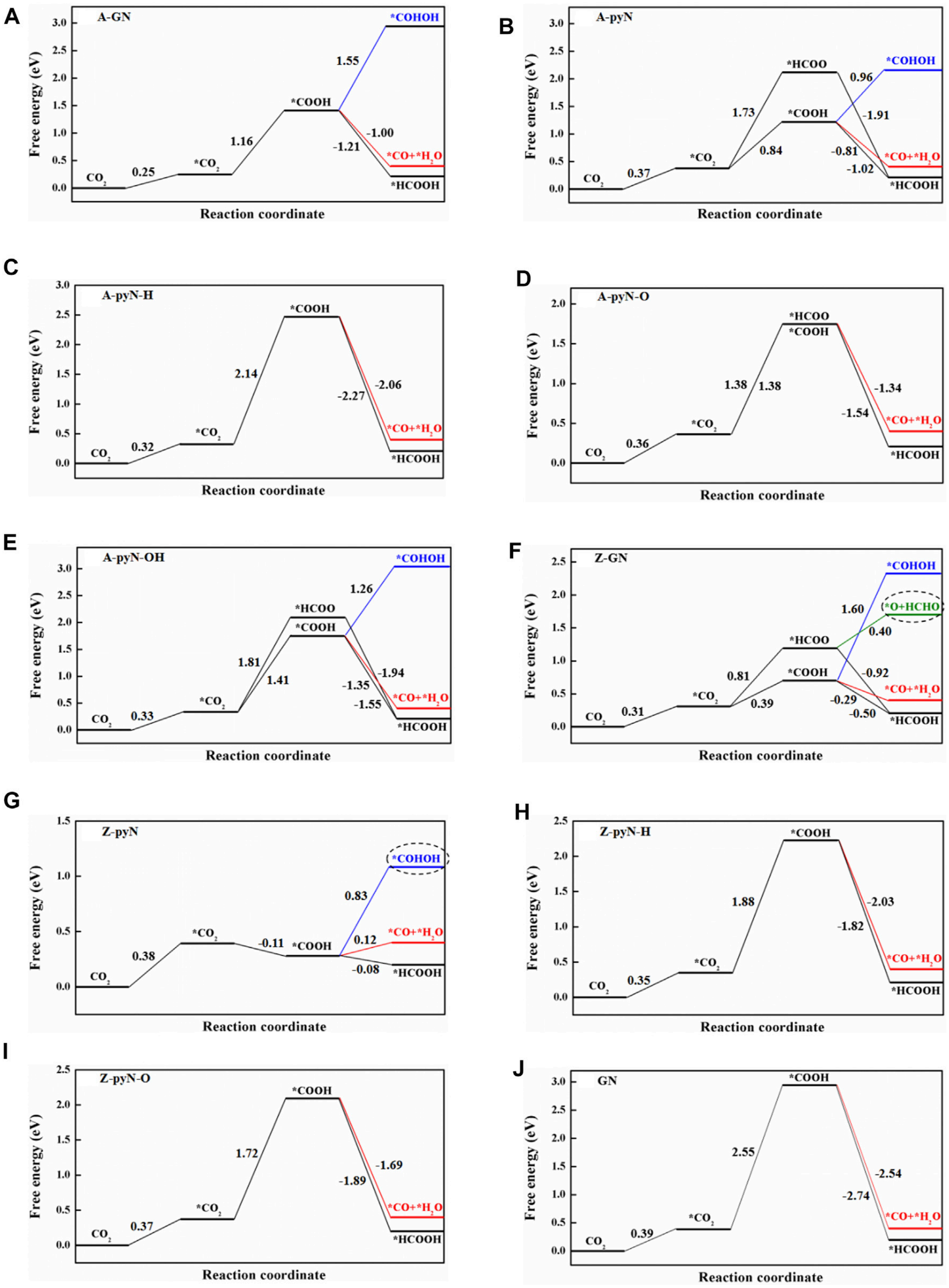

FIGURE 2 | The free energy change for reaction pathways of CO$_2$RR on various N-doped graphene. **(A)** A-GN, **(B)** A-pyN, **(C)** A-pyN-H, **(D)** A-pyN-O, **(E)** A-pyN-OH, **(F)** Z-GN, **(G)** Z-pyN, **(H)** Z-pyN-H, **(I)** Z-pyN-O, **(J)** GN.

TABLE 2 | Potential determining steps (PDSs), limiting potentials (U_L/V), and overpotentials (η/V) for CO$_2$RR on Z-GN and Z-pyN. U_0 is the equilibrium potential. Comparison has been made with previous studies. U_L, U_0, and η are all vs. the RHE.

	PDS	U_L	U_0	η	Product
Z-GN	$^*CO_2+H^+ + e^- \rightarrow ^*COOH$	−0.39	−0.25	0.14	HCOOH
Z-GN	$^*CO_2+H^+ + e^- \rightarrow ^*COOH$	−0.39	−0.11	0.28	CO
Z-GN	$^*CO_2+H^+ + e^- \rightarrow ^*HCOO$	−0.81	−0.07	0.74	HCHO
Z-pyN	$CO_2+H^+ + e^- \rightarrow ^*CO_2$	−0.38	−0.25	0.13	HCOOH
Z-pyN	$CO_2+H^+ + e^- \rightarrow ^*CO_2$	−0.38	−0.11	0.27	CO
Z-pyN	$^*COOH + H^+ + e^- \rightarrow ^*COHOH$	−0.83	0.02	0.81	CH_3OH
Z-pyN	$^*COOH + H^+ + e^- \rightarrow ^*COHOH$	−0.83	0.17	0.66	CH_4
PyrroN3	$^*COOH + H^+ + e^- \rightarrow HOOH$	−0.44	—	—	HCOOH
Edge-2gN	$CO_2+H^+ + e^- \rightarrow ^*COOH$	−0.52	—	—	CO

The "" denotes the adsorption state of the species.*

graphene nanoribbons. The HCOO intermediate could only stably exist on Z-GN among these N-doped zigzag graphene nanoribbons. To produce HCOOH, the $CO_2 \rightarrow ^*CO_2 \rightarrow ^*COOH \rightarrow ^*HCOOH$ pathway is more favorable than the $CO_2 \rightarrow ^*CO_2 \rightarrow ^*HCOO \rightarrow ^*HCOOH$ pathway (**Figure 2F**). In particular, on Z-GN, the hydrogenation of HCOO generates not only HCOOH but also O + HCHO with an energy barrier of 0.40 eV (**Figure 2F**). As illustrated in **Figure 3**, after the formation of O + HCOO, the remaining O atom could be easily hydrogenated into water due to the downhill process. The PDS for producing HCHO is the HCOO formation step with U_L = -0.81 V.

For the $^*CO_2 \rightarrow ^*COOH$ step, it occurred on Z-GN and Z-pyN most easily, in which the energy is uphill by 0.39 eV for Z-GN and downhill by -0.11 eV for Z-pyN, respectively (**Figures 2F,G**). While for the other two structures, large uphill energy barriers are required, that is, 1.88 eV for Z-pyN-H and 1.72 eV for Z-pyN-O, respectively. After the formation of COOH, its hydrogenation may generate HCOOH, CO + H_2O, or COHOH, in which the formation of HCOOH is the most favorable, followed by CO + H_2O and COHOH. Our calculations indicated that the COOH intermediate on Z-pyN needs an energy barrier of 0.83 eV to form COHOH (**Figure 4**). After the formation of COHOH, an energy increase of 0.41 eV is required to produce COH + H_2O. The further hydrogenation of COH is relatively easy due to the downhill energy process to release the two competitive final products, that is, CH_3OH and CH_4. A previous study indicated that the formation of CH_4 and CH_3OH is through CO intermediate (Hori et al., 2008), which is different from our results.

GN and PyrroN-Doped Graphene

As mentioned above, the pyrrolic N-doped structure has no catalytic activity for CO$_2$RR. For GN, the free energy increase is the largest among all the N-doped graphene structures (2.55 eV). Thus, the catalytic activity of GN is omitted.

In a word, for the studied structures, the most favorable product is HCOOH, followed by CO and COHOH. In particular, the formation of HCOOH and CO is competitive since the free energy of CO is more thermodynamically favorable by only about 0.20 eV than that of HCOOH. This energy difference is similar to the value of 0.28 eV reported earlier (Liu et al., 2016). In a word, Z-pyN and Z-GN possess the highest catalytic activity toward HCOOH due to the smallest limiting potential of −0.38 and −0.39 V, respectively (**Table 2**), which is lower than −0.44 for PyrroN3 (Liu et al., 2016).

Hydrogen Evolution Reactions

Hydrogen evolution reaction (HER) is the competitive reaction for CO$_2$RR since the evolution of H would consume the proton–electron pair (H^++e^-) and passivate the catalytic activity of CO$_2$RR. For the studied structures, the results showed that Z-pyN-O and Z-pyN have large energetic downhill for the adsorption of H*, indicating the enhanced HER in thermodynamic (**Figure 5**). For Z-GN and A-pyN, they have a negligible free energy barrier (0.03 and 0.04 eV) of H*. For the remaining structures, HER is hindered by large free energy barriers. Therefore, for the most favorable Z-pyN and

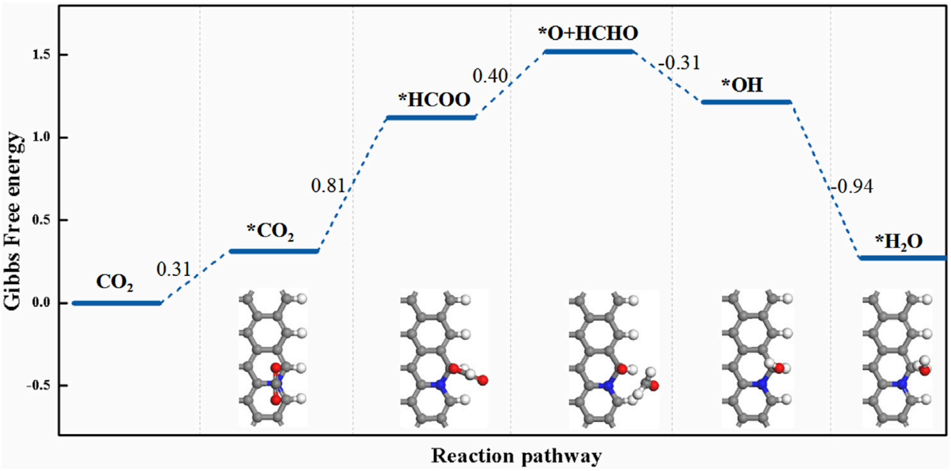

FIGURE 3 | The free energy change for the reaction of $CO_2 + 4H^+ + 4e^- \rightarrow HCHO + H_2O$ on Z-GN.

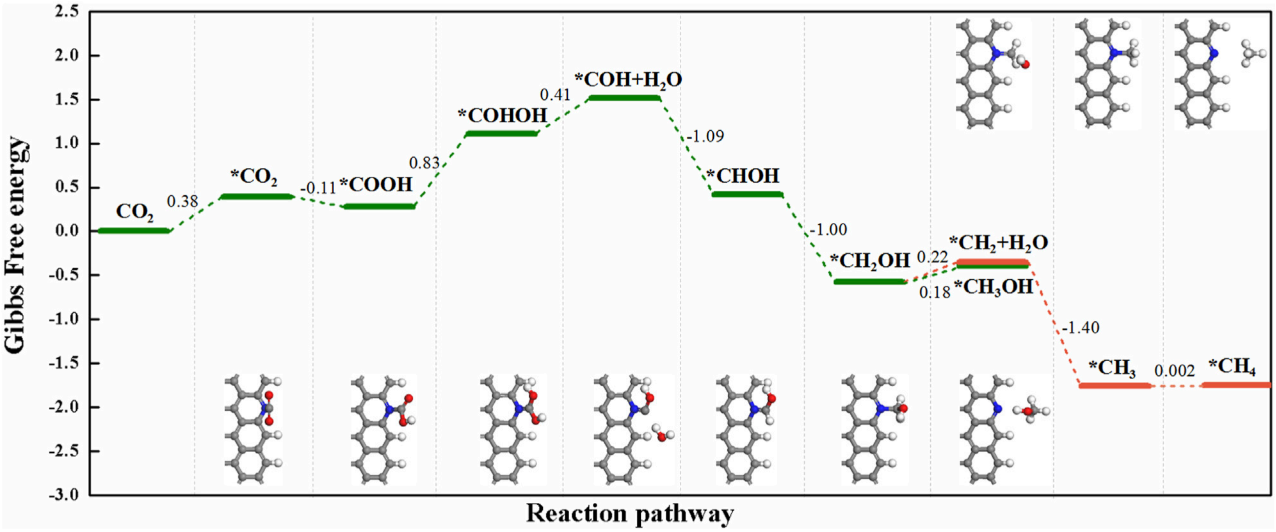

FIGURE 4 | The free energy change for the reaction of $CO_2 + 8H^+ + 8e^- \rightarrow CH_4 + H_2O$ and $CO_2 + 6H^+ + 6e^- \rightarrow CH_3OH + H_2O$ on Z-pyN.

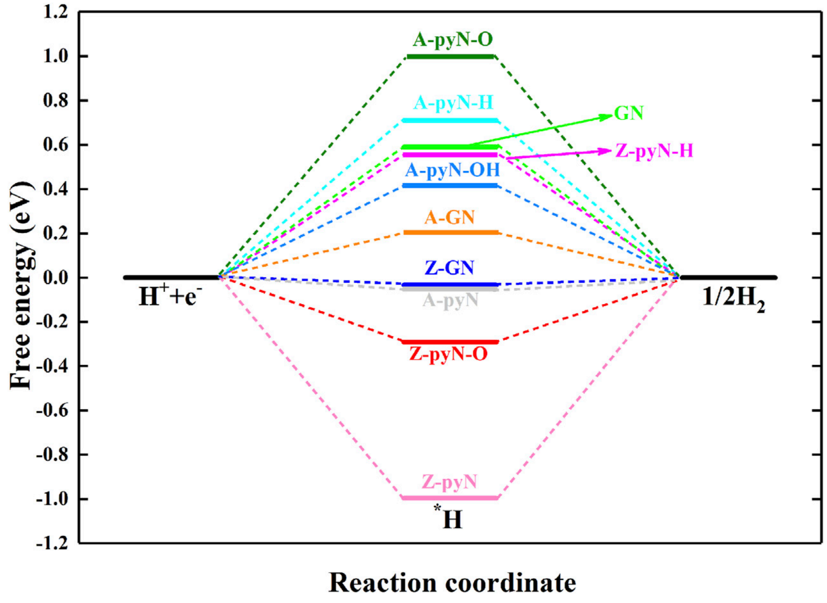

FIGURE 5 | The free energy changes for hydrogen evolution reaction (HER) on various N-doped graphene.

Z-GN, CO$_2$RR would be suppressed by HER. However, by choosing a suitable electrolyte, the activation energy of HER would be increased. For instance, according to the expression $\Delta G_{pH=}$ 2.303k_BT pH, in which pH = 0 is selected in the above study, ΔG_{pH} = 0.42 eV is obtained for pH = 7.0. Thus, the activation energy of HER on Z-GN would be increased from −0.03 to 0.39 eV, comparable to the free energy barrier of 0.38 eV in the CO$_2$RR process. Thus, the HER could be suppressed by increasing the pH value for Z-GN. While for Z-pyN, CO$_2$RR is passivated by too strong HER. In a word, Z-GN could be selected as a promising nonmetal electrocatalyst for CO$_2$RR in generating HCOOH.

CONCLUSION

We have performed the DFT method to elucidate the reaction mechanism and activity of CO$_2$RR on 11 types of N-doped graphene catalysts. It indicates that for all the studied structures, the formation of HCOOH is the most favorable, followed by CO.

Among these structures, Z-pyN- and Z-GN-doped graphene exhibit the best catalytic activity for producing HCOOH with free energy barriers of 0.38 and 0.39 eV, respectively. The potential determining step (PDS) is $CO_2 \rightarrow {}^*CO_2$ for Z-pyN and ${}^*CO_2 \rightarrow {}^*COOH$ for Z-GN, respectively. Meanwhile, CO is the competitive product which lies 0.20 eV above HCOOH. For the zigzag pyridinic N-doped graphene, it could also produce CH_3OH and CH_4 as the minor products which need to overcome an energy barrier of 0.83 eV. The minor product for the zigzag graphitic N-doped graphene is HCHO, with an energy barrier of 0.81 eV. However, for Z-pyN, CO$_2$RR is passivated by too strong HER. Meanwhile, by modifying the pH value of electrolyte, Z-GN could be selected as a promising nonmetal electrocatalyst for CO$_2$RR in generating HCOOH.

DATA AVAILABILITY STATEMENT

The original contributions presented in the study are included in the article/**Supplementary Material**; further inquiries can be directed to the corresponding author.

AUTHOR CONTRIBUTIONS

The author confirms being the sole contributor to this work and has approved it for publication.

FUNDING

We are grateful for funding support from the National Key R&D Program of China (2019YFA0308000), the Natural Science Foundation of China (no. 21873050), and the Priority Academic Program Development of Jiangsu Higher Education Institutions.

SUPPLEMENTARY MATERIAL

The Supplementary Material for this article can be found online at: https://www.frontiersin.org/articles/10.3389/fchem.2021.734460/full#supplementary-material

REFERENCES

Appel, A. M., Bercaw, J. E., Bocarsly, A. B., Dobbek, H., DuBois, D. L., Dupuis, M., et al. (2013). Frontiers, Opportunities, and Challenges in Biochemical and Chemical Catalysis of CO2Fixation. *Chem. Rev.* 113 (8), 6621–6658. doi:10.1021/cr300463y

Bai, X., Chen, W., Zhao, C., Li, S., Song, Y., Ge, R., et al. (2017). Exclusive Formation of Formic Acid from CO2 Electroreduction by a Tunable Pd-Sn Alloy. *Angew. Chem.* 129 (40), 12387–12391. doi:10.1002/ange.201707098

Blöchl, P. E. (1994). Projector Augmented-Wave Method. *Phys. Rev. B* 50 (24), 17953–17979. doi:10.1103/PhysRevB.50.17953

Cook, T. R., Dogutan, D. K., Reece, S. Y., Surendranath, Y., Teets, T. S., and Nocera, D. G. (2010). Solar Energy Supply and Storage for the Legacy and Nonlegacy Worlds. *Chem. Rev.* 110 (11), 6474–6502. doi:10.1021/cr100246c

Delley, B. (2000). From Molecules to Solids with the DMol3 Approach. *J. Chem. Phys.* 113 (18), 7756–7764. doi:10.1063/1.1316015

Faccio, R., Fernández-Werner, L., Pardo, H., Goyenola, C., Ventura, O. N., and Mombrú, Á. W. (2010). Electronic and Structural Distortions in Graphene Induced by Carbon Vacancies and Boron Doping. *J. Phys. Chem. C* 114 (44), 18961–18971. doi:10.1021/jp106764h

Gao, D., Zhou, H., Wang, J., Miao, S., Yang, F., Wang, G., et al. (2015). Size-Dependent Electrocatalytic Reduction of CO2over Pd Nanoparticles. *J. Am. Chem. Soc.* 137 (13), 4288–4291. doi:10.1021/jacs.5b00046

Geng, D., Chen, Y., Chen, Y., Li, Y., Li, R., Sun, X., et al. (2011). High Oxygen-Reduction Activity and Durability of Nitrogen-Doped Graphene. *Energy Environ. Sci.* 4, 760–764. doi:10.1039/C0EE00326C

Gong, K., Du, F., Xia, Z., Durstock, M., and Dai, L. (2009). Nitrogen-Doped Carbon Nanotube Arrays with High Electrocatalytic Activity for Oxygen Reduction. *Science* 323 (5915), 760–764. doi:10.1126/science.1168049

Grimme, S. (2006). Semiempirical GGA-type Density Functional Constructed with a Long-Range Dispersion Correction. *J. Comput. Chem.* 27 (15), 1787–1799. doi:10.1002/jcc.20495

Holby, E. F., Wu, G., Zelenay, P., and Taylor, C. D. (2014). Structure of Fe-Nx-C Defects in Oxygen Reduction Reaction Catalysts from First-Principles Modeling. *J. Phys. Chem. C* 118 (26), 14388–14393. doi:10.1021/jp503266h

Hori, Y., Kikuchi, K., Kikuchi, S., and Suzuki, S. (1985). Production of Co and Ch4in Electrochemical Reduction of Co2at Metal Electrodes in Aqueous Hydrogencarbonate Solution. *Chem. Lett.* 14 (11), 1695–1698. doi:10.1246/cl.1985.1695

Hori, Y., Kikuchi, K., Murata, A., and Suzuki, S. (1986). Production of Methane and Ethylene in Electrochemical Reduction of Carbon Dioxide at Copper Electrode in Aqueous Hydrogencarbonate Solution. *Chem. Lett.* 15 (6), 897–898. doi:10.1246/cl.1986.897

Hori, Y., Vayenas, C. G., White, R. E., and Gamboa-Aldeco, M. E. (2008). *Electrochemical CO_2 Reduction on Metal Electrodes*. New York: Springer, 89–189. doi:10.1007/978-0-387-49489-0_342

Kang, P., Zhang, S., Meyer, T. J., and Brookhart, M. (2014). Rapid Selective Electrocatalytic Reduction of Carbon Dioxide to Formate by an Iridium Pincer Catalyst Immobilized on Carbon Nanotube Electrodes. *Angew. Chem. Int. Ed.* 53 (33), 8709–8713. doi:10.1002/anie.201310722

Kim, C., Jeon, H. S., Eom, T., Jee, M. S., Kim, H., Friend, C. M., et al. (2015). Achieving Selective and Efficient Electrocatalytic Activity for CO2 Reduction Using Immobilized Silver Nanoparticles. *J. Am. Chem. Soc.* 137 (43), 13844–13850. doi:10.1021/jacs.5b06568

Kim, D., Resasco, J., Yu, Y., Asiri, A. M., and Yang, P. (2014). Synergistic Geometric and Electronic Effects for Electrochemical Reduction of Carbon Dioxide Using Gold-Copper Bimetallic Nanoparticles. *Nat. Commun.* 5, 4948. doi:10.1038/ncomms5948

Kohn, W., and Sham, L. J. (1965). Self-Consistent Equations Including Exchange and Correlation Effects. *Phys. Rev.* 140 (4A), A1133–A1138. doi:10.1103/PhysRev.140.A1133

Kondratenko, E. V., Mul, G., Baltrusaitis, J., Larrazábal, G. O., and Pérez-Ramírez, J. (2013). Status and Perspectives of CO2 Conversion into Fuels and Chemicals by Catalytic, Photocatalytic and Electrocatalytic Processes. *Energ. Environ. Sci.* 6 (11), 3112–3135. doi:10.1039/C3EE41272E

Kresse, G., and Furthmüller, J. (1996b). Efficiency of Ab-Initio Total Energy Calculations for Metals and Semiconductors Using a Plane-Wave Basis Set. *Comput. Mater. Sci.* 6 (1), 15–50. doi:10.1016/0927

Kresse, G., and Furthmüller, J. (1996a). Efficient Iterative Schemes Forab Initiototal-Energy Calculations Using a Plane-Wave Basis Set. *Phys. Rev. B* 54 (16), 11169–11186. doi:10.1103/PhysRevB.54.11169

Kumar, B., Asadi, M., Pisasale, D., Sinha-Ray, S., Rosen, B. A., Haasch, R., et al. (2013). Renewable and Metal-free Carbon Nanofibre Catalysts for Carbon Dioxide Reduction. *Nat. Commun.* 4, 2819. doi:10.1038/ncomms3819

Lee, S., Ocon, J. D., Son, Y.-i., and Lee, J. (2015). Alkaline CO2 Electrolysis toward Selective and Continuous HCOO- Production over SnO2 Nanocatalysts. *J. Phys. Chem. C* 119 (9), 4884–4890. doi:10.1021/jp512436w

Lewis, N. S., Nocera, D. G., and NoceraD, G. (2006). Powering the Planet: Chemical Challenges in Solar Energy Utilization. *Proc. Natl. Acad. Sci.* 103 (43), 15729–15735. doi:10.1073/pnas.0603395103

Li, W., Wu, J., Higgins, D. C., Choi, J.-Y., and Chen, Z. (2012). Determination of Iron Active Sites in Pyrolyzed Iron-Based Catalysts for the Oxygen Reduction Reaction. *ACS Catal.* 2 (12), 2761–2768. doi:10.1021/cs300579b

Lim, R. J., Xie, M., Sk, M. A., Lee, J.-M., Fisher, A., Wang, X., et al. (2014). A Review on the Electrochemical Reduction of CO2 in Fuel Cells, Metal Electrodes and Molecular Catalysts. *Catal. Today* 233, 169–180. doi:10.1016/j.cattod.2013.11.037

Lin, Z., Waller, G. H., Liu, Y., Liu, M., and Wong, C.-p. (2013). 3D Nitrogen-Doped Graphene Prepared by Pyrolysis of Graphene Oxide with Polypyrrole for Electrocatalysis of Oxygen Reduction Reaction. *Nano Energy* 2, 241–248. doi:10.1016/j.nanoen.2012.09.002

Liu, Y., Zhao, J., and Cai, Q. (2016). Pyrrolic-nitrogen Doped Graphene: a Metal-free Electrocatalyst with High Efficiency and Selectivity for the Reduction of Carbon Dioxide to Formic Acid: a Computational Study. *Phys. Chem. Chem. Phys.* 18, 5491–5498. doi:10.1039/C5CP07458D

Lu, Z. (2021). Computational Discovery of Energy Materials in the Era of Big Data and Machine Learning: A Critical Review. *Mater. Rep. Energ.*, 100047. doi:10.1016/j.matre.2021.100047

Lu, Z., Yang, Z., Li, C., Wang, K., Han, J., Tong, P., et al. (2021). Modulating Nanoinhomogeneity at Electrode-Solid Electrolyte Interfaces for Dendrite-Proof Solid-State Batteries and Long-Life Memristors. *Adv. Energ. Mater.* 11 (16), 2003811. doi:10.1002/aenm.202003811

Mathew, K., Kolluru, V. S. C., Mula, S., Steinmann, S. N., and Hennig, R. G. (2019). Implicit Self-Consistent Electrolyte Model in Plane-Wave Density-Functional Theory. *J. Chem. Phys.* 151 (23), 234101. doi:10.1063/1.5132354

Nie, X., Esopi, M. R., Janik, M. J., and Asthagiri, A. (2013). Selectivity of CO2Reduction on Copper Electrodes: The Role of the Kinetics of Elementary Steps. *Angew. Chem. Int. Ed.* 52 (9), 2459–2462. doi:10.1002/anie.201208320

Nørskov, J. K., Rossmeisl, J., Logadottir, A., Lindqvist, L., Kitchin, J. R., Bligaard, T., et al. (2004). Origin of the Overpotential for Oxygen Reduction at a Fuel-Cell Cathode. *J. Phys. Chem. B* 108 (46), 17886–17892. doi:10.1021/jp047349j

Perdew, J. P., Burke, K., and Ernzerhof, M. (1996). Generalized Gradient Approximation Made Simple. *Phys. Rev. Lett.* 77 (18), 3865–3868. doi:10.1103/PhysRevLett.77.3865

Qu, L., Liu, Y., Baek, J.-B., and Dai, L. (2010). Nitrogen-Doped Graphene as Efficient Metal-free Electrocatalyst for Oxygen Reduction in Fuel Cells. *ACS Nano* 4 (3), 1321–1326. doi:10.1021/nn901850u

Ren, D., Deng, Y., Handoko, A. D., Chen, C. S., Malkhandi, S., and Yeo, B. S. (2015). Selective Electrochemical Reduction of Carbon Dioxide to Ethylene and Ethanol on Copper(I) Oxide Catalysts. *ACS Catal.* 5 (5), 2814–2821. doi:10.1021/cs502128q

Shang, Y., Zhao, J.-x., Wu, H., Cai, Q.-h., Wang, X.-g., and Wang, X.-z. (2010). Chemical Functionalization of Pyridine-like and Porphyrin-like Nitrogen-Doped Carbon (CN X) Nanotubes with Transition Metal (TM) Atoms: a Theoretical Study. *Theor. Chem. Acc.* 127 (5-6), 727–733. doi:10.1007/s00214-010-0784-9

Sharma, P. P., Wu, J., Yadav, R. M., Liu, M., Wright, C. J., Tiwary, C. S., et al. (2015). Nitrogen-Doped Carbon Nanotube Arrays for High-Efficiency Electrochemical Reduction of CO2: On the Understanding of Defects, Defect Density, and Selectivity. *Angew. Chem. Int. Ed.* 54 (46), 13701–13705. doi:10.1002/anie.201506062

Sun, X., Kang, X., Zhu, Q., Ma, J., Yang, G., Liu, Z., et al. (2016). Very Highly Efficient Reduction of CO2to CH4using Metal-free N-Doped Carbon Electrodes. *Chem. Sci.* 7, 2883–2887. doi:10.1039/C5SC04158A

Thomas, C. D., Cameron, A., Green, R. E., Bakkenes, M., Beaumont, L. J., Collingham, Y. C., et al. (2004). Extinction Risk from Climate Change. *Nature* 427 (6970), 145–148. doi:10.1038/nature02121

Wang, H., Chen, Y., Hou, X., Ma, C., and Tan, T. (2016). Nitrogen-doped Graphenes as Efficient Electrocatalysts for the Selective Reduction of Carbon Dioxide to Formate in Aqueous Solution. *Green. Chem.* 18, 3250–3256. doi:10.1039/C6GC00410E

Wang, H., Jia, J., Song, P., Wang, Q., Li, D., Min, S., et al. (2017). Efficient Electrocatalytic Reduction of CO2by Nitrogen-Doped Nanoporous Carbon/Carbon Nanotube Membranes: A Step towards the Electrochemical CO2Refinery. *Angew. Chem. Int. Ed.* 56 (27), 7847–7852. doi:10.1002/anie.201703720

Wang, Q., Zhou, Z.-Y., Lai, Y.-J., You, Y., Liu, J.-G., Wu, X.-L., et al. (2014b). Phenylenediamine-Based FeNx/C Catalyst with High Activity for Oxygen Reduction in Acid Medium and its Active-Site Probing. *J. Am. Chem. Soc.* 136 (31), 10882–10885. doi:10.1021/ja505777v

Wang, X., Niu, H., Liu, Y., Shao, C., Robertson, J., Zhang, Z., et al. (2020). Theoretical Investigation on Graphene-Supported Single-Atom Catalysts for Electrochemical CO2 Reduction. *Catal. Sci. Technol.* 10 (24), 8465–8472. doi:10.1039/d0cy01870h

Wang, X., Sun, G., Routh, P., Kim, D.-H., Huang, W., and Chen, P. (2014a). Heteroatom-doped Graphene Materials: Syntheses, Properties and Applications. *Chem. Soc. Rev.* 43, 7067–7098. doi:10.1039/C4CS00141A

Wu, G., More, K. L., Johnston, C. M., and Zelenay, P. (2011). High-Performance Electrocatalysts for Oxygen Reduction Derived from Polyaniline, Iron, and Cobalt. *Science* 332 (6028), 443–447. doi:10.1126/science.1200832

Wu, J., Liu, M., Sharma, P. P., Liu, C. S., Zou, X., Zhou, X. D., et al. (2015). Achieving Highly Efficient, Selective, and Stable CO2 Reduction on Nitrogen-Doped Carbon Nanotubes. *ACS Nano* 9 (5), 5364–5371. doi:10.1021/acsnano.5b01079

Wu, J., Ma, S., Sun, J., Gold, J. I., Tiwary, C., Kim, B., et al. (2016). A Metal-free Electrocatalyst for Carbon Dioxide Reduction to Multi-Carbon Hydrocarbons and Oxygenates. *Nat. Commun.* 7, 13869. doi:10.1038/ncomms13869

Yi, J., Chen, J., Yang, Z., Dai, Y., Li, W., Cui, J., et al. (2019). Facile Patterning of Laser-Induced Graphene with Tailored Li Nucleation Kinetics for Stable Lithium-Metal Batteries. *Adv. Energ. Mater.* 9 (38), 1901796. doi:10.1002/aenm.201901796

Zhang, S., Kang, P., and Meyer, T. J. (2014a). Nanostructured Tin Catalysts for Selective Electrochemical Reduction of Carbon Dioxide to Formate. *J. Am. Chem. Soc.* 136 (5), 1734–1737. doi:10.1021/ja4113885

Zhang, S., Kang, P., Ubnoske, S., Brennaman, M. K., Song, N., House, R. L., et al. (2014b). Polyethylenimine-Enhanced Electrocatalytic Reduction of CO2to Formate at Nitrogen-Doped Carbon Nanomaterials. *J. Am. Chem. Soc.* 136 (22), 7845–7848. doi:10.1021/ja5031529

Zhu, D. D., Liu, J. L., and Qiao, S. Z. (2016). Recent Advances in Inorganic Heterogeneous Electrocatalysts for Reduction of Carbon Dioxide. *Adv. Mater.* 28 (18), 3423–3452. doi:10.1002/adma.201504766

Zhu, W., Metin, Ö., Lv, H., Guo, S., Wright, C. J., Sun, X., et al. (2013). Monodisperse Au Nanoparticles for Selective Electrocatalytic Reduction of CO2 to CO. *J. Am. Chem. Soc.* 135 (45), 16833–16836. doi:10.1021/ja409445p

Zuluaga, S., and Stolbov, S. (2011). Factors Controlling the Energetics of the Oxygen Reduction Reaction on the Pd-Co Electro-Catalysts: Insight from First Principles. *J. Chem. Phys.* 135 (13), 134702. doi:10.1063/1.3643714

Conflict of Interest: The author declares that the research was conducted in the absence of any commercial or financial relationships that could be construed as a potential conflict of interest.

ORIGINAL RESEARCH
published: 22 September 2021
doi: 10.3389/fchem.2021.739984

Promising Thermoelectric Performance in Two-Dimensional Semiconducting Boron Monolayer

*Yonglan Hu, Ding Li, Rongkun Liu, Shichang Li, Chunbao Feng, Dengfeng Li and Guangqian Ding**

School of Science, Chongqing University of Posts and Telecommunications, Chongqing, China

A heavy element is a special character for high thermoelectric performance since it generally guarantees a low lattice thermal conductivity. Here, we unexpectedly found a promising thermoelectric performance in a two-dimensional semiconducting monolayer consisting of a light boron element. Using first-principles combined with the Boltzmann transport theory, we have shown that in contrast to graphene or black phosphorus, the boron monolayer has a low lattice thermal conductivity arising from its complex crystal of hexagonal vacancies. The conduction band with an intrinsic camelback shape leads to the high DOS and a high *n*-type Seebeck coefficient, while the highly degenerate valence band along with the small hole effective mass contributes to the high *p*-type power factor. As a result, we obtained the *p*-type thermoelectric figure of merit up to 0.96 at 300 K, indicating that the boron monolayer is a promising *p*-type thermoelectric material.

Keywords: boron monolayer, thermoelectric, first-principles, Boltzmann, phonon

Edited by:
Guangzhao Wang,
Yangtze Normal University, China

Reviewed by:
Chaoyu He,
Xiangtan University, China
Hongkuan Yuan,
South University, United States

***Correspondence:**
Guangqian Ding
dinggq@cqupt.edu.cn

Specialty section:
This article was submitted to Theoretical and Computational Chemistry,
a section of the journal Frontiers in Chemistry

Received: *12 July 2021*
Accepted: *09 August 2021*
Published: *22 September 2021*

Citation:
Hu Y, Li D, Liu R, Li S, Feng C, Li D and Ding G (2021) Promising Thermoelectric Performance in Two-Dimensional Semiconducting Boron Monolayer.
Front. Chem. 9:739984.
doi: 10.3389/fchem.2021.739984

INTRODUCTION

In the past decade, people devoted themselves to improve the thermoelectric efficiency by trying to individually control the thermoelectric coefficients through low-dimensional crystals such as single layers, nanowires, 2D heterostructures, and nanotubes. The thermoelectric performance of a material is usually characterized by the dimensionless figure of merit $ZT = S^2\sigma T/\kappa$, where S is the Seebeck coefficient, σ is the electrical conductivity, κ is the thermal conductivity including both electronic and lattice contributions, and T is the absolute temperature, respectively (Mohanraman et al., 2015; Hu et al., 2021). High ZT requires a superior electronic transport but a minimized phonon transport at the same time, the latter usually arises from heavy elements (Ding et al., 2016). For instance, the lattice thermal conductivity of traditional commercial bulk thermoelectric materials such as Bi_2Te_3 and PbTe are lower than 1 W/mK (Pei and Liu, 2012; Hellman and Broido, 2014). Although the thermoelectric coefficient in some cases can be individually controlled in a low-dimensional crystal, the high lattice thermal conductivity still prevents a striking improvement of ZT (Kumar and Schwingenschlögl, 2015).

Balandin et al. (2008) experimentally reported that the thermal conductivity of single-layer graphene is higher than 4000 W/mK at room temperature. For monolayer MoS_2, it is about 100 W/mK at 300 K based on Yang's report (Jin et al., 2015). Using a molecular dynamics simulation, Xu et al. (2015) obtained the lattice thermal conductivity of phosphorene along the zigzag direction that is higher than 150 W/mK at 300 K. Among these popular single-layer crystals, it was found that an extremely high thermal conductivity leads to poor ZT, which can be ascribed to the following two factors: 1) light elements with high vibration frequency and 2) large atomic weight difference forbids the anharmonic scattering. In this regard, we intended to think that is there possibility to achieve promising thermoelectric transport in other single-layer crystal consisting of light elements? In recent years, boron, one of the carbon's nearest neighbors, demonstrated the polymorphism in two-dimensional crystals, which are called borophene. However, most of the boron monolayers were found to be metallic by experiment or theory. Interestingly, Hu *et al.* recently proposed a series of semiconducting boron monolayers formulated by the connected network of hexagonal vacancies (Xu et al., 2017). Such semiconducting phases of the boron monolayer are expected to achieve in experiments since the controlled synthesis of the boron monolayer is a mature technology (Kong et al., 2018; Kiraly et al., 2019).

The semiconducting β_1^s boron monolayer has an indirect bandgap of 0.74 eV based on HSE06 functional (Xu et al., 2017), and the multi-valley character of both conduction and valence band near the Fermi level indicates the promising electronic transport performance. In addition, the complex crystal consisting of twelve boron atoms and hexagonal vacancies leads to large number of coupled phonon branches, which points to possible low lattice thermal conductivity in the crystal. To explore the potential of the semiconducting β_1^s boron monolayer as a thermoelectric material, we studied its thermoelectric transport performance by first-principles combined with Boltzmann transport equations. We found that the lattice thermal conductivity is 20.2 W/mK at 300 K, and highly degenerate hole pockets with small effective mass lead to the high *p*-type power factor. Finally, the optimal *ZT* reaches 0.96 at 300 K for *p*-type doping, which is a recorded value among two-dimensional monolayers.

COMPUTATIONAL DETAILS

The first-principles calculations were performed within the framework of density function theory (DFT) using projector-augmented wave (PAW) (Perdew et al., 1997) pseudopotentials and Perdew–Burke–Ernzerhof (PBE) (Kresse and Furthmüller, 1996) exchange correlation functionals as implemented in VASP (Tran and Blaha, 2009). To construct the single-layer crystal, a 15-Å-thick vacuum slab was added along the *z*-direction. The plane-wave cutoff energy was set to 400 eV and the Monkhorst–Pack ***k*** mesh was 15 × 15 × 1. Geometry optimization was converged until the force acting on the ions become smaller than 10^{-3} eV/Å. When we calculated the electronic structure, a modified Becke–Johnson (mBJ) (Tran and Blaha, 2009) functional was also considered to yield the accurate effective mass and bandgap.

The electronic transport properties were calculated using the Boltzmann transport equation (BTE) under a constant relaxation time approximation as implemented in BoltzTraP (Madsen and Singh, 2006). A rigid band approximation is used to treat doping, and the Fermi level shifts up for *n*-type doping while down for the *p*-type. However, within this approximation, the Seebeck coefficient can be calculated independent of carrier relaxation time τ, while the evaluation of electrical conductivity still requires the knowledge of τ. In this regard, we employed deformation potential theory based on effective mass approximation to calculate τ (Herring and Vogt, 1956). At last, we performed phonon BTE solution as implemented in the ShengBTE (Li et al., 2014) package to calculate lattice thermal conductivity. Second- and third-order interatomic force constants (IFCs) are quite necessary inputs for pBTE, which were obtained from DFT calculations using a converged 4 × 4 × 1 supercell. The phonon spectrum was obtained from the Phonopy code (Togo et al., 2008), and a converged cutoff distance of 0.4 nm for interactive distance was used in calculating anharmonic IFCs.

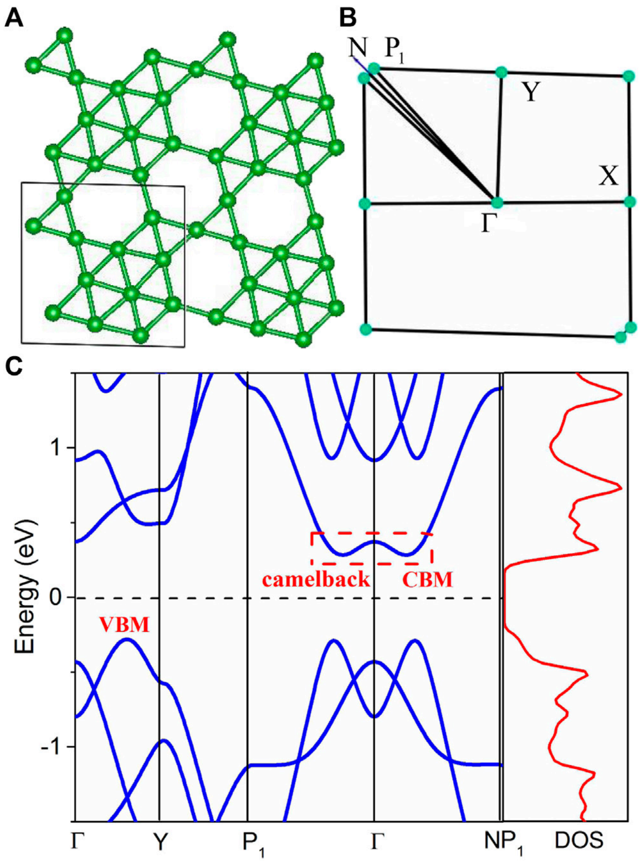

FIGURE 1 | The atomic structure **(A)** and the Brillouin zone path **(B)** of the β_1^s boron monolayer and **(C)** shows the calculated band structure and density of states.

RESULTS AND DISCUSSION

Figure 1A shows the crystal structure of the β_1^s semiconducting boron monolayer, which consists of a connected network of hexagonal vacancies that can be divided into triangle regions and heptagon regions, according to Hu *et al* (Xu et al., 2017). The space group is *Amm2* and the lattice parameter 6.12 Å after relaxation is consistent with Hu's result (Xu et al., 2017). **Figure 1B** shows the Brillouin zone path, that is, Γ-Y-P_1-Γ-N-P_1. Based on Hu *et al* (Xu et al., 2017), the HSE06 band structure indicates that the β_1^s boron monolayer is an indirect semiconductor with a bandgap of 0.74 eV, and also, the

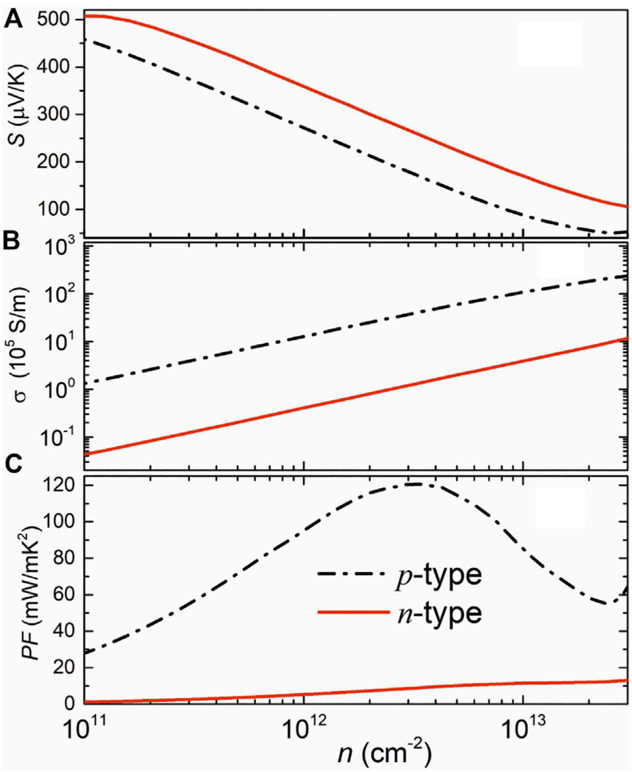

FIGURE 2 | Calculated Seebeck coefficient **(A)**, electrical conductivity **(B)**, and the power factor **(C)** of the β_1^s boron monolayer at 300 K.

TABLE 1 | Calculated DP constant, elastic modulus, carrier effective mass, carrier mobility, and carrier relaxation time at 300 K.

	E_l (eV)	C_{2D} (eVÅ^{-2})	m* (m_e)	μ (cm^{2}V1^{-1}s^{-1})	τ (10^{-14}s)
n-type	–6.93	29.2	0.998	208.6	11.797
p-type	–3.03	29.2	0.57	3,344.7	108.034

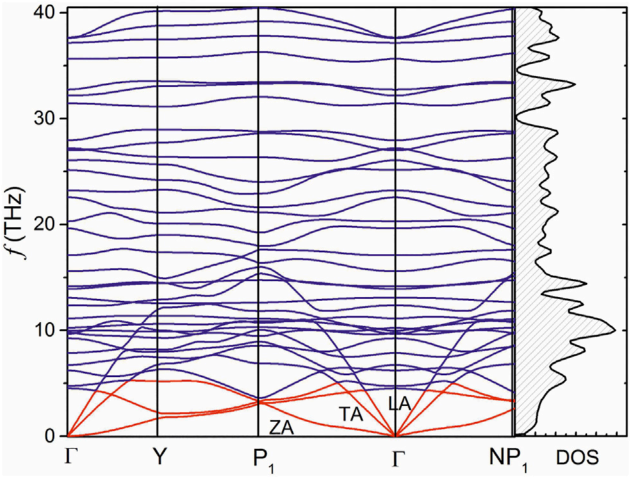

FIGURE 3 | The phonon dispersion and density of states of the β_1^s boron monolayer.

phonon spectrum and molecular dynamics simulation confirm the thermal stability of this boron monolayer. In contrast to monolayer TMDCs with a large bandgap, the moderate bandgap of the boron monolayer may possess better electronic transport performance.

As shown in **Figure 1C**, the calculated band structure of the β_1^s boron monolayer displays an indirect bandgap of 0.68 eV based on mBJ modification, which is very close to the result of HSE06 (Xu et al., 2017). The mBJ functional has been shown to yield the accurate bandgap, effective mass, and frontier-band ordering. The conduction band minimum (CBM) is located in the interval between Γ and P$_1$ points, while the valence band maximum (VBM) is located in the interval between Γ and Y points. In consistent with previous calculation, the VBM is dominated by the out-of-plane p_z orbitals while the CBM is attributed to the in-plane s+$p_{x,y}$ orbitals (Xu et al., 2017), and this semiconducting β_1^s boron monolayer was realized by modulating the in-plane s+$p_{x,y}$ orbitals and p_z-derived bands through the connected network of hexagonal vacancies, according to Hu *et al* (Xu et al., 2017).

Interestingly, the band structure of the β_1^s boron monolayer possesses several advantages of electronic transport performance. First, the lowest conduction band, shown in **Figure 1C**, exhibits a camelback shape along the P$_1$-Γ-N direction. The camelback shape is known in topological materials where the spin-orbital coupling is not large enough to cause inversion between the frontier bands (Eremeev et al., 2010). Here, this interesting band dispersion is obtained in the light β_1^s boron monolayer. The importance of the camelback shape in electronic transport is that it can increase the number of degenerate carrier pockets, which thereby increases the density of states (DOS) effective mass (Ding et al., 2019a; Ding et al., 2019b). As one can see in the right panel of **Figure 1C**, the DOS at the CBM is markedly higher than that at VBM. As a result, a higher *n*-type Seebeck coefficient can be achieved in this boron monolayer. In addition to CBM, there are these band extremes of VBM along Γ-Y, P$_1$-Γ, and Γ-N, respectively, which are highly degenerate in energy and indicate more carrier pockets joining in hole transport. The carrier effective mass near the Fermi level dominates the carrier mobility and relaxation time and plays an important role in thermoelectric transport (Peng et al., 2014). As one can see, the band near the VBM is more dispersive than that near the CBM, yielding a hole effective mass 0.57 m_0 smaller than the 0.998 m_0 of an electron.

Calculated electronic transport properties including the Seebeck coefficient, electrical conductivity, and the power factor at room temperature are shown in **Figure 2**. The Seebeck coefficient decreases while the electrical conductivity increases with the increase of carrier density since they are inversely related to carrier density. In this regard, the power factor cannot be improved infinitely but can be optimized by modulating carrier density. In **Figure 2A**, the higher *n*-type Seebeck coefficient can be attributed to the camelback-shaped

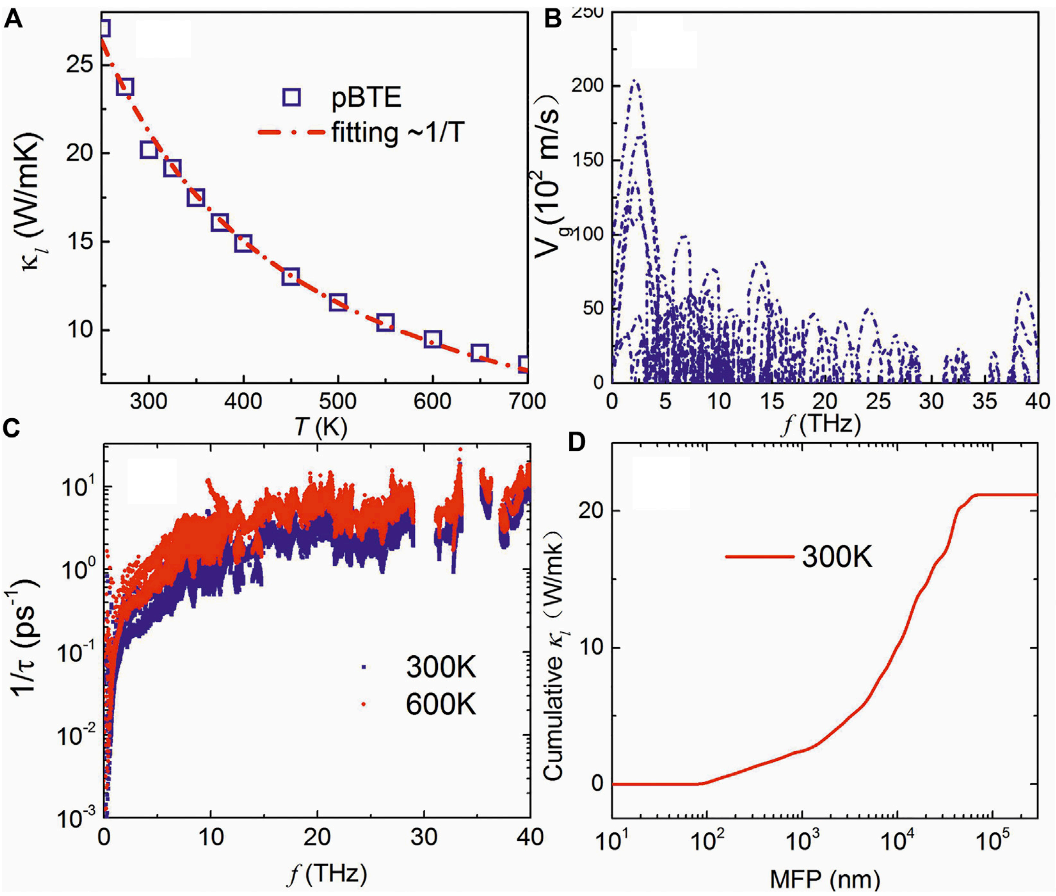

FIGURE 4 | (A) Calculated lattice thermal conductivity with respect to temperature, phonon group velocity **(B)**, and anharmonic scattering **(C)** of the β_1^s boron monolayer. **(D)** shows the cumulative lattice thermal conductivity with respect to the mean free path at 300 K.

band, as discussed above. To obtain the electrical conductivity as shown in **Figure 2B**, we employed deformation potential theory (Herring and Vogt, 1956) to calculate the carrier relaxation time. Calculated results are shown in **Table 1**. It is crucial to find that the lower deformation potential constant of holes reflects the minimal sensitivity of valence band maximum to deformation. Along with the smaller hole effective mass, a high hole mobility and long hole relaxation time were obtained, as compared to an electron. As a result, the *p*-type power factor is much higher than *n*-type, as shown in **Figure 2C**. The maximum power factor of the *p*-doped semiconducting boron monolayer reaches 121 mW/mK^2 at an optimal carrier density of 3.14×10^{12} cm^{-2}, while it is only about 17mW/mK^2 in monolayer MoS$_2$ (Jin et al., 2015). The Seebeck coefficient under this optimal carrier density for *n*- and *p*-type are 263 μV/K and 175 μV/K, respectively, which are the standard values of thermoelectric materials (Sun and Singh, 2016).

Calculated phonon dispersion of the β_1^s boron monolayer is shown in **Figure 3**. First, in contrast to graphene, in phosphorene and monolayer MoS$_2$, the twelve atoms in the unit cell leads to thirty-six phonon branches. It was found that a complex crystal with many optical modes is usually associated with low lattice thermal conductivity (Ding et al., 2018; Hu et al., 2020a; Hu et al., 2020b). A number of optical modes gather in frequency about 10 THz. High-frequency phonons with low velocity often do little contribution to lattice thermal conductivity. One can also see that the low-lying optical modes are coupled with acoustic modes, which is different from phosphorene or monolayer MoS$_2$ where there is a wide frequency gap among optical branches or between acoustic and optical branches (Fei et al., 2014; Jin et al., 2015). A strong coupling of phonon modes will increase the anharmonic scattering processes and leads to the low lattice thermal conductivity. Although the allowed phonon frequency of about 40 THz is higher than that of phosphorene and monolayer MoS$_2$ due to the light element, the allowed acoustic frequency of about 5 THz of phonon modes is quite lower than graphene, phosphorene, and monolayer MoS$_2$ (Fei et al., 2014; Jin et al., 2015; Ge et al., 2016). These advantages of low lattice thermal conductivity in the β_1^s boron monolayer are probably associated with its complex crystal of hexagonal vacancies.

Figure 4A shows the calculated lattice thermal conductivity of the boron monolayer with respect to temperature. It can be seen that the BTE results are well fitted with $\kappa \propto 1/T$. The lattice

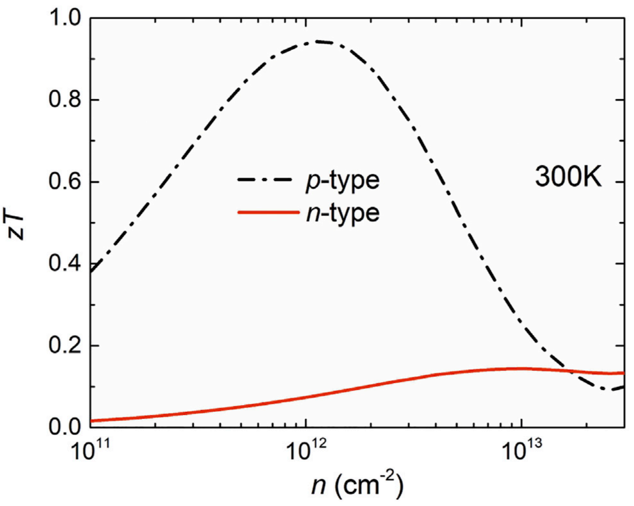

FIGURE 5 | Calculated thermoelectric figure of merit at 300 K.

thermal conductivity at room temperature is about 20 W/mK, which is much lower than that of graphene (above 4000 W/mK) (Balandin et al., 2008), phosphorene (above 150 W/mK along zigzag) (Xu et al., 2015) consisting of light element, and also monolayer MoS_2 (about 100 W/mK) (Jin et al., 2015). Thus, the β_1^s boron monolayer with a light boron element in the crystal also exhibits low lattice thermal conductivity, as compared to previous light monolayers. Such a low lattice thermal conductivity can be ascribed to the large number of optical modes and the strongly coupled phonon modes as arising from the complex unit cell with a network of hexagonal vacancies, as discussed above. The low group velocity of optical modes, as shown in **Figure 4B**, indicates that the acoustic and low-lying optical modes do most of the contribution to phonon transport. One can see from **Figure 4C** that the anharmonic scattering rate increases with the increase in temperature, and such scattering rate is much higher than monolayer MoS_2 in which the scattering rates of phonons almost lie below 1ps^{-1} (Ding et al., 2018). **Figure 4D** shows the cumulative lattice thermal conductivity as a function of mean free path at 300 K, which points to the well convergence of the lattice thermal conductivity.

Combining the electronic and phonon transport properties, we evaluated the thermoelectric performance of the β_1^s boron monolayer. **Figure 5** shows the figure of merit *ZT* values for both the *n*- and *p*-doped boron monolayer as a function of the carrier concentration at room temperature. Obviously, the *p*-type thermoelectric performance is superior to *n*-type due to the excellent *p*-type power factor. Combined with the relatively low lattice thermal conductivity, the optimal *p*-type *ZT* value of the boron monolayer reaches 0.96 at an optimal carrier concentration of about 1×10^{12} cm^{-2}, which is a recorded value among single-layer materials consisting of light elements. Our results indicate that the semiconducting β_1^s boron monolayer has a potential application in thermoelectric devices.

CONCLUSION

We have investigated the thermoelectric performance of a semiconducting β_1^s boron monolayer using first-principles combined with Boltzmann transport equations. We have shown that the high *n*-type Seebeck coefficient arises from the camelback shape of the lowest conduction band, while the highly degenerate valence band with small effective mass leads to the high hole mobility and long relaxation time, which contributes to the superior hole transport performance. Importantly, we found relatively low lattice thermal conductivity in the boron monolayer, ~20 W/mK at 300 K, as compared with graphene or phosphorene also consisting of a light element. This is primarily ascribed to the complex unit cell with the hexagonal vacancy. Finally, we obtained an optimal *p*-type *ZT* of about 0.96 at 300 K in this boron monolayer, indicating its potential as *p*-type thermoelectric materials.

DATA AVAILABILITY STATEMENT

The original contributions presented in the study are included in the article/supplementary material; further inquiries can be directed to the corresponding author.

AUTHOR CONTRIBUTIONS

GD developed the idea for the study. YH and GD did the analyses and wrote the study. DL, RL, SL, CF, and DFL conceived and designed the study. All authors analyzed the data and were involved in writing the manuscript.

FUNDING

This work is supported by the National Natural Science Foundation of China (Grant No.11804040).

REFERENCES

Balandin, A. A., Ghosh, S., Bao, W., Calizo, I., Teweldebrhan, D., Miao, F., et al. (2008). Superior thermal Conductivity of Single-Layer Graphene. *Nano Lett.* 8, 902–907. doi:10.1021/nl0731872

Ding, G., Carrete, J., Li, W., Gao, G. Y., and Yao, K. (2016). Ultralow Lattice thermal Conductivity in Topological Insulator TlBiSe2. *Appl. Phys. Lett.* 108, 233902. doi:10.1063/1.4953588

Ding, G., He, J., Gao, G. Y., and Yao, K. (2018). Two-dimensional MoS2-MoSe2 Lateral Superlattice with Minimized Lattice thermal Conductivity. *J. Appl. Phys.* 124, 165101. doi:10.1063/1.5051067

Ding, G., Hu, Y., Li, D., and Wang, X. (2019). A Comparative Study of Thermoelectric Properties between Bulk and Monolayer SnSe. *Results Phys.* 15, 102631. doi:10.1016/j.rinp.2019.102631

Ding, G., Li, S., and He, J. (2019). Origins of Promising Thermoelectric Performance in Quaternary Selenide BaAg2SnSe4. *Appl. Phys. Express* 12, 071006. doi:10.7567/1882-0786/ab29e1

Eremeev, S. V., Koroteev, Y. M., and Chulkov, E. V. (2010). Ternary Thallium-Based Semimetal Chalcogenides Tl-V-VI2 as a New Class of Three-Dimensional Topological Insulators. *JETP Lett.* 91, 594–598. doi:10.1134/S0021364010110111

Fei, R., Faghaninia, A., Soklaski, R., Yan, J.-A., Lo, C., and Yang, L. (2014). Enhanced Thermoelectric Efficiency via Orthogonal Electrical and thermal Conductances in Phosphorene. *Nano Lett.* 14, 6393–6399. doi:10.1021/nl502865s

Ge, X.-J., Yao, K.-L., and Lü, J.-T. (2016). Comparative Study of Phonon Spectrum and thermal Expansion of Graphene, Silicene, Germanene, and Blue Phosphorene. *Phys. Rev. B.* 94, 165433. doi:10.1103/PhysRevB.94.165433

Hellman, O., and Broido, D. A. (2014). Phonon thermal Transport inBi2Te3from First Principles. *Phys. Rev. B.* 90, 134309. doi:10.1103/PhysRevB.90.134309

Herring, C., and Vogt, E. (1956). Transport and Deformation-Potential Theory for many-valley Semiconductors with Anisotropic Scattering. *Phys. Rev.* 101, 944–961. doi:10.1103/PhysRev.101.944

Hu, Y., Li, D., Yin, Y., Li, S., Ding, G., Zhou, H., et al. (2020). The Important Role of Strain on Phonon Hydrodynamics in diamond-like Bi-layer Graphene. *Nanotechnology* 31, 335711. doi:10.1088/1361-6528/ab8ee1

Hu, Y., Yang, T., Li, D., Ding, G., Dun, C., Wu, D., et al. (2021). Origins of Minimized Lattice thermal Conductivity and Enhanced Thermoelectric Performance in WS2/WSe2 Lateral Superlattice. *ACS Omega* 6, 7879–7886. doi:10.1021/acsomega.1c00457

Hu, Y., Yin, Y., Li, S., Zhou, H., Li, D., and Zhang, G. (2020). Three-Fold Enhancement of In-Plane Thermal Conductivity of Borophene through Metallic Atom Intercalation. *Nano Lett.* 20, 7619–7626. doi:10.1021/acs.nanolett.0c03135

Jin, Z., Liao, Q., Fang, H., Liu, Z., Liu, W., Ding, Z., et al. (2015). A Revisit to High Thermoelectric Performance of Single-Layer MoS2. *Sci. Rep.* 5, 1–7. doi:10.1038/srep18342

Kiraly, B., Liu, X., Wang, L., Zhang, Z., Mannix, A. J., Fisher, B. L., et al. (2019). Borophene Synthesis on Au(111). *ACS Nano* 13, 3816–3822. doi:10.1021/acsnano.8b09339

Kong, L., Wu, K., and Chen, L. (2018). Recent Progress on Borophene: Growth and Structures. *Front. Phys.* 13, 138105. doi:10.1007/s11467-018-0752-8

Kresse, G., and Furthmüller, J. (1996). Efficient Iterative Schemes Forab Initiototal-Energy Calculations Using a Plane-Wave Basis Set. *Phys. Rev. B.* 54, 11169–11186. doi:10.1103/PhysRevB.54.11169

Kumar, S., and Schwingenschlögl, U. (2015). Thermoelectric Response of Bulk and Monolayer MoSe2 and WSe2. *Chem. Mater.* 27, 1278–1284. doi:10.1021/cm504244b

Li, W., Carrete, J., A. Katcho, N., and Mingo, N. (2014). ShengBTE: A Solver of the Boltzmann Transport Equation for Phonons. *Comp. Phys. Commun.* 185, 1747–1758. doi:10.1016/j.cpc.2014.02.015

Madsen, G. K. H., and Singh, D. J. (2006). BoltzTraP. A Code for Calculating Band-Structure Dependent Quantities. *Comp. Phys. Commun.* 175, 67–71. doi:10.1016/j.cpc.2006.03.007

Mohanraman, R., Lan, T.-W., Hsiung, T.-C., Amada, D., Lee, P.-C., Ou, M.-N., et al. (2015). Engineering Nanostructural Routes for Enhancing Thermoelectric Performance: Bulk to Nanoscale. *Front. Chem.* 3, 63. doi:10.3389/fchem.2015.00063

Pei, Y.-L., and Liu, Y. (2012). Electrical and thermal Transport Properties of Pb-Based Chalcogenides: PbTe, PbSe, and PbS. *J. Alloys Comp.* 514, 40–44. doi:10.1016/j.jallcom.2011.10.036

Peng, H., Kioussis, N., and Snyder, G. J. (2014). Elemental Tellurium as a Chiralp-type Thermoelectric Material. *Phys. Rev. B.* 89, 195206. doi:10.1103/PhysRevB.89.195206

Perdew, J. P., Burke, K., and Ernzerhof, M. (1997). Generalized Gradient Approximation Made Simple [Phys. Rev. Lett. 77, 3865 (1996)]. *Phys. Rev. Lett.* 78, 1396. doi:10.1103/PhysRevLett.77.386510.1103/physrevlett.78.1396

Sun, J., and Singh, D. J. (2016). Thermoelectric Properties ofMg2(Ge,Sn): Model and Optimization ofZT. *Phys. Rev. Appl.* 5, 024006. doi:10.1103/PhysRevApplied.5.024006

Togo, A., Oba, F., and Tanaka, I. (2008). First-principles Calculations of the Ferroelastic Transition between Rutile-type andCaCl2-typeSiO2at High Pressures. *Phys. Rev. B.* 78, 134106. doi:10.1103/PhysRevB.78.134106

Tran, F., and Blaha, P. (2009). Accurate Band Gaps of Semiconductors and Insulators with a Semilocal Exchange-Correlation Potential. *Phys. Rev. Lett.* 102, 226401. doi:10.1103/PhysRevLett.102.226401

Xu, S.-G., Li, X.-T., Zhao, Y.-J., Liao, J.-H., Xu, W.-P., Yang, X.-B., et al. (2017). Two-Dimensional Semiconducting Boron Monolayers. *J. Am. Chem. Soc.* 139, 17233–17236. doi:10.1021/jacs.7b08680

Xu, W., Zhu, L., Cai, Y., Zhang, G., and Li, B. (2015). Direction Dependent thermal Conductivity of Monolayer Phosphorene: Parameterization of Stillinger-Weber Potential and Molecular Dynamics Study. *J. Appl. Phys.* 117, 214308. doi:10.1063/1.4922118

Conflict of Interest: The authors declare that the research was conducted in the absence of any commercial or financial relationships that could be construed as a potential conflict of interest.

The reviewer (HY) declared a past coauthorship with one of the authors (GD) to the handling editor.

ORIGINAL RESEARCH
published: 28 September 2021
doi: 10.3389/fchem.2021.755350

Various Nodal Lines in $P6_3/mmc$-type TiTe Topological Metal and its (001) Surface State

Peng Lin*[1], *Fang Fang*[1], *Li Zhang*[2]*, *Yang Li*[1,3]* and *Kai Wang*[1,3]

[1]Engineering and Technology Center, The Fourth Medical College of Harbin Medical University, Harbin, China, [2]Changchun Institute of Technology, Changchun, China, [3]Nanoscience and Engineering and Technology Electrophysiology Research Center, The Fourth Medical College of Harbin Medical University, Harbin, China

Searching for existing topological materials is a hot topic in quantum and computational chemistry. This study uncovers $P6_3/mmc$ type TiTe compound—an existing material—is a newly discovered topological metal that hosts the various type of nodal line states. Different nodal line states normally exhibit different properties; they may have their individual applications. We report that TiTe hosts I, II, and hybrid type nodal line (NL) states at its ground state without chemical doping and strain engineering effects. Specifically, two type I NLs, two hybrid-type NLs, and one Γ—centered type II NL can be found in the $k_z = 0$ plane. Moreover, the spin-orbit coupling induced gaps for these NLs are very small and within acceptable limits. The surface states of the TiTe (001) plane were determined to provide strong evidence for the appearance of the three types of NLs in TiTe. We also provide a reference for the data of the dynamic and mechanical properties of TiTe. We expect that the proposed NL states in TiTe can be obtained in future experiments.

Keywords: DFT study, tite, nodal line states, surface states, SOC

***Correspondence:**
Kai Wang
wangkai@hrbmu.edu.cn
Li Zhang
zhangli_chemistry@126.com
Yang Li
doctoryangli@hrbmu.edu.cn

Specialty section:
This article was submitted to Theoretical and Computational Chemistry, a section of the journal Frontiers in Chemistry

Received: *08 August 2021*
Accepted: *10 September 2021*
Published: *28 September 2021*

Citation:
Lin P, Fang F, Zhang L, Li Y and Wang K (2021) Various Nodal Lines in $P6_3/mmc$-type TiTe Topological Metal and its (001) Surface State. Front. Chem. 9:755350. doi: 10.3389/fchem.2021.755350

INTRODUCTION

Searching for topological materials in realistic materials in quantum and computational chemistry is a hot research topic. Topological materials (TMs) (Cava et al., 2013; Kong and Cui, 2011; Xu et al., 2015; Strambini et al., 2016; Wang et al., 2017; Banik et al., 2018; Kageyama et al., 2018; Schoop et al., 2018; Culcer et al., 2020; Kumar et al., 2020; Li and Xia, 2020; Xu et al., 2020) enjoy nontrivial band-crossings (BCs) in their low-energy region, giving rise to novel fermionic excitations. A series of TMs, including nodal-point (Alcón et al., 2017; Fu et al., 2018a; Kong et al., 2018; Jin et al., 2019a; Jin et al., 2019b; Wang et al., 2019; Fang et al., 2020; Zhang et al., 2020), nodal-line (Chen et al., 2018; Zhou et al., 2018; Li et al., 2019; Liu et al., 2019; Sankar et al., 2019; Tang et al., 2019; Xu et al., 2019; Yi et al., 2019; Wang et al., 2020a; Zhao et al., 2020), and nodal-surface (Wu et al., 2018; Qie et al., 2019; Wang et al., 2020b) materials, have been predicted *via* symmetry and first-principle analysis. Some of them have been verified *via* experiment.

Recently, many chemists and physicists have focused on studying the nodal line (NL) type materials. The NL-type materials are very important because they can enjoy more sub-types than other types of topological materials; moreover, different sub-types generally have their physical behaviors. Many NL materials with different NL shapes have been proposed, including nodal ring (Zhang et al., 2018a), nodal chain (Bzdušek et al., 2016), nodal link (Yan et al., 2017), nodal knot (Bi et al., 2017; Ezawa, 2017), and nodal net materials (Wang et al., 2018a; Fu et al., 2018b; Feng et al.,

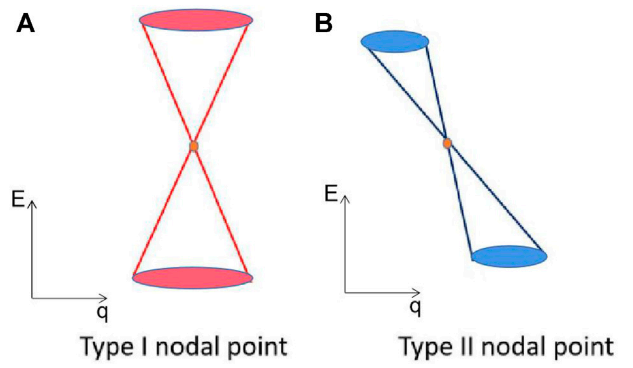

FIGURE 1 | Illustration of the type **(A)** I and **(B)** II NLs.

2018). Different shapes of the NLs usually exhibit different electronic and optical behaviors. Moreover, NLs can normally be classified into the I, II, and hybrid types (Jin et al., 2020) according to the slope of the bands around the band-crossing points (BCPs).

The I type NL is composed of all the type I BCPs, and the II type NL is formed by the type II BCPs. However, the hybrid-type NL contains I and II type NLs simultaneously. The illustration of I and II type BCPs are shown in **Figures 1A,B**, respectively. The I type BCPs show a traditional conical dispersion, whereas the II type BCPs show a titled dispersion.

A series of materials (Wang et al., 2018b; Wang et al., 2020c; Jin et al., 2020), type I or II NLs, have been studied *via* symmetry analysis and first-principles calculations. However, materials with I and II type NLs have rarely been explored in the literature. It is fascinating to investigate if I, II, and hybrid NLs can coexist in one material without strain, chemical doping, or other controlling methods.

In this work, we select $P6_3/mmc$ type TiTe material as an example and to show that the I, II, and hybrid types of NLs can coexist in realistic TiTe material (Ehrlish, 1949). The TiTe has already been realized in the experiment. We show that I, II, and hybrid NLs can be found in the kz = 0 plane of TiTe. The structural model of hexagonal $P6_3/mmc$ type TiTe with a primitive cell is exhibited in **Figures 2A,B** under different view sides. TiTe contains two Ti and two Te atoms, located at the (0 0 0)/(0, 0, 0.5) sites and the (1/3, 2/3, 0.25)/(2/3, 1/3, 0.75) sites, respectively. We optimized the lattice constants and the atomic positions based on the first-principle calculation. The obtained lattice constants of TiTe were a = b = 3.66 Å and c = 7.27 Å, agreeing well with the calculated values in the database[1].

This study reports the band structures, phonon dispersions, and topological signatures of TiTe. We uncover that TiTe is an NL metal with one pair of type I NLs, one type II NL, and one pair of hybrid NLs in the kz = 0 plane. We also examine the influence of spin-orbit coupling (SOC) on the band structures. Finally, we calculate the projected spectrum on the (001) surface of TiTe show the occurrence of drum-head-like surface states connected to the BCPs. More details about the computational methods can be found in **Supplementary Material**.

DYNAMICAL STABILITY AND MECHANICAL STABILITY

In this section, we present the study of the stabilities of TiTe with respect to dynamical and mechanical properties. Based on the bulk Brillouin zone and the selected symmetry points in **Figure 2C**. The phonon dispersion of TiTe was calculated through the force-constants method; the result is given in **Figure 3**. We conclude that the TiTe is dynamically stable because its phonon dispersion does not include imaginary frequencies.

Subsequently, the mechanical stability of TiTe is examined according to elastic stability criteria. TiTe has a $P6_3/mmc$ structure with five elastic constants—C_{11}, C_{12}, C_{13}, C_{33}, C_{44}, and C_{66}. The computed values of C_{11}, C_{12}, C_{13}, C_{33}, C_{44}, and C_{66} were 133.543, 47.021, 78.611, 173.304, 43.206, and 107.550 GPa, respectively. We conclude based on the obtained elastic constants that they meet the criteria for elastic stability, as mentioned below:

i) $C_{11} > |C_{12}|$;
ii) $2 \times C_{13}^2 < C_{33}(C_{11} + C_{12})$;
iii) $C_{44} > 0$.

Hence, TiTe is mechanically stable theoretically.

ELECTRONIC STRUCTURES AND TOPOLOGICAL SIGNATURES OF BULK TITE

Figure 4A shows the calculated total and projected density of states (DOSs). We conclude that a small peak appears at the Fermi level (E_F). Therefore, TiTe is a metallic material. The band structure of the TiTe metal is given in **Figure 4B**. We primarily focus on the bands closed to the E_F. We observe that the Ti-d orbitals dominate the total DOSs in this region (-2 to 1 eV), as shown in **Figure 4A** with a green background. However, within the −5 to −2 eV energy range, the dominating factors contributing to the total DOSs are the Ti-d and Te-p orbitals. There exists a strong hybrid phenomenon between the Ti-d and Te-p orbitals in this energy range.

We show the band structure of the TiTe in **Figure 4B** ignoring the SOC. The band structure shows a series of BCPs above and below the E_F. For clarity, we divided these BCPs into region A, region B, and region C, respectively. A, B, and C regions are marked by different colors. Two obvious BCPs—A1 and A2—located above the E_F can be found in region A. Two BCPs—B1 and B2—located very close to and below the E_F appear in region B. There are also two BCPs—C1

---

[1] .https://materialsproject.org/materials/mp-567832

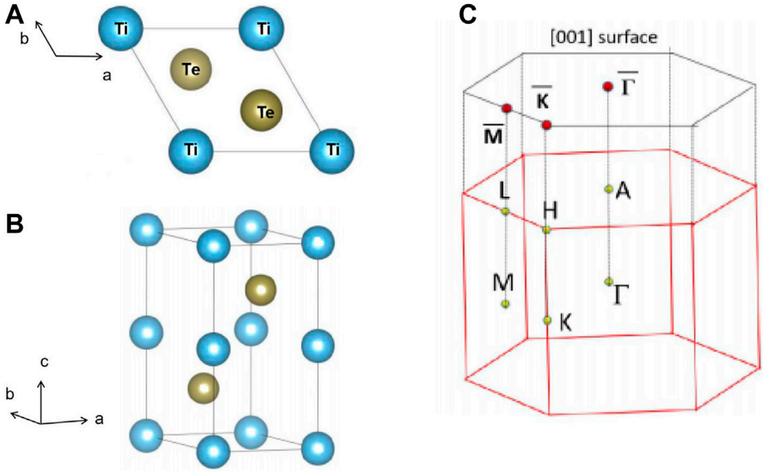

FIGURE 2 | (A,B) Structural models. **(C)** The bulk and the (001) surface Brillouin zone.

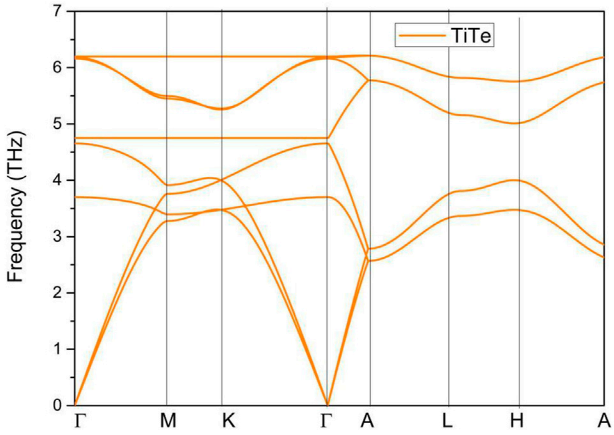

FIGURE 3 | Phonon dispersion of TiTe bulk.

and C2—in region C. However, they are slightly further away from the E_F than the other BCPs—A1, A2, B1, and B2.

Different types of BCPs are discussed in regions A, B, and C. The two BCPs in region A are I type nodal points (NPs). Weng et al. (Weng et al., 2015) stated that these doubly degenerated crossing points (A1 and A2) are not isolated points; they should belong to a line. We conclude based on the plotted Brillouin zone of 3D bulk TiTe in **Figure 2C** that the A1 and A2 NPs are located in the kz = 0 plane.

We show the K-centered 3D plotting of the band dispersion in region A of the kz = 0 plane in **Figure 5A** to demonstrate that the A1 and A2 NPs reside on an NL. We conclude that the energy variation of the NL in region A is very small. Such a flat NL is expected to host novel behaviors. **Figures 5A,B** show the highlighted NL (see the white dotted line) and the shape of the NL in region A, respectively. We conclude that the NL in region A is a type I. Furthermore, the NLs in region A are protected by two independent mechanisms: i) mirror symmetry and ii) inversion

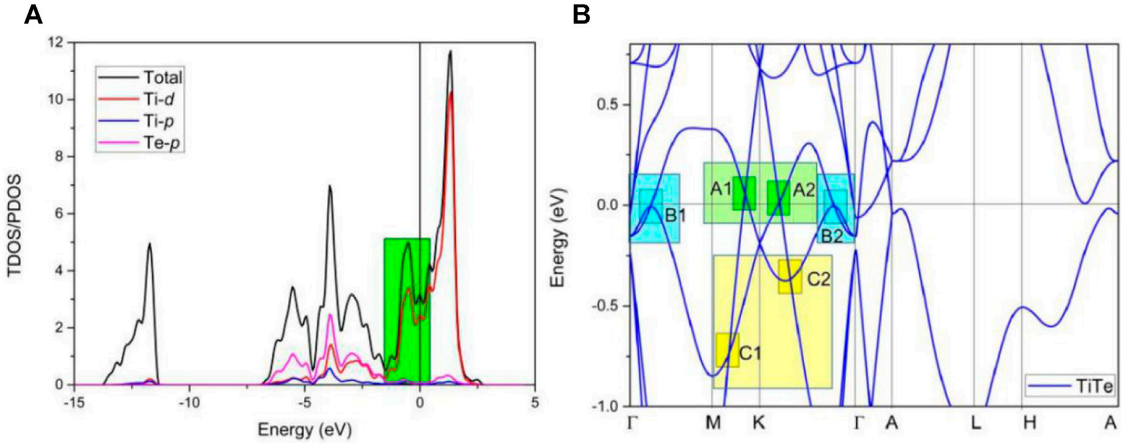

FIGURE 4 | (A) Total and projected density of states and **(B)** band structure of TiTe bulk.

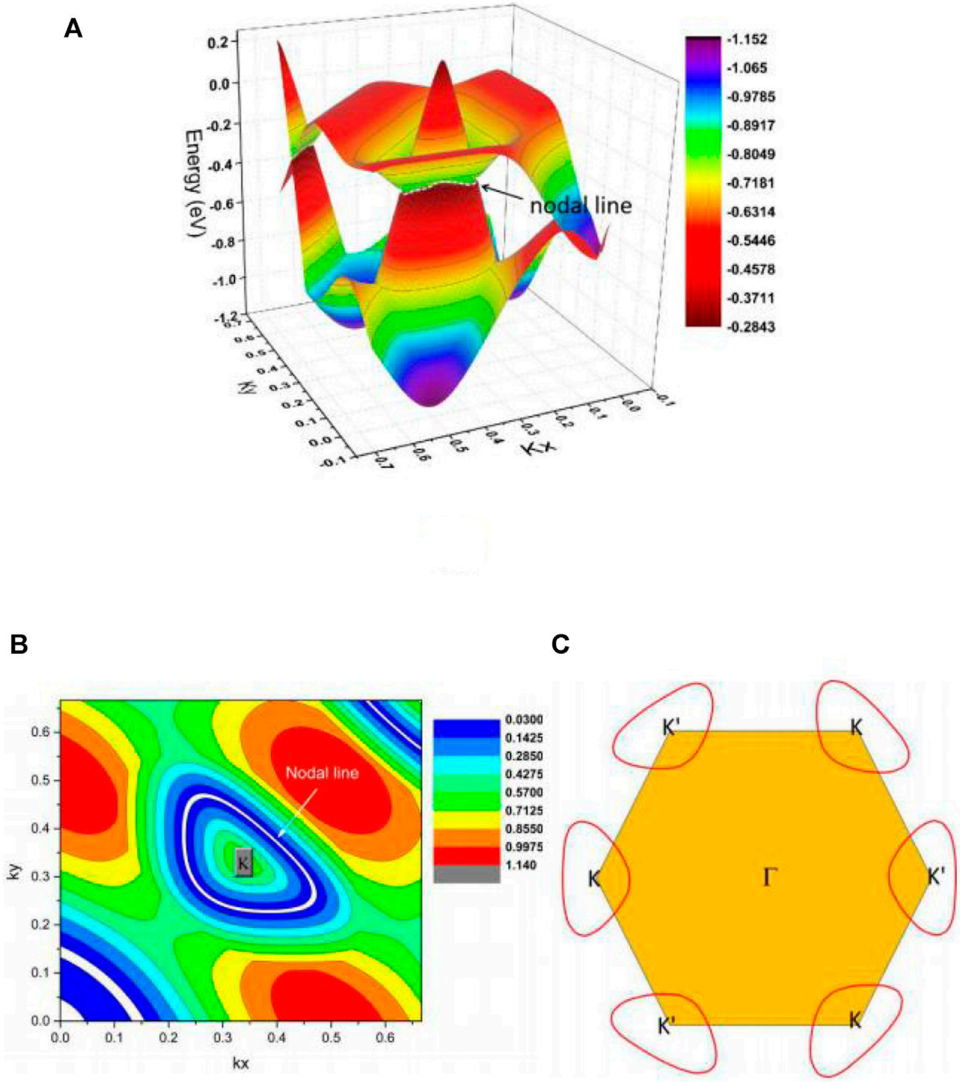

FIGURE 5 | (A) 3D band dispersion in region A of the kz = 0 plane; **(B)** the shape of the NL in region A of the kz = 0 plane; and **(C)** illustration of one pair of type I NLs in the kz = 0 plane.

symmetry and time-reversal symmetry. TiTe possesses time-reversal symmetry; therefore, one more K′-centered NL should appear in the kz = 0 plane. The shape of one of the pairs of NLs, i.e., the K and K′ centered NLs, is shown in **Figure 5C**.

In region B, two type II NPs, B1 and B2, also belong to a single NL and the Γ-centered 3D band dispersion in region B of the kz = 0 plane and the shape of the NL in region B are given in **Figures 6A,B**, respectively. We highlight NL by a white dotted line. This Γ -centered band dispersion has a small energy variation, similar to the NL in region A. **Figure 6** shows that the NL in region B is type II.

Finally, the K-centered 3D band dispersion in region C of the kz = 0 plane and the shape of the NL in region C are exhibited in **Figures 7A–C** to determine the topological signatures of the C1 and C2 NPs in region C. We conclude from the different viewpoints of the K-centered 3-D band dispersion that the energy variation of the NL is significantly large (from −0.8 to −0.3 eV). The reason for such a large energy variation is because it is a hybrid NL (Zhang et al., 2018b), containing type I and type II NPs at the same time. **Figure 4C** shows that BCP C1 is a type I; however, BCP C2 is type II. Moreover, another K′-centered hybrid NL should be located in the kz = 0 plane as required by the time-reversal symmetry (**Figure 7D**).

PROJECTED SPECTRUM ON THE TITE (001) SURFACE

In this section, we provide strong evidence for the appearance of the NLs in the three regions. NL materials

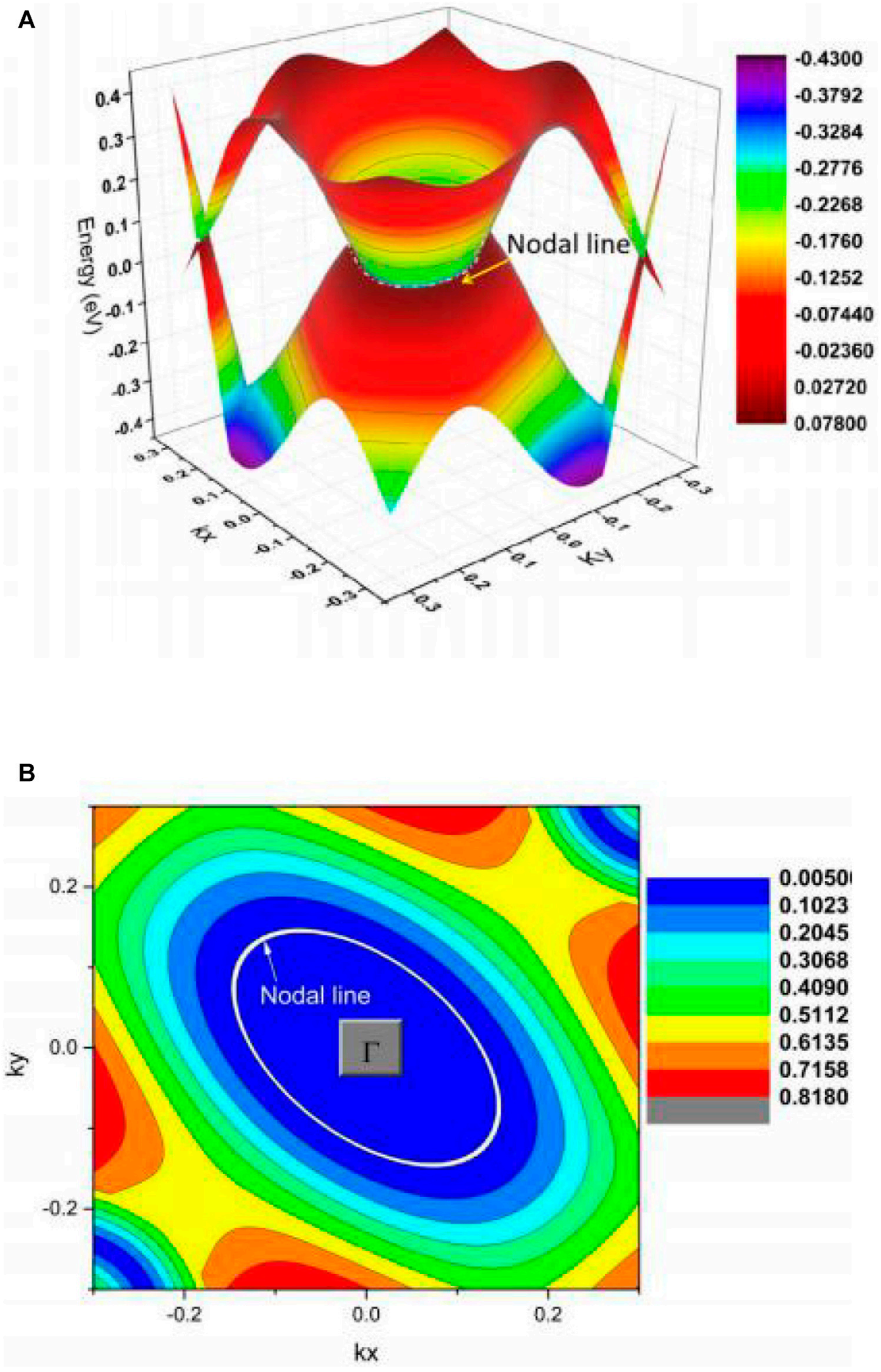

FIGURE 6 | (A) Γ-centered 3D band dispersion in region B of the kz = 0 plane and **(B)** shape of the NL in region B of the kz = 0 plane.

usually host drum-head-like (D-H-L) surface states (Wang et al., 2020d) connected to the ban-crossing points, one of its most important characters. **Figures 8A,B** show the projected spectrum on the TiTe (001) surface. We use the black circles to indicate the positions of the BCPs. The D-H-L surface states, connected to the BCPs and marked by

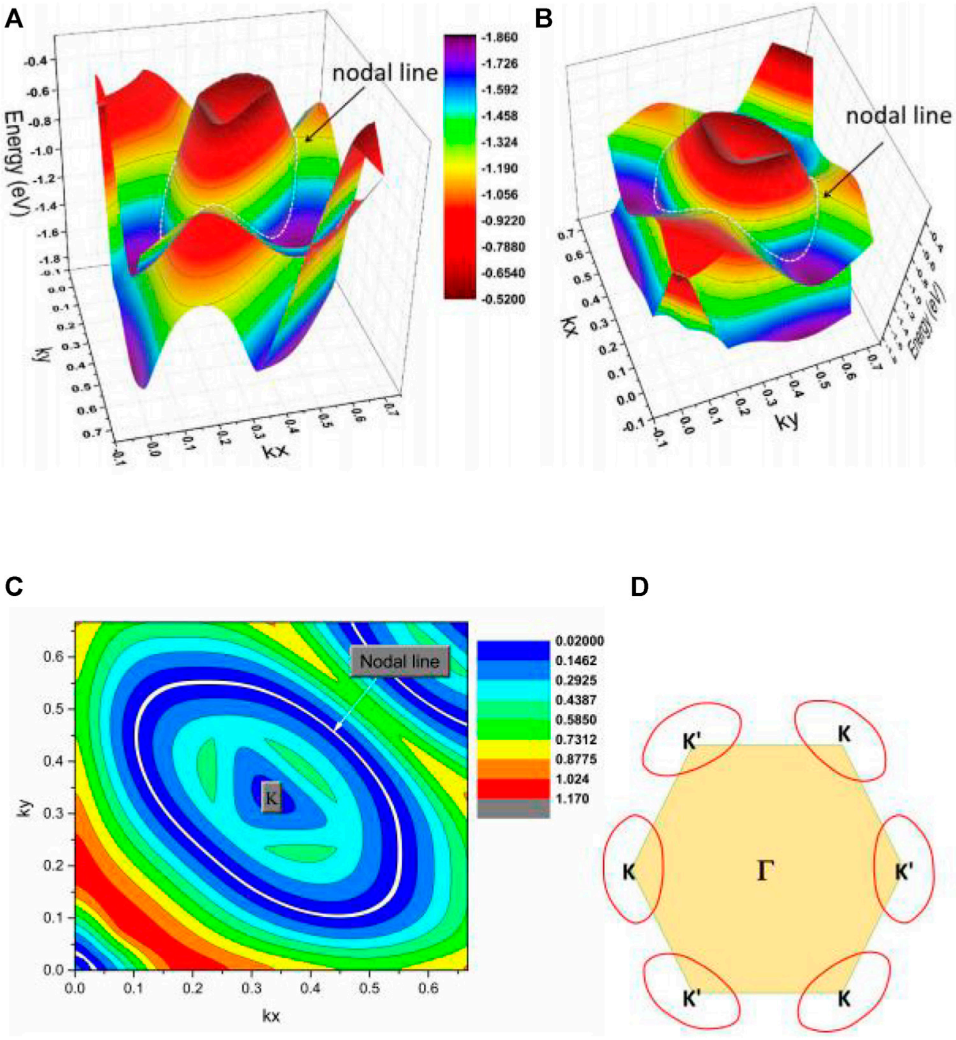

FIGURE 7 | (A,B) K-centered 3D band dispersion in region C of the kz = 0 plane from different viewpoints. **(C)** The shape of the NL in region C of the kz = 0 plane. **(D)** Illustration of one pair of hybrid type NLs in the kz = 0 plane.

arrows, can be observed. Such obvious D-H-L surface states in TiTe benefit the experimental detection. It is expected that angle-resolved optical emission spectroscopy (ARPES) can be used to detect the D-H-L surface states in TiTe directly.

EFFECT OF SOC

The SOC usually induces a gap in the BCPs in most NL materials. The SOC-induced gap is particularly very large (50–200 meV) when the material contains heavy elements (Huang et al., 2016; Yamakage et al., 2016; Wang et al., 2020e), which significantly damages the intrinsic electronic properties of the NLs. **Figure 8C** shows the band structure with SOC. Therefore, we conclude that the SOC-induced gap for these band-crossings is smaller than 28 meV and within the acceptable limits, reflecting that TiTe is an ideal NL material with robust resistance to the effects of SOC.

CONCLUSION

We prove the existence of I, II, and hybrid types of NLs in TiTe at the ground state. Moreover, TiTe is shown to be a dynamic and mechanically stable material using first-principle calculations. Furthermore, it is proved to be an ideal NL material with two type I NLs: one Γ-centered type II NL and two hybrid-type NLs in the $k_z = 0$ plane. The BCPs are robust to the SOC, and the SOC-induced gaps are quite small. The D-H-L surface states can be

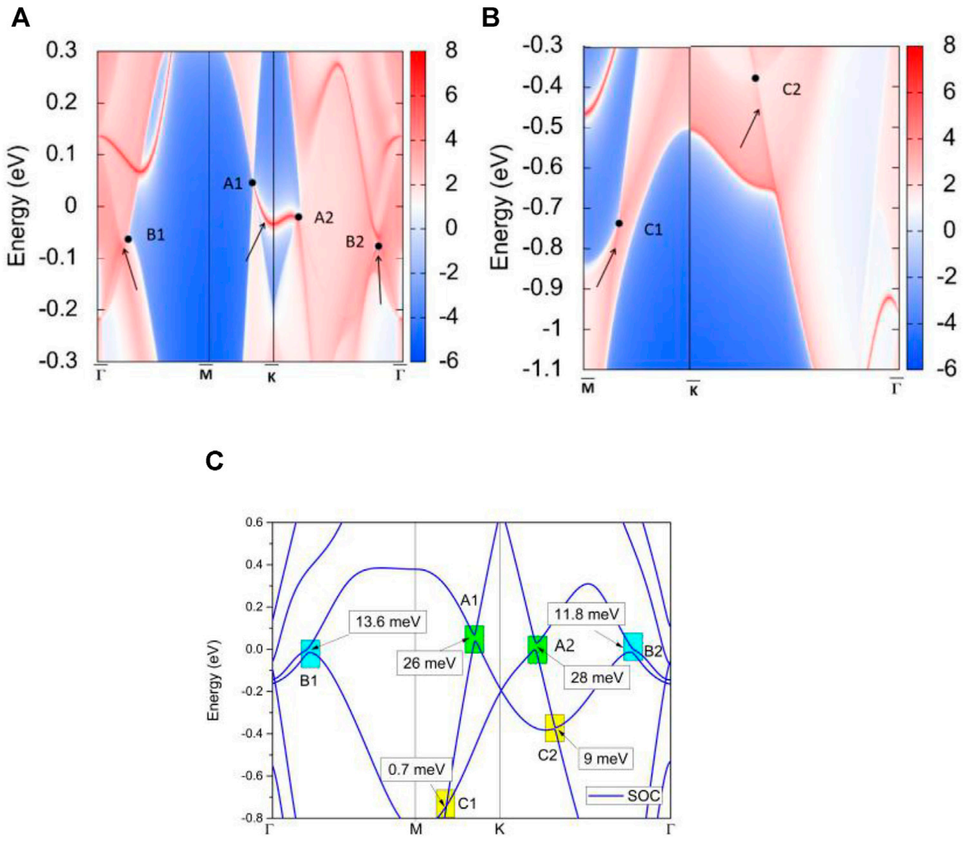

FIGURE 8 | (A,B) The projected spectrum on the (001) surface of TiTe. The BCPs—A1, A2, B1, B2, C1, and C2—and the drum-head-like surface states are highlighted by the circles and arrows, respectively. **(C)** The band structure of TiTe under spin-orbit coupling.

observed in (001) surface of the TiTe. We expect that the NLs and the (001) surface states of TiTe can be verified in an experiment.

DATA AVAILABILITY STATEMENT

The original contributions presented in the study are included in the article/**Supplementary Material**, further inquiries can be directed to the corresponding authors.

AUTHOR CONTRIBUTIONS

LZ, PL, and FF: conceptualization, methodology, software, formal analysis, data curation, and writing. KW, YL, and LZ: investigation, funding, and project administration. All authors contributed to the article and approved the submitted version.

FUNDING

This work is supported by Topic Foundation of Changchun Institute of Technology (Grant No. 320200040), Young People Foundation of Changchun Institute of Technology (Grant No. 320200033), Doctor Foundation of Changchun Institute of Technology 2021, Natural Science Foundation of Heilongjiang Province (Grant No. LH2020H067), Heilongjiang Postdoctoral Program (LBH-Q16173), Science and Technology Program of Academy of Medical Sciences of Heilongjiang Province (Grant No. 201805), Research Foundation of Education Bureau of Jilin Province (Grant No. JJKH20210666KJ).

SUPPLEMENTARY MATERIAL

The Supplementary Material for this article can be found online at: https://www.frontiersin.org/articles/10.3389/fchem.2021.755350/full#supplementary-material

REFERENCES

Alcón, I., Viñes, F., Moreira, I. P. R., and Bromley, S. T. (2017). Existence of Multi-Radical and Closed-Shell Semiconducting States in post-graphene Organic Dirac Materials. *Nat. Commun.* 8 (1), 1957–1959. doi:10.1038/s41467-017-01977-4

Banik, A., Roychowdhury, S., and Biswas, K. (2018). The Journey of Tin Chalcogenides towards High-Performance Thermoelectrics and Topological Materials. *Chem. Commun.* 54 (50), 6573–6590. doi:10.1039/c8cc02230e

Bi, R., Yan, Z., Lu, L., and Wang, Z. (2017). Nodal-knot Semimetals. *Phys. Rev. B* 96 (20), 201305. doi:10.1103/physrevb.96.201305

Bzdušek, T., Wu, Q., Rüegg, A., Sigrist, M., and Soluyanov, A. A. (2016). Inventory Asset and Fixed Asset Frauds. *Nature* 538 (7623), 75–78. doi:10.4324/9781315576787-9

Cava, R. J., Ji, H., Fuccillo, M. K., Gibson, Q. D., and Hor, Y. S. (2013). Crystal Structure and Chemistry of Topological Insulators. *J. Mater. Chem. C* 1 (19), 3176–3189. doi:10.1039/c3tc30186a

Chen, H., Zhang, S., Jiang, W., Zhang, C., Guo, H., Liu, Z., et al. (2018). Prediction of Two-Dimensional Nodal-Line Semimetals in a Carbon Nitride Covalent Network. *J. Mater. Chem. A.* 6 (24), 11252–11259. doi:10.1039/c8ta02555j

Culcer, D., Cem Keser, A., Li, Y., and Tkachov, G. (2020). Transport in Two-Dimensional Topological Materials: Recent Developments in experiment and Theory. *2d Mater.* 7 (2), 022007. doi:10.1088/2053-1583/ab6ff7

Ehrlish, P. (1949). Über Titanselenide und -telluride. *Z. fuer Anorganische Allgemeine Chem.* 260, 1–3.

Ezawa, M. (2017). Topological Semimetals Carrying Arbitrary Hopf Numbers: Fermi Surface Topologies of a Hopf Link, Solomon's Knot, Trefoil Knot, and Other Linked Nodal Varieties. *Phys. Rev. B* 96 (4), 041202. doi:10.1103/physrevb.96.041202

Fang, P., Shi, X., Liu, C., Zhai, X., Li, H., and Wang, L. (2020). Single- and Dual-Band Convertible Terahertz Absorber Based on Bulk Dirac Semimetal. *Opt. Commun.* 462, 125333. doi:10.1016/j.optcom.2020.125333

Feng, X., Yue, C., Song, Z., Wu, Q., and Wen, B. (2018). Topological Dirac Nodal-Net Fermions in AlB$_2$-type TiB$_2$ and ZrB$_2$. *Phys. Rev. Mater.* 2 (1), 014202. doi:10.1103/physrevmaterials.2.014202

Fu, B., Fan, X., Ma, D., Liu, C. C., and Yao, Y. (2018). Hourglasslike Nodal Net Semimetal in Ag$_2$BiO$_3$. *Phys. Rev. B* 98 (7), 075146. doi:10.1103/physrevb.98.075146

Fu, C., Guin, S. N., Watzman, S. J., Li, G., Liu, E., Kumar, N., et al. (2018). Large Nernst Power Factor over a Broad Temperature Range in Polycrystalline Weyl Semimetal NbP. *Energy Environ. Sci.* 11 (10), 2813–2820. doi:10.1039/c8ee02077a

Huang, H., Liu, J., Vanderbilt, D., and Duan, W. (2016). Topological Nodal-Line Semimetals in Alkaline-Earth Stannides, Germanides, and Silicides. *Phys. Rev. B* 93 (20), 201114. doi:10.1103/physrevb.93.201114

Jin, K.-H., Huang, H., Wang, Z., and Liu, F. (2019). A 2D Nonsymmorphic Dirac Semimetal in a Chemically Modified Group-VA Monolayer with a Black Phosphorene Structure. *Nanoscale* 11 (15), 7256–7262. doi:10.1039/c9nr00906j

Jin, L., Zhang, X., Dai, X., Liu, H., Chen, G., and Liu, G. (2019). Centrosymmetric Li2NaN: a superior Topological Electronic Material with Critical-type Triply Degenerate Nodal Points. *J. Mater. Chem. C* 7 (5), 1316–1320. doi:10.1039/c8tc05930f

Jin, L., Zhang, X., He, T., Meng, W., Dai, X., and Liu, G. (2020). Intermetallic α-FeSi2: Realization of Type-I, Type-II, and Hybrid Nodal Line States in a Single Material via Tunable Valleys. *J. Phys. Chem. C* 124, 12311–12317. doi:10.1021/acs.jpcc.0c02967

Kageyama, H., Hayashi, K., Maeda, K., Attfield, J. P., Hiroi, Z., Rondinelli, J. M., et al. (2018). Expanding Frontiers in Materials Chemistry and Physics with Multiple Anions. *Nat. Commun.* 9 (1), 772–815. doi:10.1038/s41467-018-02838-4

Kong, D., and Cui, Y. (2011). Opportunities in Chemistry and Materials Science for Topological Insulators and Their Nanostructures. *Nat. Chem* 3 (11), 845–849. doi:10.1038/nchem.1171

Kong, X., Li, L., and Peeters, F. M. (2018). Topological Dirac Semimetal Phase in GexSny Alloys. *Appl. Phys. Lett.* 112 (25), 251601. doi:10.1063/1.5037121

Kumar, N., Guin, S. N., Manna, K., Shekhar, C., and Felser, C. (2020). Topological Quantum Materials from the Viewpoint of Chemistry. *Chem. Rev.* 121 (5), 2780–2815. doi:10.1021/acs.chemrev.0c00732

Li, X., Liu, J., Wang, F. Q., Wang, Q., and Jena, P. (2019). Rational Design of Porous Nodal-Line Semimetallic Carbon for K-Ion Battery Anode Materials. *J. Phys. Chem. Lett.* 10 (20), 6360–6367. doi:10.1021/acs.jpclett.9b02484

Li, Y., and Xia, J. (2020). Cubic Hafnium Nitride: A Novel Topological Semimetal Hosting a 0-Dimensional (0-D) Nodal point and a 1-D Topological Nodal Ring. *Front. Chem.* 8, 727. doi:10.3389/fchem.2020.00727

Liu, Q.-B., Fu, H.-H., Xu, G., Yu, R., and Wu, R. (2019). Categories of Phononic Topological Weyl Open Nodal Lines and a Potential Material Candidate: Rb2Sn2O3. *J. Phys. Chem. Lett.* 10 (14), 4045–4050. doi:10.1021/acs.jpclett.9b01159

Qie, Y., Liu, J., Wang, S., Sun, Q., and Jena, P. (2019). Tetragonal C24: a Topological Nodal-Surface Semimetal with Potential as an Anode Material for Sodium Ion Batteries. *J. Mater. Chem. A.* 7 (10), 5733–5739. doi:10.1039/c8ta11276b

Sankar, R., Muthuselvam, I. P., Babu, K. R., Murugan, G. S., Rajagopal, K., Kumar, R., et al. (2019). Crystal Growth and Magnetic Properties of Topological Nodal-Line Semimetal GdSbTe with Antiferromagnetic Spin Ordering. *Inorg. Chem.* 58 (17), 11730–11737. doi:10.1021/acs.inorgchem.9b01698

Schoop, L. M., Pielnhofer, F., and Lotsch, B. V. (2018). Chemical Principles of Topological Semimetals. *Chem. Mater.* 30 (10), 3155–3176. doi:10.1021/acs.chemmater.7b05133

Strambini, E., D'Ambrosio, S., Vischi, F., Bergeret, F. S., Nazarov, Y. V., and Giazotto, F. (2016). The ω-SQUIPT as a Tool to Phase-Engineer Josephson Topological Materials. *Nat. Nanotech* 11 (12), 1055–1059. doi:10.1038/nnano.2016.157

Tang, M., Shen, H., Qie, Y., Xie, H., and Sun, Q. (2019). Edge-State-Enhanced CO2 Electroreduction on Topological Nodal-Line Semimetal Cu2Si Nanoribbons. *J. Phys. Chem. C* 123 (5), 2837–2842. doi:10.1021/acs.jpcc.8b08871

Wang, A., Shen, L., Zhao, M., Wang, J., Zhou, W., Li, W., et al. (2019). Tungsten Boride: a 2D Multiple Dirac Semimetal for the Hydrogen Evolution Reaction. *J. Mater. Chem. C* 7 (29), 8868–8873. doi:10.1039/c9tc01862j

Wang, B., Gao, H., Lu, Q., Xie, W., Ge, Y., Zhao, Y.-H., et al. (2018). Type-I and Type-II Nodal Lines Coexistence in the Antiferromagnetic Monolayer CrAs2. *Phys. Rev. B* 98 (11), 115164. doi:10.1103/physrevb.98.115164

Wang, J. T., Nie, S., Weng, H., Kawazoe, Y., and Chen, C. (2018). Topological Nodal-Net Semimetal in a Graphene Network Structure. *Phys. Rev. Lett.* 120 (2), 026402. doi:10.1103/PhysRevLett.120.026402

Wang, X., Cheng, Z., Zhang, G., Kuang, M., Wang, X.-L., and Chen, H. (2020). Strain Tuning of Closed Topological Nodal Lines and Opposite Pockets in Quasi-Two-Dimensional α-phase FeSi2. *Phys. Chem. Chem. Phys.* 22, 13650–13658. doi:10.1039/d0cp02334e

Wang, X., Ding, G., Cheng, Z., Surucu, G., Wang, X.-L., and Yang, T. (2020). Novel Topological Nodal Lines and Exotic Drum-head-like Surface States in Synthesized CsCl-type Binary alloy TiOs. *J. Adv. Res.* 22, 137–144. doi:10.1016/j.jare.2019.12.001

Wang, X., Ding, G., Cheng, Z., Surucu, G., Wang, X.-L., and Yang, T. (2020). Rich Topological Nodal Line Bulk States Together with Drum-head-like Surface States in NaAlGe with Anti-PbFCl Type Structure. *J. Adv. Res.* 23, 95–100. doi:10.1016/j.jare.2020.01.017

Wang, X., Ding, G., Cheng, Z., Wang, X.-L., Zhang, G., and Yang, T. (2020). Intersecting Nodal Rings in Orthorhombic-type BaLi2Sn Compound. *J. Mater. Chem. C* 8 (16), 5461–5466. doi:10.1039/d0tc00504e

Wang, X., Zhou, F., and Chen, H. (2020). Organic-inorganic Hybrid Coordination Polymer C3H9CdCl3N Co-exhibiting superior Dirac point and Nodal Surface States. *Results Phys.* 17, 103159. doi:10.1016/j.rinp.2020.103159

Wang, Z. F., Jin, K. H., and Liu, F. (2017). Computational Design of Two-dimensional Topological Materials. *Wiley Interdiscip. Rev. Comput. Mol. Sci.* 7 (4), e1304. doi:10.1002/wcms.1304

Weng, H., Liang, Y., Xu, Q., Yu, R., Fang, Z., Dai, X., et al. (2015). Topological Node-Line Semimetal in Three-Dimensional Graphene Networks. *Phys. Rev. B* 92 (4), 045108. doi:10.1103/physrevb.92.045108

Wu, W., Liu, Y., Li, S., Zhong, C., Yu, Z.-M., Sheng, X.-L., et al. (2018). Nodal Surface Semimetals: Theory and Material Realization. *Phys. Rev. B* 97 (11), 115125. doi:10.1103/physrevb.97.115125

Xu, S.-G., Zheng, B., Xu, H., and Yang, X.-B. (2019). Ideal Nodal Line Semimetal in a Two-Dimensional Boron Bilayer. *J. Phys. Chem. C* 123 (8), 4977–4983. doi:10.1021/acs.jpcc.8b12385

Xu, S.-Y., Liu, C., Kushwaha, S. K., Sankar, R., Krizan, J. W., Belopolski, I., et al. (2015). Observation of Fermi Arc Surface States in a Topological Metal. *Science* 347 (6219), 294–298. doi:10.1126/science.1256742

Xu, Y., Elcoro, L., Song, Z.-D., Wieder, B. J., Vergniory, M. G., Regnault, N., et al. (2020). High-throughput Calculations of Magnetic Topological Materials. *Nature* 586 (7831), 702–707. doi:10.1038/s41586-020-2837-0

Yamakage, A., Yamakawa, Y., Tanaka, Y., and Okamoto, Y. (2016). Line-Node Dirac Semimetal and Topological Insulating Phase in Noncentrosymmetric Pnictides CaAgX(X= P, as). *J. Phys. Soc. Jpn.* 85 (1), 013708. doi:10.7566/jpsj.85.013708

Yan, Z., Bi, R., Shen, H., Lu, L., Zhang, S. C., and Wang, Z. (2017). Nodal-link Semimetals. *Phys. Rev. B* 96 (4), 041103. doi:10.1103/physrevb.96.041103

Yi, X., Li, W. Q., Li, Z. H., Zhou, P., Ma, Z. S., and Sun, L. Z. (2019). Topological Dual Double Node-Line Semimetals NaAlSi(Ge) and Their Potential as Cathode Material for Sodium Ion Batteries. *J. Mater. Chem. C* 7 (48), 15375–15381. doi:10.1039/c9tc04096j

Zhang, L., Zhang, S.-f., Ji, W.-X., Zhang, C.-W., Li, P., Wang, P.-j., et al. (2018). Discovery of a Novel Spin-Polarized Nodal Ring in a Two-Dimensional HK Lattice. *Nanoscale* 10 (44), 20748–20753. doi:10.1039/c8nr05383a

Zhang, M.-H., Zhang, S.-F., Wang, P.-J., and Zhang, C.-W. (2020). Emergence of a Spin-valley Dirac Semimetal in a Strained Group-VA Monolayer. *Nanoscale* 12 (6), 3950–3957. doi:10.1039/c9nr09545d

Zhang, X., Yu, Z.-M., Lu, Y., Sheng, X.-L., Yang, H. Y., and Yang, S. A. (2018). Hybrid Nodal Loop Metal: Unconventional Magnetoresponse and Material Realization. *Phys. Rev. B* 97 (12), 125143. doi:10.1103/physrevb.97.125143

Zhao, Z., Zhang, Z., and Guo, W. (2020). A Family of All Sp2-Bonded Carbon Allotropes of Topological Semimetals with Strain-Robust Nodal-Lines. *J. Mater. Chem. C* 8 (5), 1548–1555. doi:10.1039/c9tc05470g

Zhou, P., Ma, Z. S., and Sun, L. Z. (2018). Coexistence of Open and Closed Type Nodal Line Topological Semimetals in Two Dimensional B2C. *J. Mater. Chem. C* 6 (5), 1206–1214. doi:10.1039/c7tc05095j

Conflict of Interest: The authors declare that the research was conducted in the absence of any commercial or financial relationships that could be construed as a potential conflict of interest.

frontiers in Chemistry

ORIGINAL RESEARCH
published: 01 October 2021
doi: 10.3389/fchem.2021.744977

Tunable Schottky Barrier and Interfacial Electronic Properties in Graphene/ZnSe Heterostructures

Wenjun Xiao[1], Tianyun Liu[1], Yuefei Zhang[1,2], Zhen Zhong[1], Xinwei Zhang[3], Zijiang Luo[4], Bing Lv[1,2], Xun Zhou[1,2], Zhaocai Zhang[3]* and Xuefei Liu[1,2]*

[1]College of Physics and Electronic Science, Guizhou Normal University, Guiyang, China, [2]Key Laboratory of Low Dimensional Condensed Matter Physics of Higher Educational Institution of Guizhou Province, Guizhou Normal University, Guiyang, China, [3]Beijing Institute of Space Science and Technology Information, Beijing, China, [4]College of Information, Guizhou University of Finance and Economics, Guiyang, China

Edited by:
Xiaotian Wang,
Southwest University, China

Reviewed by:
Yuanzheng Chen,
Southwest Jiaotong University, China
Jihua Zhang,
Guizhou Provincial Key Laboratory of Computational Nano-Material Science, China
Daoxiong Wu,
Hainan University, China

***Correspondence:**
Zhaocai Zhang
zhangzhaocai@gmail.com
Xuefei Liu
201307129@gznu.edu.cn

Specialty section:
This article was submitted to Physical Chemistry and Chemical Physics, a section of the journal Frontiers in Chemistry

Received: *27 July 2021*
Accepted: *10 August 2021*
Published: *01 October 2021*

Citation:
Xiao W, Liu T, Zhang Y, Zhong Z, Zhang X, Luo Z, Lv B, Zhou X, Zhang Z and Liu X (2021) Tunable Schottky Barrier and Interfacial Electronic Properties in Graphene/ZnSe Heterostructures. Front. Chem. 9:744977. doi: 10.3389/fchem.2021.744977

With a direct bandgap, two-dimensional (2D) ZnSe is a promising semiconductor material in photoelectric device fields. In this work, based on first-principles methods, we theoretically studied the modulation of the Schottky barrier height (SBH) by applying horizontal and vertical strains on graphene/ZnSe heterojunction. The results show that the inherent electronic properties of graphene and ZnSe monolayers are both well-conserved because of the weak van der Waals (vdW) forces between two sublayers. Under horizontal strain condition, the n(p)-type SBH decreases from 0.56 (1.62) eV to 0.21 (0.78) eV. By changing the interlayer distance in the range of 2.8 Å to 4.4 Å, the n(p)-type SBH decreases (increases) from 0.88 (0.98) eV to 0.21 (1.76) eV. These findings prove the SBH of the heterojunction to be tuned effectively, which is of great significance to optoelectronic devices, especially in graphene/ZnSe-based nano-electronic and optoelectronic devices.

Keywords: 2D heterojunction, Schottky barrier height, horizontal and vertical strain, bader charge, density function theory

INTRODUCTION

Ever since graphene was exfoliated experimentally in 2004 Novoselov et al. (2004), owing to its unique advantages, such as high charge mobility at room temperature and excellent Hall effect Novoselov et al. (2005), Zhang et al. (2005), it has attracted many theoretical and experimental attentions (Olabi et al., 2021; cao et al., 2018; Wang et al., 2020; Niu et al., 2020). Nevertheless, ZnSe as a zero bandgap material was not well-developed in graphene photonics and optoelectronics (Bonaccorso et al., 2010). In this regard, a lot of efforts have been devoted to exploring other novel two-dimensional (2D) crystal structures, and some new 2D materials were prepared (Naguib et al., 2013; Niu and Li, 2015; Liao et al., 2020). Among them, ZnSe is a direct bandgap 2D semiconductor material with a wide gap of 3.24 eV by using Heyd–Scuseria–Ernzerhof (HSE) functional (Krukau et al., 2006), and it has attracted more and more attention in recent years. For instance, ZnSe was proved to be a potential material as inorganic scintillators Jagtap et al. (2019), as well as a cathode material of battery (Zhu et al., 2019). Besides, 2D ZnSe crystals have exhibited other interesting properties, including piezoelectric and dopant-induced semi-metallic tunable bandgap Liu et al. (2014), Yu et al. (2019), Khan et al. (2020), Sun et al. (2020), enabling its great potential applications in nano-electronics and optoelectronics fields. Furthermore, the energy bands of ZnSe meet the conditions of photocatalytic water splitting. Hence, it is also expected to be developed in new energy devices (Rubini et al., 2001; Hazrati et al., 2008; Yao et al., 2020).

The van der Waals (vdW) heterostructure, as proposed by Geim and Grigorieva (2013), is composed of multiple 2D atomic layers without chemical bonds between them. Due to the weak interlayer vdW forces, heterojunction often retains the individual electronic and optical properties of a single layer, and some new physical properties may be obtained at the interface. Therefore, in recent years, the 2D vdW heterojunction has attracted extensive attention in the field of electronic and optoelectronic devices (Zhang et al., 2020a; Guo et al., 2020; Zhu et al., 2021). Many scholars have studied vdW heterojunction based on ZnSe, such as AlP/ZnSe, $ZnSe_2$/ZnSe, and CdS/ZnSe heterostructures (Dinger et al., 1999; Xiong and Zhou, 2019; Liu et al., 2020a). However, all the interfaces were constructed by two semiconductors, rather than metal/semiconductor heterojunction. In fact, the interface properties of the semiconductor/metal heterojunction such as the charge transfer and Schottky barrier play a vital role in the device performance (Zhang et al., 2020b; Robertson et al., 2020; Chen et al., 2021). How is the charge transfer between a 2D ZnSe nanosheet and graphene? How to tune the charge transfer and other electronic properties of the graphene/ZnSe interface? These questions have not been understood well yet. Hence, it is very essential to understand the interfacial properties of the ZnSe-based metal–semiconductor heterojunctions.

Besides, the 2D heterojunction Schottky barrier height (SBH) can be controlled through interlayer coupling, electric field, biaxial strain engineering, and atomic doping (Si et al., 2016; Zhang et al., 2018; Zhou et al., 2018; Zhang et al., 2020a; Nguyen et al., 2020; Liu et al., 2021). The modulation of SBH would improve the carrier transmission rate and change the type of Schottky contact. Although many studies on graphene-based vdW heterojunction have been published Georgiou et al. (2012), Si et al. (2016), Qiu et al. (2020), the electronic properties of the graphene/ZnSe heterostructure have not been clearly understood yet, as well as the SBH tunability under horizontal and vertical strain. In this study, we constructed a graphene/ZnSe heterojunction and calculated the electronic properties systematically. Our findings indicated the SBH of graphene/ZnSe could be effectively tuned by applying horizontal strain and vertical strain, which has potential applications in nano-mechanics, transistors, piezoelectric, and optoelectronics applications.

COMPUTATIONAL METHODS

In this study, all the calculations are based on the density functional theory (DFT) and projector augmented wave (PAW) Blöchl (1994), as carried out in the Vienna ab initio simulation package (VASP) (Kresse and Furthmüller, 1996). The Perdew–Burke–Ernzerhof (PBE) method based on the generalized gradient approximation (GGA) was used to describe exchange–correlation potential (Perdew et al., 1996). The geometric optimization and electronic property calculations were accomplished by applying an energy cutoff of 520 eV. The total energy convergence was set at 10^{-5} eV. The atomic structures considered were fully optimized until the convergence of force of 0.01 eV/Å. The Γ-centered Monkhorst–Pack Monkhorst and Pack (1976) is used to sample the reciprocal space with a grid density of 5 × 5×1. The weak interaction was corrected between sublayers by using Grimme's DFT-D3 method (Grimme, 2006). We used a vacuum thickness of 20 Å to avoid bonding between the periodic sublayers (Liu et al., 2020b). Dipole correction was considered to reduce the error due to the asymmetry of the graphene/ZnSe interface along the Z-direction. The VASPKIT was used to do part of data post-processing (Wang et al., 2021).

The binding energy is one of the physical quantities that determine the heterojunction structural stability (Gélinas et al., 2011). Therefore, to verify the stability, we calculated the binding energies for graphene/ZnSe vdW heterostructure as follows (Zhao-Fu et al., 2014; Guo et al., 2020) (1):

$$E_b = \frac{E_{graphene/ZnSe} - E_{graphene} - E_{ZnSe}}{A}. \tag{1}$$

Here, E_b is the heterojunction binding energy; $E_{graphene/ZnSe}$ represents the total energy of the heterostructure; $E_{graphene}$ and E_{ZnSe} are the total energy of the graphene and ZnSe monolayer, separately; and A is the interface area in the x-y plane.

RESULTS AND ANALYSIS

Structural Properties

Before constructing the graphene/ZnSe heterojunction, the lattice constants of graphene and ZnSe are relaxed to be 2.46 Å and 4.07 Å, respectively, being in great agreement with the data in the literature (Priyadharsini et al., 2016; Yang et al., 2018). To reduce the mismatch, the graphene/ZnSe heterostructure was constructed by using a 5 × 5 supercell of graphene and a 3 × 3 supercell of ZnSe, as shown in **Figure 1**. It is noted that the lattice constants in the heterostructure for graphene and ZnSe are 12.3 Å and 12.21 Å, leading to a lattice mismatch of only 0.73%. To obtain the most stable heterojunction, we considered three stacking patterns based on the main high symmetry nature, as shown in **Figure 2A**. The binding energy of three stacking patterns is shown in **Table 1**. The$_2$ stack-III pattern with a binding energy of −2.01 meVe is the most stable heterojunction. Thus, in the following calculation, we only considered the stack-III pattern.

We further investigated the binding energy of stack-III pattern under different interlayer distances, as shown in **Figure 2C**. The results of relative energy indicated the most stable interlayer distance is 3.6 Å.

Electrical Properties

As expected, graphene shows a metallic nature with the Dirac point located at the K point and crossed by the Fermi energy level, as shown in **Figure 3**. As for ZnSe, the valence band maximum (VBM) is at the Γ point, as well as the conduction band minimum (CBM), indicating that ZnSe is a direct bandgap semiconductor, with a bandgap value of 2.11 eV with PBE. According to the projected density of states (PDOS), the VBM of ZnSe was mainly contributed by the p-orbitals of Zn

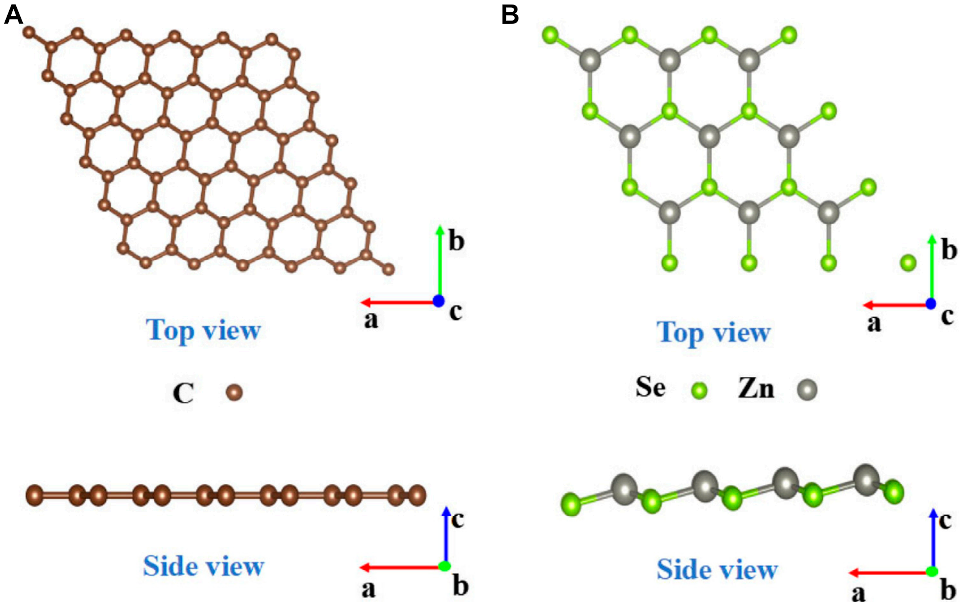

FIGURE 1 | (A) Top and side views of a 5 × 5 graphene, and **(B)** the top and side views of a 3 × 3 ZnSe supercell. The brown spheres represent C, the gray spheres represent Zn, and the green spheres represent Se.

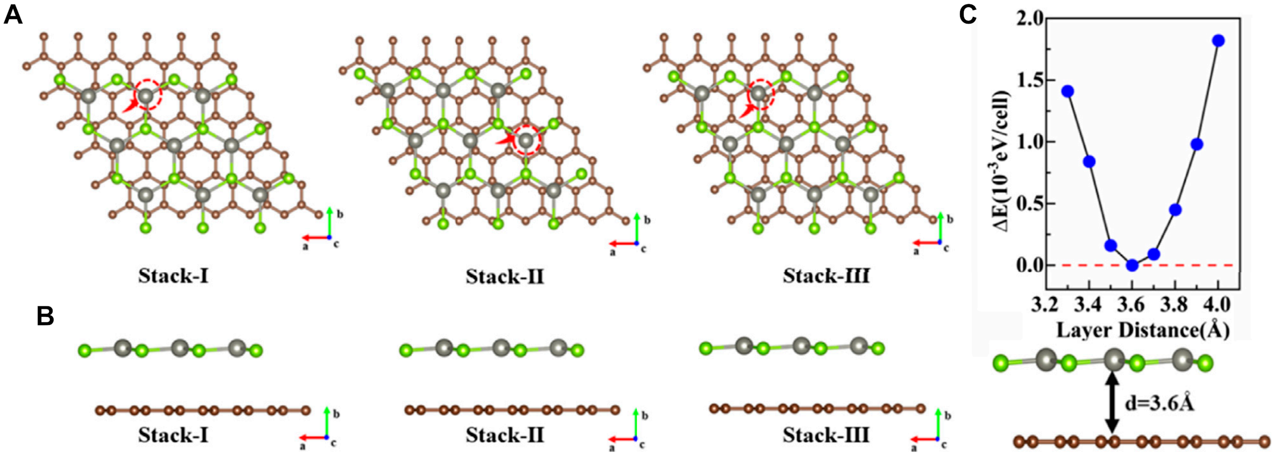

FIGURE 2 | (A), **(B)** Three stacked patterns of top and side views. **(C)** Relationship between layer spacing and binding energy of graphene/ZnSe.

TABLE 1 | Binding energy of three stacking patterns.

Stack type	$E_{graphene}/_{ZnSe}$ (eV)	$E_{graphene}$ (eV)	E_{ZnSe} (eV)	E_b (meV Å^{-2})
Stack-I	−514.61	−461.65	−49.41	−1.77
Stack-II	−514.70	−461.65	−49.41	−1.81
Stack-III	−515.11	−461.65	−49.41	−2.01

and Se, while the CBM was mainly contributed by the s-orbital electrons of Zn.

As well known, the PBE method would underestimate the bandgap of semiconductors, and the HSE method can solve this problem extremely well. However, both the PBE and HSE would predict the same band structure shape and variation trends of the ZnSe monolayer under different strains, with limited resources, so we use the PBE method to calculate all properties of the

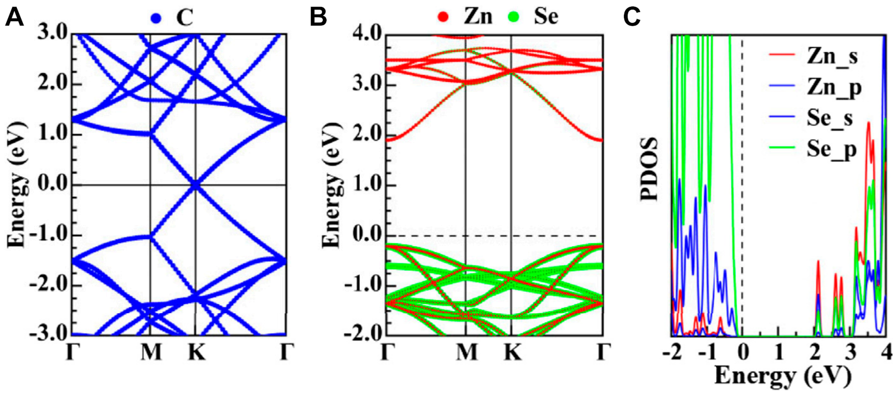

FIGURE 3 | (A) Energy band diagram of graphene. **(B)**, **(C)** Projected energy band diagram and density of states of ZnSe, respectively.

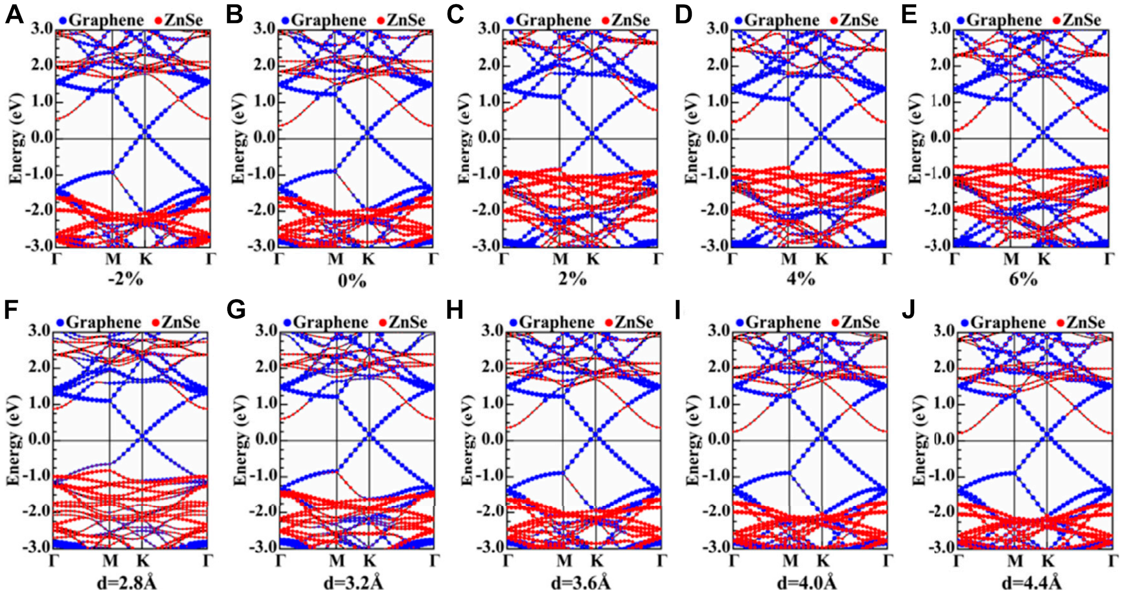

FIGURE 4 | (A–E) Projected band structures of the graphene/ZnSe heterojunction under horizontal strain. **(F–J)** Projected band structures of the graphene/ZnSe heterojunction under vertical strain.

considered systems. Next, we further researched the electronic properties of the graphene/ZnSe heterojunction by figuring out the band structures and density of states under different horizontal or vertical strains (Phuc et al., 2017).

In this study, we applied horizontal strain from −2% to +6% on the graphene/ZnSe heterojunction, with a span of 2%. The positive value indicates tensile strain, while the negative value represents compressive strain. The reason why more negative strains are not considered is that a much larger strain is hard to be experimentally achieved, and it will also make the nanomaterials nonstable (Liao et al., 2020). When the compressive strain is less than −2%, the heterojunction optimization was failed. In general, tensile strain is relatively easier than that of compressive strain to implement in engineering. Hence, we only consider the −2% horizontal compression strain but a tensile strain of 6%. The projected band structures of the graphene/ZnSe heterojunction under different horizontal strains are shown in **Figures 4A–E**. From the figure, the Dirac point is well-maintained and the Fermi level is fixed at the K point. With the increase in the tensile strain from 0 to 6%, the bandgap decreases from 1.98 to 0.99 eV, and the bandgap always maintains a direct bandgap. The electron transfer ability of graphene to ZnSe is weakened, with the increased horizontal tensile strain smaller than 4%. When the horizontal tensile strain is larger than 4%, the electron transfer ability of graphene to ZnSe is enhanced. When horizontal or vertical compressive strain is applied, the CBM of ZnSe is moved up. Additionally, it seems that the horizontal compressive strain has a smaller effect than vertical strain on the VBMs, as shown in

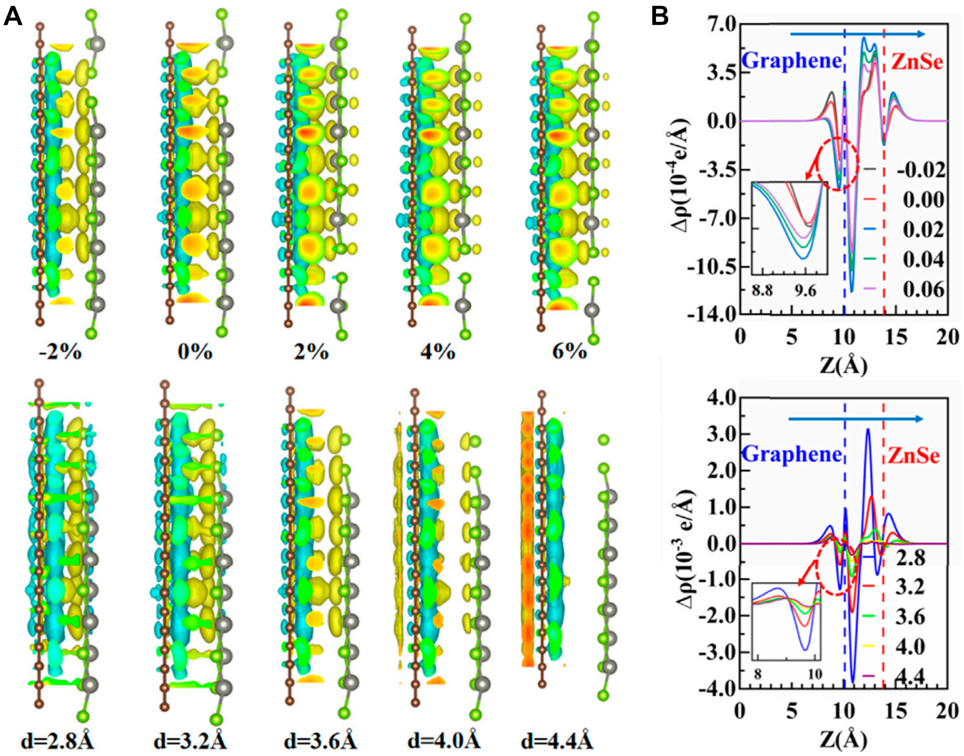

FIGURE 5 | (A) On behalf of the charge density difference of the graphene/ZnSe system under different horizontal strains and vertical strain, yellow and cyan represent the accumulation and depletion of electrons, respectively. **(B)** PCDD under horizontal strain and vertical strain.

Figures 4A, F, G. Under tensile strain, both the VBMs and CBMs would shift up (down) for horizontal (vertical) cases, except for a horizontal strain of 6% (see **Figure 4E**). These different changes of CBM and VBM would lead to the bandgap change with the external strains. The results mean that both the vertical and horizontal strain plays a pivotal role in tuning the electronic properties of the graphene/ZnSe heterojunction. These phenomenons are resulting from the charge redistribution between the two sublayers under different strains (Liu et al., 2019; Liu et al., 2020b), as verified in **Figure 5**.

Next, to investigate the charge transfers and charge redistribution more clearly, the charge density difference of the graphene/ZnSe heterojunction was analyzed under different horizontal and vertical strains, as shown in **Figure 5A**. The charge density difference shows charge accumulation in the interface region near ZnSe and depletion in the interface region close to the graphene, which suggests a charge transfer from graphene to ZnSe. But, the variations in charge redistributions under different strain conditions are found, which leads to the different change regularity of band structures.

To see the charge redistribution, the plane-averaged charge density difference (PCDD) was calculated as follows (Zhang et al., 2015):

$$\Delta\rho = \rho_{graphene/ZnSe} - \rho_{graphene} - \rho_{ZnSe}. \tag{2}$$

In this case, $\rho_{graphene/ZnSe}$, $\rho_{graphene}$, and ρ_{ZnSe} are the PCDD of the graphene/ZnSe heterojunction, the isolated graphene single layer, and the isolated ZnSe, respectively. The PCDD curve is depicted in **Figure 5B**; when the horizontal strain is applied, charge transfer is tunable and agrees with the results of Bader charge analysis (Henkelman et al., 2006), as shown in **Figure 6A**, the charge is mainly concentrated on the surface near the ZnSe of layers. While the vertical strain is applied, as expected, the smaller the interlayer distance, the stronger coupling between ZnSe and graphene was found, leading to more electrons being transferred from graphene to ZnSe. The PCDD curve also proves the accuracy of the analysis of the band structure results.

In **Figure 7C**, we further depict the plane-averaged electrostatic potentials of the graphene/ZnSe interface under different horizontal and vertical strains. The graphene layer has a deeper potential than the ZnSe layer. The potential difference of the graphene/ZnSe heterostructure is 11.92 eV under an equilibrium distance of d = 3.6 Å, which further proves that the electrons are transferred from graphene to ZnSe. As shown in **Figure 7A**, horizontal strain ranges from −2% to +6%, the potential difference between graphene and ZnSe monolayers is tuned effectively, indicating that the ability of charge transfer can be modulated by applying horizontal strain. At the tensile strain of 2%, the potential difference reached 12.26 eV, indicating that the graphene/ZnSe vdW heterojunction should be able to maintain the high carrier mobility of graphene and promote the development of new high-performance nano-electronic devices. As shown in **Figure 7B**, under a vertical strain, it shows the potential

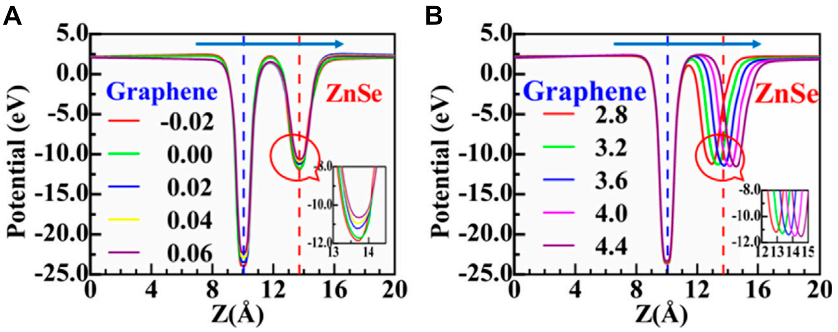

FIGURE 6 | (A, D) Variation trend of CBM, VBM, and Fermi energy levels E_F with applied strain. **(B, E)** Variation of Φ_n, Φ_p, bandgap with the strain. **(C, F)** Amount of electron transfer from graphene to ZnSe as a function of the strain.

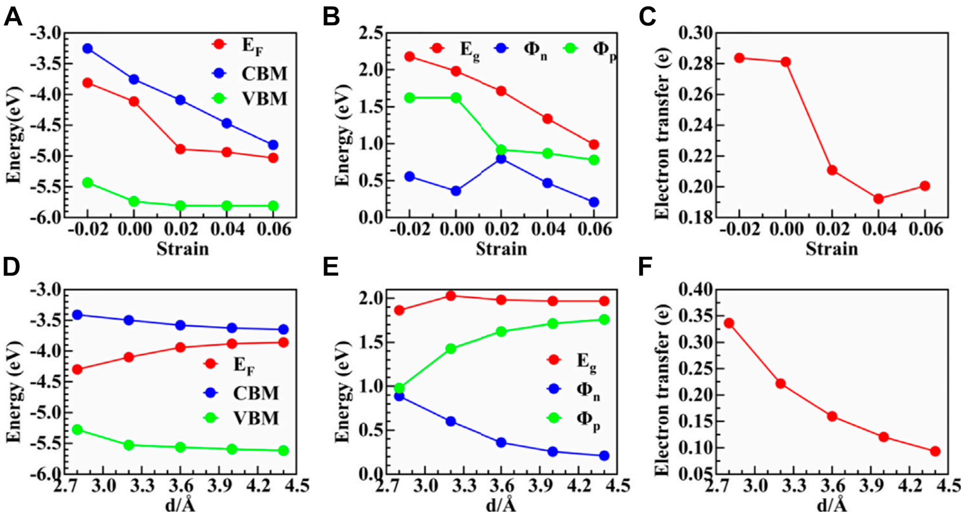

FIGURE 7 | (A), (B) Average electrostatic potential along the *z*-direction for the heterostructure under different horizontal strains and vertical strains, respectively.

difference between graphene and ZnSe under an interlayer distance of 2.8 Å and 4.4 Å is 12.38 and 11.78 eV, respectively. In other words, with the increase in the interlayer distance, the potential differences between graphene and ZnSe decrease, leading to the charge transfer from the graphene layer to the ZnSe layer being reduced, which is confirmed by the Bader charge analysis shown in **Figure 6B**.

Tunability of SBH Under Strain

The SBH of the metal/semiconductor interfacial system is an important parameter (Zhang et al., 2020b; Robertson et al., 2020; Chen et al., 2021). Therefore, it is necessary to study the SBH of the graphene/ZnSe interface to better understand this heterojunction.

Based on Bardeeen's (Bardeen, 1947) Schottky–Mott model of metal/semiconductor heterostructures, the n-type and p-type Schottky barriers are determined as follows:

$$\Phi_n = \text{CBM} - E_F \tag{3}$$

$$\Phi_p = E_F - \text{VBM}, \tag{4}$$

where the Φ_n denotes n-type SBH, Φ_p is p-type SBH, and E_F is the Fermi level. Without any horizontal or vertical strain, Φ_n and Φ_p of the graphene/ZnSe heterostructure are 0.36 and 1.62 eV, respectively, indicating that graphene/ZnSe vdW ($\Phi_n < \Phi_p$). As is well known, SBH and contact types of the heterojunction can be controlled by applying strain (Liu et al., 2019; Liu et al., 2020c). Therefore, we further investigate the effects of SBH and its tunability of the graphene/ZnSe heterojunction by applying the horizontal and vertical strains.

As shown in **Figure 7A**, the results indicate that CBM and VBM are decreased (increased) with the increase in horizontal tensile (compressive) strain and the Fermi energy level, but with a different change degree. Thus, the heterojunction bandgap was adjusted in a large range, indicating that the horizontal strain is an effective method of regulating the SBH. As is depicted more intuitively in **Figure 7B**, the results show both the n-type and p-type SBH was changed obviously under different horizontal strains. For instance, the n-type SBH can change from 0.56 to 0.21 eV, and the p-type SBH is decreased from 1.62 to 0.78 eV according to the applied strain values, but the n-type SBH contact is always maintained. Although the Ohmic contact is not realized, the large decrease in SBH would enhance the performance of the graphene/ZnSe-based nanodevices.

It should be noted that variation of heterojunction layer spacing can be achieved by experimental techniques (Zhang et al., 2014), which have been diffusely used to regulate the electronic properties and SBH of the vdW heterostructures. In this study, to understand how vertical strain regulates the graphene/ZnSe heterojunction SBH, the interlayer distance of the graphene/ZnSe heterojunction was changed from 2.8 Å to 4.4 Å. In **Figures 7D, E**, the VBM and CBM are decreased with the increase in the interlayer distance. In contrast, the Fermi energy level is shifted up until the interlayer is larger than 3.6 Å, leading to the SBH of n-type and p-type changing obviously, as shown in **Figure 7E**, and by changing the interlayer distance in the range of 2.8 Å to 4.4 Å, the n(p)-type SBH decreases (increases) from 0.88 (0.98) eV to 0.21 (1.76) eV. Thus, for the graphene/ZnSe heterostructure, the n-type Schottky is still maintained. Based on our results in **Figure 7E**, it can be informed that an n-type–to–p-type contact would be formed if the interlayer distance is smaller enough. Therefore, after the strain adjustment, graphene can be used as an ideal electrode material for ZnSe, and the SBH can be significantly tuned by applying both lateral and vertical strains, which is expected in the graphene/ZnSe-based Schottky devices.

CONCLUSION

In conclusion, we have systematically studied the electronic properties and the efficient modulations of SBH of the vdW graphene/ZnSe heterostructure by DFT calculations. The band structures, the charge density differences, and the Bader charge transfer are studied in detail. The results show that the electrons will be transformed from graphene to ZnSe, and the transfer amount can be tuned effectively by applying both horizontal and vertical strains. As a consequence, the positions of CBM and VBM as well as Fermi energy level will be changed with the strain, and thus, the SBH is modulated effectively. These findings would provide useful guidance for designing controllable graphene/ZnSe-based Schottky nanodevices.

DATA AVAILABILITY STATEMENT

The original contributions presented in the study are included in the article/supplementary material; further inquiries can be directed to the corresponding authors.

AUTHOR CONTRIBUTIONS

WX: investigation, conceptualization, methodology, data curation, visualization, validation, and writing; TL: project administration and writing—reviewing and editing; YZ: visualization; ZZ: editing; XWZ: validation; ZL: visualization and project administration; BL: software; XZ: data curation; ZCZ: writing—reviewing and editing; and XL: project administration and writing—reviewing and editing.

FUNDING

This work is supported by the National Natural Science Foundation of China (Grant No. 12164009).

REFERENCES

Bardeen, J. (1947). Surface States and Rectification at a Metal Semi-conductor Contact. *Phys. Rev.* 71, 82–105. doi:10.1103/physrev.71.717

Blöchl, P. E. (1994). Projector Augmented-Wave Method. *Phys. Rev. B.* 50, 17953–17979. doi:10.1103/physrevb.50.17953

Bonaccorso, F., Sun, Z., Hasan, T., and Ferrari, A. C. (2010). Graphene Photonics and Optoelectronics. *Nat. Photon.* 4, 611–622. doi:10.1038/nphoton.2010.186

cao, Y., Fatemi, V., Fang, S., Watanabe, K., Taniguchi, T., Kaxiras, E., et al. (2018). Unconventional Superconductivity in Magic-Angle Graphene Superlattices. *Nature* 556, 43–50. doi:10.1038/nature26160

Chen, J., Zhang, Z., Guo, Y., and Robertson, J. (2021). Schottky Barrier Heights of Defect-free metal/ZnO, CdO, MgO, and SrO Interfaces. *J. Appl. Phys.* 129, 175304. doi:10.1063/5.0047447

Dinger, A., Petillon, S., Grün, M., Hetterich, M., and Klingshirn, C. (1999). Conduction Band Offset of the CdS/ZnSe Heterostructure. *Semicond. Sci. Technol.* 14, 595–598. doi:10.1088/0268-1242/14/7/301

Geim, A. K., and Grigorieva, I. V. (2013). Van der Waals heterostructures. *Nature* 499, 419–425. doi:10.1038/nature12385

Gélinas, S., Paré-Labrosse, O., Brosseau, C.-N., Albert-Seifried, S., McNeill, C. R., Kirov, K. R., et al. (2011). The Binding Energy of Charge-Transfer Excitons Localized at Polymeric Semiconductor Heterojunctions. *J. Phys. Chem. C.* 115, 7114–7119. doi:10.1021/jp200466y

Georgiou, T., Jalil, R., Belle, B. D., Britnell, L., Gorbachev, R. V., Morozov, S. V., et al. (2012). Vertical Field-Effect Transistor Based on Graphene-WS2 Heterostructures for Flexible and Transparent Electronics. *Nat. Nanotech.* 8, 100–103. doi:10.1038/nnano.2012.224

Grimme, S. (2006). Semiempirical GGA-type Density Functional Constructed with a Long-Range Dispersion Correction. *J. Comput. Chem.* 27, 1787–1799. doi:10.1002/jcc.20495

Guo, H., Zhang, Z., Huang, B., Wang, X., Niu, H., Guo, Y., et al. (2020). Theoretical study on the photocatalytic properties of 2D InX(X = S, Se)/transition metal disulfide (MoS2 and WS2) van der Waals heterostructures. *Nanoscale* 12, 20025–20032. doi:10.1039/d0nr04725b

Hazrati, E., Hashemifar, S. J., and Akbarzadeh, H. (2008). First Principles Study of Bulk CrSe and CrSe/ZnSe(001) Interface. *J. Appl. Phys.* 104, 113719. doi:10.1063/1.3039510

Henkelman, G., Arnaldsson, A., and Jónsson, H. (2006). A Fast and Robust Algorithm for Bader Decomposition of Charge Density. *Comput. Mater. Sci.* 36, 354–360. doi:10.1016/j.commatsci.2005.04.010

Jagtap, S., Chopade, P., Tadepalli, S., Bhalerao, A., and Gosavi, S. (2019). A Review on the Progress of ZnSe as Inorganic Scintillator. *Opto-Electronics Rev.* 27, 90–103. doi:10.1016/j.opelre.2019.01.001

Khan, M. S., Shi, L., and Zou, B. (2020). Impact of Vacancy Defects on Optoelectronic and Magnetic Properties of Mn-Doped ZnSe. *Comput. Mater. Sci.* 174, 109493. doi:10.1016/j.commatsci.2019.109493

Kresse, G., and Furthmüller, J. (1996). Efficient Iterative Schemes Forab Initiototal-Energy Calculations Using a Plane-Wave Basis Set. *Phys. Rev. B.* 54, 11169–11186. doi:10.1103/physrevb.54.11169

Krukau, A. V., Vydrov, O. A., Izmaylov, A. F., and Scuseria, G. E. (2006). Influence of the Exchange Screening Parameter on the Performance of Screened Hybrid Functionals. *J. Chem. Phys.* 125, 224106. doi:10.1063/1.2404663

Liao, Y., Zhang, Z., Gao, Z., Qian, Q., and Hua, M. (2020). Tunable Properties of Novel Ga2O3 Monolayer for Electronic and Optoelectronic Applications. *ACS Appl. Mater. Inter.* 12, 30659–30669. doi:10.1021/acsami.0c04173

Liu, C., Zhang, W., Sun, J., Wen, J., Yang, Q., Cuo, H., et al. (2014). Piezoelectric Nanogenerator Based on a Flexible Carbon-fiber/ZnO-ZnSe Bilayer Structure Wire. *Appl. Surf. Sci.* 322, 95–100. doi:10.1016/j.apsusc.2014.10.081

Liu, P., Han, J., Zhu, K., Dong, Z., and Jiao, L. (2020). Heterostructure SnSe 2/ ZnSe@PDA Nanobox for Stable and Highly Efficient Sodium-Ion Storage. *Adv. Energ. Mater.* 10, 2000741. doi:10.1002/aenm.202000741

Liu, X., Gao, Z., Wang, V., Luo, Z., Lv, B., Ding, Z., et al. (2020). Extrapolated Defect Transition Level in Two-Dimensional Materials: The Case of Charged Native Point Defects in Monolayer Hexagonal Boron Nitride. *ACS Appl. Mater. Inter.* 12, 17055–17061. doi:10.1021/acsami.9b23431

Liu, X., Lv, B., Ding, Z., and Luo, Z. (2020). Van der Waals heterostructure of graphene and As2S3: Tuning the Schottky barrier height by vertical strain. *J. Cryst. Growth.* 549, 125882. doi:10.1016/j.jcrysgro.2020.125882

Liu, X., Zhang, Z., Luo, Z., Lv, B., and Ding, Z. (2019). Tunable Electronic Properties of Graphene/g-AlN Heterostructure: The Effect of Vacancy and Strain Engineering. *Nanomaterials* 9, 1674–1688. doi:10.3390/nano9121674

Liu, X., Zhang, Z., Lv, B., Ding, Z., and Luo, Z. (2021). Impact of the Vertical Strain on the Schottky Barrier Height for graphene/AlN Heterojunction: a Study by the First-Principles Method. *Eur. Phys. J. B.* 94, 1–7. doi:10.1140/epjb/s10051-020-00010-w

Monkhorst, H. J., and Pack, J. D. (1976). Special Points for Brillouin-Zone Integrations. *Phys. Rev. B.* 13, 5188–5192. doi:10.1103/physrevb.13.5188

Naguib, M., Mochalin, V. N., Barsoum, M. W., and Gogotsi, Y. (2013). 25th Anniversary Article: MXenes: A New Family of Two-Dimensional Materials. *Adv. Mater.* 26, 992–1005. doi:10.1002/adma.201304138

Nguyen, C. V., Idrees, M., Phuc, H. V., Hieu, N. N., Binh, N. T. T., Amin, B., et al. (2020). Interlayer Coupling and Electric Field Controllable Schottky Barriers and Contact Types in Graphene/PbI2 Heterostructures. *Phys. Rev. B.* 101, 235419. doi:10.1103/physrevb.101.235419

Niu, H., Zhang, Z., Wang, X., Wan, X., Shao, C., and Guo, Y. (2020). Theoretical Insights into the Mechanism of Selective Nitrate-to-Ammonia Electroreduction on Single-Atom Catalysts. *Adv. Funct. Mater.* 31, 2008533. doi:10.1002/adfm.202008533

Niu, T., and Li, A. (2015). From Two-Dimensional Materials to Heterostructures. *Prog. Surf. Sci.* 90, 21–45. doi:10.1016/j.progsurf.2014.11.001

Novoselov, K. S., Geim, A. K., Morozov, S. V., Jiang, D., Katsnelson, M. I., Grigorieva, I. V., et al. (2005). Two-dimensional Gas of Massless Dirac Fermions in Graphene. *Nature* 438, 197–200. doi:10.1038/nature04233

Novoselov, K. S., Geim, A. K., Morozov, S. V., Jiang, D., Zhang, Y., Dubonos, S. V., et al. (2004). Electric Field Effect in Atomically Thin Carbon Films. *Science* 306, 666–669. doi:10.1126/science.1102896

Olabi, A. G., Abdelkareem, M. A., Wilberforce, T., and Sayed, E. T. (2021). Application of Graphene in Energy Storage Device - A Review. *Renew. Sust. Energ. Rev.* 135, 110026. doi:10.1016/j.rser.2020.110026

Perdew, J. P., Burke, K., and Ernzerhof, M. (1996). Generalized Gradient Approximation Made Simple. *Phys. Rev. Lett.* 77, 3865–3868. doi:10.1103/physrevlett.77.3865

Phuc, H. V., Hieu, N. N., Hoi, B. D., Phuong, L. T. T., Hieu, N. V., and Nguyen, C. V. (2017). Out-of-plane Strain and Electric Field Tunable Electronic Properties and Schottky Contact of Graphene/antimonene Heterostructure. *Superlattices. Microstructures* 112, 554–560. doi:10.1016/j.spmi.2017.10.011

Priyadharsini, N., Elango, M., Vairam, S., Venkatachalam, T., and Thamilselvan, M. (2016). Effect of Temperature and pH on Structural, Optical and Electrical Properties of Ni Doped ZnSe Nanoparticles. *Optik* 127, 7543–7549. doi:10.1016/j.ijleo.2016.05.079

Qiu, B., Zhao, X. W., Hu, G. C., Yue, W. W., Yuan, X. B., and Ren, J. F. (2020). Tuning Optical Properties of Graphene/WSe2 Heterostructure by Introducing Vacancy: First Principles Calculations. *Physica E: Low-dimensional Syst. Nanostructures.* 116, 113729. doi:10.1016/j.physe.2019.113729

Robertson, J., Guo, Y., Zhang, Z., and Li, H. (2020). Extending the Metal-Induced gap State Model of Schottky Barriers. *J. Vacuum Sci. Tech. B.* 38, 042208. doi:10.1116/6.0000164

Rubini, S., Milocco, E., Sorba, L., Pelucchi, E., Franciosi, A., Garulli, A., et al. (2001). Structural and Electronic Properties of ZnSe/AlAs Heterostructures. *Phys. Rev. B.* 63, 155312. doi:10.1103/physrevb.63.155312

Si, C., Lin, Z., Zhou, J., and Sun, Z. (2016). Controllable Schottky Barrier in GaSe/ graphene Heterostructure: the Role of Interface Dipole. *2d Mater.* 4, 015027. doi:10.1088/2053-1583/4/1/015027

Sun, C., Chen, X., Hong, R., Li, X., Xu, X., Chen, X., et al. (2020). Enhancing the Photoelectrical Performance of graphene/4H-SiC/graphene Detector by Tuning a Schottky Barrier by Bias. *Appl. Phys. Lett.* 117, 071102. doi:10.1063/5.0012566

Wang, V., Xu, N., Liu, J.-C., Tang, G., and Geng, W.-T. (2021). VASPKIT: A User-Friendly Interface Facilitating High-Throughput Computing and Analysis Using VASP Code. *Comp. Phys. Commun.* 267, 108033. doi:10.1016/j.cpc.2021.108033

Wang, X., Niu, H., Liu, Y., Shao, C., Robertson, J., Zhang, Z., et al. (2020). Theoretical Investigation on Graphene-Supported Single-Atom Catalysts for Electrochemical CO2 Reduction. *Catal. Sci. Technol.* 10, 8465–8472. doi:10.1039/d0cy01870h

Xiong, A., and Zhou, X. (2019). Tunable electronic and optical properties of novel ZnSe/AlP van der Waals heterostructure. *Mater. Res. Express.* 6, 075907. doi:10.1088/2053-1591/ab15ea

Yang, H., Li, J., Yu, L., Huang, B., Ma, Y., and Dai, Y. (2018). A Theoretical Study on the Electronic Properties of In-Plane CdS/ZnSe Heterostructures: Type-II Band Alignment for Water Splitting. *J. Mater. Chem. A.* 6, 4161–4166. doi:10.1039/c7ta10624f

Yao, F., Zhou, X., and Xiong, A. (2020). Tunable electronic and optical properties of two-dimensional ZnSe/AlAs van der Waals heterostructure. *Appl. Phys. A.* 126, 1–10. doi:10.1007/s00339-020-03674-4

Yu, J. H., Kim, J., Hyeon, T., and Yang, J. (2019). Facile Synthesis of Manganese (II)-doped ZnSe Nanocrystals with Controlled Dimensionality. *J. Chem. Phys.* 151, 244701. doi:10.1063/1.5128511

Zhang, X., Meng, F., Christianson, J. R., Arroyo-Torres, C., Lukowski, M. A., Liang, D., et al. (2014). Vertical Heterostructures of Layered Metal Chalcogenides by van der Waals Epitaxy, *Nano Lett.* 14, 3047–3054. doi:10.1021/nl501000k

Zhang, Y., Tan, Y.-W., Stormer, H. L., and Kim, P. (2005). Experimental Observation of the Quantum Hall Effect and Berry's Phase in Graphene. *Nature* 438, 201–204. doi:10.1038/nature04235

Zhang, Z., Cao, R., Wang, C., Li, H.-B., Dong, H., Wang, W.-h., et al. (2015). GaN as an Interfacial Passivation Layer: Tuning Band Offset and Removing Fermi Level Pinning for III-V MOS Devices. *ACS Appl. Mater. Inter.* 7, 5141–5149. doi:10.1021/am507287f

Zhang, Z., Guo, Y., and Robertson, J. (2020). Origin of Weaker Fermi Level Pinning and Localized Interface States at Metal Silicide Schottky Barriers. *J. Phys. Chem. C* 124, 19698–19703. doi:10.1021/acs.jpcc.0c06228

Zhang, Z., Huang, B., Qian, Q., Gao, Z., Tang, X., and Li, B. (2020). Strain-tunable III-nitride/ZnO Heterostructures for Photocatalytic Water-Splitting: A Hybrid Functional Calculation. *APL Mater.* 8, 041114. doi:10.1063/5.0005648

Zhang, Z., Qian, Q., Li, B., and Chen, K. J. (2018). Interface Engineering of Monolayer MoS2/GaN Hybrid Heterostructure: Modified Band Alignment for Photocatalytic Water Splitting Application by Nitridation Treatment. *ACS Appl. Mater. Inter.* 10, 17419–17426. doi:10.1021/acsami.8b01286

Zhao-Fu, Z., Tie-Ge, Z., Hai-Yang, Z., and Xiang-Lei, W. (2014). First-principles Calculations of 5d Atoms Doped Hexagonal-AlN Sheets: Geometry, Magnetic Property and the Influence of Symmetry and Symmetry-Breaking on the Electronic Structure. *Chin. Phys. B.* 23, 016801. doi:10.1088/1674-1056/23/1/016801

Zhou, W., Guo, Y., Liu, J., Wang, F. Q., Li, X., and Wang, Q. (2018). 2D SnSe-Based vdW Heterojunctions: Tuning the Schottky Barrier by Reducing Fermi Level Pinning. *Nanoscale* 10, 13767–13772. doi:10.1039/c8nr02843e

Zhu, L., Wang, Z., Wang, L., Xie, L., Li, J., and Cao, X. (2019). ZnSe Embedded in N-Doped Carbon Nanocubes as Anode Materials for High-Performance Li-Ion Batteries. *Chem. Eng. J.* 364, 503–513. doi:10.1016/j.cej.2019.01.191

Zhu, X. T., Xu, Y., Cao, Y., Zhao, Y. Q., Sheng, W., Nie, G.-Z., et al. (2021). Investigation of the Electronic Structure of Two-Dimensional GaN/Zr2CO2 hetero-junction: Type-II Band Alignment with Tunable Bandgap. *Appl. Surf. Sci.* 542, 148505. doi:10.1016/j.apsusc.2020.148505

Conflict of Interest: The authors declare that the research was conducted in the absence of any commercial or financial relationships that could be construed as a potential conflict of interest.

frontiers in Chemistry

ORIGINAL RESEARCH
published: 29 October 2021
doi: 10.3389/fchem.2021.773015

Modified Embedded-Atom Interatomic Potential Parameters of the Ti–Cr Binary and Ti–Cr–N Ternary Systems

Shoubing Ding[1,2], Yue Li[1], Yiying Luo[1], Zhimin Wu[1]* and Xinqiang Wang[2]*

[1]Chongqing Key Laboratory of Photoelectric Functional Materials, College of Physics and Electronic Engineering, Chongqing Normal University, Chongqing, China, [2]School of Physics, Chongqing University, Chongqing, China

The second nearest-neighbor modified embedded-atom method (2NN MEAM) potential parameters of the Ti–Cr binary and Ti–Cr–N ternary systems are optimized in accordance with the 2NN MEAM method. The novel constructed potential parameters can well reproduce the multiple fundamental physical characteristics of binary and ternary systems and reasonably agree with the first-principles calculation or experimental data. Thus, the newly constructed 2NN MEAM potential parameters can be used for atomic simulations to determine the underlying principle of the hardness enhancement of TiN/CrN multilayered coatings.

Keywords: Ti-Cr-N ternary system, atomic simulation, multilayered coatings, 2NN MEAM, interaction potential
PACS:31.15.bu; 62.20.dq; 68.35.-p; 71.15.Nc

Edited by:
Xiaotian Wang,
Southwest University, China

Reviewed by:
Tong Liu,
Xihua University, China
Faling Ling,
Chongqing University of Posts and Telecommunications, China
Zhifeng Liu,
Inner Mongolia University, China

***Correspondence:**
Zhimin Wu
zmwu@cqnu.edu.cn
Xinqiang Wang
xqwang@cqu.edu.cn

Specialty section:
This article was submitted to Theoretical and Computational Chemistry,
a section of the journal Frontiers in Chemistry

Received: 09 September 2021
Accepted: 23 September 2021
Published: 29 October 2021

Citation:
Ding S, Li Y, Luo Y, Wu Z and Wang X (2021) Modified Embedded-Atom Interatomic Potential Parameters of the Ti–Cr Binary and Ti–Cr–N Ternary Systems.
Front. Chem. 9:773015.
doi: 10.3389/fchem.2021.773015

INTRODUCTION

Transition metal nitride multilayer coatings are widely applied because of their excellent hardness, high thermal and chemical stability, and high oxidation and wear resistance (Chu et al., 1999; Zhou et al., 1999; Lee et al., 2005). TiN/CrN multilayered coating, a typical example that comprises alternating lamellas of its two mononitrides, exhibits much higher hardness while maintaining excellent corrosion resistance, high thermal stability, and oxidation resistance of CrN (Su et al., 2008; Luo et al., 2011; Koseki et al., 2015). Therefore, TiN/CrN multilayered coatings are promising for industrial fields such as for use in cutting tools, wherein both hardness and temperature stability are significantly important characteristics (Barshilia et al., 2003). Hence, investigating the improved chemical and mechanical characteristics of TiN/CrN multilayered coatings to clarify the underlying mechanism is fundamentally significant.

Indeed, extensive research has been conducted *via* experimental and computational simulations to identify the reason for the property improvement afforded by TiN/CrN multilayered coatings (Nordin et al., 1999; Mendibide et al., 2005; Steyer et al., 2008; Yin et al., 2012). Nordin et al. determined that the interfaces quantity in the multilayers significantly impacts the corrosion resistance of TiN/CrN multilayered coatings (Nordin et al., 1999). Moreover, Mendibide et al. discovered that the crack propagation mode shift caused by the fluctuating residual stress field can improve the wear resistance of TiN/CrN multilayered coatings (Mendibide et al., 2005; Steyer et al., 2008). Furthermore, the tensile behavior has recently been shown to be extremely important for learning the mechanical properties of multilayers since it is strongly correlative with the fracture and dislocation nucleation (Yin et al., 2012). However, sufficient information about the tensile process and ultimate geometry is difficult to experimentally obtain, particularly at the atomic level. Atomic simulations, such as the first-principles calculation on the basis of the density functional theory (DFT) and molecular dynamics (MD) simulation, afford microstructural information about the multilayered coatings and provide another useful method for investigating the physical characteristics of TiN/CrN multilayered coatings. In fact, numerous first-principles computing has been performed for transition metal nitride multilayered coatings (Stampfl and Freeman, 2012; Yin et al., 2012; Yin et al., 2014). But because of the size (or atoms quantity) constraints for constructing the supercell, DFT mainly focuses on the framework, stability, and strength of the interfaces in multilayered coatings. DFT is still difficult to apply in the investigation of a complex system's properties, especially the evolution of defects during the tensile process.

MD simulation, where over a million atoms are considered, is a useful method for gaining insights into the deformation and evolution of multilayered coatings. However, interatomic potentials need to be selected before the physical properties of TiN/CrN multilayered coatings are studied using MD simulation. The quality of interatomic potentials significantly affects the validity and dependability of MD simulations. A good interatomic potential could correctly reproduce multiple fundamental physical characteristics of correlative material systems. Therefore, 2NN MEAM potential (Lee and Baskes, 2000; Lee et al., 2001), developed from the embedded-atom method, is thought to be highly suitable for the multilayers as it can describe various elements using the same functional formalism (Daw and Baskes, 1983; Foiles et al., 1986).

For TiN/CrN multilayered coatings, the 2NN MEAM potential parameters of the Ti–Cr–N ternary system are needed to clarify the underlying mechanism of the hardness enhancement; However, they are not yet available. The 2NN MEAM potential parameters of a multicomponent alloy system can be determined by the 2NN MEAM potential parameters of the unary and binary systems. Thus, to obtain the potential parameters of the Ti–Cr–N ternary system, the potential parameters of the unary (Ti, Cr, and N) and binary (Ti–N, Cr–N, and Ti–Cr) systems are required. The potential parameters of Ti (Kim et al., 2006), Cr (Ding and Wang, 2019), N (Baskes, 1992), Ti–N(Ding and Wang, 2019) and Cr–N(Ding and Wang, 2019) systems are already obtained. Hence, before calculating the potential parameters of the Ti–Cr–N ternary system, the parameters of the Ti–Cr binary system shall be obtained.

As a part of the long-term project investigating the underlying mechanism of the hardness enhancement of TiN/CrN multilayered coatings at the atomic level and developing interatomic potential parameters of relevant systems to enable such investigations, this study aims to develop the potential parameters of the Ti–Cr binary system and extend them to the Ti–Cr–N ternary system. The rest part is described as below. The 2NN MEAM method and how to determine the potential parameters are depicted in *Methodology*. In *Verification of the Interaction Potential*, the reliability of the newly developed potential parameters is checked by the comparison of fundamental physical characteristics of correlative materials with the available experimental data and first-principles calculation results. Finally, *Summary* presents a summary.

METHODOLOGY

Interaction Potential

In 2NN MEAM potential, the total energy of a multicomponent system is expressed as

$$E = \sum_i \left[F_i\left(\bar{\rho}_i\right) + \frac{1}{2} \sum_{j(\neq i)} S_{ij}\phi_{ij}\left(R_{ij}\right) \right], \tag{1}$$

where F_i is the embedding function for embedding the atom i within a background electron density $\bar{\rho}_i$ and the pair potential $\phi_{ij}\left(R_{ij}\right)$ and screening function S_{ij} are evaluated at the distances of atoms i, j, and R_{ij}. To calculate the energy, F_i and $\phi_{ij}(R_{ij})$ are required.

The embedding energy F_i is as follows (Baskes, 1992):

$$F\left(\bar{\rho}\right) = AE_c\left(\frac{\bar{\rho}}{\rho^0}\right)\ln\left(\frac{\bar{\rho}}{\rho^0}\right), \tag{2}$$

where A is a tunable parameter, and E_c and $\overline{\rho^0}$ are the cohesive energy and background electron density of a reference framework, respectively. The detailed mathematical forms of 2NN MEAM can be found in literature (Baskes, 1997; Lee and Baskes, 2000; Lee et al., 2001; Kim et al., 2006) and is not repeated here. Only the major aspects of the model that determine ternary interaction potentials are concisely described in this section.

In 2NN MEAM potential, no unequivocal functional expression is assigned to the pair interaction $\phi_{ij}(R_{ij})$. However, a reference framework is defined, wherein each atom is sitting in the exact lattice points. The total energy per atom is achieved as a function of the nearest-neighbor distance using the state universal equation presented by Rose et al. (1984). Then, $\phi_{ij}(R_{ij})$ is estimated by the embedding energy and the total energy per atom. The universal equation of state is

$$E^u(R) = -E_c\left(1 + a^* + da^{*3}\right)e^{-a^*}, \tag{3}$$

Here, d is a tunable parameter,

$$a^* = \alpha\left(\frac{R}{r_e} - 1\right), \tag{4}$$

and

$$\alpha = \left(\frac{9B\Omega}{Ec}\right)^{\frac{1}{2}}. \tag{5}$$

In **Equations 3–5**, r_e, B, Ω and E_c represent the nearest-neighbor distance, the bulk modulus, the equilibrium atomic volume, and the cohesive energy of the equilibrium reference framework, respectively. The values of them and d are supposed or determined via first-principles computing or experiments.

In 2NN MEAM, the pair interaction between constituent elements needs to be confirmed to explain a multicomponent system. The total energy of a reference framework can be obtained as below:

$$E^u(R) = F\left(\overline{\rho^0}(R)\right) + \frac{Z_1}{2}\phi(R) + \frac{Z_2S}{2}\phi(aR), \tag{6}$$

where Z_1, Z_2 and a represent the number of first and second nearest-neighbor atoms, and the ratio between them, respectively. Additionally, S represents the screening factor for the 2NN interactions. For a given reference, the values of S and a are constants. Then, the pair potentials can be obtained from **Eqs 3, 6**:

$$\phi(R) = \psi(R) + \sum_{n=1}(-1)^n\left(\frac{Z_2S}{Z_1}\right)^n\psi(a^nR), \tag{7}$$

where

$$\psi(R) = \phi(R) + \frac{Z_2S}{Z_1}\phi(aR). \tag{8}$$

Here, the summation is always executed unless an accurate energy value per atom is acquired.

The many-body screening involved in MEAM (Baskes, 1997) differentiates it from other empirical potentials. The S_{ij} represents the impact of the neighbor atom k on the interaction between atoms i and j, which is the product of the screening factors determined by all the other neighbor atoms k:

$$S_{ij} = \prod_{k\neq i,j} S_{ikj}. \tag{9}$$

The screening factor S_{ikj} is defined as a function of C, which is determined as

$$S_{ikj} = f_c\left[\frac{C - C_{\min}}{C_{\max} - C_{\min}}\right], \tag{10}$$

where $C_{\max}$ and $C_{\min}$ are the maximum and minimum values of the screening range determined by C, respectively. C can be calculated as follows:

$$x^2 + \frac{1}{C}y^2 = \left(\frac{1}{2}R_{ij}\right)^2. \tag{11}$$

Here, x and y are the coordinates of k relative to the ellipse, which is determined through the positions of atoms i, j, and k. C can be computed from the relative distances among the three atoms, i, j, and k:

$$C = \frac{2\left(X_{ik} + X_{kj}\right) - \left(X_{ik} - X_{kj}\right)^2 - 1}{1 - \left(X_{ik} - X_{kj}\right)^2}, \tag{12}$$

where $X_{ik} = \left(\frac{R_{ik}}{R_{ij}}\right)^2$ and $X_{kj} = \left(\frac{R_{kj}}{R_{ij}}\right)^2$. The Smooth Cutoff Function f_c is Defined as

$$f_c(x) = \begin{cases} 1 & x \geq 1 \\ \left[1 - (1-x)^4\right]^2 & 0 < x < 1 \\ 0 & x \leq 0 \end{cases}. \tag{13}$$

Determination of the Potential Parameters of the Ti–Cr Binary System

2NN MEAM interaction potential parameters for the Ti, Cr, N, Cr–N and Ti–N systems have already been developed (Baskes, 1992; Kim et al., 2006; Ding and Wang, 2019), as shown in **Tables 1, 2**. Thus, only the 2NN MEAM potential parameters for the Ti–Cr binary system need to be confirmed. As shown in **Table 1**, 14 independent parameters are present for each unary system. Among them, E_c, r_e, α, and d are associated with the state universal equation. Moreover, the parameter A appears in the embedding function. The decay lengths ($\beta^{(0)}$, $\beta^{(1)}$, $\beta^{(2)}$, and $\beta^{(3)}$) and the weight factors ($t^{(1)}$, $t^{(2)}$, and $t^{(3)}$) are for the electron density. Additionally, $C_{\min}$ and $C_{\max}$ are associated with the many-body screening effect. For each binary system, 13 independent parameters are required besides of the unary parameters: E_c, r_e, α, d, $C_{\min}(i\text{–}i\text{–}j)$, $C_{\min}(j\text{–}j\text{–}i)$, $C_{\min}(i\text{–}j\text{–}i)$, $C_{\min}(j\text{–}i\text{–}j)$, $C_{\max}(i\text{–}i\text{–}j)$, $C_{\max}(j\text{–}j\text{–}i)$, $C_{\max}(i\text{–}j\text{–}i)$, $C_{\max}(j\text{–}i\text{–}j)$, and ρ_0. These are improved by fitting the alloy system target property, got from experiments or first-principles computing. E_c, r_e, and α can be achieved from the experimental data if a stable phase is selected as the reference framework. The atomic electron density scaling factor ρ_0 is the ratio of $\overline{\rho}_B^0$ and $\overline{\rho}_A^0$ (A–B = Ti–N, Cr–N, and Ti–Cr).

For the Ti–Cr binary system, in the potential parameters optimization process, the BCC_B2 framework is selected as the reference framework, and the elastic constants are adopted as the target property. Since no information is present regarding the lattice parameter and cohesive energy of B2-type TiCr, the initial values of E_c, r_e, and α are obtained *via* first-principles calculation using the Vienna *ab* initio simulation package, VASP (Kresse, 1995; Kresse and Furthmuller, 1996b; Kresse and Furthmuller, 1996a). The parameter d for the system is set as the average of d for the Ti and Cr unary systems since lacking the necessary data for determining its value. The remaining parameters, four $C_{\min}$ and four $C_{\max}$, have a major impact on the characteristics of a binary system. Empirically, all the $C_{\max}$s can assume appropriate values, which shall be large enough so that the first nearest neighbor of the reference framework is fully unscreened for considerable large thermal vibration. All the $C_{\max}$s are set to 2.8 herein. Both $C_{\min}$(Ti–Ti–Cr) and $C_{\min}$(Cr–Cr–Ti) can be set as the average of $C_{\min}$(Ti–Ti–Ti) and $C_{\min}$(Cr–Cr–Cr), obtained in the Ti and Cr unary systems, respectively. Therefore, only the parameters $C_{\min}$(Ti–Cr–Ti) and $C_{\min}$(Cr–Ti–Cr) need to be obtained by fitting to the elastic constants of the alloy system. The obtained 2NN MEAM interaction potential parameters of the Ti–Cr binary system are presented in **Table 2**.

Determination of the Potential Parameters of the Ti–Cr–N Ternary System

To extend the formalism of 2NN MEAM interaction potentials to a ternary system, besides of the parameters of the unary and binary components, three C$_{\min}(i\text{–}k\text{–}j)$ and $C_{\max}(i\text{–}k\text{–}j)$ parameters are required. The C$_{\min}(i\text{–}k\text{–}j)$ and $C_{\max}(i\text{–}k\text{–}j)$

TABLE 1 | The 2NN MEAM interaction potential parameters for Ti, Cr and N. The units of the cohesive energy E_c and the equilibrium nearest-neighbor distance r_e are eV and Å, respectively. All the other parameters are dimensionless. The reference structures for Ti, Cr and N are hcp, fcc and dimer, respectively.

	E_c	r_e	α	A	$\beta^{(0)}$	$\beta^{(1)}$	$\beta^{(2)}$	$\beta^{(3)}$	$t^{(1)}$	$t^{(2)}$	$t^{(3)}$	C_{min}	C_{max}	d
Ti[a]	4.87	2.92	4.63	1.17	1.32	0.0	1.95	5.0	5.3	14.1	-5.0	1.0	1.44	0.0
Cr[b]	4.1	2.495	5.58	0.42	6.81	1.0	1.0	1.0	0.3	5.9	-10.4	0.71	2.8	0.0
N[c]	4.88	1.10	5.96	1.8	2.75	4.0	4.0	4.0	0.05	1.0	0.0	2.0	2.8	0.0

[a] *Ref.(Kim et al., 2006).*
[b] *Ref.(Ding and Wang, 2019).*
[c] *Ref.(Baskes, 1992).*

TABLE 2 | The 2NN MEAM interaction potential parameters for the binary systems.

Parameter	Ti-N	Cr-N	Ti-Cr
E_c	6.61	5.22	4.605
r_e	2.121	2.074	2.6
a	4.829	4.52	4.551
d	0.0	0.0	0.0
C_{min} (*i-i-j*)	1.457	1.273	1.20
C_{min} (*j-j-i*)	1.457	1.273	1.20
C_{min} (*i-j-i*)	0.90	0.46	0.49
C_{min} (*j-i-j*)	0.22	0.872	0.26
C_{max} (*i-i-j*)	2.8	2.8	2.8
C_{max} (*j-j-i*)	2.8	2.8	2.8
C_{max} (*i-j-i*)	2.8	2.8	2.8
C_{max} (*j-i-j*)	2.8	2.8	2.8
ρ_0	18	18	1

reflect the screening degree of the third atom (C) on the interaction between two neighboring A and B atoms of various types. For the Ti–Cr–N ternary system, the parameters are $C_{\min}$(Ti–Cr–N), $C_{\min}$(Ti–N–Cr), $C_{\min}$(Cr–Ti–N), $C_{\max}$(Ti–Cr–N), $C_{\max}$(Ti–N–Cr), and $C_{\max}$(Cr–Ti–N) (**Figure 1**).

Due to the difficulty in acquiring enough data to uniquely confirm the ternary PPs, the method for developing the interaction potential parameters of the binary system is generally not applicable for the ternary system. Kim et al. (2009) proposed another approach for obtaining the 2NN MEAM interaction potential parameters of a ternary system in accordance with a type of averaging concept. The method is widely used since it greatly simplifies the optimization process of the interaction potential parameters of a ternary system (Ko and Lee, 2013; Kim et al., 2015; Ding and Wang, 2020). Therefore, the six unknown 2NN MEAM interaction potential parameters of the Ti–Cr–N ternary system can be calculated as follows:

$$C_{min}(Ti-Cr-N) = \left[0.5\left(C_{min}^{Ti-Cr-Ti}\right)^{\frac{1}{2}} + 0.5\left(C_{min}^{N-Cr-N}\right)^{\frac{1}{2}}\right]^2, \quad (14)$$

$$C_{min}(Ti-N-Cr) = \left[0.5\left(C_{min}^{Ti-N-Ti}\right)^{\frac{1}{2}} + 0.5\left(C_{min}^{Cr-N-Cr}\right)^{\frac{1}{2}}\right]^2, \quad (15)$$

$$C_{min}(Cr-Ti-N) = \left[0.5\left(C_{min}^{Cr-Ti-Cr}\right)^{\frac{1}{2}} + 0.5\left(C_{min}^{N-Ti-N}\right)^{\frac{1}{2}}\right]^2, \quad (16)$$

$$C_{max}(Ti-Cr-N) = \left[0.5\left(C_{max}^{Ti-Cr-Ti}\right)^{\frac{1}{2}} + 0.5\left(C_{max}^{N-Cr-N}\right)^{\frac{1}{2}}\right]^2, \quad (17)$$

$$C_{max}(\mathrm{Ti-N-Cr}) = \left[0.5\left(C_{\mathrm{max}}^{\mathrm{Ti-N-Ti}}\right)^{\frac{1}{2}} + 0.5\left(C_{\mathrm{max}}^{\mathrm{Cr-N-Cr}}\right)^{\frac{1}{2}}\right]^2, \quad (18)$$

$$C_{max}(Cr-Ti-N) = \left[0.5\left(C_{max}^{Cr-Ti-Cr}\right)^{\frac{1}{2}} + 0.5\left(C_{max}^{N-Ti-N}\right)^{\frac{1}{2}}\right]^2. \quad (19)$$

The values of all the interaction potential parameters on the right-hand side of **Eqs 14–19** are presented in **Table 2**. The

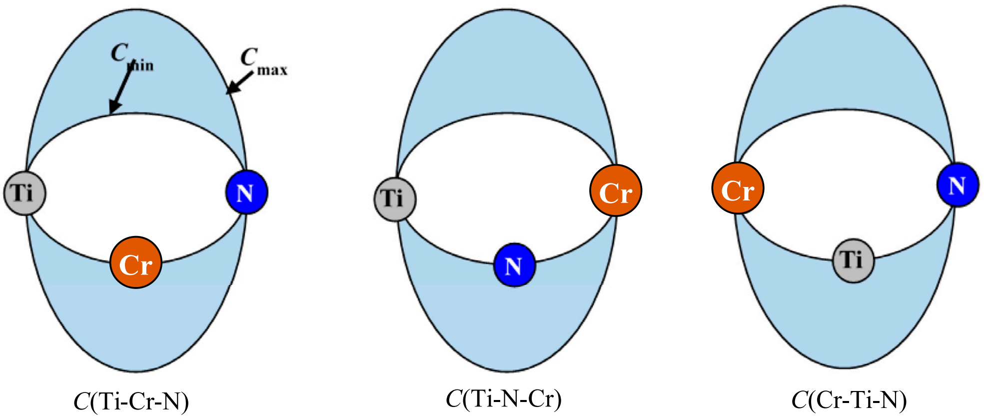

FIGURE 1 | Diagram of the three cases for the interactions screening between two neighboring atoms of various types by a third atom in the Ti–Cr–N ternary system.

TABLE 3 | The 2NN MEAM interaction potential parameters for Ti-Cr-N ternary system.

Parameter	Ti-Cr-N
C_{min}(Ti-Cr-N)	0.667
C_{min}(Ti-N-Cr)	0.662
C_{min}(Cr-Ti-N)	0.24
C_{max}(Ti-Cr-N)	2.8
C_{max}(Ti-N-Cr)	2.8
C_{max}(Cr-Ti-N)	2.8

obtained potential parameters of the Ti–Cr–N ternary system are presented in **Table 3**.

VERIFICATION OF THE INTERACTION POTENTIAL

As mentioned in the introduction, the most important validation in the optimization of 2NN MEAM interaction potential parameters is whether the fundamental characteristics of the systems can be reproduced using the obtained interaction potential parameters. For this, the structural, elastic, and surface characteristics of the binary Ti–Cr and ternary Ti–Cr–N systems—which are obtained using the 2NN MEAM interaction potential with the parameters indicated in **Tables 2**, **3**—are compared with the test or other theoretical data. All molecular dynamics simulations in this work are implemented with the January 26, 2017 version of the large-scale atomic/molecular massively parallel simulator package, LAMMPS (Plimpton, 1995). Furthermore, first-principles computing is conducted using VASP to get the physical characteristics of the materials for which the experimental data are not obtained or the theoretical results are less.

Ti–Cr Binary System

To check the obtained potential parameters reliability for the Ti–Cr binary system, the lattice parameter, cohesive energy, and elastic constants of B2-type TiCr are computed using the newly developed 2NN MEAM potential parameters. Since no information is available regarding these for comparison, their first-principles values are also calculated using VASP modes PW91 and PBE. **Table 4** compares the obtained results of the developed MEAM and first-principles. The table shows that the results well agree, except that C_{44} is slightly overestimated by the 2NN MEAM potential parameters.

To assess the transferability of the developed 2NN MEAM potential parameters, the lattice parameters and cohesive energies of the Laves phase C14-type $TiCr_2$, C15-type $TiCr_2$, and C15-type Ti_2Cr are calculated and compared with the test and other calculation results in **Table 5**. The results of the developed MEAM well agree with the first-principles computing results with an error of about 5%, indicating that the present constructed potentials are suitable for the Ti–Cr alloy system in different frameworks. This result indicates that the newly constructed 2NN MEAM potential parameters are reliable.

TABLE 4 | Comparison of the lattice parameter, cohesive energy and elastic constants of B2-type TiCr calculated by the present developed 2NN MEAM potentials with the first-principles calculation results. The units of the lattice parameter *a,* cohesive energy E_c and elastic constants are Å, eV and GPa, respectively.

Structure	Property	Present MEAM	First-principles	
			PW91	PBE
B2-type TiCr	*a*	3.02	3.039	3.035
	E_c	4.604	4.685	4.685
	C_{11}	183.3	204.6	235.9
	C_{12}	96.5	80.6	126.6
	C_{44}	70.2	41	28.2

Besides, the surface energies of the (001), (110), and (111) surfaces of the B2-type TiCr at 0 K are computed by the established potential parameters. Additionally, the approach put forward by Boettger (1994) is performed to obtain the surface energies:

$$\sigma = \frac{E_{slab}^{N} - N\Delta E}{2A}, \tag{20}$$

where E_{slab}^{N} represents the total energy of an N-layer slab, A represents the surface area, and ΔE represents the incremental energy impacted by $\left(E_{slab}^{N} - E_{slab}^{N-2}\right)/2$.

The obtained results are shown in **Table 6** and compared to the first-principles computing results. The comparison shows that the results of the developed MEAM are in good agreement with those of the first-principles computing. Moreover, the surface energy orientation dependency is well reproduced. Note that such an agreement is hard to achieve with the previous MEAM potential parameters. Therefore, the newly developed 2NN MEAM potential parameters are reliable.

Ti–Cr–N Ternary System

As stated above, the newly developed 2NN MEAM potential parameters of the Ti–Cr binary system can describe the fundamental physical characteristics of the correlative alloys reasonably well. Thus, only the reliability of the potential parameters of the Ti–Cr–N ternary system, which is acquired by combining the already published Ti–N (Ding and Wang, 2019) and Cr–N (Ding and Wang, 2019) potential parameters and the developed Ti–Cr binary potential parameters, needs to be confirmed. Thus, the lattice parameters and enthalpy of formation of the FCC $Ti_xCr_{1-x}N$ solid solutions with varying atomic concentrations are calculated. In our calculations, the solid solutions (SS) are formulated by substituting part of Ti atoms in a supercell (2 × 1 × 1) of the B1-type TiN with Cr atoms. Since no information is available about these characteristics, the first-principles calculation values are calculated for comparison. The obtained results are compared in **Figures 2A,B** for lattice parameters and enthalpy of formation, respectively. The figure shows that the results of the newly developed 2NN MEAM conform to first-principles computing results. Moreover, note that the lattice parameters and

TABLE 5 | Comparison of the present 2NN MEAM lattice parameters and cohesive energies of the Laves phase C14-, C15-type $TiCr_2$ and C15-type Ti_2Cr with other calculation results. The units of the lattice parameter *a* and the cohesive energy E_c are Å and eV, respectively.

Structure	Property	Present MEAM	Exp	First-principles	
				Present	Previous
C14-type $TiCr_2$	*a*	4.857	4.932[a],4.900[b]	4.859[c]	4.885[d],4.882[e]
	c	7.837	7.961[a],7.927[b]	7.779[c]	7.830[d],7.831[e]
	E_c	4.476	-	4.616[c]	4.765[e]
C15-type $TiCr_2$	*a*	6.847	6.910[a]	6.854[c]	6.857[d]
	E_c	4.469	-	4.471[c]	-
C15-type Ti_2Cr	*a*	11.297	-	11.312[c]	-
	E_c	4.698	-	4.968[c]	-

[a] *Ref.(Murray, 1981).*
[b] *Ref.(Cuff et al., 1952).*
[c] *The first-principles calculation performed in present work.*
[d] *Ref.(Chen et al., 2005).*
[e] *Ref.(Nong et al., 2013).*

TABLE 6 | Comparison of the surface energies of B2-type TiCr at 0 K calculated using the present 2NN MEAM potential with the first-principles calculation results. The unit of the surface energy is J/m^2.

Surface	Present MEAM	First-principles
(001)	2.389	1.833
(110)	2.486	2.152
(111)	4.180	4.323

enthalpy of formation of the FCC $Ti_xCr_{1-x}N$ SS decrease with increasing Cr atomic concentration, and this trend is also accurately reproduced by the developed 2NN MEAM potential parameters.

To further assess the transferability of the developed potential parameters for the Ti–Cr–N ternary system, the work of adhesion of the TiN/CrN interface are computed and compared to the first-principles computing values (**Table 7**). The results obtained by the newly developed potential parameters conform to the first-principles computing results, denoting the reliability of the potential parameters of the newly developed Ti–Cr–N ternary system.

It has been shown that the developed potential parameters of the Ti–Cr–N ternary system can reasonably accurately reproduce the different fundamental characteristics of the relevant systems. Thus, the developed 2NN MEAM potential parameters can used for performing large-scale atomistic simulations to investigate the enhanced chemical and mechanical characteristics of TiN/CrN multilayered coatings.

SUMMARY

In this research, the potential parameters for the Ti–Cr binary and the Ti–Cr–N ternary systems on the basis of 2NN MEAM formalism are developed. To verify the dependability of the newly developed potential parameters, the structural, elastic, and surface characteristics of the correlative systems are calculated using the newly developed potential parameters. The developed

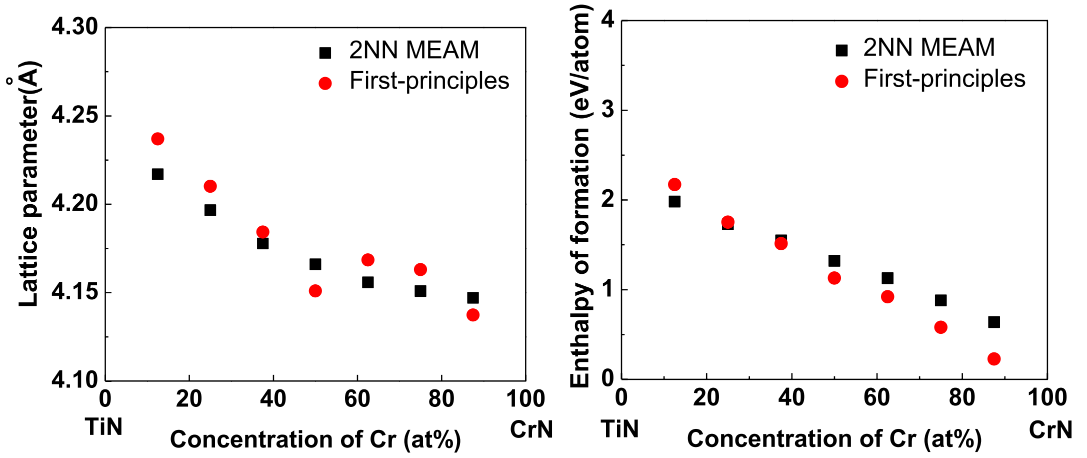

FIGURE 2 | Comparisons of the MEAM and first-principles results for **(A)** the lattice parameter and **(B)** enthalpy of formation of FCC $Ti_xCr_{1-x}N$ solid solution changing with the atom concentration.

TABLE 7 | The adhesion energies of the TiN/CrN interface calculated by the present ternary potential, comparing with the first-principles calculation values. The unit of the adhesion energy is J/m^2.

Interface	Present MEAM	First-principles		
		Present[a]	Yin[b]	Chen[c]
(100)	3.839	3.637	3.36	3.47
(110)	5.22	5.328	-	5.79
(111)	8.102	7.679	9.27	-

[a] *The first-principles calculation performed in present work.*

[b] *Ref. (Yin et al., 2014).*

[c] *Ref. (Chen and Bielawski, 2008).*

interatomic potential parameters accurately reproduced the multiple fundamental characteristics of relevant systems conforming to the first-principles calculation and/or experimental results. This study can also contribute to construct the 2NN MEAM potentials parameters of other binary and ternary systems and clarify the underlying mechanism of the hardness enhancement of TiN/CrN multilayered coatings using atomistic simulations.

DATA AVAILABILITY STATEMENT

The original contributions presented in the study are included in the article/Supplementary Material, further inquiries can be directed to the corresponding authors.

AUTHOR CONTRIBUTIONS

All authors listed have made a substantial, direct and intellectual contribution to the work, and approved it for publication.

ACKNOWLEDGMENTS

The authors acknowledge the financial supports from the science and technology research program of Chongqing Education Commission of China (Grant No. KJQN202000505), the Chongqing Natural Science Foundation of China (Grant No. cstc2019jcyj-msxmX0251), and the Doctoral Fund Project of Chongqing Normal University (Grant No. 20XLB001).

REFERENCES

Barshilia, H. C., Jain, A., and Rajam, K. S. (2003). Structure, Hardness and thermal Stability of Nanolayered TiN/CrN Multilayer Coatings. *Vacuum* 72 (3), 241–248. doi:10.1016/j.vacuum.2003.08.003

Baskes, M. I. (1997). Determination of Modified Embedded Atom Method Parameters for Nickel. *Mater. Chem. Phys.* 50 (2), 152–158. doi:10.1016/S0254-0584(97)80252-0

Baskes, M. I. (1992). Modified Embedded-Atom Potentials for Cubic Materials and Impurities. *Phys. Rev. B.* 46 (5), 2727–2742. doi:10.1103/PhysRevB.46.2727

Boettger, J. C. (1994). Nonconvergence of Surface Energies Obtained from Thin-Film Calculations. *Phys. Rev. B.* 49 (23), 16798–16800. doi:10.1103/PhysRevB.49.16798

Chen, K., and Bielawski, M. (2008). Interfacial Fracture Toughness of Transition Metal Nitrides. *Surf. Coat. Tech.* 203 (5-7), 598–601. doi:10.1016/j.surfcoat.2008.05.040

Chen, X. Q., Wolf, W., Podloucky, R., and Rogl, R. (2005). Ab Initio study of Ground-State Properties of the Laves Phase Compounds TiCr2,ZrCr2, and HfCr2. *Phys. Rev. B.* 71 (17) 174101. doi:10.1103/physrevb.71.179901

Chu, X., Wong, M. S., Sproul, W. D., and Barnett, S. A. (1999). Deposition, Structure, and Hardness of Polycrystalline Transition-Metal Nitride Superlattice Films. *J. Mater. Res.* 14 (6), 2500–2507. doi:10.1557/Jmr.1999.0335

Cuff, F. B., Grant, N. J., and Floe, C. F. (1952). Titanium-Chromium Phase Diagram. *Jom* 4 (8), 848–853. doi:10.1007/bf03398150

Daw, M. S., and Baskes, M. I. (1983). Semiempirical, Quantum Mechanical Calculation of Hydrogen Embrittlement in Metals. *Phys. Rev. Lett.* 50 (17), 1285–1288. doi:10.1103/PhysRevLett.50.1285

Ding, S. B., and Wang, X. Q. (2020). Strain Rate and Temperature Effects on the Mechanical Properties of TiN/VN Composite: Molecular Dynamics Study. *J. Alloys Comp.* 814 152151. doi:10.1016/j.jallcom.2019.152151

Ding, S., and Wang, X. (2019). A Systematic Study on the MEAM Interatomic Potentials of the Transition Metal Nitrides TMNs (TM=Ti, V, Cr, Fe) Binary Systems. *J. Alloys Comp.* 805, 1081–1089. doi:10.1016/j.jallcom.2019.07.114

Foiles, S. M., Baskes, M. I., and Daw, M. S. (1986). Embedded-Atom-Method Functions for the Fcc Metals Cu, Ag, Au, Ni, Pd, Pt, and Their Alloys. *Phys. Rev. B.* 33 (12), 7983–7991. doi:10.1103/PhysRevB.33.7983

Kim, H.-K., Jung, W.-S., and Lee, B.-J. (2009). Modified Embedded-Atom Method Interatomic Potentials for the Fe-Ti-C and Fe-Ti-N Ternary Systems. *Acta Materialia* 57 (11), 3140–3147. doi:10.1016/j.actamat.2009.03.019

Kim, Y.-K., Jung, W.-S., and Lee, B.-J. (2015). Modified Embedded-Atom Method Interatomic Potentials for the Ni-Co Binary and the Ni-Al-Co Ternary Systems. *Model. Simul. Mater. Sci. Eng.* 23 (5), 055004. doi:10.1088/0965-0393/23/5/055004

Kim, Y. M., Lee, B. J., and Baskes, M. I. (2006). Modified Embedded-Atom Method Interatomic Potentials for Ti and Zr. *Phys. Rev. B.* 74 (1), 014101. doi:10.1103/physrevb.74.014101

Ko, W.-S., and Lee, B.-J. (2013). Modified Embedded-Atom Method Interatomic Potentials for Pure Y and the V-Pd-Y Ternary System. *Model. Simul. Mater. Sci. Eng.* 21 (8), 085008. doi:10.1088/0965-0393/21/8/085008

Koseki, S., Inoue, K., Morito, S., Ohba, T., and Usuki, H. (2015). Comparison of TiN-Coated Tools Using CVD and PVD Processes during Continuous Cutting of Ni-Based Superalloys. *Surf. Coat. Tech.* 283, 353–363. doi:10.1016/j.surfcoat.2015.10.071

Kresse, G. (1995). Ab Initio molecular Dynamics for Liquid Metals. *J. Non-Crystalline Sol.* 192-193, 222–229. doi:10.1016/0022-3093(95)00355-X

Kresse, G., and Furthmüller, J. (1996a). Efficiency of Ab-Initio Total Energy Calculations for Metals and Semiconductors Using a Plane-Wave Basis Set. *Comput. Mater. Sci.* 6 (1), 15–50. doi:10.1016/0927-0256(96)00008-0

Kresse, G., and Furthmüller, J. (1996b). Efficient Iterative Schemes Forab Initiototal-Energy Calculations Using a Plane-Wave Basis Set. *Phys. Rev. B.* 54 (16), 11169–11186. doi:10.1103/PhysRevB.54.11169

Lee, B.-J., and Baskes, M. I. (2000). Second Nearest-Neighbor Modified Embedded-Atom-Method Potential. *Phys. Rev. B.* 62 (13), 8564–8567. doi:10.1103/PhysRevB.62.8564

Lee, B. J., Baskes, M. I., Kim, H., and Cho, Y. K. (2001). Second Nearest-Neighbor Modified Embedded Atom Method Potentials for Bcc Transition Metals. *Phys. Rev. B.* 64 (18) 184102. doi:10.1103/physrevb.64.184102

Lee, S. Y., Kim, S. D., and Hong, Y. S. (2005). Application of the Duplex TiN Coatings to Improve the Tribological Properties of Electro Hydrostatic Actuator Pump Parts. *Surf. Coat. Tech.* 193 (1-3), 266–271. doi:10.1016/j.surfcoat.2004.07.053

Luo, Q., Wang, S. C., Zhou, Z., and Chen, L. (2011). Structure Characterization and Tribological Study of Magnetron Sputtered Nanocomposite nc-TiAlV(N,C)/a-C Coatings. *J. Mater. Chem.* 21 (26), 9746–9756. doi:10.1039/c1jm10707k

Mendibide, C., Steyer, P., and Millet, J.-P. (2005). Formation of a Semiconductive Surface Film on Nanomultilayered TiN/CrN Coatings and its Correlation with Corrosion protection of Steel. *Surf. Coat. Tech.* 200 (1-4), 109–112. doi:10.1016/j.surfcoat.2005.02.060

Murray, J. L. (1981). The Cr–Ti (Chromium-titanium) System. *Bull. Alloy Phase Diagrams* 2 (2), 174–181. doi:10.1007/BF02881474

Nong, Z.-S., Zhu, J.-C., Cao, Y., Yang, X.-W., Lai, Z.-H., and Liu, Y. (2013). A First-Principles Study on the Structural, Elastic and Electronic Properties of the C14 Laves Phase Compounds TiX2 (X=Cr, Mn, Fe). *Physica B: Condensed Matter* 419, 11–18. doi:10.1016/j.physb.2013.03.012

Nordin, M., Herranen, M., and Hogmark, S. (1999). Influence of Lamellae Thickness on the Corrosion Behaviour of Multilayered PVD TiN CrN Coatings. *Thin Solid Films* 348 (1-2), 202–209. doi:10.1016/S0040-6090(99)00192-3

Plimpton, S. (1995). Fast Parallel Algorithms for Short-Range Molecular Dynamics. *J. Comput. Phys.* 117 (1), 1–19. doi:10.1006/jcph.1995.1039

Rose, J. H., Smith, J. R., Guinea, F., and Ferrante, J. (1984). Universal Features of the Equation of State of Metals. *Phys. Rev. B.* 29 (6), 2963–2969. doi:10.1103/PhysRevB.29.2963

Stampfl, C., and Freeman, A. J. (2012). Structure and Stability of Transition Metal Nitride Interfaces from First-Principles: AlN/VN, AlN/TiN, and VN/TiN. *Appl. Surf. Sci.* 258 (15), 5638–5645. doi:10.1016/j.apsusc.2012.02.046

Steyer, P., Mege, A., Pech, D., Mendibide, C., Fontaine, J., Pierson, J.-F., et al. (2008). Influence of the Nanostructuration of PVD Hard TiN-Based Films on the Durability of Coated Steel. *Surf. Coat. Tech.* 202 (11), 2268–2277. doi:10.1016/j.surfcoat.2007.08.073

Su, C.-Y., Pan, C.-T., Liou, T.-P., Chen, P.-T., and Lin, C.-K. (2008). Investigation of the Microstructure and Characterizations of TiN/CrN Nanomultilayer Deposited by Unbalanced Magnetron Sputter Process. *Surf. Coat. Tech.* 203 (5-7), 657–660. doi:10.1016/j.surfcoat.2008.05.057

Yin, D., Peng, X., Qin, Y., and Wang, Z. (2012). Impact of Residual Stress on the Adhesion and Tensile Fracture of TiN/CrN Multi-Layered Coatings from First Principles. *Physica E: Low-dimensional Syst. Nanostructures* 44 (9), 1838–1845. doi:10.1016/j.physe.2012.05.008

Yin, D., Yang, Y., Peng, X., Qin, Y., and Wang, Z. (2014). Tensile and Fracture Process of the TiN/VN Interface from First Principles. *Ceramics Int.* 40 (9), 14453–14462. doi:10.1016/j.ceramint.2014.07.016

Zhou, Y. M., Asaki, R., Soe, W. H., Yamamoto, R., Chen, R., and Iwabuchi, A. (1999). Hardness Anomaly, Plastic Deformation Work and Fretting Wear Properties of Polycrystalline TiN/CrN Multilayers. *Wear* 236 (1-2), 159–164. doi:10.1016/S0043-1648(99)00272-0

Conflict of Interest: The authors declare that the research was conducted in the absence of any commercial or financial relationships that could be construed as a potential conflict of interest.

frontiers
in Chemistry

ORIGINAL RESEARCH
published: 11 November 2021
doi: 10.3389/fchem.2021.796323

Computational Simulation of the Electronic State Transition in the Ternary Hexagonal Compound BaAgBi

***Yu Chang*[1]*, Xin Wang*[2]**, Sanggyun Na*[2]* *and Weiwei Zhang*[2]**

[1]Tonghua Normal University, Tonghua, China, [2]Wonkwang University, Iksan, South Korea

Topological properties in metals or semimetals have sparked tremendous scientific interest in quantum chemistry because of their exotic surface state behavior. The current research focus is still on discovering ideal topological metal material candidates. We propose a ternary compound with a hexagonal crystal structure, BaAgBi, which was discovered to exhibit two Weyl nodal ring states around the Fermi energy level without the spin–orbit coupling (SOC) effect using theoretical calculations. When the SOC effect is considered, the topological phases transform into two Dirac nodal line states, and their locations also shift from the Weyl nodal rings. The surface states of both the Weyl nodal ring and Dirac nodal lines were calculated on the (001) surface projection using a tight-binding Hamiltonian, and clear drumhead states were observed, with large spatial distribution areas and wide energy variation ranges. These topological features in BaAgBi can be very beneficial for experimental detection, inspiring further experimental investigation.

Keywords: first-principles calculation, electronic band structure, topological nodal line, DFT, ternary hexagonal compound

Edited by:
Junjie He,
Charles University, Czechia

Reviewed by:
Xiaoming Zhang,
Hebei University of Technology, China
Tie Yang,
Southwest University, China

****Correspondence:***
Xin Wang
dlcrystal622@wku.ac.kr
Sanggyun Na
nsghy@wku.ac.kr

Specialty section:
This article was submitted to Theoretical and Computational Chemistry,
a section of the journal Frontiers in Chemistry

Received: *16 October 2021*
Accepted: *26 October 2021*
Published: *11 November 2021*

Citation:
Chang Y, Wang X, Na S and Zhang W (2021) Computational Simulation of the Electronic State Transition in the Ternary Hexagonal Compound BaAgBi. Front. Chem. 9:796323. doi: 10.3389/fchem.2021.796323

INTRODUCTION

Since the discovery of topological insulators, the study of topological properties in materials has sparked extremely large research attention in material science, particularly in solid-state physics and chemistry (Bradlyn et al., 2017; Yan and Felser, 2017; Schoop et al., 2018). With the ongoing development, the current research into topological materials has been expanded into metals or semimetals (Burkov, 2016; Yan and Felser, 2017; Yu et al., 2017; Zhang et al., 2019a; Gao et al., 2019). Contrary to that in conventional topological insulators, the topological states in metals are characterized by linear band crossings in the low-energy region around the Fermi level, and they are protected by structural symmetry and nontrivial band topology. Topological states in metals can be classified into different types based on different band crossing conditions and intertwining shapes. For example, nodal point (Zhang et al., 2017a; Cano et al., 2019; He et al., 2019; Li et al., 2020; Li and Xia, 2020), nodal line (Chang et al., 2016a; Hosen et al., 2018; Kim et al., 2018; Takane et al., 2018; Zheng et al., 2019; Wang et al., 2020a; Wang et al., 2020b; He et al., 2020; Jin et al., 2020; Wang et al., 2021a; He et al., 2021; Zhou et al., 2021), and nodal surface (Fu et al., 2019; Yang et al., 2019; Yang et al., 2020; Yang and Zhang, 2020) can be differentiated by their band crossing dimensionality: Weyl (Huang et al., 2015; Soluyanov et al., 2015; Chang et al., 2016b; Jia et al., 2016; Wang et al., 2018a), triple (Jin et al., 2019a; Bhattacharya et al., 2021), Dirac (Galanakis and Mavropoulos, 2007; Heikkilä and Volovik, 2011; He et al., 2016; Zhang et al., 2017b; Zhang et al., 2018a; Wang et al., 2018b; Wang et al., 2019), sextuple, and octuple topological states (Bradlyn et al., 2016), which can also be distinguished by their band crossing degeneracy. Some other classifications can also be defined based on their band dispersion rates or band crossing shapes (Bzdušek et al., 2016; Chen et al., 2017; Wang et al., 2017; Zhang et al., 2018b).

For topological nodal points or nodal lines, their linear band crossings are often associated with protected surface states (Zhang et al., 2017a; Zhang et al., 2017b; Chen et al., 2017; Sheng et al., 2017; Jin et al., 2019b; Zhang et al., 2019b; He et al., 2019; Liu et al., 2019; Wang et al., 2020c; Wang et al., 2020d; Wang et al., 2020e; Meng et al., 2020; Yang et al., 2021), i.e., Fermi arc states connecting the nodal points and drumhead surface states concatenating the nodal lines. The nodal line can be regarded as a link between innumerous nodal points, and the corresponding drumhead surface state is a union of infinite Fermi arc states. In this regard, studying nodal line metals or even employing them for future applications is advantageous simply because it could provide more possibilities and varieties. The current research focus is on discovering nodal line metals with clean band structures, and more topological metal materials are being discovered and even designed as the theoretical calculation tools and computation power improve. Some of them have also been successfully verified through experimental characterizations (Jia et al., 2016; Du et al., 2017; Wang et al., 2017; Hosen et al., 2018; Kim et al., 2018; Takane et al., 2018; Fu et al., 2019; Wang et al., 2021a). However, the number of ideal topological metals is still very limited even with high-throughput computation methods.

Herein, we present BaAgBi, a ternary compound with a hexagonal structure. When the spin–orbit coupling (SOC) effect is not considered, its metallic band structures exhibit multiple band crossing points near the Fermi level, which correspond to two Weyl nodal ring states, according to the first-principles calculations. The detailed energy variation and spatial distribution of the nodal rings are examined using a three-dimensional band dispersion scan. When the SOC effect is considered, the original Weyl nodal rings are gapped out, and new Dirac nodal line states emerge, with their locations shifted as well. The corresponding surface states for both the Weyl nodal rings and Dirac nodal lines were calculated by constructing a tight-binding Hamiltonian and a surface slab model, and clear drumhead states were discovered along the (001) surface projection spectrum. This BaAgBi material can serve as an ideal nodal line metal for studying the related exotic physical properties since these surface states with large energy variations and wide spatial distributions can be very useful for experimental detection.

COMPUTATIONAL METHODOLOGY

We used the Vienna ab initio simulation package (VASP) (Hafner, 2008) to perform the first-principles calculations to examine the electronic band structures of the BaAgBi material. Under the density functional theory (Payne et al., 1992), the generalized gradient approximation (Perdew et al., 1996) of the Perdew–Burke–Ernzerhof (PBE) functional (Ernzerhof and Scuseria, 1999) was used to determine the correlation exchange potential. A cutoff energy of 500 eV was selected for the plane wave set, and a Monkhorst–Pack k-mesh of $9 \times 9 \times 5$ was used for the first Brillouin zone sampling. The structure was fully relaxed when the total force per atom was less than 1×10^{-3} eV/Å, and the energy convergence was reached when the total energy difference per atom was smaller than 5×10^{-6} eV. The open-source VASPKIT package (Wang et al., 2021b) was used to extract the calculation data. Maximally localized Wannier functions were constructed with the Wannier90 (Mostofi et al., 2008; Mostofi et al., 2014) code to investigate the topological properties, and based on them, the surface states were calculated using the WANNIERTOOLS package (Wu et al., 2018).

RESULTS AND DISCUSSIONS

The ternary compound, BaAgBi, has a hexagonal structure with space group $P6_3/mmc$ (No. 194). As shown in **Figure 1A**, the unit cell of BaAgBi contains two Ag atoms at the 2a Wyckoff sites (0, 0, 0), two Ba atoms at the 2c Wyckoff sites (1/3, 2/3, 1/4), and two Bi atoms at the 2d Wyckoff sites (1/3, 2/3, 3/4). The calculated lattice constants are a = b = 5.823 Å and c = 7.040 Å, which are used in the electronic band structure analysis. Before we proceed, it is necessary to note that the current crystal has two symmetry operations: spatial inversion symmetry Ψ and time-reversal symmetry T, which are very important for the investigation of its topological properties.

The electronic band structures of BaAgBi were calculated, and the results are shown in **Figure 2A**. Notably, the Fermi energy level is shifted to 0 eV in the figure, and only the bands near the Fermi level are shown. The SeeK-path tool was used to select the k paths, and their location in the first Brillouin zone is shown in **Figure 1B**. There are several bands across the Fermi energy, indicating that the BaAgBi compound has a metallic feature. Furthermore, these bands exhibit multiple crossing points around the Fermi level, as labeled in the figure. A closer examination reveals that these band crossings belong to two pairs formed from three bands that are red, green, and blue. Overall, these band crossings points are located along two high symmetry paths, Γ–M and K–Γ. As shown in **Figure 1B**, these two paths belong to the same plane of $k_z = 0$ at the Γ point. Since the BaAgBi crystal has both spatial inversion symmetry and time-reversal symmetry, these crossing points should not be isolated but should belong to the nodal rings. A precise band dispersion scan was performed along the whole plane of $k_z = 0$, and the results are reported in the supplementary materials. According to the results, these three bands did form two nodal rings, which are centered at the Γ point. **Figure 3A** shows the location and distribution of the two Weyl nodal rings. The big red nodal ring has a rounded hexagram shape, whereas the small blue nodal ring has a circle shape. The bigger nodal ring has a much larger energy variation than the smaller one. They are both classified as Type-I because of the reverse band dispersion rates around them.

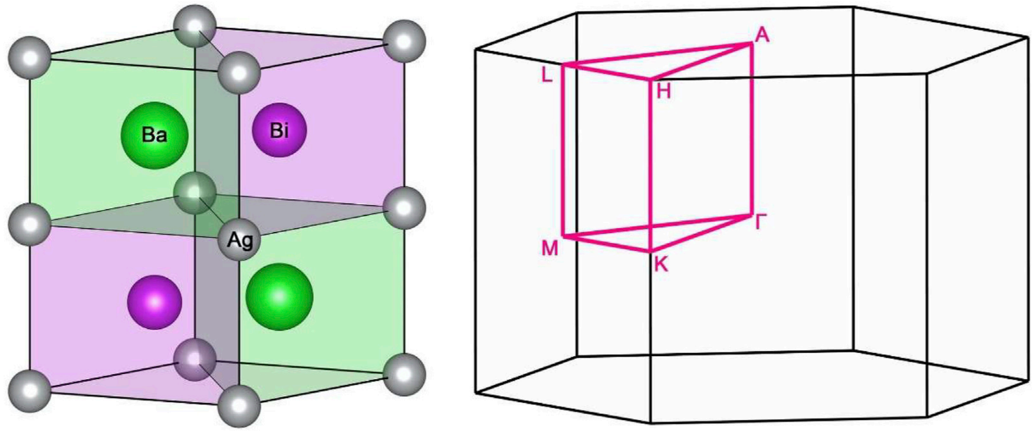

FIGURE 1 | (A) The crystal structure of the BaAgBi material and **(B)** its corresponding Brillouin zone, with high symmetry points and paths marked.

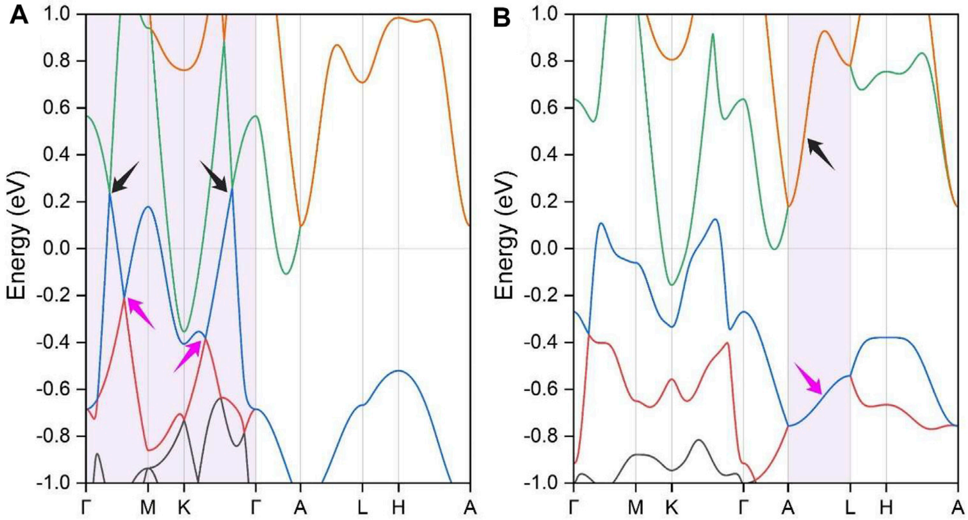

FIGURE 2 | The calculated electronic band structures of the BaAgBi material **(A)** without the SOC effect and **(B)** with the SOC effect. The topological band crossing areas are indicated by the arrows. In this figure, each band is highlighted by different colors.

Since the BaAgBi material contains heavy metal elements, the SOC effect should be considered. Thus, we calculated the band structures under the SOC effect, and the results are displayed in **Figure 2B**. Note that every band in **Figure 2** is doubly degenerate. When the SOC effect is neglected, it can be observed that the original nodal ring band crossing states along the Γ–M and K–Γ paths are completed destroyed. The inclusion of the SOC effect is well known to gap out topological band crossings, and this behavior is particularly noticeable in the current material because of the presence of all three heavy metal elements. However, as indicated by the arrows in the figure, two new band crossing lines emerge, forming two Dirac nodal lines along the A–L path in the $k_z = \pi$ plane. Based on the rotation symmetry of the BaAgBi compound, there should be two more pairs of the same Dirac nodal lines in the same plane, all of which are symmetrically equivalent. A precise band dispersion scan was also performed, and the results are reported in the supplementary materials, from which these Dirac nodal lines can be clearly observed. Under the SOC effect, the two Weyl nodal ring states transform into two Dirac nodal line states, and their locations also shift from the $k_z = 0$ plane to the $k_z = \pi$ plane. **Figure 3B** shows a schematic illustration of the location and distribution of the two Dirac nodal lines, which have hexagonal star lines.

The three dimensional band dispersion has been scanned along the $k_z = 0$ plane for the two Weyl nodal rings and along the $k_z = \pi$ plane for the Dirac nodal lines, and the calculation results are reported in **Figures 4**, **5**, respectively. The crossing lines are marked by the red and blue dot in the figure and their exact spatial location are shown in the right panel of each figure.

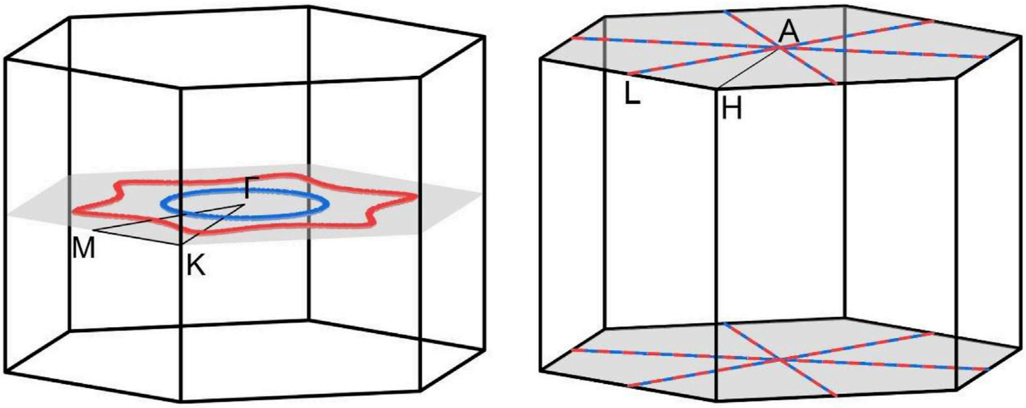

FIGURE 3 | The illustration of **(A)** the location and distribution of the two Weyl nodal rings along the $k_z = 0$ plane and **(B)** the two Dirac nodal lines along the $k_z = \pi$ the plane. The high symmetry points and paths are also displayed for enhanced visualization.

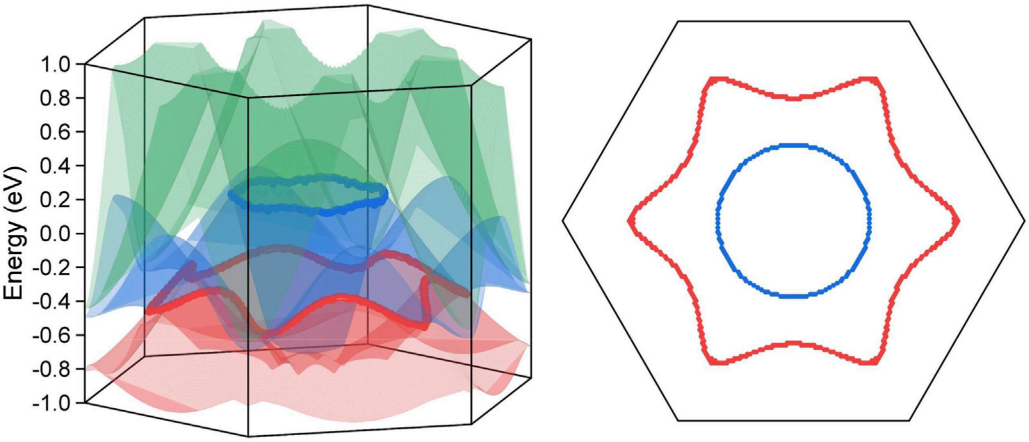

FIGURE 4 | The three dimensional surface dispersion of the three crossing bands along the $k_z = 0$ plane for BaAgBi without SOC effect in the left panel. The crossing lines are labelled by red and blue dots, which correspond to the two Weyl nodal rings. The exact spatial distribution of the two Wey nodal rings along the $k_z = 0$ plane in the right panel.

In general, topological nodal ring or line states are characterized by drumhead surface states, which can be located either outside or inside the projected nodal ring or line. To examine the surface states associated with the Weyl nodal rings and the Dirac nodal lines in the BaAgBi material, we constructed a tight-binding Hamiltonian by projecting the Bloch states to atomic orbitals with maximally localized Wannier functions, as employed in the Wannier90 code. We built a slab model along the (001) surface and then calculated the corresponding surface states because the location of the nodal rings and lines are all parallel to this surface (**Figure 3**). **Figure 6A** illustrates the (001) surface slab model with only a thickness of three unit cells, but 20 layers were used for the calculations.

Figures 6B,C show the calculated topological surface states along the (001) surface projection for both the two Weyl nodal rings and the two Dirac nodal lines, respectively. It is worth noting that the bulk band structures are also overlayed on the surface projection, and they exhibit very good correspondence, particularly in the topological band crossing areas. As indicated by the black arrows in the figure, multiple drumhead surface states can be clearly observed, and they are all emitted from the nodal ring or nodal line crossing points. The surface states of the smaller Weyl nodal ring are well separated from the bulk band projection, while those of the larger ones are buried within the bulk states. The band projection with the SOC effect in **Figure 6C** is substantially more complicated than the clean band spectrum without the SOC effect in **Figure 6B**. However, the drumhead states are still noticeable. These surface states have a relatively large energy variation range and a relatively wide spatial distribution area, both of which are beneficial for further experimental detection. We highly encourage that ARPES experiments be performed to detect its surface states in the future.

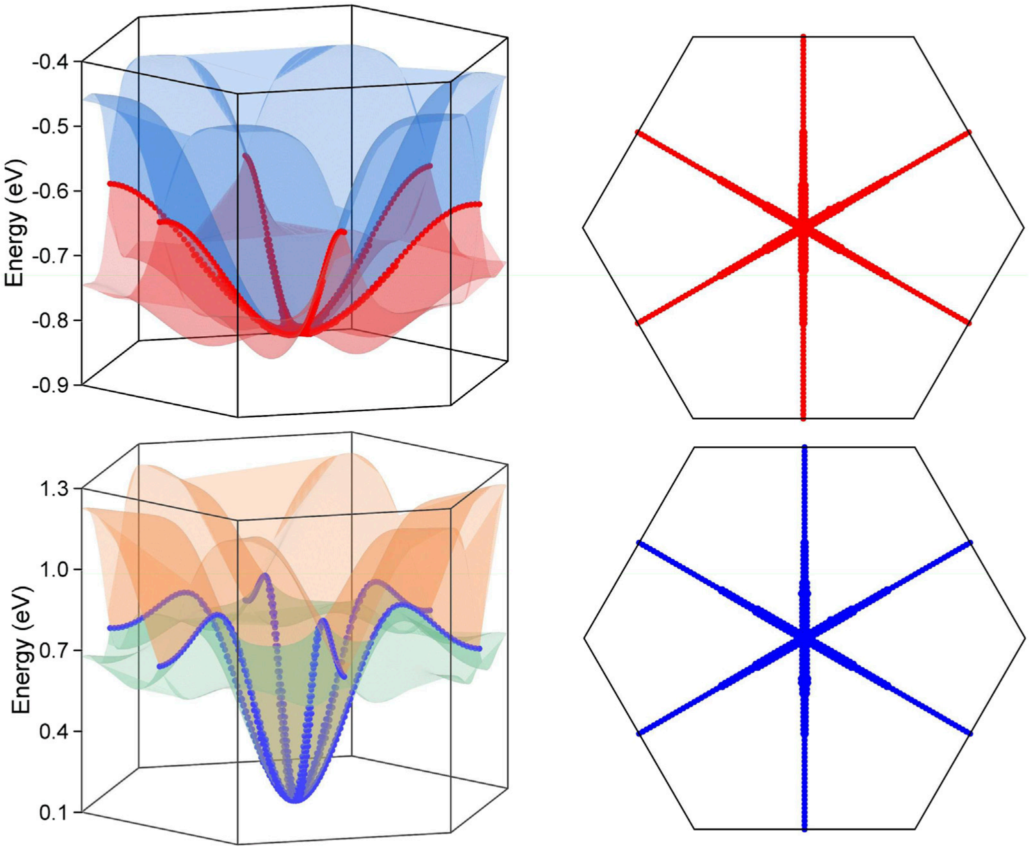

FIGURE 5 | The three dimensional surface dispersion of the crossing bands along the $k_z = \pi$ plane for BaAgBi with SOC effect in the left panel. The crossing lines are labelled by red and blue dots, which correspond to the two Dirac nodal lines. The exact spatial distribution of the two Dirac nodal rings along the $k_z = \pi$ plane in the right panel.

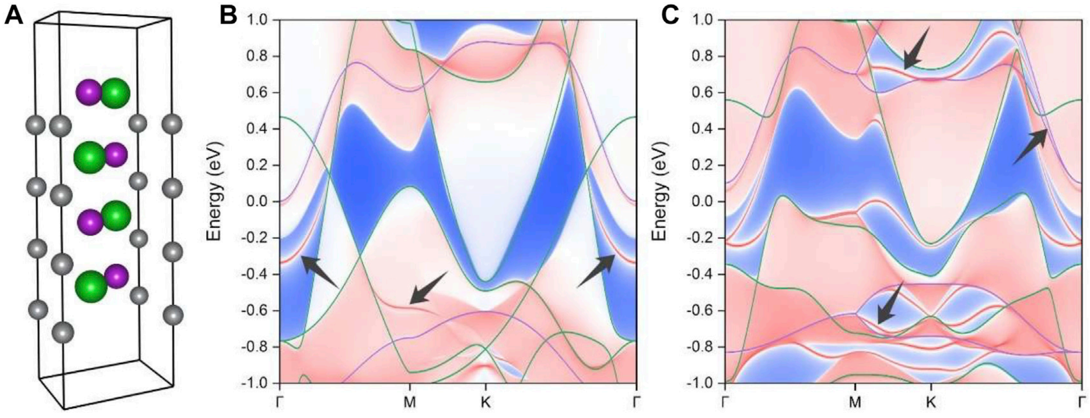

FIGURE 6 | (A) The slab model along the (001) surface with only a thickness of three unit cells for the surface state calculation. The calculated surface band projections **(B)** without and **(C)** with the SOC effect. The drumhead surface states that originated from the topological crossing points are indicated by the black arrows.

CONCLUSION

In this work, we used first-principles calculations to systematically study the topological properties of the ternary compound, BaAgBi. The calculated electronic band structures revealed the metallic feature of BaAgBi. Additionally, multiple topological band crossing points were discovered near the Fermi energy level. When the SOC effect was neglected, two Weyl nodal ring states were observed along the $k_z = 0$ plane. However, the topological states transformed into two Dirac nodal lines under the SOC effect, and their spatial distribution also shifted into the $k_z = \pi$ plane. The surface projected states of BaAgBi along the (001) plane were calculated on a 20-layer surface slab model using a tight-binding Hamiltonian constructed from maximally localized Wannier functions. The Weyl nodal rings and the Dirac nodal lines both had a clear drumhead surface spectrum. Their spatial distributions and energy variations are very large, which can be beneficial for further experimental investigation.

DATA AVAILABILITY STATEMENT

The original contributions presented in the study are included in the article/supplementary material, further inquiries can be directed to the corresponding author.

AUTHOR CONTRIBUTIONS

YC: Software, methodology, and writing. SN, XW, and WZ: Reviewing and editing. All authors contributed to the article and approved the submitted version.

FUNDING

This research was funded by Jilin Province Department of Education grant number "JJKH2021561SK" and funded by Jilin Province Education and Science plan project grant number "GH20304." This research was supported by Wonkwang University in 2021.

REFERENCES

Bhattacharya, A., Bhardwaj, V., Mani, B. K., Dutt, J. K., and Chatterjee, R. (2021). Strain-tunable Triple point Fermions in Diamagnetic Rare-Earth Half-Heusler Alloys. *Sci. Rep.* 11 (1), 12029. doi:10.1038/s41598-021-90850-y

Bradlyn, B., Cano, J., Wang, Z., Vergniory, M. G., Felser, C., Cava, R. J., et al. (2016). Beyond Dirac and Weyl Fermions: Unconventional Quasiparticles in Conventional Crystals. *Science* 353 (6299), aaf5037. doi:10.1126/science.aaf5037

Bradlyn, B., Elcoro, L., Cano, J., Vergniory, M. G., Wang, Z., Felser, C., et al. (2017). Topological Quantum Chemistry. *Nature* 547 (7663), 298–305. doi:10.1038/nature23268

Burkov, A. A. (2016). Topological Semimetals. *Nat. Mater* 15 (11), 1145–1148. doi:10.1038/nmat4788

Bzdušek, T., Wu, Q., Rüegg, A., Sigrist, M., and Soluyanov, A. A. (2016). Nodal-chain Metals. *Nature* 538 (7623), 75–78. doi:10.1038/nature19099

Cano, J., Bradlyn, B., and Vergniory, M. G. (2019). Multifold Nodal Points in Magnetic Materials. *Apl Mater.* 7 (10), 101125. doi:10.1063/1.5124314

Chang, G., Xu, S.-Y., Zheng, H., Singh, B., Hsu, C.-H., Bian, G., et al. (2016a). Room-temperature Magnetic Topological Weyl Fermion and Nodal Line Semimetal States in Half-Metallic Heusler Co2TiX (X=Si, Ge, or Sn). *Sci. Rep.* 6 (1), 38839. doi:10.1038/srep38839

Chang, T.-R., Xu, S.-Y., Chang, G., Lee, C.-C., Huang, S.-M., Wang, B., et al. (2016b). Prediction of an Arc-Tunable Weyl Fermion Metallic State in MoxW1−xTe2. *Nat. Commun.* 7 (1), 10639. doi:10.1038/ncomms10639

Chen, C., Su, Z., Zhang, X., Chen, Z., and Sheng, X.-L. (2017). From Multiple Nodal Chain to Dirac/Weyl Semimetal and Topological Insulator in Ternary Hexagonal Materials. *J. Phys. Chem. C* 121 (51), 28587–28593. doi:10.1021/acs.jpcc.7b11075

Du, Y., Tang, F., Wang, D., Sheng, L., Kan, E.-j., Duan, C.-G., et al. (2017). CaTe: a New Topological Node-Line and Dirac Semimetal. *Npj Quant Mater.* 2 (1), 3. doi:10.1038/s41535-016-0005-4

Ernzerhof, M., and Scuseria, G. E. (1999). Assessment of the Perdew-Burke-Ernzerhof Exchange-Correlation Functional. *J. Chem. Phys.* 110 (11), 5029–5036. doi:10.1063/1.478401

Fu, B.-B., Yi, C.-J., Zhang, T.-T., Caputo, M., Ma, J.-Z., Gao, X., et al. (2019). Dirac Nodal Surfaces and Nodal Lines in ZrSiS. *Sci. Adv.* 5 (5), eaau6459. doi:10.1126/sciadv.aau6459

Galanakis, I., and Mavropoulos, P. (2007). Spin-polarization and Electronic Properties of Half-Metallic Heusler Alloys Calculated from First Principles. *J. Phys. Condens. Matter* 19 (31), 315213. doi:10.1088/0953-8984/19/31/315213

Gao, H., Venderbos, J. W. F., Kim, Y., and Rappe, A. M. (2019). Topological Semimetals from First Principles. *Annu. Rev. Mater. Res.* 49 (1), 153–183. doi:10.1146/annurev-matsci-070218-010049

Hafner, J. (2008). Ab-initiosimulations of Materials Using VASP: Density-Functional Theory and beyond. *J. Comput. Chem.* 29 (13), 2044–2078. doi:10.1002/jcc.21057

He, J., Ma, S., Lyu, P., and Nachtigall, P. (2016). Unusual Dirac Half-Metallicity with Intrinsic Ferromagnetism in Vanadium Trihalide Monolayers. *J. Mater. Chem. C* 4 (13), 2518–2526. doi:10.1039/C6TC00409A

He, T. L., Zhang, X. M., Liu, Y., Dai, X. F., and Liu, G. D. (2020). *Phys. Rev. B* 102, 075133. doi:10.1103/physrevb.102.075133

He, T., Zhang, X., Meng, W., Jin, L., Dai, X., and Liu, G. (2019). Topological Nodal Lines and Nodal Points in the Antiferromagnetic Material β-Fe2PO5. *J. Mater. Chem. C* 7 (40), 12657–12663. doi:10.1039/C9TC04046C

He, T., Zhang, X., Wang, L., Liu, Y., Dai, X., Wang, L., et al. (2021). Ideal Fully Spin-Polarized Type-II Nodal Line State in Half-Metals X2YZ4 (X=K, Cs, Rb, Y Cr, Cu, Z=Cl, F). *Mater. Today Phys.* 17, 100360. doi:10.1016/j.mtphys.2021.100360

Heikkilä, T. T., and Volovik, G. E. (2011). Dimensional Crossover in Topological Matter: Evolution of the Multiple Dirac point in the Layered System to the Flat Band on the Surface. *Jetp Lett.* 93 (2), 59–65. doi:10.1134/s002136401102007x

Hosen, M. M., Dhakal, G., Dimitri, K., Maldonado, P., Aperis, A., Kabir, F., et al. (2018). Discovery of Topological Nodal-Line Fermionic Phase in a Magnetic Material GdSbTe. *Sci. Rep.* 8 (1), 13283. doi:10.1038/s41598-018-31296-7

Huang, S.-M., Xu, S.-Y., Belopolski, I., Lee, C.-C., Chang, G., Wang, B., et al. (2015). A Weyl Fermion Semimetal with Surface Fermi Arcs in the Transition Metal Monopnictide TaAs Class. *Nat. Commun.* 6, 7373. doi:10.1038/ncomms8373

Jia, S., Xu, S.-Y., and Hasan, M. Z. (2016). Weyl Semimetals, Fermi Arcs and Chiral Anomalies. *Nat. Mater* 15 (11), 1140–1144. doi:10.1038/nmat4787

Jin, L., Zhang, X., Dai, X., Liu, H., Chen, G., and Liu, G. (2019a). Centrosymmetric Li2NaN: a superior Topological Electronic Material with Critical-type Triply Degenerate Nodal Points. *J. Mater. Chem. C* 7 (5), 1316–1320. doi:10.1039/C8TC05930F

Jin, L., Zhang, X., He, T., Meng, W., Dai, X., and Liu, G. (2019b). Topological Nodal Line State in Superconducting NaAlSi Compound. *J. Mater. Chem. C* 7 (34), 10694–10699. doi:10.1039/C9TC03464A

Jin, L., Zhang, X., Liu, Y., Dai, X., Shen, X., Wang, L., et al. (2020). Two-dimensional Weyl Nodal-Line Semimetal in a D0 Ferromagnetic K2N Monolayer with a High Curie Temperature. *Phys. Rev. B* 102, 125118. doi:10.1103/physrevb.102.125118

Kim, K., Seo, J., Lee, E., Ko, K.-T., Kim, B. S., Jang, B. G., et al. (2018). Large anomalous Hall current induced by topological nodal lines in a ferromagnetic van der Waals semimetal. *Nat. Mater* 17 (9), 794–799. doi:10.1038/s41563-018-0132-3

Li, Y., and Xia, J. (2020). Cubic Hafnium Nitride: A Novel Topological Semimetal Hosting a 0-Dimensional (0-D) Nodal Point and a 1-D Topological Nodal Ring. *Front. Chem.* 8, 727. doi:10.3389/fchem.2020.00727

Li, Y., Xia, J., and Srivastava, V. (2020). The Tetragonal Monoxide of Platinum: A New Platform for Investigating Nodal-Line and Nodal-Point Semimetallic Behavior. *Front. Chem.* 8, 704. doi:10.3389/fchem.2020.00704

Liu, Q.-B., Fu, H.-H., Xu, G., Yu, R., and Wu, R. (2019). Categories of Phononic Topological Weyl Open Nodal Lines and a Potential Material Candidate: Rb2Sn2O3. *J. Phys. Chem. Lett.* 10 (14), 4045–4050. doi:10.1021/acs.jpclett.9b01159

Meng, W., Zhang, X., He, T., Jin, L., Dai, X., Liu, Y., et al. (2020). Ternary Compound HfCuP: An Excellent Weyl Semimetal with the Coexistence of Type-I and Type-II Weyl Nodes. *J. Adv. Res.* 24, 523–528. doi:10.1016/j.jare.2020.05.026

Mostofi, A. A., Yates, J. R., Lee, Y.-S., Souza, I., Vanderbilt, D., and Marzari, N. (2008). wannier90: A Tool for Obtaining Maximally-Localised Wannier Functions. *Computer Phys. Commun.* 178 (9), 685–699. doi:10.1016/j.cpc.2007.11.016

Mostofi, A. A., Yates, J. R., Pizzi, G., Lee, Y.-S., Souza, I., Vanderbilt, D., et al. (2014). An Updated Version of Wannier90: A Tool for Obtaining Maximally-Localised Wannier Functions. *Computer Phys. Commun.* 185 (8), 2309–2310. doi:10.1016/j.cpc.2014.05.003

Payne, M. C., Teter, M. P., Allan, D. C., Arias, T. A., and Joannopoulos, J. D. (1992). Iterative Minimization Techniques Forab Initiototal-Energy Calculations: Molecular Dynamics and Conjugate Gradients. *Rev. Mod. Phys.* 64 (4), 1045–1097. doi:10.1103/RevModPhys.64.1045

Perdew, J. P., Burke, K., and Ernzerhof, M. (1996). Generalized Gradient Approximation Made Simple. *Phys. Rev. Lett.* 77 (18), 3865–3868. doi:10.1103/PhysRevLett.77.3865

Schoop, L. M., Pielnhofer, F., and Lotsch, B. V. (2018). Chemical Principles of Topological Semimetals. *Chem. Mater.* 30 (10), 3155–3176. doi:10.1021/acs.chemmater.7b05133

Sheng, X.-L., Yu, Z.-M., Yu, R., Weng, H., and Yang, S. A. (2017). d Orbital Topological Insulator and Semimetal in the Antifluorite Cu2S Family: Contrasting Spin Helicities, Nodal Box, and Hybrid Surface States. *J. Phys. Chem. Lett.* 8 (15), 3506–3511. doi:10.1021/acs.jpclett.7b01390

Soluyanov, A. A., Gresch, D., Wang, Z., Wu, Q., Troyer, M., Dai, X., et al. (2015). Type-II Weyl Semimetals. *Nature* 527 (7579), 495–498. doi:10.1038/nature15768

Takane, D., Nakayama, K., Souma, S., Wada, T., Okamoto, Y., Takenaka, K., et al. (2018). Observation of Dirac-like Energy Band and Ring-Torus Fermi Surface Associated with the Nodal Line in Topological Insulator CaAgAs. *Npj Quant Mater.* 3, 3. doi:10.1038/s41535-017-0074-z

Wang, L. R., Jin, L., Liu, G. D., Liu, Y., Dai, X. F., and Zhang, X. M. (2021a). *Appl. Mater. Today* 23, 10105. doi:10.1038/ncomms10556

Wang, Q., Xu, Y., Lou, R., Liu, Z., Li, M., Huang, Y., et al. (2018a). Large Intrinsic Anomalous Hall Effect in Half-Metallic Ferromagnet Co3Sn2S2 with Magnetic Weyl Fermions. *Nat. Commun.* 9 (1), 3681. doi:10.1038/s41467-018-06088-2

Wang, S.-S., Liu, Y., Yu, Z.-M., Sheng, X.-L., and Yang, S. A. (2017). Hourglass Dirac Chain Metal in Rhenium Dioxide. *Nat. Commun.* 8 (1), 1844. doi:10.1038/s41467-017-01986-3

Wang, V., Xu, N., Liu, J.-C., Tang, G., and Geng, W.-T. (2021b). VASPKIT: A User-Friendly Interface Facilitating High-Throughput Computing and Analysis Using VASP Code. *Computer Phys. Commun.* 267, 108033. doi:10.1016/j.cpc.2021.108033

Wang, X., Cheng, Z., Zhang, G., Kuang, M., Wang, X.-L., and Chen, H. (2020b). Strain Tuning of Closed Topological Nodal Lines and Opposite Pockets in Quasi-Two-Dimensional α-phase FeSi2. *Phys. Chem. Chem. Phys.* 22 (24), 13650–13658. doi:10.1039/D0CP02334E

Wang, X., Ding, G., Cheng, Z., Surucu, G., Wang, X.-L., and Yang, T. (2020c). Novel Topological Nodal Lines and Exotic Drum-head-like Surface States in Synthesized CsCl-type Binary alloy TiOs. *J. Adv. Res.* 22, 137–144. doi:10.1016/j.jare.2019.12.001

Wang, X., Ding, G., Cheng, Z., Surucu, G., Wang, X.-L., and Yang, T. (2020d). Rich Topological Nodal Line Bulk States Together with Drum-head-like Surface States in NaAlGe with Anti-PbFCl Type Structure. *J. Adv. Res.* 23, 95–100. doi:10.1016/j.jare.2020.01.017

Wang, X., Ding, G., Cheng, Z., Wang, X.-L., Zhang, G., and Yang, T. (2020e). Intersecting Nodal Rings in Orthorhombic-type BaLi2Sn Compound. *J. Mater. Chem. C* 8 (16), 5461–5466. doi:10.1039/D0TC00504E

Wang, X., Ding, G., Khandy, S. A., Cheng, Z., Zhang, G., Wang, X.-L., et al. (2020a). Unique Topological Nodal Line States and Associated Exceptional Thermoelectric Power Factor Platform in Nb3GeTe6 Monolayer and Bulk. *Nanoscale* 12 (32), 16910–16916. doi:10.1039/D0NR03704D

Wang, Y.-p., Li, S.-s., Zhang, C.-w., Zhang, S.-f., Ji, W.-x., Li, P., et al. (2018b). High-temperature Dirac Half-Metal PdCl3: a Promising Candidate for Realizing Quantum Anomalous Hall Effect. *J. Mater. Chem. C* 6 (38), 10284–10291. doi:10.1039/C8TC02500B

Wu, Q., Zhang, S., Song, H.-F., Troyer, M., and Soluyanov, A. A. (2018). WannierTools: An Open-Source Software Package for Novel Topological Materials. *Computer Phys. Commun.* 224, 405–416. doi:10.1016/j.cpc.2017.09.033

Wang, X., Ding, G., Cheng, Z., Yuan, H., Wang, X.-L., Yang, T., et al. (2019). R3c-type LnNiO3(Ln = La, Ce, Nd, Pm, Gd, Tb, Dy, Ho, Er, Lu) Half-Metals with Multiple Dirac Cones: a Potential Class of Advanced Spintronic Materials. *Int. Union Crystallogr. J.* 6(6), 990–995. doi:10.1107/S2052252519012570

Yan, B., and Felser, C. (2017). Topological Materials: Weyl Semimetals. *Annu. Rev. Condens. Matter Phys.* 8 (1), 337–354. doi:10.1146/annurev-conmatphys-031016-025458

Yang, T., Cheng, Z., Wang, X., and Wang, X.-L. (2021). Nodal Ring Spin Gapless Semiconductor: New Member of Spintronic Materials. *J. Adv. Res.* 28, 43–49. doi:10.1016/j.jare.2020.06.016

Yang, T., Ding, G., Cheng, Z., Wang, X., and Zhang, G. (2020). Diverse Topological States in a Ternary NdAsPd Compound. *J. Mater. Chem. C* 8 (23), 7741–7748. doi:10.1039/D0TC02024A

Yang, T., and Zhang, X. (2020). Nearly Flat Nodal Surface States in Pseudo-one-dimensional Molybdenum Monochalcogenides X(MoS)3 (X = K, Rb, and Cs). *J. Mater. Chem. C* 8 (26), 9046–9054. doi:10.1039/D0TC01978J

Yang, Y., Xia, J.-p., Sun, H.-x., Ge, Y., Jia, D., Yuan, S.-Q., et al. (2019). Observation of a Topological Nodal Surface and its Surface-State Arcs in an Artificial Acoustic crystal. *Nat. Commun.* 10 (1), 5185. doi:10.1038/s41467-019-13258-3

Yu, R., Fang, Z., Dai, X., and Weng, H. (2017). Topological Nodal Line Semimetals Predicted from First-Principles Calculations. *Front. Phys.* 12 (3). doi:10.1007/s11467-016-0630-1

Zhang, C., Jiao, Y., Kou, L., Liao, T., and Du, A. (2018a). Predicting Multiple Dirac-Cones and Ultrahigh Fermi Velocity in perovskite$R\bar{3}c$phase LaCuO3. *J. Mater. Chem. C* 6 (23), 6132–6137. doi:10.1039/C8TC00872H

Zhang, T.-T., Yu, Z.-M., Guo, W., Shi, D., Zhang, G., and Yao, Y. (2017a). From Type-II Triply Degenerate Nodal Points and Three-Band Nodal Rings to Type-II Dirac Points in Centrosymmetric Zirconium Oxide. *J. Phys. Chem. Lett.* 8 (23), 5792–5797. doi:10.1021/acs.jpclett.7b02642

Zhang, T., Jiang, Y., Song, Z., Huang, H., He, Y., Fang, Z., et al. (2019a). Catalogue of Topological Electronic Materials. *Nature* 566 (7745), 475–479. doi:10.1038/s41586-019-0944-6

Zhang, X., Fu, B., Jin, L., Dai, X., Liu, G., and Yao, Y. (2019b). Topological Nodal Line Electrides: Realization of an Ideal Nodal Line State Nearly Immune from Spin-Orbit Coupling. *J. Phys. Chem. C* 123 (42), 25871–25876. doi:10.1021/acs.jpcc.9b08446

Zhang, X., Jin, L., Dai, X., Chen, G., and Liu, G. (2018b). Ideal Inner Nodal Chain Semimetals in Li2XY (X = Ca, Ba; Y = Si, Ge) Materials. *J. Phys. Chem. Lett.* 9 (18), 5358–5363. doi:10.1021/acs.jpclett.8b02204

Zhang, X., Jin, L., Dai, X., and Liu, G. (2017b). Topological Type-II Nodal Line Semimetal and Dirac Semimetal State in Stable Kagome Compound Mg3Bi2. *J. Phys. Chem. Lett.* 8 (19), 4814–4819. doi:10.1021/acs.jpclett.7b02129

Zheng, B., Xia, B., Wang, R., Zhao, J., Chen, Z., Zhao, Y., et al. (2019). Tunable Ferromagnetic Weyl Fermions from a Hybrid Nodal Ring. *Npj Comput. Mater.* 5 (1), 74. doi:10.1038/s41524-019-0214-z

Zhou, F., Liu, Y., Kuang, M., Wang, P., Wang, J., Yang, T., et al. (2021). Time-reversal-breaking Weyl Nodal Lines in Two-Dimensional A3C2 (A = Ti, Zr, and Hf) Intrinsically Ferromagnetic Materials with High Curie Temperature. *Nanoscale* 13 (17), 8235–8241. doi:10.1039/D1NR00139F

Conflict of Interest: The authors declare that the research was conducted in the absence of any commercial or financial relationships that could be construed as a potential conflict of interest.

ORIGINAL RESEARCH
published: 12 November 2021
doi: 10.3389/fchem.2021.796695

Ab Initio Calculations for the Electronic, Interfacial and Optical Properties of Two-Dimensional AlN/Zr_2CO_2 Heterostructure

Kai Ren[1†], Ruxin Zheng[1†], Junbin Lou[2], Jin Yu[3], Qingyun Sun[1*] and Jianping Li[4*]

[1]School of Mechanical and Electronic Engineering, Nanjing Forestry University, Nanjing, China, [2]School of Information Science and Engineering, Jiaxing University, Jiaxing, China, [3]School of Materials Science and Engineering, Southeast University, Nanjing, China, [4]School of Automotive and Transportation Engineering, Shenzhen Polytechnic, Shenzhen, China

Edited by:
Zhaofu Zhang,
University of Cambridge,
United Kingdom

Reviewed by:
Chao Zhang,
Anhui University of Science and Technology, China
Huasong Qin,
Xi'an Jiaotong University, China

***Correspondence:**
Jianping Li
szyljp0170@szpt.edu.cn
Qingyun Sun
sunqingyun@njfu.edu.cn

†These authors have contributed equally to this work and share first authorship

Specialty section:
This article was submitted to Theoretical and Computational Chemistry,
a section of the journal Frontiers in Chemistry

Received: 17 October 2021
Accepted: 25 October 2021
Published: 12 November 2021

Citation:
Ren K, Zheng R, Lou J, Yu J, Sun Q and Li J (2021) Ab Initio Calculations for the Electronic, Interfacial and Optical Properties of Two-Dimensional AlN/Zr_2CO_2 Heterostructure.
Front. Chem. 9:796695.
doi: 10.3389/fchem.2021.796695

Recently, expanding the applications of two-dimensional (2D) materials by constructing van der Waals (vdW) heterostructures has become very popular. In this work, the structural, electronic and optical absorption performances of the heterostructure based on AlN and Zr_2CO_2 monolayers are studied by first-principles simulation. It is found that AlN/Zr_2CO_2 heterostructure is a semiconductor with a band gap of 1.790 eV. In the meanwhile, a type-I band structure is constructed in AlN/Zr_2CO_2 heterostructure, which can provide a potential application of light emitting devices. The electron transfer between AlN and Zr_2CO_2 monolayer is calculated as 0.1603 |e| in the heterostructure, and the potential of AlN/Zr_2CO_2 heterostructure decreased by 0.663 eV from AlN layer to Zr_2CO_2 layer. Beisdes, the AlN/Zr_2CO_2 vdW heterostructure possesses excellent light absorption ability of in visible light region. Our research provides a theoretical guidance for the designing of advanced functional heterostructures.

Keywords: first-principles calculation, AlN/Zr_2CO_2, type-I band alignment, applications, heterostructure

INTRODUCTION

In 2004, the graphene was prepared and discovered to possess abundant interesting performances (Geim and Novoselov, 2007), which has also encouraged researchers to explore other two-dimensional (2D) materials (Pumera and Sofer, 2017; Sun et al., 2020a; Wang et al., 2020a; Sun and Schwingenschlögl, 2020; Zhang et al., 2021a; Tan et al., 2021) different with bulk materials (Chen et al., 2021). These 2D materials have attracted much attentions because of their unique electronic (Qi et al., 2020), magnetic (Wang et al., 2020b), thermal (Xie et al., 2014; Qin et al., 2019a), mechanical (Qin and Liu, 2017) and optical properties (Wang et al., 2020c). For example, at room temperature, black phosphorus with a thickness of less than 7.5 nm can display transistor performance, and the leakage current modulation order is 10^5 (Li et al., 2014). Arsenene can adjust its band gap by applying external strain on the surface (Kamal and Ezawa, 2015). Based on transition-metal dichalcogenides (TMDs), PtS_2, the mobility of field effect transistors (FETs) has been proved to be at least 200 $cm^2/V{\cdot}s$ (Pi et al., 2019). All those desirable characteristics promise 2D materials in future advanced applications, such as, photocatalyst (Wang et al., 2019; Zhang et al., 2020a), metal-ion batteries (Sun and Schwingenschlögl, 2021a), and photoelectric devices (Zhang et al., 2020b; Lou et al., 2021).

Recently, in order to further extend the performance and application range of these 2D materials, the prediction of new 2D materials (Sun et al., 2020b; Ding et al., 2020; Sun and Schwingenschlögl,

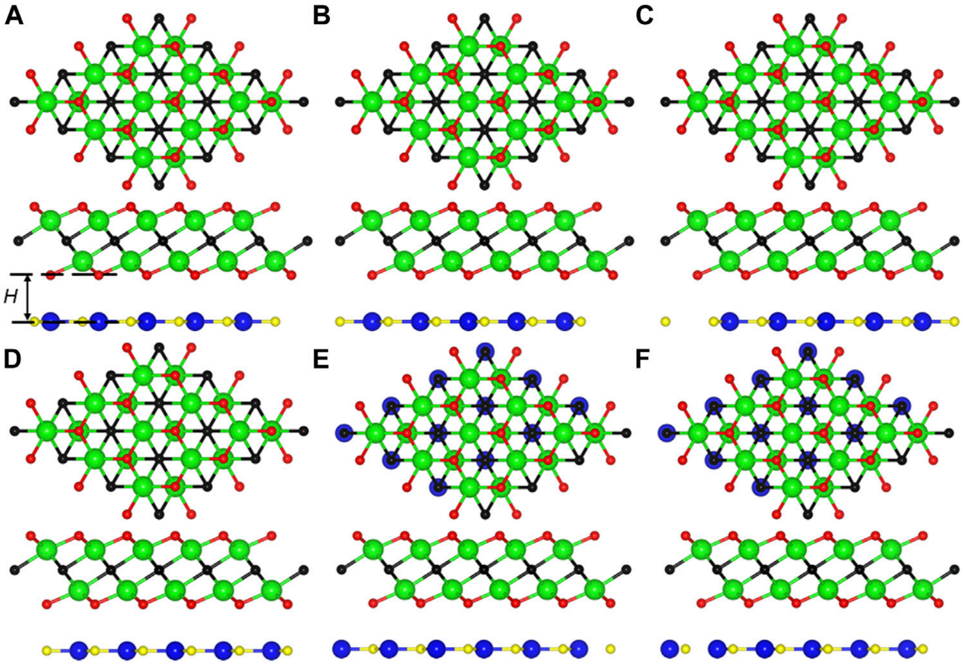

FIGURE 1 | The top and side views of the **(A)** AO-1, **(B)** AO-2, **(C)** AO-3, **(D)** AO-4, **(E)** AO-5, **(F)** AO-6 stacking configurations for the AlN/Zr_2CO_2 heterostructure, the blue, yellow, cyan, black and red balls represent the Al, N, Zr, C, and O atoms, respectively.

2021b; Zhang et al., 2021b; Sun et al., 2021) and the modification of known 2D materials have become more and more exciting (Liu et al., 2019; Sun et al., 2019; Zhang et al., 2020c; Wang et al., 2021; Zheng et al., 2021). In many modification methods, two different materials are usually combined as a heterostructure by horizontal (Qin et al., 2019b; Ren et al., 2020a) or vertical direction [(Wang et al., 2020d), (Wang et al., 2020c)]. In particular, the vertical heterostructure is constructed by weak van der Waals (vdW) force at the interface instead of covalent bond, which can result tremendous and novel performances. For example, the type-II heterostructure possesses staggered band alignment, which has ability to separate the photogenerated electrons and holes, revealing a promising application as photocatalyst. It also has been proved by some theoretical and experimental investigations, such as TMDs/BP (Ren et al., 2019a), *h*-BN/C_2N (Wang et al., 2020e), TMDs/$Mg(OH)_2$ (Luo et al., 2019) etc. The type-I band structure in heterostructure can make the charge transfer from wide band gap materials to narrow band gap materials, which can be pretty reflected in light-emitting devices such as LEDs (Bellus et al., 2017; Ren et al., 2021b). Interestingly, the band structure of black/red phosphorus heterostructure can be transformed from type-I to Z-scheme system by quantum confinement effect (Shi et al., 2019). TMDs based heterostructure, such as $MoTe_2/WSe_2$, has excellent photoluminescence (about 1.1 eV from $MoTe_2$), which provides promising optoelectronic applications (Yamaoka et al., 2018). Furthermore, type-I heterostructure also can be used as a photocatalyst for water splitting because of remarkable light absorption characteristics (Do et al., 2020; Zhu et al., 2021a). More recently, 2D aluminum nitride (AlN) has attracted significant focus because of novel electronic (Zhang, 2012) and magnetic (Zhang and Zheng, 2011) performances, which also can be tuned by doping (Bai et al., 2015). Besides, some heterostructure constructed by AlN also have been studied, such as BiSb/AlN (Singh and Romero, 2017) and AlN/BP (Yang et al., 2017) etc. Importantly, it has been reported that the AlN films can be prepared on 6H–SiC substrates by various sputtering pressures by RF reactive magnetron sputtering (Kuang et al., 2012) and the AlN nanowires was also has been synthetized (Xu et al., 2003), which demonstrated the preparation method for AlN monolayer. At the same time, the Zr_2CO_2 as a MXene materials has been studied extensively to form vdW heterostructure (Zhu et al., 2021b). InSe/Zr_2CO_2 heterostructure possesses unique electron mobility (about 10^4 $cm^2/V{\cdot}s$) as a photocatalyst (He et al., 2019). MoS_2/Zr_2CO_2 heterostructure also has decent band edge positions for the redox reaction of the water splitting (Xu et al., 2020). Interestingly, Zr_2CO_2/blue phosphorene heterostructure has a transformable band structure between type-I and type-II under external strain (Guo et al., 2017). Moreover, the MXene also can be prepared by suitable means (Lei et al., 2015). Therefore, both AlN and MXene possess possibility of preparation, which also show the future synthetic work on AlN/MXene heterostructure. And the investigations about the heterostructure based on AlN and Zr_2CO_2 monolayer are rare, it is excited to explore the novel properties and the potential application of the AlN/Zr_2CO_2 heterostructure.

In this work, the AlN and Zr_2CO_2 are selected to build a heterostructure. Using first-principle theoretical calculation methods, the structural and electronic natures of the AlN/Zr_2CO_2 heterostructure are addressed, which shows that the type-I band alignment in AlN/Zr_2CO_2 heterostructure gives a potential usage of light-emitting devices. Then, the interfacial performances of the heterostructure are calculated by charge density and potential drop. Finally, the light absorption capacity of the AlN/Zr_2CO_2 heterostructure is explored.

Computing Method

In this simulations work, the calculations were performed by first-principles method using density functional theory by the circumstances of Vienna ab initio simulation package (Kresse and Furthmüller, 1996a; Kresse and Furthmüller, 1996b; Capelle, 2006). The generalized gradient approximation and the projector augmented wave potentials were considered to explain the exchange correlation functional (Kresse and Joubert, 1999; Grimme, 2006). Besides, the DFT-D3 method was conducted using Grimme to demonstrate the weak disperson forces (Grimme et al., 2010). Furthermore, the Heyd–Scuseria–Ernzerhof hybrid method was used for decent electronic and optical results of the studied system (Heyd et al., 2005). Moreover, the energy cut-off was 500 eV. The Monkhorst–Pack *k*-point grids was 15 × 15 × 1 and the vacuum space was set as 25 Å, which can efficiently prevent the interaction of nearby layers. The convergence standard for force and energy were limited in 0.01 $eV·Å^{-1}$ and smaller than 0.01 meV, respectively.

RESULTS AND DISCUSSION

First, the AlN/Zr_2CO_2 is optimized by a decent lattice constant of 3.365 Å, which is comparable with of the AlN (3.127 Å) (Ren et al., 2020b) and Zr_2CO_2 (3.294 Å) (Guo et al., 2017) monolayers. When monolayered AlN and Zr_2CO_2 are combined to form the heterostructure, considering that there are various combination modes of AlN and Zr_2CO_2 monolayers, we only select the most representative highly symmetrical combination configurations among them. These six combination styles of AlN/Zr_2CO_2 heterostructure are shown as **Figures 1A–F**, named AO-1 to AO-6, respectively. For AO-1, the N and Al atoms are located on the upper O and upper Zr atoms, respectively. The AO-2 is obtained by putting the N and Al atoms on the C and lower O atoms, respectively. The AO-3 is built by locating the N and Al atoms on the C and lower Zr atoms, respectively. Then, fixing the N and Al atoms on the lower O and lower Zr atoms, respectively, can construct the AlN/Zr_2CO_2 heterostructure by AO-4 configuration. Differently, locating the N and Al atoms on the lower O and C atoms, respectively, can build the AO-5 configuration. Furthermore, AO-6 configuration is constructed by fixing the N and Al atoms on upper O and C atoms, respectively. Besides, the most stable stacking configuration of the AlN/Zr_2CO_2 heterostructure is decided by the binding energy, represented by E_b as follow:

TABLE 1 | The optimized distance of interface (*H*, Å) and the bond length (*L*, Å) of the AlN/Zr_2CO_2 heterostructure with different stacking styles.

	H	$L_{Al–N}$	$L_{Zr–C}$	$L_{Zr–O}$
AO-1	1.909	1.943	2.388	2.110
AO-2	2.231	1.945	2.373	2.139
AO-3	3.235	1.943	2.387	2.137
AO-4	3.626	1.943	2.387	2.136
AO-5	3.475	1.943	2.387	2.137
AO-6	2.710	1.943	2.387	2.131

$$E_b = E_{AlN/ZrCO2} - E_{AlN} - E_{Zr2CO2} \tag{1}$$

where $E_{AlN/Zr2CO2}$, E_{AlN} and E_{Zr2CO2} are showing the total energy of the AlN/Zr_2CO_2 system, original AlN and Zr_2CO_2 monolayers, respectively. Furthermore, the calculation demonstrations that the stacked structure in **Figure 1A** is the most stable heterostructure with binding energy of −36.05 $meV/Å^2$, which also proves that the single-layer AlN and Zr_2CO_2 are constructed by vdW force (Chen et al., 2013). In addition, the distance of interface and the bond length of these different stacking configurations of the optimized AlN/Zr_2CO_2 heterostructure are calculated in **Table 1**. Moreover, the following discussion in this work is based on the most stable stacking structure of AO-1.

The projected band energy of AlN/Zr_2CO_2 vdW heterostructure is obtained by HSE06 calculation, as shown in **Figure 2A**. One can clearly find that AlN/Zr_2CO_2 has a semiconductor nature with indirect band gap of 1.790 eV. In addition, the red and black marks are contributed from AlN and Zr_2CO_2 monolayers, respectively, suggesting that the (conduction band minimum) CBM and (the valence band maximum) VBM of AlN/Zr_2CO_2 vdW heterostructure are mainly resulted by Zr_2CO_2 monolayer. Thus, a type-I band structure is constructed in AlN/Zr_2CO_2 vdW heterostructure. Besides, the partial density of AlN/Zr_2CO_2 vdW heterostructure, as shown in **Figures 2B, 2is** also obtained to further prove the characteristics of intrinsic type-I band structure. It is obvious that the CBM and the VBM of the AlN/Zr_2CO_2 vdW heterostructure are mainly donated by Zr and O atoms, respectively.

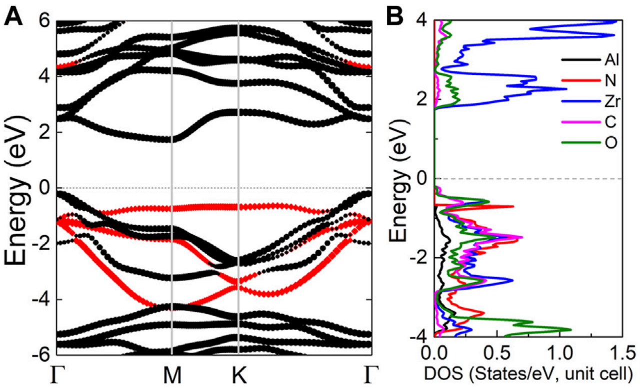

FIGURE 2 | (A) The projected band structure and **(B)** the partial density of states of the AlN/Zr_2CO_2 vdW heterostructure, the Fermi level is expressed by 0 shown as dash line.

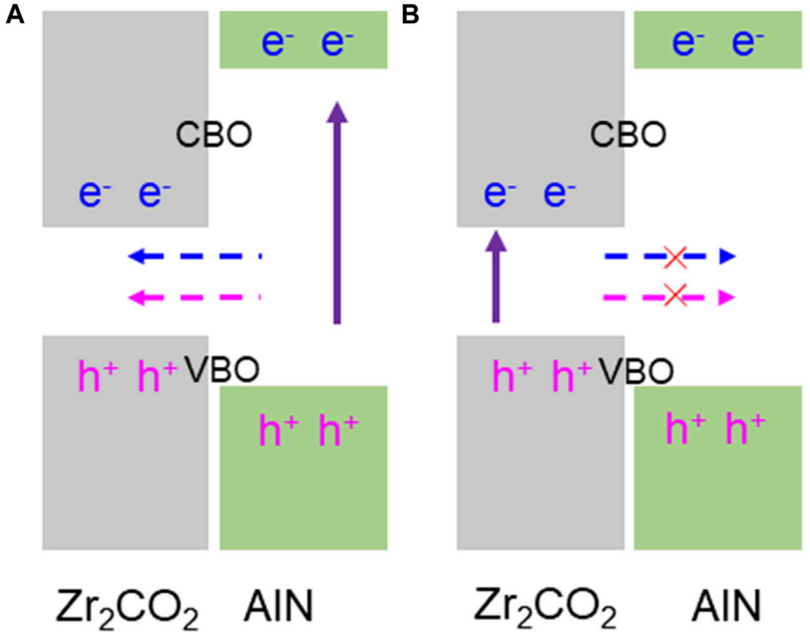

FIGURE 3 | Band alignment schematic of the excited charge transfer mode of the AlN/Zr_2CO_2 vdW heterostructure: **(A)** feasible and **(B)** limited charge migration mode.

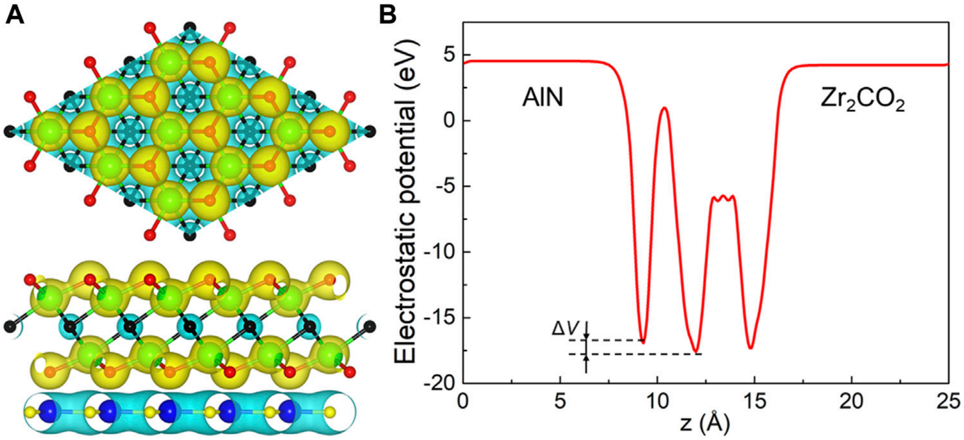

FIGURE 4 | (A) The charge density difference and the **(B)** potential drop of the AlN/Zr_2CO_2 vdW heterostructure. The yellow and cyan regions contribute the gaining and losing of electrons, respectively.

Such type-I band structure in the AlN/Zr_2CO_2 vdW heterostructure provides some important advanced applications in nano-devices. In AlN/Zr_2CO_2 vdW heterostructure, as shown in **Figure 3A**, CBM and VBM of AlN/Zr_2CO_2 vdW heterostructure are contributed by single-layer Zr_2CO_2, and the band gap of single-layer Zr_2CO_2 is less than that of single-layer AlN. When AlN/Zr_2CO_2 vdW heterostructure is excited by some external conditions, the electrons in the broad-band gap AlN monolayer are inspired and transferred to the CBM, generating holes at the VBM. It is worth noting that under the action of conduction band offset, CBO (valence band offset, VBO), electrons (holes) at the CBM (VBM) of the AlN layer can be transferred to the CBM (VBM) of the Zr_2CO_2 layer. Besides, the obtained CBO and VBO in AlN/Zr_2CO_2 vdW heterostructure are 2.432 and 0.471 eV respectively. While the electrons and holes excited in the relatively narrow-band gap of Zr_2CO_2 layer cannot be transferred to AlN layer due to low energy, in **Figure 3B**, which explains the AlN/Zr_2CO_2 vdW heterostructure can be considered as a potential light-emitting device material.

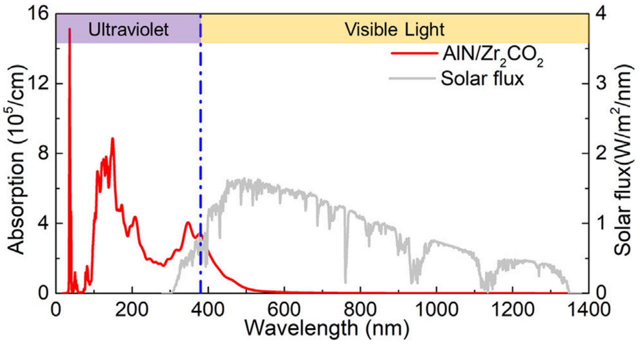

FIGURE 5 | The light absorption spectrum of the AlN/Zr$_2$CO$_2$ vdW heterostructure.

Then, we discussed the interface properties of AlN/Zr$_2$CO$_2$ vdW heterostructure by the charge density difference ($\Delta\rho$) and the potential drop (ΔV) in the interface. The charge density difference across the interface of the AlN/Zr$_2$CO$_2$ vdW heterostructure is calculated by:

$$\Delta\rho = \rho_{\mathrm{AlN/Zr2CO2}} - \rho_{\mathrm{AlN}} - \rho_{\mathrm{Zr2CO2}}, \tag{2}$$

where $\rho_{\mathrm{AlN/Zr2CO2}}$, ρ_{AlN} and ρ_{Zr2CO2} represent the charge density of the AlN/Zr$_2$CO$_2$ vdW heterostructure, monolayered AlN and Zr$_2$CO$_2$, respectively. Demonstrated by **Figure 4A**, the Zr$_2$CO$_2$ layer acts as an electron acceptor and AlN is an electron donor layer. Through Bader charge analysis (Tang et al., 2009), the obtained charge transfer from AlN layer to Zr$_2$CO$_2$ layer is 0.1603 $|e|$ in AlN/Zr$_2$CO$_2$ vdW heterostructure. Importantly, there is a certain degree of potential drop across the interface of the AlN/Zr$_2$CO$_2$ vdW heterostructure, shown as **Figure 4B**, and the calculated potential drop of 0.663 eV also play a critical role to assist the migration of the excited electrons and holes between the AlN/Zr$_2$CO$_2$ vdW heterostructure (Wang et al., 2018).

In order to produce more efficient light-emitting device, active materials should be able to effectively absorb light in the visible and near-infrared regions, especially type-I heterostructure. Therefore, we investigated the light absorption performance of AlN/Zr$_2$CO$_2$ vdW heterostructure by the calculation:

$$\alpha(\omega) = \frac{\sqrt{2}\omega}{c}\left\{\left[\varepsilon_1^2(\omega) + \varepsilon_2^2(\omega)\right]^{1/2} - \varepsilon_1(\omega)\right\}^{1/2}, \tag{3}$$

where ω is the angular frequency; α shows absorption coefficient and c is the speed of light. Besides, $\varepsilon_1(\omega)$ is used to explain the dielectric constant for real parts, which the imaginary one is demonstrated by $\varepsilon_2(\omega)$. As shown in **Figure 5** (the data source of solar flux is obtained from NREL website), AlN/Zr$_2$CO$_2$ vdW heterostructure demonstrates capacity to absorb sunlight over a wide range in the visible region the AlN/Zr$_2$CO$_2$ vdW heterostructure possesses a lot of absorption peaks. In ultraviolet region (left side of blue dotted line), the AlN/Zr$_2$CO$_2$ vdW heterostructure exhibits an absorption peak of 3.97×10^5 cm^{-1}at the wavelength as 344 nm. In the in the visible region (right side of blue dotted line), the obtained absorption peak is 3.14×10^5 cm^{-1} locating at the wavelength of 369 nm, which is higher than other studied 2D heterostructures, such as WS$_2$/GeC (2.651×10^5 cm^{-1}) (Ren et al., 2021a), Arsenene/GaS (1.403×10^5 cm^{-1}) (Li et al., 2021), g-GaN/BSe (1.470×10^5 cm^{-1}) (Ren et al., 2019c) etc. The calculated results demonstrate the AlN/Zr$_2$CO$_2$ vdW heterostructure possesses excellent light absorption capacity.

CONCLUSION

In conclusion, the AlN and Zr$_2$CO$_2$ monolayers are constructed by vdW force to form a heterostructure. And the most stable AlN/Zr$_2$CO$_2$ is decided by the lowest binding energy of about –36.05 meV/Å^2. The, the HSE06 obtained projected band structure shows the AlN/Zr$_2$CO$_2$ vdW heterostructure possesses semiconductor nature with a band gap of 1.790 eV, and presents a type-I energy band alignment, which is a satisfaction candidate for light-emitting devices. Furthermore, the interface characteristics of AlN/Zr$_2$CO$_2$ vdW heterostructure is investigated by charge density difference (0.1603$|e|$ from AlN layer to Zr$_2$CO$_2$ layer) and potential drop (0.663 eV). Moreover, the AlN/Zr$_2$CO$_2$ vdW heterostructure explains a remarkable light absorption performance, which can further offer excellent technical guidance for nano light-emitting device materials.

DATA AVAILABILITY STATEMENT

The raw data supporting the conclusions of this article will be made available by the authors, without undue reservation.

AUTHOR CONTRIBUTIONS

All authors listed have made a substantial, direct, and intellectual contribution to the work and approved it for publication.

FUNDING

This investigation was supported by the Open Fund Project of Maanshan Engineering Technology, Research Center of Advanced Design for Automotive Stamping Dies (Grant number: QMSG202105).

ACKNOWLEDGMENTS

KR thanks the potential help by Xiaoqian Xu.

REFERENCES

Bai, Y., Deng, K., and Kan, E. (2015). Electronic and Magnetic Properties of an AlN Monolayer Doped with First-Row Elements: a First-Principles Study. *RSC Adv.* 5, 18352–18358. doi:10.1039/c4ra13522a

Bellus, M. Z., Li, M., Lane, S. D., Ceballos, F., Cui, Q., Zeng, X. C., et al. (2017). Type-I van der Waals heterostructure formed by MoS_2 and ReS_2 monolayers. *Nanoscale Horiz.* 2, 31–36. doi:10.1039/c6nh00144k

Capelle, K. (2006). A Bird's-Eye View of Density-Functional Theory. *Braz. J. Phys.* 36, 1318–1343. doi:10.1590/s0103-97332006000700035

Chen, M., Lu, Y., Wang, Z., Lan, H., Sun, G., and Ni, Z. (2021). Melt Pool Evolution on Inclined NV E690 Steel Plates during Laser Direct Metal Deposition. *Opt. Laser Techn.* 136, 106745. doi:10.1016/j.optlastec.2020.106745

Chen, X., Tian, F., Persson, C., Duan, W., and Chen, N.-x. (2013). Interlayer Interactions in Graphites. *Sci. Rep.* 3, 3046. doi:10.1038/srep03046

Ding, X.-Y., Zhang, C., Wang, D.-Q., Li, B.-S., Wang, Q., Yu, Z. G., et al. (2020). A New Carbon Allotrope:T_5-Carbon. *Scripta Materialia* 189, 72–77. doi:10.1016/j.scriptamat.2020.08.004

Do, T.-N., Idrees, M., Binh, N. T. T., Phuc, H. V., Hieu, N. N., Hoa, L. T., et al. (2020). Type-I band alignment of BX-ZnO (X = As, P) van der as high-efficiency water splitting photocatalysts: a first-principles study. *RSC Adv.* 10, 44545–44550. doi:10.1039/d0ra09701b

Geim, A. K., and Novoselov, K. S. (2007). The Rise of Graphene. *Nat. Mater* 6, 183–191. doi:10.1038/nmat1849

Grimme, S., Antony, J., Ehrlich, S., and Krieg, H. (2010). A Consistent and Accurate Ab Initio Parametrization of Density Functional Dispersion Correction (DFT-D) for the 94 Elements H-Pu. *J. Chem. Phys.* 132, 154104. doi:10.1063/1.3382344

Grimme, S. (2006). Semiempirical GGA-type Density Functional Constructed with a Long-Range Dispersion Correction. *J. Comput. Chem.* 27, 1787–1799. doi:10.1002/jcc.20495

Guo, Z., Miao, N., Zhou, J., Sa, B., and Sun, Z. (2017). Strain-mediated type-I/type-II transition in MXene/Blue phosphorene van der Waals heterostructures for flexible optical/electronic devices. *J. Mater. Chem. C* 5, 978–984. doi:10.1039/c6tc04349f

He, Y., Zhang, M., Shi, J.-j., Cen, Y.-l., and Wu, M. (2019). Improvement of Visible-Light Photocatalytic Efficiency in a Novel InSe/Zr_2CO_2 Heterostructure for Overall Water Splitting. *J. Phys. Chem. C* 123, 12781–12790. doi:10.1021/acs.jpcc.9b01175

Heyd, J., Peralta, J. E., Scuseria, G. E., and Martin, R. L. (2005). Energy Band Gaps and Lattice Parameters Evaluated with the Heyd-Scuseria-Ernzerhof Screened Hybrid Functional. *J. Chem. Phys.* 123, 174101. doi:10.1063/1.2085170

Kamal, C., and Ezawa, M. (2015). Arsenene: Two-Dimensional Buckled and Puckered Honeycomb Arsenic Systems. *Phys. Rev. B* 91, 085423. doi:10.1103/physrevb.91.085423

Kresse, G., and Furthmüller, J. (1996). Efficiency of Ab-Initio Total Energy Calculations for Metals and Semiconductors Using a Plane-Wave Basis Set. *Comput. Mater. Sci.* 6, 15–50. doi:10.1016/0927-0256(96)00008-0

Kresse, G., and Furthmüller, J. (1996). Efficient Iterative Schemes Forab Initiototal-Energy Calculations Using a Plane-Wave Basis Set. *Phys. Rev. B* 54, 11169–11186. doi:10.1103/physrevb.54.11169

Kresse, G., and Joubert, D. (1999). From Ultrasoft Pseudopotentials to the Projector Augmented-Wave Method. *Phys. Rev. B* 59, 1758–1775. doi:10.1103/physrevb.59.1758

Kuang, X.-P., Zhang, H.-Y., Wang, G.-G., Cui, L., Zhu, C., Jin, L., et al. (2012). AlN Films Prepared on 6H-SiC Substrates under Various Sputtering Pressures by RF Reactive Magnetron Sputtering. *Appl. Surf. Sci.* 263, 62–68. doi:10.1016/j.apsusc.2012.08.121

Lei, J.-C., Zhang, X., and Zhou, Z. (2015). Recent Advances in MXene: Preparation, Properties, and Applications. *Front. Phys.* 10, 276–286. doi:10.1007/s11467-015-0493-x

Li, J., Huang, Z., Ke, W., Yu, J., Ren, K., and Dong, Z. (2021). High solar-to-hydrogen efficiency in Arsenene/GaX (X = S, Se) van der Waals heterostructure for photocatalytic water splitting. *J. Alloy. Compound.* 866. doi:10.1016/j.jallcom.2021.158774

Li, L., Yu, Y., Ye, G. J., Ge, Q., Ou, X., Wu, H., et al. (2014). Black Phosphorus Field-Effect Transistors. *Nat. Nanotech* 9, 372–377. doi:10.1038/nnano.2014.35

Liu, X., Zhang, Z., Luo, Z., Lv, B., and Ding, Z. (2019). Tunable Electronic Properties of Graphene/g-AlN Heterostructure: The Effect of Vacancy and Strain Engineering. *Nanomaterials* 9, 1674. doi:10.3390/nano9121674

Lou, J., Ren, K., Huang, Z., Huo, W., Zhu, Z., and Yu, J. (2021). Electronic and Optical Properties of Two-Dimensional Heterostructures Based on Janus XSSe (X = Mo, W) and $Mg(OH)_2$: a First Principles Investigation. *RSC Adv.* 11, 29576–29584. doi:10.1039/d1ra05521f

Luo, Y., Wang, S., Ren, K., Chou, J.-P., Yu, J., Sun, Z., et al. (2019). Transition-metal dichalcogenides/$Mg(OH)_2$ van der Waals heterostructures as promising water-splitting photocatalysts: a first-principles study. *Phys. Chem. Chem. Phys.* 21, 1791–1796. doi:10.1039/c8cp06960c

Pi, L., Li, L., Liu, K., Zhang, Q., Li, H., and Zhai, T. (2019). Recent Progress on 2D Noble-Transition-Metal Dichalcogenides. *Adv. Funct. Mater.* 29, 1904932. doi:10.1002/adfm.201904932

Pumera, M., and Sofer, Z. (2017). 2D Monoelemental Arsenene, Antimonene, and Bismuthene: Beyond Black Phosphorus. *Adv. Mater.* 29, 1605299. doi:10.1002/adma.201605299

Qi, K., Xing, X., Zada, A., Li, M., Wang, Q., Liu, S.-y., et al. (2020). Transition Metal Doped ZnO Nanoparticles with Enhanced Photocatalytic and Antibacterial Performances: Experimental and DFT Studies. *Ceramics Int.* 46, 1494–1502. doi:10.1016/j.ceramint.2019.09.116

Qin, H., and Liu, Y. (2017). Interlayer Shear Behaviors of Graphene-Carbon Nanotube Network. *J. Appl. Phys.* 122, 125108. doi:10.1063/1.4992025

Qin, H., Pei, Q.-X., Liu, Y., and Zhang, Y.-W. (2019). The Mechanical and thermal Properties of MoS_2-WSe_2 Lateral Heterostructures. *Phys. Chem. Chem. Phys.* 21, 15845–15853. doi:10.1039/c9cp02499a

Qin, H., Pei, Q.-X., Liu, Y., and Zhang, Y.-W. (2019). Thermal Transport in Graphene-Based Layered Materials: An Analytical Model Validated with Extensive Molecular Dynamics Simulations. *Carbon* 155, 114–121. doi:10.1016/j.carbon.2019.08.062

Ren, K., Liu, X., Chen, S., Cheng, Y., Tang, W., and Zhang, G. (2020). Remarkable Reduction of Interfacial Thermal Resistance in Nanophononic Heterostructures. *Adv. Funct. Mater.* 30, 2004003. doi:10.1002/adfm.202004003

Ren, K., Luo, Y., Wang, S., Chou, J.-P., Yu, J., Tang, W., et al. (2019). A van der Waals Heterostructure Based on Graphene-like Gallium Nitride and Boron Selenide: A High-Efficiency Photocatalyst for Water Splitting. *ACS Omega* 4, 21689–21697. doi:10.1021/acsomega.9b02143

Ren, K., Shu, H., Huo, W., Cui, Z., Yu, J., and Xu, Y. (2021a). Mechanical, Electronic and Optical Properties of Novel B_2P_6 Monolayer: Ultrahigh Carrier Mobility and Strong Optical Absorption. *Phys. Chem. Chem. Phys.*. doi:10.1039/D1CP03838A

Ren, K., Sun, M., Luo, Y., Wang, S., Yu, J., and Tang, W. (2019). First-principle Study of Electronic and Optical Properties of Two-Dimensional Materials-Based Heterostructures Based on Transition Metal Dichalcogenides and boron Phosphide. *Appl. Surf. Sci.* 476, 70–75. doi:10.1016/j.apsusc.2019.01.005

Ren, K., Wang, S., Luo, Y., Chou, J.-P., Yu, J., Tang, W., et al. (2020). High-efficiency photocatalyst for water splitting: a Janus MoSSe/XN (X = Ga, Al) van der Waals heterostructure. *J. Phys. D: Appl. Phys.* 53, 185504. doi:10.1088/1361-6463/ab71ad

Ren, K., Zheng, R., Xu, P., Cheng, D., Huo, W., Yu, J., et al. (2021b). Electronic and Optical Properties of Atomic-Scale Heterostructure Based on MXene and MN (M = Al, Ga): A DFT Investigation. *Nanomaterials* 11, 2236. doi:10.3390/nano11092236

Shi, R., Liu, F., Wang, Z., Weng, Y., and Chen, Y. (2019). Black/red Phosphorus Quantum Dots for Photocatalytic Water Splitting: from a Type I Heterostructure to a Z-Scheme System. *Chem. Commun.* 55, 12531–12534. doi:10.1039/c9cc06146k

Singh, S., and Romero, A. H. (2017). Giant Tunable Rashba Spin Splitting in a Two-Dimensional BiSb Monolayer and in BiSb/AlN Heterostructures. *Phys. Rev. B* 95, 165444. doi:10.1103/physrevb.95.165444

Sun, M., Chou, J.-P., Hu, A., and Schwingenschlögl, U. (2019). Point Defects in Blue Phosphorene. *Chem. Mater.* 31, 8129–8135. doi:10.1021/acs.chemmater.9b02871

Sun, M., Luo, Y., Yan, Y., and Schwingenschlögl, U. (2021). Ultrahigh Carrier Mobility in the Two-Dimensional Semiconductors B8Si4, B8Ge4, and B8Sn4. *Chem. Mater.* 33, 6475–6483. doi:10.1021/acs.chemmater.1c01824

Sun, M., and Schwingenschlögl, U. (2020). B_2P_6: A Two-Dimensional Anisotropic Janus Material with Potential in Photocatalytic Water Splitting and Metal-Ion Batteries. *Chem. Mater.* 32, 4795–4800. doi:10.1021/acs.chemmater.0c01536

Sun, M., and Schwingenschlögl, U. (2021). Structure Prototype Outperforming MXenes in Stability and Performance in Metal-Ion Batteries: A High Throughput Study. *Adv. Energ. Mater.* 11, 2003633. doi:10.1002/aenm.202003633

Sun, M., and Schwingenschlögl, U. (2021). Unique Omnidirectional Negative Poisson's Ratio in δ-Phase Carbon Monochalcogenides. *J. Phys. Chem. C* 125, 4133–4138. doi:10.1021/acs.jpcc.0c11555

Sun, M., Schwingenschlögl, U., and δ-, C. S. (2020). A Direct-Band-Gap Semiconductor Combining Auxeticity, Ferroelasticity, and Potential for High-Efficiency Solar Cells. *Phys. Rev. Appl.* 14, 044015. doi:10.1103/physrevapplied.14.044015

Sun, M., Yan, Y., and Schwingenschlögl, U. (2020). Beryllene: A Promising Anode Material for Na- and K-Ion Batteries with Ultrafast Charge/Discharge and High Specific Capacity. *J. Phys. Chem. Lett.* 11, 9051–9056. doi:10.1021/acs.jpclett.0c02426

Tan, Z.-L., Wei, J.-X., Liu, Y., Rehman, W., Hou, L.-R., and Yuan, C.-Z. (2021). V_2CT_x MXene and its Derivatives: Synthesis and Recent Progress in Electrochemical Energy Storage Applications. *Rare Met.*, 1–23.

Tang, W., Sanville, E., and Henkelman, G. (2009). A Grid-Based Bader Analysis Algorithm without Lattice Bias. *J. Phys. Condens. Matter* 21, 084204. doi:10.1088/0953-8984/21/8/084204

Wang, B., Wang, X., Wang, P., Yang, T., Yuan, H., Wang, G., et al. (2019). Bilayer $MoSe_2/HfS_2$ Nanocomposite as a Potential Visible-Light-Driven Z-Scheme Photocatalyst. *Nanomaterials* 9, 1706. doi:10.3390/nano9121706

Wang, G., Gong, L., Li, Z., Wang, B., Zhang, W., Yuan, B., et al. (2020). A Two-Dimensional CdO/CdS Heterostructure Used for Visible Light Photocatalysis. *Phys. Chem. Chem. Phys.* 22, 9587–9592. doi:10.1039/d0cp00876a

Wang, G., Li, Z., Wu, W., Guo, H., Chen, C., Yuan, H., et al. (2020). A Two-Dimensional h-BN/C_2N Heterostructure as a Promising Metal-free Photocatalyst for Overall Water-Splitting. *Phys. Chem. Chem. Phys.* 22, 24446–24454. doi:10.1039/d0cp03925j

Wang, G., Tang, W., Geng, L., Li, Y., Wang, B., Chang, J., et al. (2020). Rotation Tunable Photocatalytic Properties of ZnO/GaN Heterostructures. *Phys. Status Solidi B* 257, 1900663. doi:10.1002/pssb.201900663

Wang, G., Zhang, L., Li, Y., Zhao, W., Kuang, A., Li, Y., et al. (2020). Biaxial Strain Tunable Photocatalytic Properties of 2D ZnO/GeC Heterostructure. *J. Phys. D: Appl. Phys.* 53, 015104. doi:10.1088/1361-6463/ab440e

Wang, K., Ren, K., Cheng, Y., Zhang, M., Wang, H., and Zhang, G. (2020). Effects of Molecular Adsorption on the Spin-Wave Spectrum and Magnon Relaxation in Two-Dimensional $Cr_2Ge_2Te_6$. *Phys. Chem. Chem. Phys.* 22, 22047–22054. doi:10.1039/d0cp03884a

Wang, S., Tian, H., Ren, C., Yu, J., and Sun, M. (2018). Electronic and Optical Properties of Heterostructures Based on Transition Metal Dichalcogenides and Graphene-like Zinc Oxide. *Sci. Rep.* 8, 12009. doi:10.1038/s41598-018-30614-3

Wang, Z., Zhang, Z., Liu, S., Shao, C., Robertson, J., and Guo, Y. (2021). Impact of Carbon-Carbon Defects at the SiO2/4H-SiC (0001) Interface: a First-Principles Calculation. *J. Phys. D: Appl. Phys.* 55, 025109. doi:10.1088/1361-6463/ac2bc9

Xie, G., Shen, Y., Wei, X., Yang, L., Xiao, H., Zhong, J., et al. (2014). A Bond-Order Theory on the Phonon Scattering by Vacancies in Two-Dimensional Materials. *Sci. Rep.* 4, 5085. doi:10.1038/srep05085

Xu, C., Xue, L., Yin, C., and Wang, G. (2003). Formation and Photoluminescence Properties of AlN Nanowires. *Phys. Stat. Sol. (A)* 198, 329–335. doi:10.1002/pssa.200306612

Xu, X., Ge, X., Liu, X., Li, L., Fu, K., Dong, Y., et al. (2020). Two-dimensional M_2CO_2/MoS_2 (M = Ti, Zr and Hf) van der Waals heterostructures for overall water splitting: A density functional theory study. *Ceramics Int.* 46, 13377–13384. doi:10.1016/j.ceramint.2020.02.119

Yamaoka, T., Lim, H. E., Koirala, S., Wang, X., Shinokita, K., Maruyama, M., et al. (2018). Efficient Photocarrier Transfer and Effective Photoluminescence Enhancement in Type I Monolayer $MoTe_2/WSe_2$ Heterostructure. *Adv. Funct. Mater.* 28, 1801021. doi:10.1002/adfm.201801021

Yang, Q., Tan, C.-J., Meng, R.-S., Jiang, J.-K., Liang, Q.-H., Sun, X., et al. (2017). AlN/BP Heterostructure Photocatalyst for Water Splitting. *IEEE Electron. Device Lett.* 38, 145–148. doi:10.1109/led.2016.2633487

Zhang, C.-w. (2012). First-principles Study on Electronic Structures and Magnetic Properties of AlN Nanosheets and Nanoribbons. *J. Appl. Phys.* 111, 043702. doi:10.1063/1.3686144

Zhang, C.-w., and Zheng, F.-b. (2011). First-principles Prediction on Electronic and Magnetic Properties of Hydrogenated AlN Nanosheets. *J. Comput. Chem.* 32, 3122–3128. doi:10.1002/jcc.21902

Zhang, C., Cao, Y., Liu, Y., Hu, H.-J., Yu, Z. G., and Zhang, Y.-W. (2021). Bct-C_5: A New Body-Centered Tetragonal Carbon Allotrope. *Diamond Relat. Mater.* 119, 108571. doi:10.1016/j.diamond.2021.108571

Zhang, C., Zhou, H., Chen, S., Zhang, G., Yu, Z. G., Chi, D., et al. (2021). Recent Progress on 2D Materials-Based Artificial Synapses. *Crit. Rev. Solid State. Mater. Sci.*, 1–26. doi:10.1080/10408436.2021.1935212

Zhang, Z., Guo, Y., and Robertson, J. (2020). Origin of Weaker Fermi Level Pinning and Localized Interface States at Metal Silicide Schottky Barriers. *J. Phys. Chem. C* 124. doi:10.1021/acs.jpcc.0c06228

Zhang, Z., Guo, Y., and Robertson, J. (2020). Termination-dependence of Fermi Level Pinning at Rare-Earth arsenide/GaAs Interfaces. *Appl. Phys. Lett.* 116, 251602. doi:10.1063/5.0007479

Zhang, Z., Huang, B., Qian, Q., Gao, Z., Tang, X., and Li, B. (2020). Strain-tunable III-nitride/ZnO Heterostructures for Photocatalytic Water-Splitting: A Hybrid Functional Calculation. *APL Mater.* 8, 041114. doi:10.1063/5.0005648

Zheng, Z., Ren, K., Huang, Z., Zhu, Z., Wang, K., Shen, Z., et al. (2021). Remarkably Improved Curie Temperature for Two-Dimensional CrI_3 by Gas Molecular Adsorption: a DFT Study. *Semicond. Sci. Tech.* 36 (7), 075015. doi:10.1088/1361-6641/ac01a2

Zhu, X. T., Xu, Y., Cao, Y., Zhao, Y. Q., Sheng, W., Nie, G.-Z., et al. (2021). Investigation of the Electronic Structure of Two-Dimensional GaN/Zr_2CO_2 hetero-junction: Type-II Band Alignment with Tunable Bandgap. *Appl. Surf. Sci.* 542, 148505. doi:10.1016/j.apsusc.2020.148505

Zhu, Z., Ren, K., Shu, H., Cui, Z., Huang, Z., Yu, J., et al. (2021). First-Principles Study of Electronic and Optical Properties of Two-Dimensional WSSe/BSe van der Waals Heterostructure with High Solar-to-Hydrogen Efficiency. *Catalysts* 11, 991. doi:10.3390/catal11080991

Conflict of Interest: The authors declare that the research was conducted in the absence of any commercial or financial relationships that could be construed as a potential conflict of interest.

frontiers
in Chemistry

ORIGINAL RESEARCH
published: 15 November 2021
doi: 10.3389/fchem.2021.789522

Obvious Surface States Connecting to the Projected Triple Points in NaCl's Phonon Dispersion

Li Zhang[1*†], *Fang Fang*[2†], *Lixin Cheng*[2], *Huiming Lin*[3] *and Kai Wang*[2*]

[1] College of Mechanics, Changchun Institute of Technology, Changchun, China, [2] Engineering and Technology Center, The Fourth Medical College of Harbin Medical University, Harbin, China, [3] School of Chemistry, Harbin Normal University, Harbin, China

With the development of computer technology and theoretical chemistry, the speed and accuracy of first-principles calculations have significantly improved. Using first-principles calculations to predict new topological materials is a hot research topic in theoretical and computational chemistry. In this work, we focus on a well-known material, sodium chloride (NaCl), and propose that the triple point (TP), quadratic contact triple point (QCTP), linear and quadratic nodal lines can be found in the phonon dispersion of NaCl with $Fm\bar{3}m$ type structure. More importantly, we propose that the clear surface states connected to the projected TP and QCTP are visible on the (001) surface. It is hoped that further experimental investigation and verification for these properties as mentioned above.

Keywords: DFT, first-principles calculations, phonon dispersion, surface state, NaCl

Edited by:
Junjie He,
Charles University, Czechia

Reviewed by:
Zhimin Wu,
Chongqing Normal University, China
Minquan Kuang,
Southwest University, China

Correspondence:
Kai Wang
wangkai@hrbmu.edu.cn
Li Zhang
lizhang@ccit.edu.cn

†These authors have contributed equally to this work

Specialty section:
This article was submitted to Theoretical and Computational Chemistry,
a section of the journal Frontiers in Chemistry

Received: *05 October 2021*
Accepted: *18 October 2021*
Published: *15 November 2021*

Citation:
Zhang L, Fang F, Cheng L, Lin H and Wang K (2021) Obvious Surface States Connecting to the Projected Triple Points in NaCl's Phonon Dispersion.
Front. Chem. 9:789522.
doi: 10.3389/fchem.2021.789522

INTRODUCTION

The recent rapid development in topological materials (Kong and Cui, 2011; Cava et al., 2013; Banik et al., 2018; Kumar et al., 2020; Li and Wei, 2021) makes chemists expect these materials to solve the current challenges in quantum chemistry. A series of topological materials, including topological insulators (Müchler et al., 2012; Bradlyn et al., 2017; Kou et al., 2017; Martín Pendás et al., 2019; Isaeva and Ruck, 2020), spin-gapless semiconductors (Gao et al., 2016; Wang et al., 2016; Wang, 2017; Sun et al., 2020; Yue et al., 2020), and topological semimetals/metals (Zhou et al., 2018a; Schoop et al., 2018; Xu et al., 2020a; Klemenz et al., 2020; Zhao et al., 2020), were predicted by researchers, and some of them are confirmed in experiments. Among them, topological semimetals/metals (Zhong et al., 2016; Zhang et al., 2018; Jin et al., 2019a; Jin et al., 2019b; He et al., 2019; Wang et al., 2020a; Wang et al., 2020b; Xu et al., 2020b; Guo et al., 2020; Jin et al., 2021) always have nontrivial band crossings in their electronic band structures. In addition to their potential applications in technology, they also provide a platform for the study of basic quasiparticles in low cost experiments.

Recently, parallel to electrons, topological concepts have been extended to boson systems such as phonons in crystal materials, classical elastic waves in macroscopic artificial phonon crystals, and magnetic oscillators in magnets. Especially important is that the topological phonon in crystal materials (Jin et al., 2018; Liu et al., 2019; Zheng et al., 2019; Liu et al., 2020; Xie et al., 2021) can provide a potential prospect for regulating heat transfer and electron-phonon interaction. It should be emphasized that the phonon is not limited by the principle of Pauli incompatibility, which means that the experimental detection can be carried out in the whole frequency region of the phonon spectrum.

This work will focus on a famous realistic material, sodium chloride (NaCl). NaCl is with the $Fm\bar{3}m$ type cubic structure and with the space group number 225. The experimental lattice constants

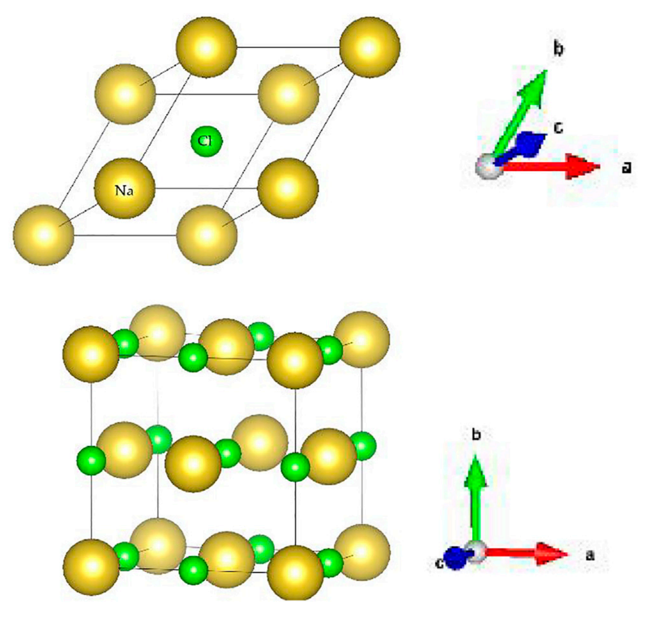

FIGURE 1 | (Upper) primitive cell and **(Bottom)** unit cell of NaCl material.

of sodium chloride (Abrahams and Bernstein, 1965) are $a = b = c =$ 5.62 Å. The Na locates at 4a (0, 0, 0) Wyckoff position, and the Cl locates at 4b (0.5, 0.5, 0.5) Wyckoff position. In this work, using the first principles calculations, we will study the topological signatures of the NaCl's phonon dispersion. We found that triple points with linear phonon bands dispersion and quadratic phonon bands dispersion coexist in NaCl's phonon dispersion. More importantly, we will exhibit the interesting phonon surface states of the (001) plane. The authors hoped that the uncovered triple points and their connected surface states in the NaCl phonon system could be confirmed in experiment soon.

METHODS

The crystal structure of Fm$\bar{3}$ m NaCl is selected from the Materials Project database (Materials Project, 2021). Some material information, including the magnetic ordering, final magnetic moment, formation energy/atom, band structure, and the phonon dispersion of NaCl, can be found in ref. (Materials Project, 2021). One concludes from ref. (Materials Project, 2021) that NaCl is a nonmagnetic semiconductor with a band-gap value of 5.145 eV. The obtained lattice constants based on first-principle calculations are $a = b = c = 5.6916$ Å, consisting well with the experiment values (Abrahams and Bernstein, 1965). The primitive cell and the unit cell of the NaCl are shown in **Figure 1**. The yellow and green balls represent the Na and Cl atoms, respectively. This work will focus on the phonon dispersion of NaCl because we would like to uncover its topological signatures. The phonon dispersion of NaCl is determine based on the density functional perturbation theory with the PHONOPY codes (Togo and Tanaka, 2015), and the topological surface properties are constructed by the WANNIERTOOLS package (Wu et al., 2018) based on the phononic Wannier tight-binding Hamiltonian.

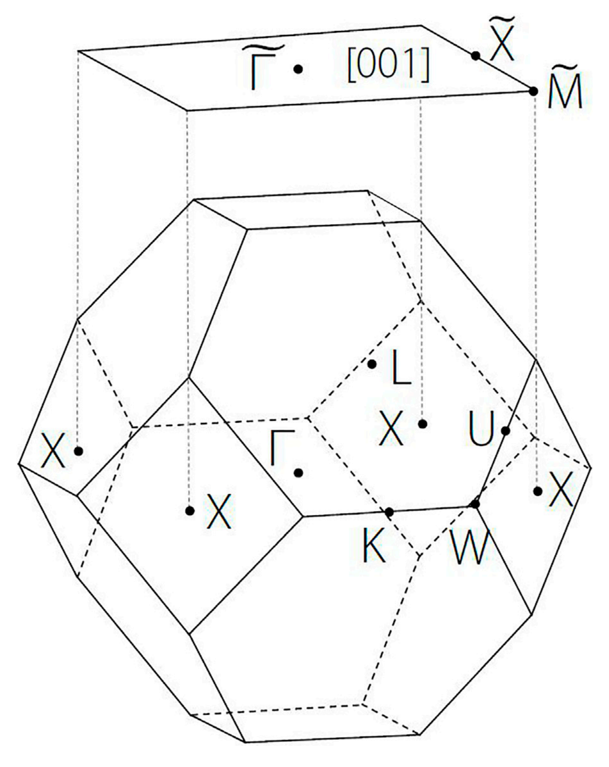

FIGURE 2 | Three-dimensional Brillouin zone (BZ) and the two-dimensional (001) surface BZ. The X, K, W, Y, L, Γ are the symmetry points of 3D BZ. Γ, X, and X points are projected to $\tilde{\boldsymbol{\Gamma}}$, $\tilde{\mathbf{X}}$, and $\tilde{\mathbf{M}}$ points of the (001) surface.

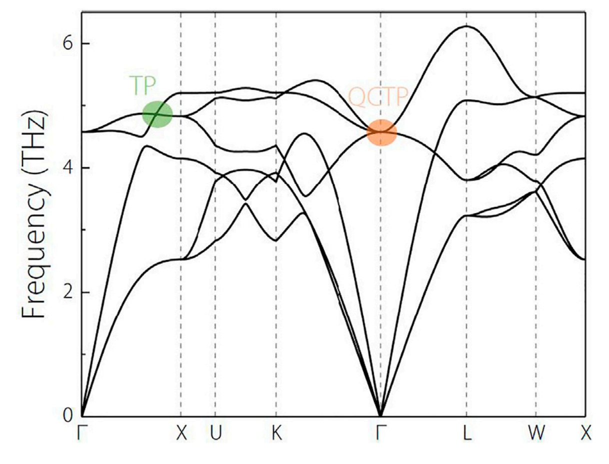

FIGURE 3 | Phonon dispersion of NaCl along the **Γ**-X-U-K-**Γ**-L-W-X paths.

Calculated Phonon Dispersion and the Related Topological Signatures

In **Figure 2**, we plotted the three-dimensional BZ and some high symmetry points, X, K, W, Y, L, and Γ. Along the Γ-X-U-K-Γ-L-W-X paths, the phonon dispersion of NaCl is calculated, and the results are shown in **Figure 3**. During the phonon dispersion

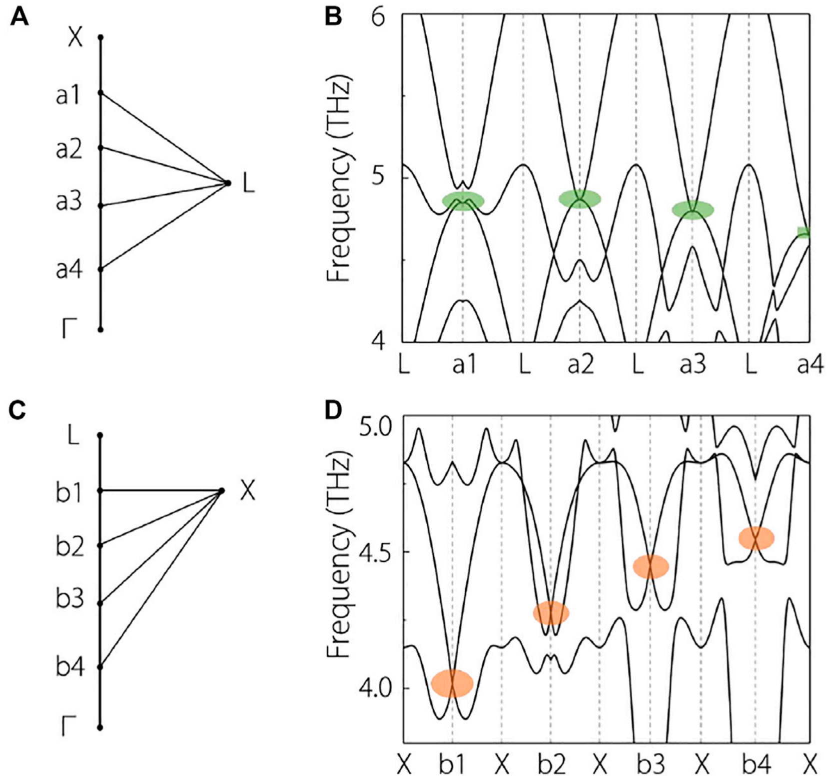

FIGURE 4 | (A), **(C)** some selected symmetry points along the X-**Γ** and the L-**Γ**, respectively. **(B)** and **(D)** calculated phonon dispersions along the L-an and X-bn (*n* = 1–4). The linear two-degenerate points and the quadratic two-degenerate points are highlighted with orange and green circles, respectively.

calculations, we built a $2\times2\times2$ supercell for the NaCl system. From **Figure 3**, at first glance, one concludes that the NaCl is dynamically stable because the NaCl system has no imaginary frequencies.

Moreover, from **Figure 3**, one obtains the following information: 1) Along the Γ-X path and in the range of 4–5 THz frequencies, there are one doubly-degenerate phonon band and a non-degenerate phonon band, and these two bands cross at a point (see the green circle in **Figure 3**) along the Γ-X path. This point along the Γ-X path is a triple point; 2) along the K – Γ path and in the range of 4-5 THz frequencies, one concludes that three phonon bands touched at the Γ point, forming a triple point (see the orange circle region in **Figure 3**). However, we would like to point out that the triple point on the Γ-X and at Γ are different because the point on the Γ-X is with linear band dispersion and the point at the Γ is with a quadratic band dispersion. Hence, the triple point on the Γ-X is called triple point (TP) (Zhu et al., 2016; Tian et al., 2021), and the triple point at the Γ is usually called quadratic contact triple point (QCTP) (Hu et al., 2019). QCTP features a quadratic band splitting along any direction in momentum space. Along the Γ – L path, one can see that there are also a doubly degenerate band and a non-degenerate band in the range of 4.5–6 THz frequencies.

One may wonder whether the doubly degenerate band along the Γ-X (around the TP) and the Γ-L (around the QCTP) paths

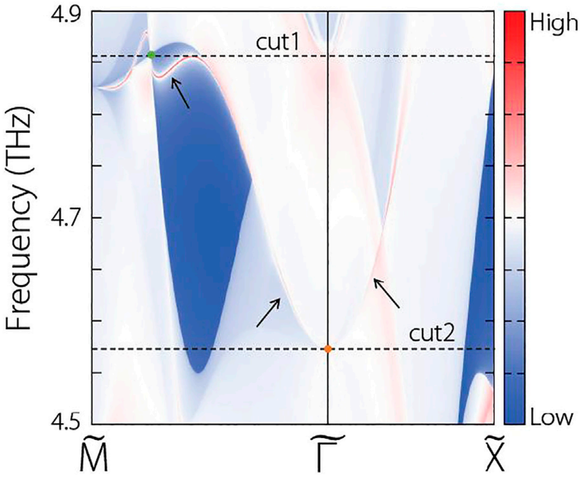

FIGURE 5 | Calculated surface states along the **M̃** – **Γ̃** – **X̃** paths of the (001) surface.

are the same. In the following, we will answer this question affirmatively. To better answer this question, in **Figure 4A,C**, we divided the Γ-X (around the TP) and Γ-L (around the QCTP) paths into five parts and selected some more symmetry points. Namely, we selected a1-a4 along the X-Γ and b1-b4 along the L-Γ

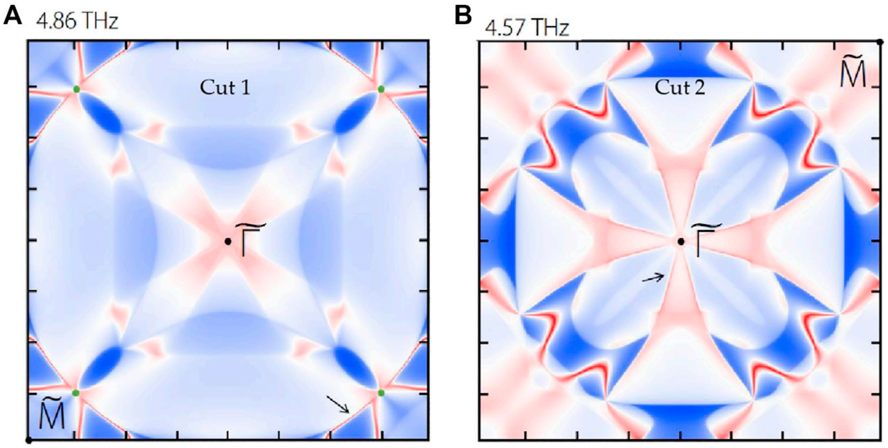

FIGURE 6 | Calculated iso-frequency surface contours at **(A)** 4.86 THz and **(B)** 4.57 THz.

paths, respectively. The phonon dispersions along the L-an and X-bn ($n = 1, 2, 3, 4$) are shown in **Figure 4B,D**, respectively. One finds the points at a1, a2, a3 a4 are all with a quadratic band splitting, however, for the points b1, b2, b3, b4, they are with a classic linear band splitting. Hence, the doubly degenerate band along the X-Γ, is composed of doubly degenerate points with linear band splitting, forming a linear nodal line (Zhou et al., 2018b; Chen et al., 2018; Chang et al., 2019; Yan et al., 2019; Li et al., 2020a; Kirby et al., 2020; Meng et al., 2020; Wang and Yang, 2021). The doubly degenerate band along the $\Gamma - \mathrm{L}$, is composed of doubly degenerate points with quadratic band splitting, forming a quadratic nodal line (Yu et al., 2019; Wang et al., 2020c).

A summary of this section is shown as follow: NaCl phonon hosts a QCTP at the Γ point, a TP along the X-Γ path, a two-degenerate linear nodal line along the X-Γ path, and a quadratic nodal line along the $\Gamma - \mathrm{L}$. It is hoped that such rich topological signatures in NaCl can be confirmed in experiment soon.

Calculated Surface States on (001) Surface BZ

In this section, we come to study the project surface states of the [001] NaCl phonons. As shown in **Figure 2**, we selected some symmetry points, Γ, X and X, and projected these points to $\widetilde{\Gamma}$, $\widetilde{X}$, and $\widetilde{M}$ points of the (001) surface. In **Figure 5**, we collected the results and labeled the positions of the projected TP (green dot) and the projected QCTP (orange dot). One concludes that prominent surface states (Xu et al., 2015; Morali et al., 2019; Li et al., 2020b) connected to the projected TP, which is benefit for experimental detection. Although the surface state connected to the QCTP is a little fuzzy, we can observe its trend and general shape.

For clarity, we also exhibit the iso-frequency surface contours at 4.86 THz and 4.57 THz in **Figure 6A,B**, respectively. In **Figure 6A**, the positions of the projected TP and the connected surface states are marked by a green dot and black arrows, respectively. In **Figure 6B**, the positions of the projected QCTP and the connected surface states are marked by a black dot and black arrows, respectively. The projected TP/QCTP connected surface states are visible.

SUMMARY

In this study, we proposed the topological signatures of the NaCl's phonon dispersion. A systematic theoretical investigation found that this material hosts quadratic and linear nodal lines, TP and QCTP in its phonon dispersion. The QCTP is located at the Γ position, the TP is along the X-Γ, the linear nodal line is along the X-Γ path, and the quadratic nodal line is along the $\Gamma - \mathrm{L}$. Besides, the surface states are computed and clear surface arc states connected to the projected TP and QCTP can be observed on the (001) surface. Further experimental investigation and verification for these rich topological signatures are expected.

DATA AVAILABILITY STATEMENT

The original contributions presented in the study are included in the article/Supplementary Material, further inquiries can be directed to the corresponding authors.

AUTHOR CONTRIBUTIONS

LZ, and FF: conceptualization, methodology, software, formal analysis, data curation, and writing. KW, LC, HL, and LZ: investigation, funding, and project administration. All authors contributed to the article and approved the submitted version.

FUNDING

This work is supported by Topic Foundation of Changchun Institute of Technology (Grant No. 320200040), Young People Foundation of Changchun Institute of Technology

(Grant No. 320200033), Doctor Foundation of Changchun Institute of Technology 2021, Natural Science Foundation of Heilongjiang Province (Grant No. LH 2020H067), Heilongjiang Postdoctoral Program (LBH-Q16173), Science and Technology Program of Academy of Medical Sciences of Heilongjiang Province (Grant No. 201805), Research Foundation of Education Bureau of Jilin Province (Grant No. JJKH20210666KJ).

REFERENCES

Abrahams, S. C., and Bernstein, J. L. (1965). Accuracy of an Automatic Diffractometer. Measurement of the Sodium Chloride Structure Factors. *Acta Crystallogr.* 18 (5), 926–932. doi:10.1107/s0365110x65002244

Banik, A., Roychowdhury, S., and Biswas, K. (2018). The Journey of Tin Chalcogenides towards High-Performance Thermoelectrics and Topological Materials. *Chem. Commun.* 54 (50), 6573–6590. doi:10.1039/c8cc02230e

Bradlyn, B., Elcoro, L., Cano, J., Vergniory, M. G., Wang, Z., Felser, C., et al. (2017). Topological Quantum Chemistry. *Nature* 547 (7663), 298–305. doi:10.1038/nature23268

Cava, R. J., Ji, H., Fuccillo, M. K., Gibson, Q. D., and Hor, Y. S. (2013). Crystal Structure and Chemistry of Topological Insulators. *J. Mater. Chem. C* 1 (19), 3176–3189. doi:10.1039/c3tc30186a

Chang, T. R., Pletikosic, I., Kong, T., Bian, G., Huang, A., Denlinger, J., et al. (2019). Realization of a Type-II Nodal-Line Semimetal in Mg_3Bi_2. *Adv. Sci.* 6 (4), 1800897. doi:10.1002/advs.201800897

Chen, H., Zhang, S., Jiang, W., Zhang, C., Guo, H., Liu, Z., et al. (2018). Prediction of Two-Dimensional Nodal-Line Semimetals in a Carbon Nitride Covalent Network. *J. Mater. Chem. A* 6 (24), 11252–11259. doi:10.1039/c8ta02555j

Gao, G., Ding, G., Li, J., Yao, K., Wu, M., and Qian, M. (2016). Monolayer MXenes: Promising Half-Metals and Spin Gapless Semiconductors. *Nanoscale* 8 (16), 8986–8994. doi:10.1039/c6nr01333c

Guo, C., Zhao, B., Huang, D., and Fan, S. (2020). Radiative thermal Router Based on Tunable Magnetic Weyl Semimetals. *ACS Photon.* 7 (11), 3257–3263. doi:10.1021/acsphotonics.0c01376

He, T., Zhang, X., Meng, W., Jin, L., Dai, X., and Liu, G. (2019). Topological Nodal Lines and Nodal Points in the Antiferromagnetic Material β-Fe_2PO_5. *J. Mater. Chem. C* 7 (40), 12657–12663. doi:10.1039/c9tc04046c

Hu, J., Wu, W., Zhong, C., Liu, N., Ouyang, C., Yang, H. Y., et al. (2019). Three-dimensional Honeycomb Carbon: Junction Line Distortion and Novel Emergent Fermions. *Carbon* 141, 417–426. doi:10.1016/j.carbon.2018.09.027

Isaeva, A., and Ruck, M. (2020). Crystal Chemistry and Bonding Patterns of Bismuth-Based Topological Insulators. *Inorg. Chem.* 59 (6), 3437–3451. doi:10.1021/acs.inorgchem.9b03461

Jin, L., Wang, L., Zhang, X., Liu, Y., Dai, X., Gao, H., et al. (2021). Fully Spin-Polarized Weyl Fermions and In/out-Of-Plane Quantum Anomalous Hall Effects in a Two-Dimensional D0 Ferromagnet. *Nanoscale* 13 (11), 5901–5909. doi:10.1039/d0nr07556f

Jin, L., Zhang, X., Dai, X., Liu, H., Chen, G., and Liu, G. (2019). Centrosymmetric Li_2NaN: a superior Topological Electronic Material with Critical-type Triply Degenerate Nodal Points. *J. Mater. Chem. C* 7 (5), 1316–1320. doi:10.1039/c8tc05930f

Jin, L., Zhang, X., He, T., Meng, W., Dai, X., and Liu, G. (2019). Topological Nodal Line State in Superconducting NaAlSi Compound. *J. Mater. Chem. C* 7 (34), 10694–10699. doi:10.1039/c9tc03464a

Jin, Y., Wang, R., and Xu, H. (2018). Recipe for Dirac Phonon States with a Quantized valley berry Phase in Two-Dimensional Hexagonal Lattices. *Nano Lett.* 18 (12), 7755–7760. doi:10.1021/acs.nanolett.8b03492

Kirby, R. J., Ferrenti, A., Weinberg, C., Klemenz, S., Oudah, M., Lei, S., et al. (2020). Transient Drude Response Dominates Near-Infrared Pump-Probe Reflectivity in Nodal-Line Semimetals ZrSiS and ZrSiSe. *J. Phys. Chem. Lett.* 11 (15), 6105–6111. doi:10.1021/acs.jpclett.0c01377

Klemenz, S., Hay, A. K., Teicher, S. M. L., Topp, A., Cano, J., and Schoop, L. M. (2020). The Role of Delocalized Chemical Bonding in Square-Net-Based Topological Semimetals. *J. Am. Chem. Soc.* 142 (13), 6350–6359. doi:10.1021/jacs.0c01227

Kong, D., and Cui, Y. (2011). Opportunities in Chemistry and Materials Science for Topological Insulators and Their Nanostructures. *Nat. Chem.* 3 (11), 845–849. doi:10.1038/nchem.1171

Kou, L., Ma, Y., Sun, Z., Heine, T., and Chen, C. (2017). Two-dimensional Topological Insulators: Progress and Prospects. *J. Phys. Chem. Lett.* 8 (8), 1905–1919. doi:10.1021/acs.jpclett.7b00222

Kumar, N., Guin, S. N., Manna, K., Shekhar, C., and Felser, C. (2020). Topological Quantum Materials from the Viewpoint of Chemistry. *Chem. Rev.* 121 (5), 2780–2815. doi:10.1021/acs.chemrev.0c00732

Li, C. Z., Wang, A. Q., Li, C., Zheng, W. Z., Brinkman, A., Yu, D. P., et al. (2020). Fermi-arc Supercurrent Oscillations in Dirac Semimetal Josephson Junctions. *Nat. Commun.* 11 (1), 1150–1157. doi:10.1038/s41467-020-15010-8

Li, Y., Xia, J., and Srivastava, V. (2020). The Tetragonal Monoxide of Platinum: a New Platform for Investigating Nodal-Line and Nodal-point Semimetallic Behavior. *Front. Chem.* 8, 704. doi:10.3389/fchem.2020.00704

Li, Z., and Wei, B. (2021). Topological Materials and Topologically Engineered Materials: Properties, Synthesis, and Applications for Energy Conversion and Storage. *J. Mater. Chem. A* 9 (3), 1297–1313. doi:10.1039/d0ta11072h

Liu, Q.-B., Fu, H.-H., Xu, G., Yu, R., and Wu, R. (2019). Categories of Phononic Topological Weyl Open Nodal Lines and a Potential Material Candidate: Rb2Sn2O3. *J. Phys. Chem. Lett.* 10 (14), 4045–4050. doi:10.1021/acs.jpclett.9b01159

Liu, Q. B., Qian, Y., Fu, H. H., and Wang, Z. (2020). Symmetry-enforced Weyl Phonons. *npj Comput. Mater.* 6 (1), 1–6. doi:10.1038/s41524-020-00358-8

Martín Pendás, A., Contreras-García, J., Pinilla, F., Mella, J. D., Cardenas, C., and Muñoz, F. (2019). A Chemical Theory of Topological Insulators. *Chem. Commun.* 55 (82), 12281–12287. doi:10.1039/c9cc04054d

Meng, W., Liu, Y., Zhang, X., Dai, X., and Liu, G. (2020). A Nonsymmorphic-Symmetry-Protected Hourglass Weyl Node, Hybrid Weyl Node, Nodal Surface, and Dirac Nodal Line in Pd_4X (X = S, Se) Compounds. *Phys. Chem. Chem. Phys.* 22 (39), 22399–22407. doi:10.1039/d0cp03686b

Morali, N., Batabyal, R., Nag, P. K., Liu, E., Xu, Q., Sun, Y., et al. (2019). Fermi-arc Diversity on Surface Terminations of the Magnetic Weyl Semimetal $Co_3Sn_2S_2$. *Science* 365 (6459), 1286–1291. doi:10.1126/science.aav2334

Müchler, L., Zhang, H., Chadov, S., Yan, B., Casper, F., Kübler, J., et al. (2012). Topological Insulators from a Chemist's Perspective. *Angew. Chem. Int. Ed.* 51 (29), 7221–7225. doi:10.1002/anie.201202480

Schoop, L. M., Pielnhofer, F., and Lotsch, B. V. (2018). Chemical Principles of Topological Semimetals. *Chem. Mater.* 30 (10), 3155–3176. doi:10.1021/acs.chemmater.7b05133

Sun, Q., Ma, Y., and Kioussis, N. (2020). Two-dimensional Dirac Spin-Gapless Semiconductors with Tunable Perpendicular Magnetic Anisotropy and a Robust Quantum Anomalous Hall Effect. *Mater. Horiz.* 7 (8), 2071–2077. doi:10.1039/d0mh00396d

Tian, L., Liu, Y., Yu, W. W., Zhang, X., and Liu, G. (2021). Triple Degenerate point in Three Dimensions: Theory and Realization. *Phys. Rev. B* 104 (4), 045137. doi:10.1103/physrevb.104.045137

Togo, A., and Tanaka, I. (2015). First Principles Phonon Calculations in Materials Science. *Scripta Materialia* 108, 1–5. doi:10.1016/j.scriptamat.2015.07.021

Wang, J. R., Li, W., and Zhang, C. J. (2020). Possible Instabilities in Quadratic and Cubic Nodal-Line Fermion Systems with Correlated Interactions. *Phys. Rev. B* 102 (8), 085132. doi:10.1103/physrevb.102.085132

Wang, S., and Yang, B. (2021). Dirac Nodal Line Semimetal of Three-Dimensional Cross-Linked Graphene Network as Anode Materials for Li-Ion Battery beyond Graphite. *ACS Appl. Energ. Mater.* 4 (3), 2091–2097. doi:10.1021/acsaem.0c02408

Wang, X.-L. (2017). Dirac Spin-Gapless Semiconductors: Promising Platforms for Massless and Dissipationless Spintronics and New (Quantum) Anomalous Spin Hall Effects. *Natl. Sci. Rev.* 4 (2), 252–257. doi:10.1093/nsr/nww069

Wang, X., Cheng, Z., Wang, J., Wang, X.-L., and Liu, G. (2016). Recent Advances in the Heusler Based Spin-Gapless Semiconductors. *J. Mater. Chem. C* 4 (30), 7176–7192. doi:10.1039/c6tc01343k

Wang, X., Ding, G., Cheng, Z., Surucu, G., Wang, X.-L., and Yang, T. (2020). Novel Topological Nodal Lines and Exotic Drum-head-like Surface States in Synthesized CsCl-type Binary alloy TiOs. *J. Adv. Res.* 22, 137–144. doi:10.1016/j.jare.2019.12.001

Wang, X., Ding, G., Cheng, Z., Surucu, G., Wang, X.-L., and Yang, T. (2020). Rich Topological Nodal Line Bulk States Together with Drum-head-like Surface States in NaAlGe with Anti-PbFCl Type Structure. *J. Adv. Res.* 23, 95–100. doi:10.1016/j.jare.2020.01.017

Wu, Q., Zhang, S., Song, H.-F., Troyer, M., and Soluyanov, A. A. (2018). WannierTools: An Open-Source Software Package for Novel Topological Materials. *Comput. Phys. Commun.* 224, 405–416. doi:10.1016/j.cpc.2017.09.033

Xie, C., Liu, Y., Zhang, Z., Zhou, F., Yang, T., Kuang, M., et al. (2021). Sixfold Degenerate Nodal-point Phonons: Symmetry Analysis and Materials Realization. *Phys. Rev. B* 104 (4), 045148. doi:10.1103/physrevb.104.045148

Xu, L., Zhang, X., Meng, W., He, T., Liu, Y., Dai, X., et al. (2020). Centrosymmetric TiS as a Novel Topological Electronic Material with Coexisting Type-I, Type-II and Hybrid Nodal Line States. *J. Mater. Chem. C* 8 (40), 14109–14116. doi:10.1039/d0tc03600e

Xu, S.-Y., Liu, C., Kushwaha, S. K., Sankar, R., Krizan, J. W., Belopolski, I., et al. (2015). Observation of Fermi Arc Surface States in a Topological Metal. *Science* 347 (6219), 294–298. doi:10.1126/science.1256742

Xu, Y., Elcoro, L., Song, Z.-D., Wieder, B. J., Vergniory, M. G., Regnault, N., et al. (2020). High-throughput Calculations of Magnetic Topological Materials. *Nature* 586 (7831), 702–707. doi:10.1038/s41586-020-2837-0

Materials Project (2021). Available at: https://materialsproject.org/materials/mp-22862/ (Accessed October 23, 2021).

Yan, L., Liu, P.-F., Bo, T., Zhang, J., Tang, M.-H., Xiao, Y.-G., et al. (2019). Emergence of Superconductivity in a Dirac Nodal-Line Cu_2Si Monolayer: Ab Initio Calculations. *J. Mater. Chem. C* 7 (35), 10926–10932. doi:10.1039/c9tc03740c

Yu, Z.-M., Wu, W., Sheng, X.-L., Zhao, Y. X., and Yang, S. A. (2019). Quadratic and Cubic Nodal Lines Stabilized by Crystalline Symmetry. *Phys. Rev. B* 99 (12), 121106. doi:10.1103/physrevb.99.121106

Yue, Z., Li, Z., Sang, L., and Wang, X. (2020). Spin-Gapless Semiconductors. *Small* 16 (31), 1905155. doi:10.1002/smll.201905155

Zhang, X., Guo, R., Jin, L., Dai, X., and Liu, G. (2018). Intermetallic Ca_3Pb: a Topological Zero-Dimensional Electride Material. *J. Mater. Chem. C* 6 (3), 575–581. doi:10.1039/c7tc04989g

Zhao, Z., Zhang, Z., and Guo, W. (2020). A Family of All Sp^2-Bonded Carbon Allotropes of Topological Semimetals with Strain-Robust Nodal-Lines. *J. Mater. Chem. C* 8 (5), 1548–1555. doi:10.1039/c9tc05470g

Zheng, B., Xia, B., Wang, R., Zhao, J., Chen, Z., Zhao, Y., et al. (2019). Tunable Ferromagnetic Weyl Fermions from a Hybrid Nodal Ring. *npj Comput. Mater.* 5 (1), 1–7. doi:10.1038/s41524-019-0214-z

Zhong, C., Chen, Y., Xie, Y., Yang, S. A., Cohen, M. L., and Zhang, S. B. (2016). Towards Three-Dimensional Weyl-Surface Semimetals in Graphene Networks. *Nanoscale* 8 (13), 7232–7239. doi:10.1039/c6nr00882h

Zhou, P., Ma, Z. S., and Sun, L. Z. (2018). Coexistence of Open and Closed Type Nodal Line Topological Semimetals in Two Dimensional B2C. *J. Mater. Chem. C* 6 (5), 1206–1214. doi:10.1039/c7tc05095j

Zhou, P., Ma, Z. S., and Sun, L. Z. (2018). Coexistence of Open and Closed Type Nodal Line Topological Semimetals in Two Dimensional B_2C. *J. Mater. Chem. C* 6 (5), 1206–1214. doi:10.1039/c7tc05095j

Zhu, Z., Winkler, G. W., Wu, Q., Li, J., and Soluyanov, A. A. (2016). Triple point Topological Metals. *Phys. Rev. X* 6 (3), 031003. doi:10.1103/physrevx.6.031003

Conflict of Interest: The authors declare that the research was conducted in the absence of any commercial or financial relationships that could be construed as a potential conflict of interest.

frontiers in Chemistry

ORIGINAL RESEARCH
published: 19 November 2021
doi: 10.3389/fchem.2021.788813

Band Bending Mechanism in CdO/Arsenene Heterostructure: A Potential Direct Z-scheme Photocatalyst

Kai Ren[1†]*, *Ruxin Zheng*[1†], *Jin Yu*[2], *Qingyun Sun*[1]* and *Jianping Li*[3]

[1]School of Mechanical and Electronic Engineering, Nanjing Forestry University, Nanjing, China, [2]School of Materials Science and Engineering, Southeast University, Nanjing, China, [3]School of Automotive and Transportation Engineering, Shenzhen Polytechnic, Shenzhen, China

For the few years, two-dimensional (2D) materials have aroused general focus. In order to expand the properties and application range of 2D materials, two different layered materials are usually combined into heterostructure through van der Waals (vdW) interaction. In this research, based on first-principles simulation, we propose CdO/Arsenene (CdO/As) vdW heterostructure as a semiconductor possessing a direct bandgap by 2.179 eV. Besides, the CdO/As vdW heterostructure presents type-II band alignment, which can be used as a remarkable photocatalyst. Importantly, the CdO/As heterostructure demonstrates a direct Z-type principle photocatalyst by exploring the band bending mechanism in the heterostructure. Furthermore, we calculated the light absorption characteristics of CdO/As vdW heterostructure by optical absorption spectrum and conversion efficiency of a novel solar-to-hydrogen efficiency (η_{STH}) about 11.67%, which is much higher than that of other 2D photocatalysts. Our work can provide a theoretical guidance for the designing of Z-scheme photocatalyst.

Keywords: two-dimensional, heterostructure, first-principles calculation, Z-scheme, photocatalyst

Edited by:
Guangzhao Wang,
Yangtze Normal University, China

Reviewed by:
Chengyong Zhong,
Chengdu University, China
Jiaren Yuan,
Jiangsu University, China

***Correspondence:**
Kai Ren
kairen@njfu.edu.cn
Qingyun Sun
sunqingyun@njfu.edu.cn

[†]*These authors have contributed equally to this work and share first authorship*

Specialty section:
This article was submitted to Theoretical and Computational Chemistry,
a section of the journal Frontiers in Chemistry

Received: *03 October 2021*
Accepted: *18 October 2021*
Published: *19 November 2021*

Citation:
Ren K, Zheng R, Yu J, Sun Q and Li J (2021) Band Bending Mechanism in CdO/Arsenene Heterostructure: A Potential Direct Z-scheme Photocatalyst. Front. Chem. 9:788813. doi: 10.3389/fchem.2021.788813

INTRODUCTION

Since graphene was discovered in 2004 (Geim and Novoselov, 2007), it has continuously promoted the research and development of two-dimensional (2D) materials (Miró et al., 2014; Zhong et al., 2019a; He et al., 2019; Sun et al., 2019; Qi et al., 2020; Cui et al., 2021; Dai et al., 2021). After a long time of study on 2D materials, it was found that 2D material has extensive applications and is considered to be one of the most attractive and interesting material fields. All 2D materials show outstanding properties (Vahedi Fakhrabad et al., 2015; Xu et al., 2016; Zhong et al., 2017; Yuan et al., 2018; Sun and Schwingenschlögl, 2020; Luo et al., 2021), for example, the transition metal dichalcogenides (TMDs) materials have remarkable mechanical (Liu and Li, 2015), electronic (Zhang and Singh, 2009), optical (He et al., 2014), magnetic (Yuan et al., 2020) and thermal stability (Ding et al., 2016). Phosphorous possesses novel physical, chemical, optical properties and electrical conductivity (Li and Chen, 2014; Lee et al., 2016). Metal carbide (MXene) has excellent magnetic, thermoelectric properties and carrier mobility. In particular, Cr_2TiC_2 monolayer is a new 2D bipolar antiferromagnetic semiconductor and can be used as antiferromagnetic spin field effect transistor (He et al., 2018). The Hf_2CO_2 shows the excellent thermal conductivity (about 86.25–131.2 $W\,m^{-1}\cdot K^{-1}$) along the armchair direction, and the expansion coefficient at room temperature is about $6.094 \times 10^{-6}\,K^{-1}$ (Ren et al., 2021), and the carrier mobility reaches about 1,531.48 $cm^2/V\cdot s$ (Cai et al., 2014). All these excellent performances explain that 2D materials show potential usage in photocatalysis, photovoltaic devices and heterostructure (Xu et al., 2015; Zhong et al., 2019b; Wang et al., 2020a; Sun et al., 2020b; Wang et al., 2020b; Sun and Schwingenschlögl, 2021a; Sun and Schwingenschlögl, 2021b; Lou et al., 2021; Sun et al., 2021; Zhu et al., 2021).

When TiO_2 was found to be able to produce hydrogen (H_2) from ultraviolet irradiated water in 1972 (Fujishima and Honda, 1972), many studies have been carried out using semiconductors as photocatalysts to decompose water (Yuan et al., 2016; Yang et al., 2017; Liu et al., 2018; Wang et al., 2020c; Yong et al., 2020). When the semiconductor is illuminated, the electrons are inspired to move from the valence band maximum (VBM) to the conduction band minimum (CBM), generating holes at the VBM (Maeda and Domen, 2007). However, recompositing rate of photogenerated electron–hole pairs is extraordinary increased due to the simultaneous reduction and oxidation reactions on the surface of monolayer material during water splitting. The popular way to solve this problem is to construct the type-II heterostructure (Ren et al., 2020a), which can effectively separate photogenerated electrons and holes. All 2D heterostructures are formed by van der Waals force (vdW) interaction, which produces more novel properties on the basis of original properties (Ren et al., 2019a), inducing more fantastic optical (Wang et al., 2018), interface properties (Ren et al., 2020b), carrier mobility (Luo et al., 2019) and Gibbs free energy (Ren et al., 2019b). In particular, the Z-scheme photocatalyst has become more and more popular because its special and efficient catalytic mechanism (Xu et al., 2018), such as As/PtS_2 (Ren et al., 2020c), $MoSe_2$/HfS_2 (Wang et al., 2019), TiO_2/CdS (Meng et al., 2017) etc., which are proved to possess novel catalytic performance by theoretical and experimental methods. Recently, it has been reported that a hexagonal monolayer semiconductor CdO was prepared by chemical spray pyrolysis and has got a lot of attention due to its outstanding mechanical and stability properties (Subramanyam et al., 1998; Zhuang and Hennig, 2013; Chaurasiya and Dixit, 2019; Chaurasiya et al., 2019; Ali et al., 2021). In addition, heterostructures based on CdO monolayer [such as ZnO/CdO (Sang et al., 2012), CdO/GaS (Zhao et al., 2021), etc.] also demonstrate unusual structural and electronic properties (Sang et al., 2012; Zhao et al., 2021). At the same time, Arsenene (As) is also a 2D material with many special properties, in particular, the band gap can be adjusted by applying external strain on the surface (Kamal and Ezawa, 2015). However, the heterostructures constructed by CdO and As are rarely reported, who share the same honeycomb hexagonal structure. Besides, considering that both CdO and As possess excellent electronic and optical characteristics, it is worth to explore the potential applications of heterostructure based on CdO and As monolayers.

In this study, performing first-principles calculations, the electronic characteristic of the CdO, As and CdO/As heterostructure are investigated with semiconductor nature. Furthermore, the CdO/As heterostructure has a type-II band structure to separate the photogenerated electrons and holes continuously. Interestingly, the bend bending style in CdO/As heterostructure demonstrates a potential direct Z-type photocatalyst and the optical performance is also addressed.

MATERIALS AND METHODS

Considering the density functional theory (DFT), all simulation studies in this work were implemented by Vienna *ab initio* simulation software package (VASP) (Capelle, 2006; Togo et al., 2008; Togo and Tanaka, 2015). The core electron is described by projection enhanced wave potential (PAW) (Kresse and Joubert, 1999). The commutative relevant functional was explored, which is introduced by generalized gradient approximation (GGA) and Perdew–Burke–Ernzerhof (PBE) functional (Perdew et al., 1996; Grimme, 2006). At the same time, the weak dispersion force was considered by DFT-D3 with Grimme method (Grimme et al., 2010). Heyd–Scuseria–Ernzerhof mixed functional was used to obtain more accurate electronic and optical properties (Heyd et al., 2003). The parameters of 550 eV and 17 × 17 × 1 were used for the energy cut-off and the Monkhorst–Pack *k*-point grids in the first Brillouin zone. A vacuum space of 25 Å was used in the calculation to keep away from the interaction between adjacent mirror layers. The relaxation of the structure is simulated by conjugate gradient method. The Hellmann–Feynman force on each atom is limited to 0.01 eV $Å^{-1}$.

According to the calculation method of solar-to-hydrogen efficiency (η_{STH}) proposed by Yang etc (Xu et al., 2016) (η_{STH}), where $\eta_{STH} = \eta_{abs} \times \eta_{cu}$, and η_{abs}, η_{cu} represents light absorption and carrier efficiency, respectively. Besides, the η_{abs} is calculated by:

$$\eta_{abs} = \frac{\int_{E_g}^{\infty} P(h\omega)d(h\omega)}{\int_{0}^{\infty} P(h\omega)d(h\omega)} \tag{1}$$

where $P(h\omega)$ is the solar energy flux by AM1.5G with the photon energy $h\omega$. Eg is the bandgap of studied materials. Furthermore, the η_{cu} is decided by:

$$\eta_{cu} = \frac{\Delta G \int_{E}^{\infty} \frac{P(h\omega)}{h\omega} d(h\omega)}{\int_{E_g}^{\infty} P(h\omega)d(h\omega)} \tag{2}$$

where ΔG is 1.23 eV for the potential difference in water splitting. E is the photon energy using for water splitting, which is calculated by:

$$E = \begin{cases} E_g, (\chi(H_2) \geq 0.2, \chi(O_2) \geq 0.6) \\ E_g + 0.2 - \chi(H_2), (\chi(H_2) < 0.2, \chi(O_2) \geq 0.6) \\ E_g + 0.6 - \chi(O_2), (\chi(H_2) \geq 0.2, \chi(O_2) < 0.6) \\ E_g + 0.8 - \chi(H_2) - \chi(O_2), (\chi(H_2) < 0.2, \chi(O_2) < 0.6) \end{cases} \tag{3}$$

where $\chi(H_2)$ and $\chi(O_2)$ are demonstrating the over potential for HER and OER, respectively.

RESULTS AND DISCUSSION

First, the crystal structures of single-layer CdO and As was constructed and optimized. The side and top views of CdO and As monolayers are shown in **Figures 1A,C**, respectively. The lattice constants of CdO and As are calculated to be 3.684 and 3.607 Å, showing a small lattice mismatch of 2.11% for the CdO/

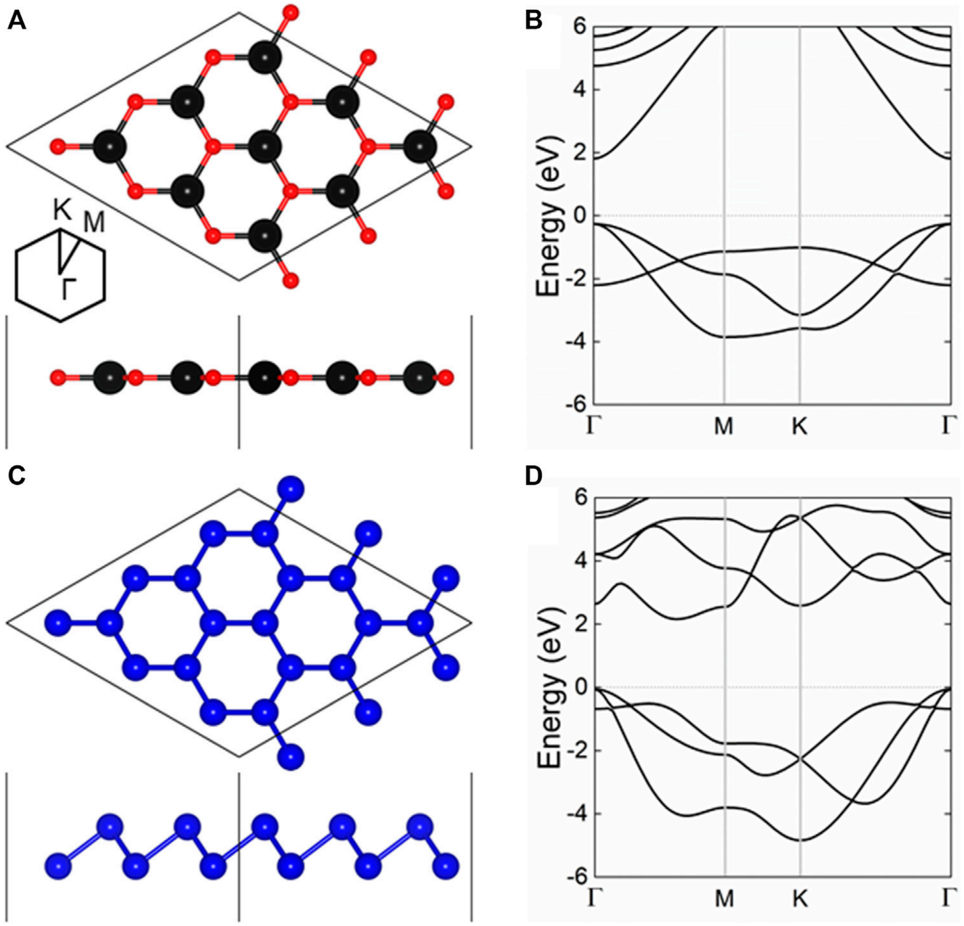

FIGURE 1 | The **(A,C)** crystal structure and the **(B,D)** band structure of the **(A,B)** CdO and **(C,D)** As monolayers; the black, red and blue balls represent Cd, O and As atoms, respectively; the Fermi level is 0 shown as gray dashed line.

As heterostructure, respectively. Besides, the energy band structures of monolayered CdO and As are calculated by HSE06 method, shown in **Figures 1B,D**, respectively. It can be clearly seen that monolayered CdO and As are semiconductors with the band gaps of 2.073 and 2.234 eV, respectively. For single-layer CdO, the CBM and VBM are located at *Γ* point, showing a direct bandgap structure. While the CBM of As monolayer is located between *Γ* and M points, the VBM exists at Γ points. Besides, the bond lengths of Cd–O and As–As in single-layer CdO and single-layer As were calculated to be 2.127 and 2.506 Å, respectively. Furthermore, all the above calculated results of CdO and As are almost consistent with previous investigations (Ren et al., 2020c; Zhao et al., 2021).

When monolayered CdO and As combine to form a heterostructure, 6 most representative highly symmetrical configurations have be considered. The side and top views of these 6 stacking combinations are shown in **Figure 2**. Among these 6 heterostructures, the most stable structure is determined by the binding energy (E_{binding}) between single-layer CdO and As. The investigation shows that the smaller the binding energy is, the more stable the heterostructure is (Singh et al., 2015). The binding energy of CdO/As heterostructures is determined as following:

$$E_{binding} = E_{\text{CdO/As}} - E_{\text{CdO}} - E_{\text{As}}, \tag{4}$$

where $E_{\text{CdO/As}}$, E_{CdO} and E_{As} show the total energy of CdO/As heterostructure, single-layer CdO and As respectively. The binding energy of the most stable structure among the 6 stacked heterostructures is $-36.64\,\text{meV/Å}^2$ for the CA_5 configuration, which is smaller than that in the vdW bonding in weak interlayer interactions in graphites of about $-18\,\text{meV/Å}^2$, shown as **Figure 2E**, suggesting that there is also a weak vdW force between CdO and As monolayers (Chen et al., 2013). The optimized bond length of Cd–O and As–As in CdO/As heterostructure are 2.082 and 2.504 Å, respectively, which just changed a little comparing with that in CdO and As monolayers, further showing the vdW interaction in CdO/As heterostructure. At the same time, we calculated the different interface distance (d_{H}) of CdO/As vdW heterostructure, shown in **Table 1**. Furthermore, the discussed properties of the CdO/As vdW heterostructure is based on CA_5 stacking configuration.

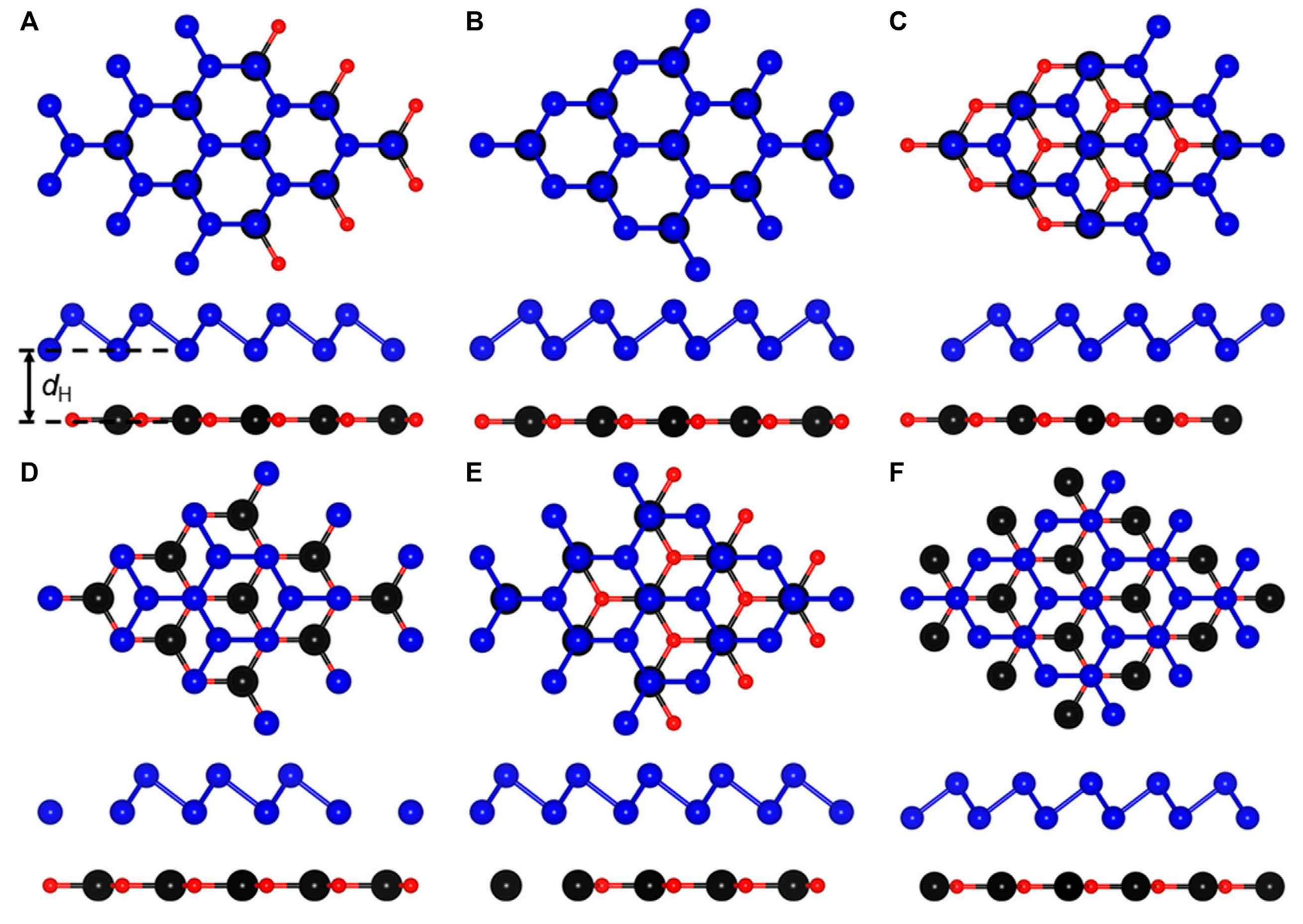

FIGURE 2 | The CdO/As heterostructure constructing by **(A)** CA_1, **(B)** CA_2, **(C)** CA_3, **(D)** CA_4, **(E)** CA_5 and **(F)** CA_6 configurations.

TABLE 1 | The binding energy ($E_{binding}$, meV/Å^2), interface distance (d_H, Å) and the bond length (L, Å) of the different stacking style CdO/As heterostructure.

	$E_{binding}$	d_H	$L_{As\text{–}As}$	$L_{Cd\text{–}O}$
CA_1	−32.07	3.158	2.503	2.082
CA_2	−28.62	3.334	2.509	2.083
CA_3	−32.67	3.119	2.501	2.082
CA_4	−28.19	3.332	2.508	2.084
CA_5	−36.64	2.892	2.504	2.082
CA_6	−35.17	2.972	2.505	2.083

The projected band structure of CdO/As vdW heterostructure is calculated using HSE06 method, shown **Figure 3A**. Obviously, it can be clearly seen that CdO/As vdW heterostructure demonstrates the nature of semiconductor and shows a direct bandgap of 2.179 eV. Besides, it also can be seen that the CBM and VBM of CdO/As vdW heterostructure are located as Γ point contributed by As and CdO monolayers, respectively, which reveals a type-II band style. Then, such type-II band structure is further proved using the band-resolved charge densities for the CdO/As vdW heterostructure shown in **Figure 3B**. When the CdO/As vdW heterostructure is illuminated by the light, expressed by **Figure 3C** the photogenerated electrons will move from the VB of both CdO and As monolayers to the CB and the holes are keep. Then, by the assistance of the valence band offset (conduction band offset), the photogenerated electrons (holes) at CB (VB) of the CdO (As) layer migrate to the CB (VB) of the As (CdO) layer, thus, the photogenerated electrons and holes are effectively separated. Therefore, the gained type-II band alignment of CdO/As vdW heterostructure can effectively resist the recomposite of photogenerated electrons and holes, showing potential candidate use in application as a photocatalyst for water splitting.

Next, we explain how the direct Z-scheme structure can be used as a photocatalyst in CdO/As vdW heterostructure. It is of great significance to calculate the work function (W) difference between single-layer CdO and single-layer As, which is a prerequisite for driving charge redistribution and forming built-in electric field through CdO/As vdW heterostructure interface (Bai et al., 2015; Liu et al., 2016). Shown in **Figure 4A**, Before the intercourse of single-layer CdO and single-layer As, the work functions of CdO (W_2) and As (W_1) are calculated to be 5.783 and 5.443 eV respectively. It can be seen from the calculation results that W_1 is less than W_2. According to the electron transfer mechanism, it can be concluded that

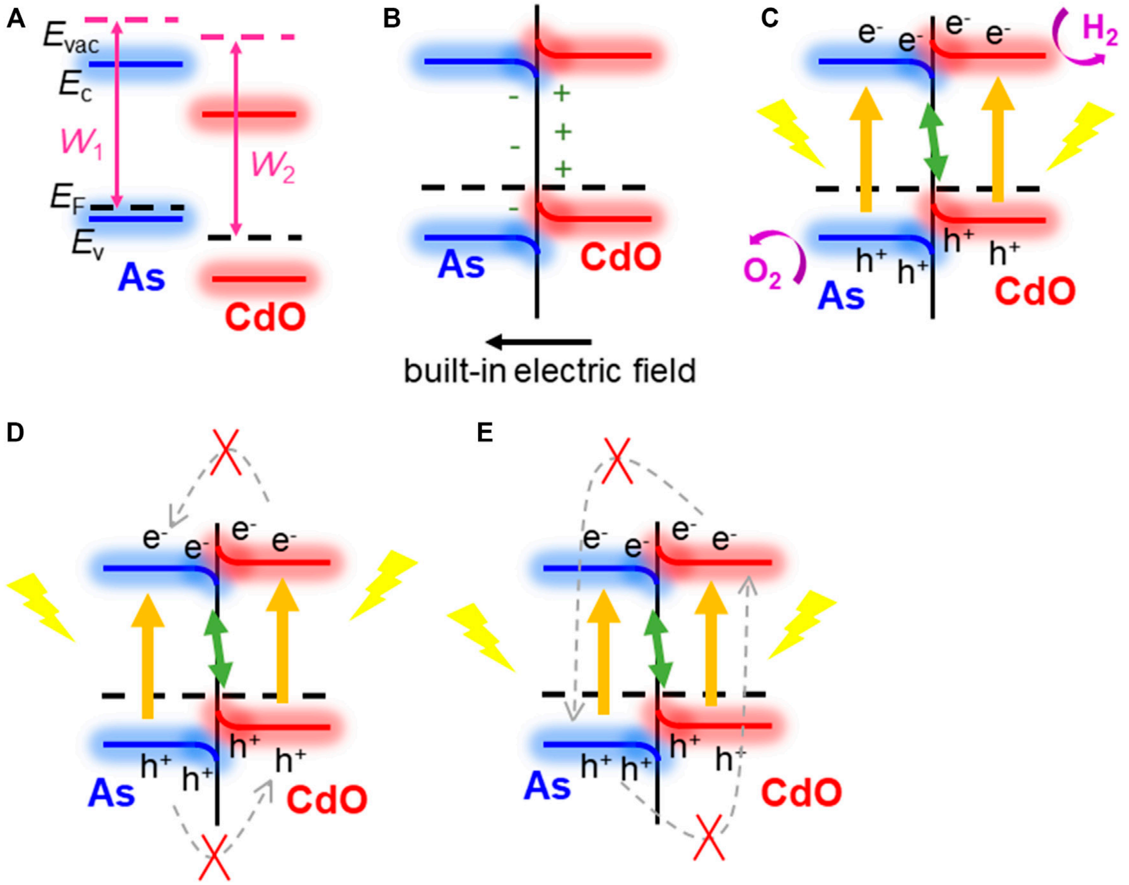

FIGURE 3 | (A) The projected band structure and **(B)** the band-resolved charge densities of the CdO/As vdW heterostructure; the Fermi level is zero energy indicated by gray dashed line. **(C)** Schematic of the migration for the CdO/As vdW heterostructure using as a photocatalyst.

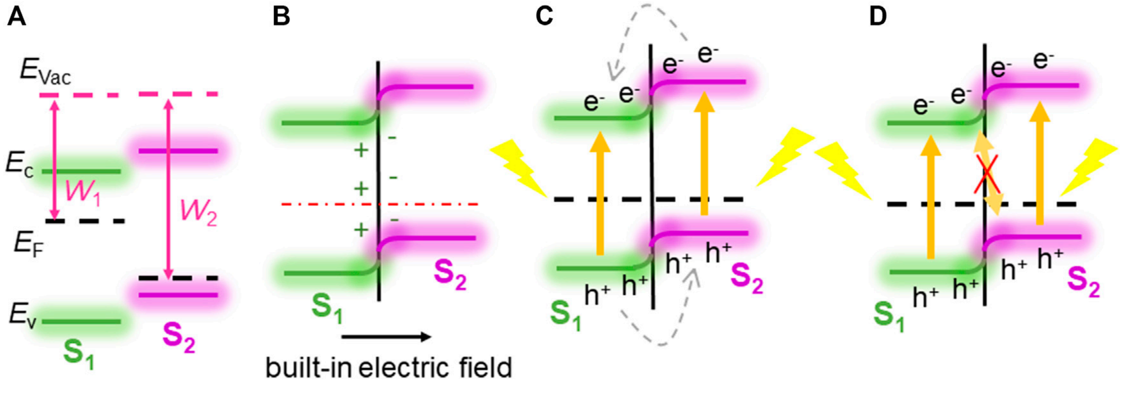

FIGURE 4 | The direct Z-scheme mechanism demonstration for CdO/As vdW heterostructure: **(A)** before combining, **(B)** in combining; **(C–E)** photoinduced charge carrier migration process.

electrons will be transferred from CdO layer to As layer until the Fermi level conforms to the equilibrium of Anderson rule (Zhang and Yates, 2012), shown in **Figure 4B**. Due to the transfer of electrons from CdO layer to As layer, positive holes are left in CdO layer, while negative electrons are accumulated in As layer, and a built-in electric field is generated at the interface. Subsequently, the electrons in the CdO layer and the negative charges in the As layer repel each other, which leads to the

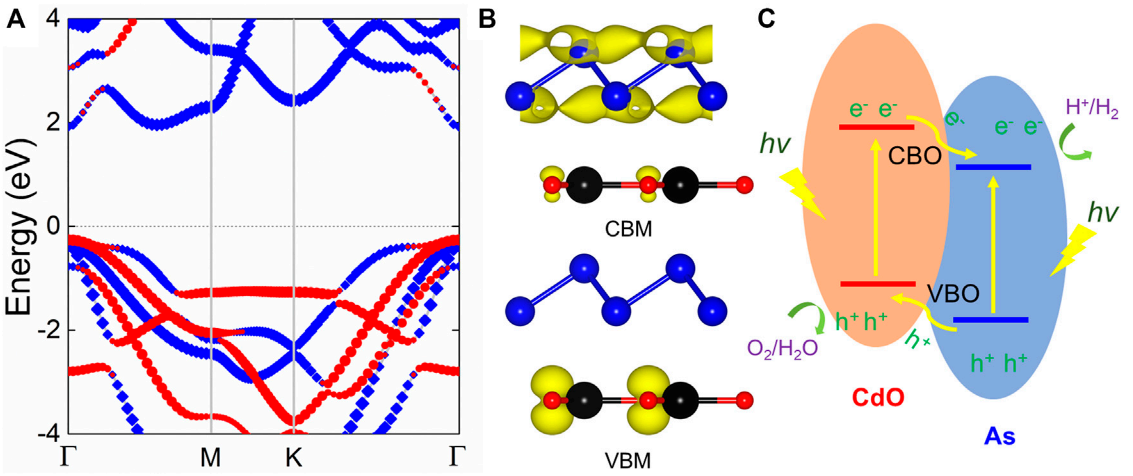

FIGURE 5 | The p–n heterostructure schematic illustration: **(A)** before combining, **(B)** in combining, **(C)** transformation of photogenerated charge carriers in p–n heterostructure, and **(D)** suppressed transformation of photogenerated charge carrier in direct Z-scheme style.

upward bending of the CdO band and the downward bending of the As layer at the interface for the same reason (Zhang and Yates, 2012; Huang et al., 2017). After photon excitation, both CdO and As can induce electrons and holes, as shown in **Figure 4C**. In this case of band bending, it is best to use the direct Z-scheme to transform the structure (Xu et al., 2018). The bending mode and built-in electric field of the band support the recomposite of light photogenerated holes in the VB of the CdO and photogenerated electrons in the CB of the As. Furthermore, this built-in electric field and extra potential barrier, which is also generated by band bending, will obstacle the flowing of the photogenerated electrons from CB of the CdO to the As, and the photogenerated holes from VB of the As to CdO, shown as **Figure 4D**. The built-in electric field also has ability to prevent the recomposite of the photogenerated electron in the CB of the CdO to the holes in the VB of the As, explained as **Figure 4E**. Therefore, the CdO/As vdW heterostructure can be considered as a potential direct Z-type photocatalyst in water splitting.

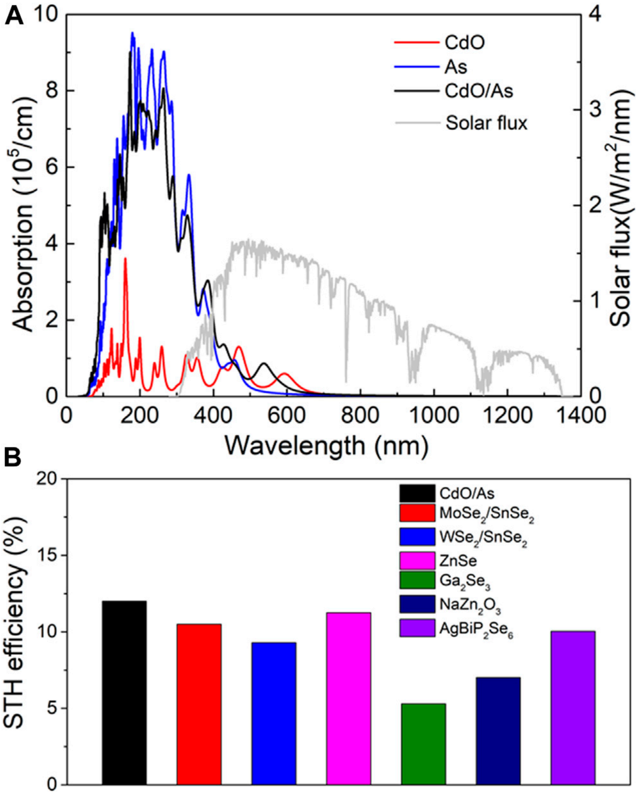

FIGURE 6 | (A) The HSE06 method obtained optical absorption spectrum and **(B)** the STH efficiency of CdO/As vdW heterostructure comparing with other 2D materials (Fan et al., 2019; Jin et al., 2019; Yang et al., 2019).

However, the process that the built-in electric field generated by the band bending trend inducing the photogenerated electrons and holes moving mode provides the Z-scheme photocatalytic mechanism for CdO/As vdW heterostructure to decompose the water is not coincidental. It is contributed form the critical band bending trend of the CdO/As vdW heterostructure. In contrast, another band bending method, such as p–n heterostructure, will not result the Z-scheme photocatalytic path for the photoinduced charges. As shown in **Figure 5A**, when the heterostructure is formed by n-type (work function of W_1) and p-type semiconductors (work function of W_2), the W_1 is smaller than W_2, free electrons can move from n-type material to p-type material, inducing the band of the n-type semiconductor bending upward, while the band of the p-type semiconductor bending downward across the interface of the heterostructure. Subsequently, the built-in electric field is constructed, as shown in **Figure 5B**. Under this built-in electric field assistances, the electrons at the CB of the p-type material will prefer moving to the CB of the n-type material, and the photogenerated holes at the VB of the n-type semiconductor will choose to migrate to the VB of the p-type semiconductor (**Figure 5C**). Moreover, even the

TABLE 2 | The energy conversion efficiency of light absorption (η_{abs}), carrier utilization (η_{cu}) and STH (η_{STH}) of the monolayered CdO, As and CdO/As vdW heterostructure.

2D materials	η_{abs} (%)	η_{cu} (%)	η_{STH} (%)
CdO	63.3	22.6	14.3
As	36.4	28.4	10.3
CdO/As	58.1	20.1	11.67

band alignment of this heterostructure satisfy the band edge positions of the Z-scheme photocatalyst, the built-in electric field resulted by this band bending trend will not boost a combination for the photoinduced electrons at the CB of the n-type semiconductor and the photoinduced holes at the VB of the p-type semiconductor (**Figure 5D**) (Xu et al., 2018). Therefore, the direct Z-scheme mechanism is an intrinsic property of the CdO/As vdW heterostructure.

As a potential candidate for direct Z-scheme photocatalyst to decompose water, the optical property is essential performance to be assessed. The optical absorption spectrum of the CdO, As and CdO/As vdW heterostructure are calculated in **Figure 6A**, which evidently explain the CdO/As vdW heterostructure can improve the visible light absorption capacity (wavelength range 380–800 nm). The obtained excellent absorption peak of the CdO/As vdW heterostructure is 8.47 × 104 cm^{-1} at the wavelength of 542 nm. Besides, enhancing solar energy conversion efficiency is the ultimate target for that, which demonstrates the indeed usage of solar energy for HER and OER (Lu et al., 2019). Therefore, we calculated STH efficiency (η_{STH}) for the CdO/As vdW heterostructure. The obtained η_{abs} and η_{cu} are 58.1 and 20.1%, respectively. The η_{STH} of the monolayered CdO, As and CdO/As vdW heterostructure is also calculated in the **Table 2**. The obtained η_{STH} of the CdO/As vdW heterostructure as 11.67% indicates such Z-scheme photocatalyst possesses a novel STH efficiency, which is also higher than other reported photocatalysts, shown in **Figure 6B**. It worth noting that we assumed the 100% efficiency of the catalytic reaction for the calculations of the STH efficiency (Fu et al., 2018).

CONCLUSIONS

Based on the first-principles calculation, firstly, we systematically studied the geometry and band structure of single-layer CdO and As. Then, the CdO/As heterostructure is constructed using vdW forces possessing a direct bandgap as 2.179 eV and a type-II band alignment structure is realized, which can limit the recomposite of photogenerated electron–hole pairs. Next, the band bending configuration of CdO/As vdW heterostructure is addressed, which demonstrates the potential Z-scheme conversion mechanism using as a photocatalyst for HER and OER. Furthermore, the excellent η_{STH} of CdO/As vdW heterostructure is obtained by 11.67%. All our results show that the CdO/As vdW heterostructure can be used as a potential direct Z-scheme photocatalyst for water splitting.

DATA AVAILABILITY STATEMENT

The raw data supporting the conclusion of this article will be made available by the authors, without undue reservation.

AUTHOR CONTRIBUTIONS

Conceptualization, KR, JL, and RZ; methodology, KR; software, JY; validation, QS; formal analysis, KR and JL; investigation, RZ; resources, KR; data curation, KR; writing—original draft preparation, RZ; writing—review and editing, RZ; visualization, RZ; supervision, QS; project administration, QS; funding acquisition, KR.

ACKNOWLEDGMENTS

This investigation thanks the Collaborative education project of industry university cooperation of the Ministry of Education (Grant number: 202002276033).

REFERENCES

Ali, A., Zhang, J.-M., Shahid, I., Muhammad, I., Ahmad, I., and Kabir, F. (2021). Theoretical study on the electronic structure, optical and photocatalytic properties of type-II As/CdO van der Waals heterostructure. *Physica E: Low-dimensional Syst. Nanostructures* 134, 114888. doi:10.1016/j.physe.2021.114888

Bai, S., Jiang, J., Zhang, Q., and Xiong, Y. (2015). Steering Charge Kinetics in Photocatalysis: Intersection of Materials Syntheses, Characterization Techniques and Theoretical Simulations. *Chem. Soc. Rev.* 44, 2893–2939. doi:10.1039/c5cs00064e

Cai, Y., Zhang, G., and Zhang, Y.-W. (2014). Polarity-Reversed Robust Carrier Mobility in Monolayer MoS_2 Nanoribbons. *J. Am. Chem. Soc.* 136, 6269–6275. doi:10.1021/ja4109787

Capelle, K. (2006). A Bird's-Eye View of Density-Functional Theory. *Braz. J. Phys.* 36, 1318–1343. doi:10.1590/s0103-97332006000700035

Chaurasiya, R., and Dixit, A. (2019). Point Defects Induced Magnetism in CdO Monolayer: A Theoretical Study. *J. Magnetism Magn. Mater.* 469, 279–288. doi:10.1016/j.jmmm.2018.08.076

Chaurasiya, R., Raman, R., Tyagi, S., and Dixit, A. (2019). Strain Modulated Optoelectronic Properties of CdO Monolayer. *J. Elec Materi* 48, 3963–3969. doi:10.1007/s11664-019-07160-3

Chen, X., Tian, F., Persson, C., Duan, W., and Chen, N.-x. (2013). Interlayer Interactions in Graphites. *Sci. Rep.* 3, 3046. doi:10.1038/srep03046

Cui, Z., Luo, Y., Yu, J., and Xu, Y. (2021). Tuning the Electronic Properties of MoSi2N4 by Molecular Doping: A First Principles Investigation. *Physica E: Low-dimensional Syst. Nanostructures* 134, 114873. doi:10.1016/j.physe.2021.114873

Dai, C., Yin, Z., Wang, P., Miao, Q., and Chen, J. (2021). Analysis on Ground Surface in Ultrasonic Face Grinding of Silicon Carbide (SiC) Ceramic with Minor Vibration Amplitude. *Ceramics International* 47, 21959–21968. doi:10.1016/j.ceramint.2021.04.214

Ding, Z., Pei, Q.-X., Jiang, J.-W., Huang, W., and Zhang, Y.-W. (2016). Interfacial thermal Conductance in graphene/MoS_2 Heterostructures. *Carbon* 96, 888–896. doi:10.1016/j.carbon.2015.10.046

Fan, Y., Wang, J., and Zhao, M. (2019). Spontaneous Full Photocatalytic Water Splitting on 2D $MoSe_2$/$SnSe_2$ and WSe_2/$SnSe_2$ vdW Heterostructures. *Nanoscale* 11, 14836–14843. doi:10.1039/c9nr03469b

Fu, C.-F., Sun, J., Luo, Q., Li, X., Hu, W., and Yang, J. (2018). Intrinsic Electric Fields in Two-Dimensional Materials Boost the Solar-To-Hydrogen Efficiency for Photocatalytic Water Splitting. *Nano Lett.* 18, 6312–6317. doi:10.1021/acs.nanolett.8b02561

Fujishima, A., and Honda, K. (1972). Electrochemical Photolysis of Water at a Semiconductor Electrode. *Nature* 238, 37–38. doi:10.1038/238037a0

Geim, A. K., and Novoselov, K. S. (2007). The Rise of Graphene. *Nat. Mater* 6, 183–191. doi:10.1038/nmat1849

Grimme, S., Antony, J., Ehrlich, S., and Krieg, H. (2010). A Consistent and Accurate Ab Initio Parametrization of Density Functional Dispersion Correction (DFT-D) for the 94 Elements H-Pu. *J. Chem. Phys.* 132, 154104. doi:10.1063/1.3382344

Grimme, S. (2006). Semiempirical GGA-type Density Functional Constructed with a Long-Range Dispersion Correction. *J. Comput. Chem.* 27, 1787–1799. doi:10.1002/jcc.20495

He, J., Ding, G., Zhong, C., Li, S., Li, D., and Zhang, G. (2018). Cr_2TiC_2-based Double MXenes: Novel 2D Bipolar Antiferromagnetic Semiconductor with Gate-Controllable Spin Orientation toward Antiferromagnetic Spintronics. *Nanoscale* 11, 356–364. doi:10.1039/c8nr07692h

He, J., Ding, G., Zhong, C., Li, S., Li, D., and Zhang, G. (2019). Remarkably Enhanced Ferromagnetism in a Super-exchange Governed $Cr_2Ge_2Te_6$ Monolayer via Molecular Adsorption. *J. Mater. Chem. C* 7, 5084–5093. doi:10.1039/c8tc05530k

He, J., Hummer, K., and Franchini, C. (2014). Stacking Effects on the Electronic and Optical Properties of Bilayer Transition Metal Dichalcogenides MoS_2, $MoSe_2$, WS_2, and WSe_2. *Phys. Rev. B* 89, 075409. doi:10.1103/physrevb.89.075409

Heyd, J., Scuseria, G. E., and Ernzerhof, M. (2003). Hybrid Functionals Based on a Screened Coulomb Potential. *J. Chem. Phys.* 118, 8207–8215. doi:10.1063/1.1564060

Huang, Z.-F., Song, J., Wang, X., Pan, L., Li, K., Zhang, X., et al. (2017). Switching Charge Transfer of $C_3N_4/W_{18}O_{49}$ from Type-II to Z-Scheme by Interfacial Band Bending for Highly Efficient Photocatalytic Hydrogen Evolution. *Nano Energy* 40, 308–316. doi:10.1016/j.nanoen.2017.08.032

Jin, H., Zhang, H., Li, J., Wang, T., Wan, L., Guo, H., et al. (2019). Data-Driven Systematic Search of Promising Photocatalysts for Water Splitting under Visible Light. *J. Phys. Chem. Lett.* 10, 5211–5218. doi:10.1021/acs.jpclett.9b01977

Kamal, C., and Ezawa, M. (2015). Arsenene: Two-Dimensional Buckled and Puckered Honeycomb Arsenic Systems. *Phys. Rev. B* 91, 085423. doi:10.1103/physrevb.91.085423

Kresse, G., and Joubert, D. (1999). From Ultrasoft Pseudopotentials to the Projector Augmented-Wave Method. *Phys. Rev. B* 59, 1758–1775. doi:10.1103/physrevb.59.1758

Lee, T., Kim, S., and Jang, H. (2016). Black Phosphorus: Critical Review and Potential for Water Splitting Photocatalyst. *Nanomaterials* 6, 194. doi:10.3390/nano6110194

Li, Y., and Chen, X. (2014). Dirac Fermions in Blue-Phosphorus. *2d Mater.* 1, 031002. doi:10.1088/2053-1583/1/3/031002

Liu, E., Chen, J., Ma, Y., Feng, J., Jia, J., Fan, J., et al. (2018). Fabrication of 2D SnS_2/g-C_3n_4 Heterojunction with Enhanced H_2 Evolution during Photocatalytic Water Splitting. *J. Colloid Interf. Sci.* 524, 313–324. doi:10.1016/j.jcis.2018.04.038

Liu, J., Cheng, B., and Yu, J. (2016). A New Understanding of the Photocatalytic Mechanism of the Direct Z-Scheme G-C_3N_4/TiO_2 heterostructure. *Phys. Chem. Chem. Phys.* 18, 31175–31183. doi:10.1039/c6cp06147h

Liu, X., and Li, Z. (2015). Electric Field and Strain Effect on Graphene-MoS_2 Hybrid Structure: Ab Initio Calculations. *J. Phys. Chem. Lett.* 6, 3269–3275. doi:10.1021/acs.jpclett.5b01233

Lou, J., Ren, K., Huang, Z., Huo, W., Zhu, Z., and Yu, J. (2021). Electronic and Optical Properties of Two-Dimensional Heterostructures Based on Janus XSSe (X = Mo, W) and Mg(OH)2: a First Principles Investigation. *RSC Adv.* 11, 29576–29584. doi:10.1039/d1ra05521f

Lu, B., Zheng, X., and Li, Z. (2019). Few-Layer P_4O_2: A Promising Photocatalyst for Water Splitting. *ACS Appl. Mater. Inter.* 11, 10163–10170. doi:10.1021/acsami.8b21001

Luo, Y., Ren, C., Xu, Y., Yu, J., Wang, S., and Sun, M. (2021). A First Principles Investigation on the Structural, Mechanical, Electronic, and Catalytic Properties of Biphenylene. *Sci. Rep.* 11, 19008. doi:10.1038/s41598-021-98261-9

Luo, Y., Ren, K., Wang, S., Chou, J.-P., Yu, J., Sun, Z., et al. (2019). First-Principles Study on Transition-Metal Dichalcogenide/BSe van der Waals Heterostructures: A Promising Water-Splitting Photocatalyst. *J. Phys. Chem. C* 123, 22742–22751. doi:10.1021/acs.jpcc.9b05581

Maeda, K., and Domen, K. (2007). New Non-oxide Photocatalysts Designed for Overall Water Splitting under Visible Light. *J. Phys. Chem. C* 111, 7851–7861. doi:10.1021/jp070911w

Meng, A., Zhu, B., Zhong, B., Zhang, L., and Cheng, B. (2017). Direct Z-Scheme TiO_2/CdS Hierarchical Photocatalyst for Enhanced Photocatalytic H_2-Production Activity. *Appl. Surf. Sci.* 422, 518–527. doi:10.1016/j.apsusc.2017.06.028

Miró, P., Audiffred, M., and Heine, T. (2014). An Atlas of Two-Dimensional Materials. *Chem. Soc. Rev.* 43, 6537–6554. doi:10.1039/c4cs00102h

Perdew, J. P., Burke, K., and Ernzerhof, M. (1996). Generalized Gradient Approximation Made Simple. *Phys. Rev. Lett.* 77, 3865–3868. doi:10.1103/physrevlett.77.3865

Qi, K., Xing, X., Zada, A., Li, M., Wang, Q., Liu, S.-y., et al. (2020). Transition Metal Doped ZnO Nanoparticles with Enhanced Photocatalytic and Antibacterial Performances: Experimental and DFT Studies. *Ceramics Int.* 46, 1494–1502. doi:10.1016/j.ceramint.2019.09.116

Ren, K., Sun, M., Luo, Y., Wang, S., Yu, J., and Tang, W. (2019). First-principle Study of Electronic and Optical Properties of Two-Dimensional Materials-Based Heterostructures Based on Transition Metal Dichalcogenides and boron Phosphide. *Appl. Surf. Sci.* 476, 70–75. doi:10.1016/j.apsusc.2019.01.005

Ren, K., Tang, W., Sun, M., Cai, Y., Cheng, Y., and Zhang, G. (2020). A direct Z-scheme PtS_2/arsenene van der Waals heterostructure with high photocatalytic water splitting efficiency. *Nanoscale* 12, 17281–17289. doi:10.1039/d0nr02286a

Ren, K., Wang, K., Cheng, Y., Tang, W., and Zhang, G. (2020). Two-dimensional Heterostructures for Photocatalytic Water Splitting: a Review of Recent Progress. *Nano Futures* 4, 032006. doi:10.1088/2399-1984/abacab

Ren, K., Wang, S., Luo, Y., Chou, J.-P., Yu, J., Tang, W., et al. (2020). High-efficiency photocatalyst for water splitting: a Janus MoSSe/XN (X = Ga, Al) van der Waals heterostructure. *J. Phys. D: Appl. Phys.* 53, 185504. doi:10.1088/1361-6463/ab71ad

Ren, K., Yu, J., and Tang, W. (2019). A two-dimensional vertical van der Waals heterostructure based on g-GaN and $Mg(OH)_2$ used as a promising photocatalyst for water splitting: A first-principles calculation. *J. Appl. Phys.* 126, 065701. doi:10.1063/1.5099125

Ren, K., Zheng, R., Xu, P., Cheng, D., Huo, W., Yu, J., et al. (2021). Electronic and Optical Properties of Atomic-Scale Heterostructure Based on MXene and MN (M = Al, Ga): A DFT Investigation. *Nanomaterials* 11, 2236. doi:10.3390/nano11092236

Sang, H. L., Parish, C. M., and Xu, J. (2012). Anisotropic Epitaxial ZnO/CdO Core/shell Heterostructure Nanorods. *Nanoscale. Res. Lett.* 7, 626.

Singh, A. K., Mathew, K., Zhuang, H. L., and Hennig, R. G. (2015). Computational Screening of 2D Materials for Photocatalysis. *J. Phys. Chem. Lett.* 6, 1087–1098. doi:10.1021/jz502646d

Subramanyam, T. K., Uthanna, S., and Srinivasulu Naidu, B. (1998). Preparation and Characterization of CdO Films Deposited by Dc Magnetron Reactive Sputtering. *Mater. Lett.* 35, 214–220. doi:10.1016/s0167-577x(97)00246-2

Sun, M., Chou, J.-P., Hu, A., and Schwingenschlögl, U. (2019). Point Defects in Blue Phosphorene. *Chem. Mater.* 31, 8129–8135. doi:10.1021/acs.chemmater.9b02871

Sun, M., Luo, Y., Yan, Y., and Schwingenschlögl, U. (2021). Ultrahigh Carrier Mobility in the Two-Dimensional Semiconductors B_8Si_4, B_8Ge_4, and B_8Sn_4. *Chem. Mater.* 33, 6475–6483. doi:10.1021/acs.chemmater.1c01824

Sun, M., and Schwingenschlögl, U. (2020). B_2P_6: A Two-Dimensional Anisotropic Janus Material with Potential in Photocatalytic Water Splitting and Metal-Ion Batteries. *Chem. Mater.* 32, 4795–4800. doi:10.1021/acs.chemmater.0c01536

Sun, M., and Schwingenschlögl, U. (2021). Structure Prototype Outperforming MXenes in Stability and Performance in Metal-Ion Batteries: A High Throughput Study. *Adv. Energ. Mater.* 11, 2003633. doi:10.1002/aenm.202003633

Sun, M., and Schwingenschlögl, U. (2021). Unique Omnidirectional Negative Poisson's Ratio in δ-Phase Carbon Monochalcogenides. *J. Phys. Chem. C* 125, 4133–4138. doi:10.1021/acs.jpcc.0c11555

Sun, M., and Schwingenschlögl, U. (2020). δ-CS: A Direct-Band-Gap Semiconductor Combining Auxeticity, Ferroelasticity, and Potential for

High-Efficiency Solar Cells. *Phys. Rev. Appl.* 14, 044015. doi:10.1103/physrevapplied.14.044015

Togo, A., Oba, F., and Tanaka, I. (2008). First-principles Calculations of the Ferroelastic Transition between Rutile-type and $CaCl_2$-type SiO_2 at High Pressures. *Phys. Rev. B* 78, 134106. doi:10.1103/physrevb.78.134106

Togo, A., and Tanaka, I. (2015). First Principles Phonon Calculations in Materials Science. *Scripta Materialia* 108, 1–5. doi:10.1016/j.scriptamat.2015.07.021

Vahedi Fakhrabad, D., Shahtahmasebi, N., and Ashhadi, M. (2015). Optical Excitations and Quasiparticle Energies in the AlN Monolayer Honeycomb Structure. *Superlattices and Microstructures* 79, 38–44. doi:10.1016/j.spmi.2014.12.012

Wang, B.-J., Li, X.-H., Cai, X.-L., Yu, W.-Y., Zhang, L.-W., Zhao, R.-Q., et al. (2018). Blue Phosphorus/$Mg(OH)_2$ van der Waals Heterostructures as Promising Visible-Light Photocatalysts for Water Splitting. *J. Phys. Chem. C* 122, 7075–7080. doi:10.1021/acs.jpcc.7b12408

Wang, B., Wang, X., Wang, P., Yang, T., Yuan, H., Wang, G., et al. (2019). Bilayer $MoSe_2$/HfS_2 Nanocomposite as a Potential Visible-Light-Driven Z-Scheme Photocatalyst. *Nanomaterials* 9, 1706. doi:10.3390/nano9121706

Wang, B., Wang, X., Yuan, H., Zhou, T., Chang, J., and Chen, H. (2020). Direct Z-Scheme Photocatalytic Overall Water Splitting on Two Dimensional $MoSe_2$/SnS_2 Heterojunction. *Int. J. Hydrogen Energ.* 45, 2785–2793. doi:10.1016/j.ijhydene.2019.11.178

Wang, G., Gong, L., Li, Z., Wang, B., Zhang, W., Yuan, B., et al. (2020). A Two-Dimensional CdO/CdS Heterostructure Used for Visible Light Photocatalysis. *Phys. Chem. Chem. Phys.* 22, 9587–9592. doi:10.1039/d0cp00876a

Wang, G., Zhang, L., Li, Y., Zhao, W., Kuang, A., Li, Y., et al. (2020). Biaxial Strain Tunable Photocatalytic Properties of 2D ZnO/GeC Heterostructure. *J. Phys. D: Appl. Phys.* 53, 015104. doi:10.1088/1361-6463/ab440e

Xu, G., Yuan, J., Tao, X., Ding, B., Dou, H., Yan, X., et al. (2015). Absorption Mechanism of Carbon-Nanotube Paper-Titanium Dioxide as a Multifunctional Barrier Material for Lithium-Sulfur Batteries. *Nano Res.* 8, 3066–3074. doi:10.1007/s12274-015-0812-0

Xu, Q., Zhang, L., Yu, J., Wageh, S., Al-Ghamdi, A. A., and Jaroniec, M. (2018). Direct Z-Scheme Photocatalysts: Principles, Synthesis, and Applications. *Mater. Today* 21, 1042–1063. doi:10.1016/j.mattod.2018.04.008

Xu, Z., Li, Y., Li, C., and Liu, Z. (2016). Tunable Electronic and Optical Behaviors of Two-Dimensional Germanium Carbide. *Appl. Surf. Sci.* 367, 19–25. doi:10.1016/j.apsusc.2016.01.136

Yang, H., Ma, Y., Zhang, S., Jin, H., Huang, B., and Dai, Y. (2019). GeSe@SnS: Stacked Janus Structures for Overall Water Splitting. *J. Mater. Chem. A.* 7, 12060–12067. doi:10.1039/c9ta02716e

Yang, Q., Tan, C.-J., Meng, R.-S., Jiang, J.-K., Liang, Q.-H., Sun, X., et al. (2017). AlN/BP Heterostructure Photocatalyst for Water Splitting. *IEEE Electron. Device Lett.* 38, 145–148. doi:10.1109/led.2016.2633487

Yong, X., Zhang, J., and Ma, X. (2020). Effects of Intrinsic Defects on the Photocatalytic Water-Splitting Activities of $PtSe_2$. *Int. J. Hydrogen Energ.* 45, 8549–8557. doi:10.1016/j.ijhydene.2020.01.066

Yuan, J., Cai, Y., Shen, L., Xiao, Y., Ren, J.-C., Wang, A., et al. (2018). One-dimensional Thermoelectrics Induced by Rashba Spin-Orbit Coupling in Two-Dimensional BiSb Monolayer. *Nano Energy* 52, 163–170. doi:10.1016/j.nanoen.2018.07.041

Yuan, J., Yang, Y., Cai, Y., Wu, Y., Chen, Y., Yan, X., et al. (2020). Intrinsic Skyrmions in Monolayer Janus Magnets. *Phys. Rev. B* 101, 094420. doi:10.1103/physrevb.101.094420

Yuan, L., Han, C., Yang, M.-Q., and Xu, Y.-J. (2016). Photocatalytic Water Splitting for Solar Hydrogen Generation: Fundamentals and Recent Advancements. *Int. Rev. Phys. Chem.* 35, 1–36. doi:10.1080/0144235x.2015.1127027

Zhang, L., and Singh, D. J. (2009). Electronic Structure and Thermoelectric Properties of Layered PbSe-WSe_2 Materials. *Phys. Rev. B* 80, 075117. doi:10.1103/physrevb.80.075117

Zhang, Z., and Yates, J. T., Jr. (2012). Band Bending in Semiconductors: Chemical and Physical Consequences at Surfaces and Interfaces. *Chem. Rev.* 112, 5520–5551. doi:10.1021/cr3000626

Zhao, H., Li, E., Liu, C., Shen, Y., Shen, P., Cui, Z., et al. (2021). DFT computation of two-dimensional CdO/GaS van der Waals heterostructure: Tunable absorption spectra for water splitting application. *Vacuum* 192, 110434. doi:10.1016/j.vacuum.2021.110434

Zhong, C., Chen, Y., Xie, Y., Sun, Y.-Y., and Zhang, S. (2017). Semi-Dirac Semimetal in Silicene Oxide. *Phys. Chem. Chem. Phys.* 19, 3820–3825. doi:10.1039/c6cp08439g

Zhong, C., Wu, W., He, J., Ding, G., Liu, Y., Li, D., et al. (2019). Two-dimensional Honeycomb Borophene Oxide: strong Anisotropy and Nodal Loop Transformation. *Nanoscale* 11, 2468–2475. doi:10.1039/c8nr08729f

Zhong, C., Zhang, W., Ding, G., and He, J. (2019). Three-dimensional Graphene Networks Modified with Acetylenic Linkages for High-Performance Optoelectronics and Li-Ion Battery Anode Material. *Carbon* 154, 478–484. doi:10.1016/j.carbon.2019.08.030

Zhu, Z., Ren, K., Shu, H., Cui, Z., Huang, Z., Yu, J., et al. (2021). First-Principles Study of Electronic and Optical Properties of Two-Dimensional WSSe/BSe van der Waals Heterostructure with High Solar-to-Hydrogen Efficiency. *Catalysts* 11, 991. doi:10.3390/catal11080991

Zhuang, H. L., and Hennig, R. G. (2013). Computational Identification of Single-Layer CdO for Electronic and Optical Applications. *Appl. Phys. Lett.* 103, 487. doi:10.1063/1.4831972

Conflict of Interest: The authors declare that the research was conducted in the absence of any commercial or financial relationships that could be construed as a potential conflict of interest.

frontiers in Chemistry

REVIEW
published: 06 December 2021
doi: 10.3389/fchem.2021.786607

Research Progress of Gas Sensing Performance of 2D Hexagonal WO_3

Yueqi Li, Qin Zhou, Shoubing Ding and Zhimin Wu**

Chongqing Key Laboratory of Photoelectric Functional Materials, College of Physics and Electronic Engineering, Chongqing Normal University, Chongqing, China

Metal oxide semiconductor gas sensing materials have attracted great research interest in the gas sensor field due to their outstanding physical and chemical properties, low cost, and easy preparation. Among them, two-dimensional hexagonal tungsten trioxide (2D h-WO_3) is especially interesting because of its high sensitivity and selectivity to some gases. We firstly introduce the characteristics of 2D h-WO_3 gas sensing materials and discuss the effects of microstructure, oxygen vacancy, and doping modification on the gas sensing properties of 2D h-WO_3 mainly. Finally, we explore the application of 2D h-WO_3 gas sensing materials and propose some research directions.

Keywords: 2D, hexagonal WO_3, gas sensing, oxygen vacancy, metal oxide semiconductor

Edited by:
Zhaofu Zhang,
University of Cambridge,
United Kingdom

Reviewed by:
Nan Yang,
Xingtai University, China
Hao Luo,
Southwest University of Science and Technology, China
Xiaochuan Duan,
Taiyuan University of Technology, China
Qingkai Qian,
Chongqing University, China

****Correspondence:***
Shoubing Ding
shoubingding@cqnu.edu.cn
Zhimin Wu
zmwu@cqnu.edu.cn

Specialty section:
This article was submitted to Physical Chemistry and Chemical Physics,
a section of the journal Frontiers in Chemistry

Received: *01 October 2021*
Accepted: *08 November 2021*
Published: *06 December 2021*

Citation:
Li Y, Zhou Q, Ding S and Wu Z (2021) Research Progress of Gas Sensing Performance of 2D Hexagonal WO_3. Front. Chem. 9:786607. doi: 10.3389/fchem.2021.786607

INTRODUCTION

As a critical component of the intelligent detection system, the gas sensor (Lee et al., 2018) has been widely used in environmental monitoring (Ji et al., 2019a), respiratory analysis, explosive gases, and automobile exhaust detection. Based on different working mechanisms, the developed gas sensors include semiconductor gas sensors (Morrison, 1987a; Zhang et al., 2021), polymer gas sensors (Zee and Judy, 2001), and electrochemical gas sensors (Tierney and Kim, 1993). Among them, the semiconductor gas sensors can also be divided into resistive and non-resistive types, while the resistive semiconductor gas sensors have advantages of high sensitivity and easy preparation (Seiyama et al., 1962). Meanwhile, compared with carbon and other organic gas sensing materials, the resistive metal oxide gas sensors (Nazemi et al., 2019) have become the research hotspot due to their high responsivity (Demarne and Grisel, 1988) and excellent selectivity (Morrison, 1987b). As a highly sensitive metal oxide gas sensing material, tungsten trioxide (WO_3) has attracted extensive attention because of its unique physical and chemical properties (Salje and Viswanathan, 1975), and its applications in photocatalysis (Dong et al., 2017) and electrochromic (Adhikari and Sarkar, 2014).

WO_3 is a typical metal oxide semiconductor with various phase transition structures, while different phases can induce different gas sensitivity. The stable structures at room temperature are m-WO_3 and h-WO_3. In recent years, as the most stable structure, m-WO_3 has attracted much attention (Hübner et al., 2010; Oison et al., 2011), but bulk m-WO_3 gas sensors are not sensitive to some gases at 25°C–500°C, such as CO (Ahsan et al., 2012) and H_2S (Szilágyi et al., 2010). Therefore, it is urgent to improve the gas sensitivity of WO_3 at room temperature effectively. Xu et al. (2008) found that the sensitivity of h-WO_3 almost linearly increases with CO concentration at room temperature. Szilágyi et al. (2010) found that h-WO_3 becomes more sensitive than m-WO_3 compared to m-WO_3 when the concentration of H_2S is 10 ppm. Meanwhile, the large hexagonal and trigonal tunnel structures of h-WO_3 result in it having a high specific surface area (as shown in **Figure 1**) (Balaji et al., 2009), indicating that h-WO_3 is an excellent candidate material for gas sensors.

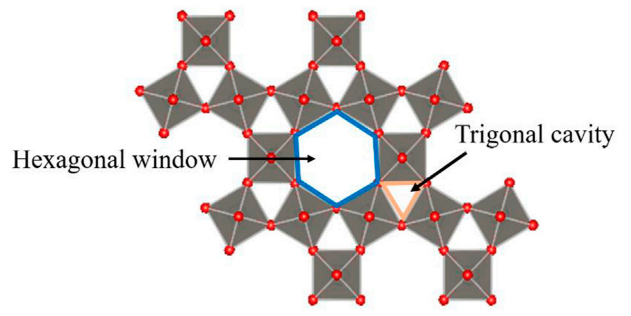

FIGURE 1 | The hexagonal window and trigonal cavity of the hexagonal WO_3(001) surface (Balaji et al., 2009).

To effectively improve the gas sensitivity of the material, various preparation methods have been used to prepare WO_3 nanomaterials on various dimensions (0D, 1D, 2D, and 3D) (Qin et al., 2010; Zhang et al., 2010; D'Arienzo et al., 2014). Among them, 2D nanomaterials are widely used because of their high specific surface area and abundant oxygen vacancies (Yang et al., 2016; Liu et al., 2017; Yang et al., 2017). The unique characteristics of 2D WO_3 nanostructure compared with the bulk material include (1) higher specific surface area, which will provide more interaction area between tested gases and gas sensor surface molecules; (2) quantum confinement effects, due to the inherently small size of nanostructure materials, that can significantly affect charge transport, electronic band structure, and optical properties (Zheng et al., 2011). Based on this, we mainly review the effects of microstructure, oxygen vacancy, and doping modification on the gas sensing performance of 2D h-WO_3 and explore the application prospect of the 2D h-WO_3 gas sensor.

CHARACTERISTICS OF 2D h-WO_3 GAS SENSING MATERIAL

As a kind of metal oxide semiconductor, 2D h-WO_3 gas sensing material has been an excellent candidate material for gas sensors due to its advantages of easy preparation, stable crystal structure, high specific surface area, and abundant oxygen vacancies.

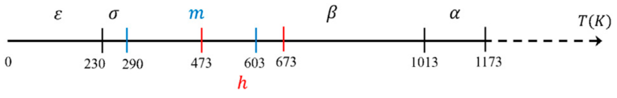

FIGURE 2 | Stability temperature domains of the different polymorphs of WO_3 (Gerand et al., 1979; Roussel et al., 2000).

Easy Preparation

Table 1 shows some typical preparation methods of 2D h-WO_3. Among them, the hydrothermal method is the most widely used. According to this method (Kitagawa et al., 2009; Szilágyi et al., 2010; Ji et al., 2019b), $(NH_4)_{10}W_{12}O_{41}\cdot 5H_2O$ is firstly put into a high-pressure cauldron as the raw material. Then, under high temperature and high pressure, $(NH_4)_{10}W_{12}O_{41}\cdot 5H_2O$ recrystallizes to obtain precipitates (h-WO_3 crystals). Finally, the precipitates are removed and washed several times with deionized water to obtain the final product. Compared with vapor/liquid phase deposition methods, the hydrothermal method is simple and economical, and can prepare nanomaterials with high purity, good chemical uniformity and high dispersion. 2D h-WO_3 is classified as the surface-controlled gas sensor by a gas sensing mechanism.

Stable Crystal Structure

The phases of WO_3 can transform when it is annealed under different conditions. However, it does not simply form new nanostructures, but the original WO_6 octahedron distorts and twists to a certain extent and thus can form different crystal phases. The phase transition with temperature of WO_3 is shown in **Figure 2** (Salje et al., 1997; Vogt et al., 1999; Roussel et al., 2000), which is monoclinic II (ε-WO_3 < –43°C) → triclinic (–43°C < σ-WO_3 < 17°C) → monoclinic I (17°C < m-WO_3 < 330°C) → orthorhombic (330°C < β-O_3 < 740°C) → tetragonal (740°C < α-WO_3). Meanwhile, Gerand et al. (1979) found that stable hexagonal WO_3 (h-WO_3) can be prepared by dehydration method at 200°C–400°C.

Tian et al. (2020) has calculated the gas (O_2) sensing on hexagonal WO_3 (001) surface by using the pseudopotentials method based on the density functional theory (DFT). The formation energy (E_{form}) of the h-WO_3 (001) monolayer is

TABLE 1 | The preparation methods and types of 2D h-WO_3.

Structure	Materials	Method	Gas	Type
2D h-WO_3	Nanosheet	Hydrothermal method	NH_3[a]	Surface-controlled gas sensor
	Nanosheet	Hydrothermal method	H_2S[b]	
	Film	Hydrothermal method	NO_2[c]	
	Film	Sol-gel polymerization	H_2[d]	
	Film	Acidic precipitation	NH_3[e]	

[a] Ji et al.(2019b).
[b] Szilágyi et al.(201).
[c] Kitagawa et al.(2009).
[d] Zhang et al.(2019).
[e] Balázsi et al.(2008).

TABLE 2 | The carrier mobility μ at T = 300 K.

Material	μ (10^3 cm^2 V^{-1} s^{-1})
h-WO_3 monolayer[a]	0.886
Graphene[b]	15.000
InP_3[c]	1.919
SnP_3[d]	7.150
GeP_3[e]	0.360
MoS_2[f]	0.201
2D MoS_2 flake[g]	0.600
SnO_2 bulk[h]	0.160
WO_3 bulk[h]	0.010

[a] Sone et al.(2018).
[b] Novoselov et al.(2004).
[c] Miao et al.(2017).
[d] Ghosh et al.(2018).
[e] Gerand et al.(1979).
[f] Cai et al.(2014).
[g] Alsaif et al.(2016).
[h] Yamazoe et al.(2003).

−5.87 eV, indicating that the h-WO_3 (001) monolayer is stable. The carrier mobility μ calculated from the energy band is 886 $cm^2V^{-1}s^{-1}$ (as shown in **Table 2**) at T = 300 K. The value is higher than that of 2D GeP_3 (Gerand et al., 1979) and MoS_2 (Cai et al., 2014) and is about 88 times higher than that of bulk WO_3 (Yamazoe et al., 2003), which implies that 2D h-WO_3 may have excellent gas sensing performance.

High Specific Surface Area

Sun et al. (2015) investigated the high surface area tunnels in 3D h-WO_3 by low-pressure CO_2 adsorption isotherms with nonlocal density functional theory fitting (NLDET), transmission electron microscopy (TEM), and thermal gravimetric analysis. They found that h-WO_3 has a large hexagonal tunnel structure (the diameter is 3.67 Å) and high specific surface area (45.585 m^2/g). Meanwhile, the large lateral size and ultrathin thickness of 2D materials provide it with ultrahigh specific surface areas and high ratios of exposed surface atoms (Zhang, 2015), significantly improving the gas sensing performance of 2D h-WO_3.

Abundant Oxygen Vacancies

The conduction band of 2D WO_3 mainly consists of W-5d electrons, and the valence band mainly consists of O-2p electrons (Niklasson et al., 2004). Chatten et al. (2005) found that abundant oxygen vacancies are related to the energy gap between O-2p and W-5d orbitals in non-stoichiometric tungsten oxide. Makarov and Trontelj (1996) pointed out that the oxygen vacancies in 2D WO_3 can affect the conductivity and carrier concentration, and further affect the gas sensing performance of WO_3. For example, Tian et al. (2020) found that oxygen vacancies provide electrons to O_2 gas molecules on the WO-terminated h-WO_3 (001) surface, thus effectively improving the gas sensing performance of h-WO_3 (001) surface to O_2.

INFLUENCING FACTORS OF 2D h-WO_3 ON GAS SENSING PERFORMANCE

When the gas sensors are exposed to the air, O_2 molecules are physically or chemically adsorbed on the surface of 2D h-WO_3. The oxygen will be dissociated and capture the electrons from the conduction bands of 2D h-WO_3, generating ionized oxygen species (mainly O^-). This leads to a decrease in the number of electrons on the surface and forming an electron depletion region (EDR), which causes the first change in resistance. When the sensors are exposed to the target gas, the gas molecules are adsorbed on the surface of 2D h-WO_3. Then, the gas molecules react with pre-absorbed oxygen and change the number of the electrons of ionized oxygen species, increasing the density of carriers in the 2D h-WO_3. It results in the second change in resistance (Deng et al., 2015; Li et al., 2015; Liu et al., 2016).

Effect of Microstructure on Gas Sensing Performance of 2D h-WO_3

Figure 3 shows different microstructures of h-WO_3. It can be seen that h-WO_3 nanosheets and films can provide more gas molecular absorption sites because of their obvious orientation, small particle size, large specific surface area, and no agglomeration. However, h-WO_3 nanoparticles, nanowires, and nanospheres have a negative effect on gas transportation and reaction due to serious agglomeration or large particle size. Moreover, we also find from **Table 3** that h-WO_3 nanosheets and films have the highest responsiveness (R) and wider detection scope (S) to H_2, NH_3, H_2S, and NO_2, compared with nanowires, nanorods, nanospheres, and nanoparticles. Different h-WO_3 nanomaterials have exhibited different gas sensing performance due to their different microstructures. Among them, 2D h-WO_3 nanomaterials show important application prospects in the gas sensing field due to their excellent gas sensing performance.

Effect of Oxygen Vacancy on Gas Sensing Performance of 2D h-WO_3

In 1964, Kevane (1964) found that oxygen vacancies are easy to form in the preparation of metal oxide semiconductors. Makarov and Trontelj (1996) found that the oxygen vacancies would affect the conductivity, thus further affecting the gas sensing performance of WO_3. However, the expression of oxygen vacancy on metal oxide semiconductor surfaces is not in agreement (Gillet et al., 2003). Until 2018, Tian et al. (2018) established a theory based on surface oxygen density (*do*) and unitedly expressed the oxygen vacancies on the WO_3 surface (**Table 4**). The O-terminated and WO-terminated h-WO_3 (001) surfaces with and without oxygen vacancy are denoted as O- for O-terminated, Vac O- for defective O-terminated, WO- for WO-terminated, and Vac WO- for defective WO-terminated, respectively. The surface oxygen densities are defined as $d_o = 1$, $1 > d_o > 0$, $d_o = 0$, $0 > d_o > -1$. Based on this, oxygen vacancies of the 2D h-WO_3 surface can be expressed by surface oxygen density.

Recently, Tian et al. (2014) investigated the effect of oxygen vacancy on the gas sensing performance of CO on 2D h-WO_3 (001) surface by using the first-principles calculations (**Table 5**). They found that the adsorption energy and charge transfer of CO of the defective O-terminated h-WO_3 (001) surface decrease by

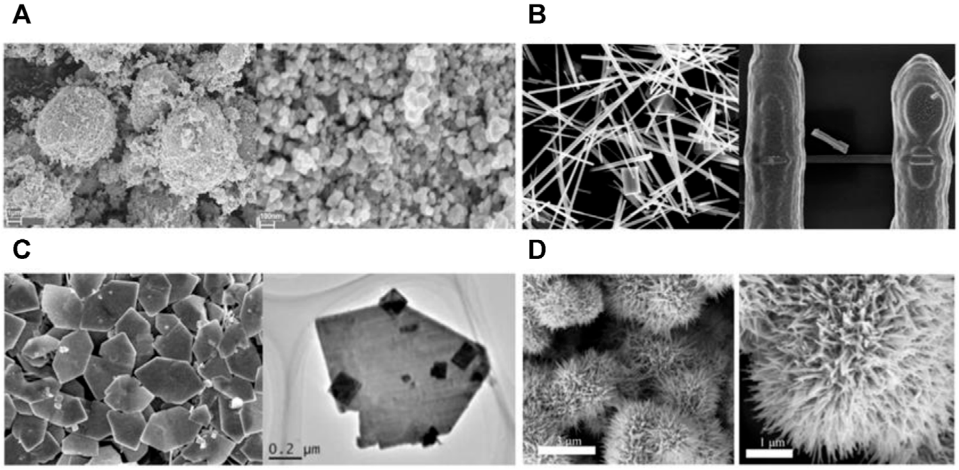

FIGURE 3 | The microstructure of h-WO_3 nanoparticle, nanowire, film, and nanosphere **(A)** 0D h-WO_3 nanoparticle (Szilágyi et al., 2010). **(B)** 1D h-WO_3 nanowire (Liu et al., 2014). **(C)** 2D h-WO_3 film (Meng et al., 2015). **(D)** 3D h-WO_3 nanosphere (Zhang et al., 2019).

TABLE 3 | Relationship between microstructure, particle size, and gas sensitivity of H_2, NH_3, H_2S, and NO_2 in h-WO_3 (*S* is the detection scope, *R* is the responsiveness, and *C* is concentration).

Gas	Material	Size/nm	T/°C	S/ppm	R	
					$R = R_a/R_g$	C/ppm
	Film[a]	110–320	450	200	151.9	200
H_2	Nanoflower[b]	450–600	270	100	2.5–5	100
	Nanosphere[c]	500–2000	250	10–80	0–5	80
	Nanoparticle[d]	50–100	300	10–50	5–5.5	50
NH_3	Nanorod[e]	30–100	400	50–200	22.5	200
	Nanosheet[f]	50–350	350	50–250	36.3	100
	Nanoparticle[g]	50–100	200	—	—	200
H_2S	Nanowire[h]	50–500	20	—	—	—
	Nanosheet[i]	—	330	0–40	45.86	40
	Nanoparticle[j]	700–1,000	75	1–10	5.8	10
NO_2	Film[k]	1,000–2000	200	0.01–0.5	10^4	0–0.1
	Nanosphere[l]	500–2000	250	10–80	60–65	80

[a] *Sone et al.(2018).*
[b] *Zhang et al.(2019).*
[c] *Wei et al.(2017).*
[d] *Wang et al.(2007).*
[e] *Szilágyi et al.(2009).*
[f] *Ji et al.(2019b).*
[g] *Liu et al.(2014).*
[h] *Shi et al.(2016).*
[i] *Szilágyi et al.(2010).*
[j] *Meng et al.(2015).*
[k] *Kitagawa et al.(2009).*
[l] *Zhang et al.(2019).*

0.68 eV and 0.002e, respectively, compared with the O-terminated h-WO_3 (001) surface. For defective WO-terminated, the values of decrease are 0.4 eV and 0.011e, respectively. The result shows that the adsorption and sensing ability of CO on the defective O- and WO-terminated h-WO_3 (001) surface decreases. The oxygen vacancy inhibits the oxidation reaction of reducing gas CO on the 2D h-WO_3 (001) surface, which reduces the gas sensing performance of the 2D h-WO_3.

TABLE 4 | The relationship between surface oxygen vacancy and oxygen density of 2D h-WO_3 (Tian et al., 2018).

2D h-WO_3(001)	Surface oxygen density d_o
O-	1
Vac O-	$1 > d_o > 0$
WO-	0
Vac WO-	$0 > d_o > -1$

Oxygen vacancy also inhibits the gas sensing performance of other reducing gases (H_2S, CH_4, H_2) on the 2D h-WO_3 (001) surface (Szilágyi et al., 2010; Tian et al., 2017; Wu et al., 2019) (**Table 5**). However, the inhibitory effect of oxygen vacancy on H_2S and CH_4 is unapparent. Although the gas sensing performance of H_2S is inhibited by oxygen vacancy, the value (1.85 eV) is still large enough for effective adsorption of H_2S on the surface. The adsorption sensing ability of CH_4 on the 2D h-WO_3 (001) surface is weak and the inhibition of oxygen vacancy makes it difficult to spontaneously adsorb on defective WO-terminated h-WO_3 (001) surface. Moreover, oxygen vacancy has the strongest inhibitory effect on the gas sensing performance of H_2 on the 2D h-WO_3 (001) surface. The adsorption energy decreases from 2.62 to 0.16 eV and the charge transfer decreases from 0.635e to 0.065e. The gas adsorption ability of H_2 on the 2D h-WO_3 (001) surface greatly reduces with the decrease of surface oxygen density.

More recently, Tian et al. (2020) investigated the effect of oxygen vacancy on the gas sensing performance of O_2 on the 2D h-WO_3 (001) surface (**Table 5**) by the first principles with pseudopotentials method based on the DFT. They found that the adsorption energy of O_2 of the defective O-terminated h-WO_3 (001) surface increases by 0.05 eV and the charge transfer decreases by 0.104e compared with the O-terminated h-WO_3 (001) surface. For the defective WO-terminated surface, the values of increase are 5.65 eV and 0.077e, relatively. The result

TABLE 5 | The adsorption energy and charge transfer of O_2, CO, H_2, H_2S, and CH_4 on 2D h-WO_3 (001) surface with oxygen vacancy (d_o is surface oxygen density, C is charge transfer, ΔC is the variation of charge transfer, ↑ is promotion, ↓ is reduction).

Gas	d_o	Configurations	E_{ads}/eV	ΔE_{ads}/eV	C/e	ΔC/e	Effect
CO[a]	1	OC-O_{1c}	2.64	0	0.5	0	—
	$1 > d_o > 0$	OC-O_{1c}	1.96	−0.68	0.498	−0.002	↓
	0	OC-W_{5c}	0.97	0	0.14	0	—
	$0 > d_o > -1$	OC-W_{5c}	0.57	−0.4	-0.129	−0.011	↓
H_2S[b]	1	H_2S/Pt_4	2.78	0	0.483	0	—
	$1 > d_o > 0$	H_2S/Pt_2	1.85	−0.93	0.474	−0.009	↓
H_2[c]	1	H_2-O_{1c}-P	2.62	0	0.635	0	—
	$1 > d_o > 0$	H_2-Pre-O_{1c}	0.60	−2.02	0.621	−0.014	↓
	0	H_2-O_{2c}-P_1	0.19	0	0.09	0	—
	$0 > d_o > -1$	H_2-W_{4c}-P	0.16	−0.03	0.065	−0.025	↓
CH_4[d]	1	H_2CH_2-O_{1c}	0.12	0	0.012	0	—
	$1 > d_o > 0$	HCH_3-W_{5c}	0.18	−0.06	0.049	+0.037	↓
	0	H_2CH_2-W_{5c}	0.11	0	0.01	0	—
	$0 > d_o > -1$	—	−6.15	—	—	—	↓
O_2[e]	1	O_2-O_{1c}-P	0.19	0	0.198	0	—
	$1 > d_o > 0$	O_2-W_{5c}-P	0.24	+0.05	−0.094	−0.104	↑
	0	O_2-O_{1c}-V	1.65	0	−0.389	0	—
	$0 > d_o > -1$	O_2-Vac-V	7.30	+5.65	−0.466	+0.077	↑

[a] Tian et al. (2014).
[b] Szilágyi et al.(2010).
[c] Tian et al.(2017).
[d] Wu et al.(2019).
[e] Tian et al.(2020).

shows that the adsorption and sensing ability of O_2 are improved on the defective O- and WO-terminated h-WO_3 (001) surface. The oxygen vacancy activates the O-O bond of O_2 and promotes the reduction reaction of oxidizing gas O_2 on the 2D h-WO_3 (001) surface, which improves the gas sensing performance of the 2D h-WO_3.

These results indicate that the effect of oxygen vacancy on gases with different redox properties is different. For reducing gases, the oxygen vacancy inhibits their oxidation reactions on the 2D h-WO_3 (001) surface and then reduces the gas sensing performance of the reducing gases. On the contrary, for oxidizing gases, the oxygen vacancy promotes the reduction reaction and then improves the gas sensing performance.

Effect of Doping Modification on Gas Sensing Performance of 2D h-WO_3

Various methods have been performed to improve the gas sensing performance, to overcome the defects of pure metal oxides such as low sensitivity, low selectivity, and long response time for some gases (Liu et al., 2019). Among them, noble metal doping is one of the most common and effective methods. Due to the high electronic activity of noble metal elements, the activation energy of the reaction can be reduced during the contact reaction between the gas sensing material and the target gas, thus improving the gas sensing performance of the materials (Xu et al., 1990) when they react with target gases. Based on this, noble metals such as Au, Ag, Pd, and Pt are usually doped on WO_3 films to improve their sensitivity and selectivity to NO_x (Penza et al., 1998; Chen and Tsang, 2003), H_2S (Stankova et al., 2004; Hurtado-Aular et al., 2021), CH_3COCH_3 (Feng et al., 2021), etc.

TABLE 6 | Adsorption energy and charge transfer of CO and H_2S on noble metal doped 2D h-WO_3 (001) surface.

Gas	Surface	E_{ads}/eV	Charge transfer/e
CO[a]	Clean	−0.69	+0.08
	Cu	−1.79	+0.02
	Ag	−0.97	+0.04
	Au	−2.06	+0.07

[a] Hurtado-Aular et al.(2021).

Recently, the gas sensing performance of CO adsorption on the 2D h-WO_3 (001) surface doped with noble metals Cu, Ag, and Au were investigated by using DFT (as shown in **Table 6**) (Hurtado-Aular et al., 2021). They found that the incorporation of Au and Cu atoms improves the surface activity of the material and the absorptivity of CO on the 2D h-WO_3 (001) surface. Meanwhile, the doped Au and Cu atoms provide a large number of electrons. The charge transfer increases, which effectively improves the sensing performance of CO on the 2D h-WO_3 (001) surface.

Theoretically, noble metal doping promotes the adsorption and sensing ability of the target gas on 2D h-WO_3 surface, and then improves the gas sensing performance of 2D h-WO_3. However, the experimental study on the mechanism of improving the gas sensing performance of noble metal doped h-WO_3 films is still insufficient.

SUMMARY AND PROSPECT

The research progress of the gas sensing performance of 2D h-WO_3 has been reviewed. Firstly, we briefly summarize the characteristics of 2D h-WO_3 gas sensing materials. Then, the effects of microstructure, oxygen vacancy, and doped metal on the performance of 2D h-WO_3 gas sensors are mainly discussed. We find that the 2D h-WO_3 gas sensor has better gas sensing performance than other WO_3 nanomaterials due to their small particle size and large specific surface area. Moreover, the effect of oxygen vacancy on the gas sensitivity of different oxidation-reducing gases on 2D h-WO_3 is different. Besides, we also note that noble metal doping can improve the gas sensing performance of 2D h-WO_3 due to the high electronic activity of noble metals and the reduction of reaction activation energy.

As we all know, 2D h-WO_3 is an excellent candidate material for metal oxide semiconductor gas sensors, which has vital research significance and wide application prospects in gas sensors. However, there are still some unsolved problems in 2D h-WO_3 that need to be completely solved, such as the low sensitivity and low selectivity to some gases. To solve the above problems, the possible solutions include the following: (1) Photoactivation method (i.e., activation of reactants by light), which can improve the sensitivity and selectivity effectively. Deng et al. (2012) activated mesoporous WO_3 sensing material and improved the sensitivity of WO_3 to HCHO by using visible light irradiation at room temperature. Moreover, Trawka et al. (2016) enhanced the sensitivity and selectivity of WO_3-based gas sensors greatly by ultraviolet irradiation. (2) Noble metal doping method improves sensitivity and selectivity. Adding precious metal catalysts has become an important method to improve the gas sensing performance of metal oxide semiconductors, because the catalyst has a great influence on the resistance and sensitivity of semiconductor gas sensing materials (Krebs and Grisel, 1993).

AUTHOR CONTRIBUTIONS

All authors listed have made a substantial, direct, and intellectual contribution to the work, and approved it for publication.

FUNDING

The work described in this paper is supported by Chongqing Natural Science Foundation of China (Grant No. cstc2019jcyj-msxmX0251), the Science and Technology Research Program of Chongqing Education Commission of China (Grant No. KJQN202000505), the Doctoral Fund Project of Chongqing Normal University (Grant No. 20XLB001), and the undergraduate innovation and entrepreneurship training program of Chongqing (Grant No. S202110637121).

REFERENCES

Adhikari, S., and Sarkar, D. (2014). High Efficient Electrochromic WO_3 Nanofibers. *Electrochimica Acta* 138, 115–123. doi:10.1016/j.electacta.2014.06.062

Ahsan, M., Tesfamichael, T., Ionescu, M., Bell, J., and Motta, N. (2012). Low Temperature CO Sensitive Nanostructured WO_3 Thin Films Doped with Fe. *Sensors Actuators B: Chem.* 162 (1), 14–21. doi:10.1016/j.snb.2011.11.038

Alsaif, M. M. Y. A., Chrimes, A. F., Daeneke, T., Balendhran, S., Bellisario, D. O., Son, Y., et al. (2016). High-Performance Field Effect Transistors Using Electronic Inks of 2D Molybdenum Oxide Nanoflakes. *Adv. Funct. Mater.* 26 (1), 91–100. doi:10.1002/adfm.201503698

Balaji, S., Djaoued, Y., Albert, A.-S., Ferguson, R. Z., and Brüning, R. (2009). Hexagonal Tungsten Oxide Based Electrochromic Devices: Spectroscopic Evidence for the Li Ion Occupancy of Four-Coordinated Square Windows. *Chem. Mater.* 21 (7), 1381–1389. doi:10.1021/cm8034455

Balázsi, C., Wang, L., Zayim, E. O., Szilágyi, I. M., Sedlacková, K., Pfeifer, J., et al. (2008). Nanosize Hexagonal Tungsten Oxide for Gas Sensing Applications. *J. Eur. Ceram. Soc.* 28 (5), 913–917. doi:10.1016/j.jeurceramsoc.2007.09.001

Cai, Y., Zhang, G., and Zhang, Y.-W. (2014). Polarity-Reversed Robust Carrier Mobility in Monolayer MoS_2 Nanoribbons. *J. Am. Chem. Soc.* 136 (17), 6269–6275. doi:10.1021/ja4109787

Chatten, R., Chadwick, A. V., Rougier, A., and Lindan, P. J. D. (2005). The Oxygen Vacancy in Crystal Phases of WO_3. *J. Phys. Chem. B* 109 (8), 3146–3156. doi:10.1021/jp045655r

Chen, L., and Tsang, S. C. (2003). Ag Doped WO_3-Based Powder Sensor for the Detection of NO Gas in Air. *Sensors Actuators B: Chem.* 89 (1), 68–75. doi:10.1016/S0925-4005(02)00430-6

D'Arienzo, M., Armelao, L., Mari, C. M., Polizzi, S., Ruffo, R., Scotti, R., et al. (2014). Surface Interaction of WO_3 Nanocrystals with NH_3. Role of the Exposed crystal Surfaces and Porous Structure in Enhancing the Electrical Response. *RSC Adv.* 4 (22), 11012–11022. doi:10.1039/C3RA46726K

Demarne, V., and Grisel, A. (1988). An Integrated Low-Power Thin-Film CO Gas Sensor on Silicon. *Sensors and Actuators* 13 (4), 301–313. doi:10.1016/0250-6874(88)80043-X

Deng, J., Zhang, R., Wang, L., Lou, Z., and Zhang, T. (2015). Enhanced Sensing Performance of the Co_3O_4 Hierarchical Nanorods to NH_3 Gas. *Sensors Actuators B: Chem.* 209, 449–455. doi:10.1016/j.snb.2014.11.141

Deng, L., Ding, X., Zeng, D., Tian, S., Li, H., and Xie, C. (2012). Visible-light Activate Mesoporous WO_3 Sensors with Enhanced Formaldehyde-Sensing Property at Room Temperature. *Sensors Actuators B: Chem.* 163 (1), 260–266. doi:10.1016/j.snb.2012.01.049

Dong, P., Hou, G., Xi, X., Shao, R., and Dong, F. (2017). WO_3-based Photocatalysts: Morphology Control, Activity Enhancement and Multifunctional Applications. *Environ. Sci. Nano* 4 (3), 539–557. doi:10.1039/C6EN00478D

Feng, D.-L., Zhu, Z.-Y., Du, L.-L., Xing, X.-X., Wang, C., Chen, J., et al. (2021). Improved Sensing Performance of WO_3 Nanoparticles Decorated with Ag and Pt Nanoparticles. *Rare Met.* 40 (6), 1642–1650. doi:10.1007/s12598-020-01666-0

Gerand, B., Nowogrocki, G., Guenot, J., and Figlarz, M. (1979). Structural Study of a New Hexagonal Form of Tungsten Trioxide. *J. Solid State. Chem.* 29 (3), 429–434. doi:10.1016/0022-4596(79)90199-3

Ghosh, B., Puri, S., Agarwal, A., and Bhowmick, S. (2018). SnP_3: A Previously Unexplored Two-Dimensional Material. *J. Phys. Chem. C* 122 (31), 18185–18191. doi:10.1021/acs.jpcc.8b06668

Gillet, M., Lemire, C., Gillet, E., and Aguir, K. (2003). The Role of Surface Oxygen Vacancies upon WO_3 Conductivity. *Surf. Sci.* 532-535, 519–525. doi:10.1016/S0039-6028(03)00477-1

Hübner, M., Simion, C. E., Haensch, A., Barsan, N., and Weimar, U. (2010). CO Sensing Mechanism with WO_3 Based Gas Sensors. *Sensors Actuators B: Chem.* 151 (1), 103–106. doi:10.1016/j.snb.2010.09.040

Hurtado-Aular, O., Añez, R., and Sierraalta, A. (2021). DFT+U Study of the Electronic Structure Changes of WO_3 Monoclinic and Hexagonal Surfaces upon Cu, Ag, and Au Adsorption. Applications for CO Adsorption. *Surf. Sci.* 714, 121907. doi:10.1016/j.susc.2021.121907

Ji, H., Zeng, W., and Li, Y. (2019a). Gas Sensing Mechanisms of Metal Oxide Semiconductors: a Focus Review. *Nanoscale* 11 (47), 22664–22684. doi:10.1039/C9NR07699A

Ji, H., Zeng, W., Xu, Y., and Li, Y. (2019b). Nanosheet-assembled Hierarchical WO_3 Flower-like Nanostructures: Hydrothermal Synthesis and NH_3-sensing Properties. *Mater. Lett.* 250, 155–158. doi:10.1016/j.matlet.2019.05.023

Kevane, C. J. (1964). Oxygen Vacancies and Electrical Conduction in Metal Oxides. *Phys. Rev.* 133 (5A), A1431–A1436. doi:10.1103/PhysRev.133.A1431

Kitagawa, C., Takahashi, A., Okochi, Y., and Tamaki, J. J. S. (2009). WO_3 Crystals and Their NO_2-Sensing Properties. *Sensors Mater.* 21 (5), 259–264. doi:10.18494/SAM.2009.611

Krebs, P., and Grisel, A. (1993). A Low Power Integrated Catalytic Gas Sensor. *Sensors Actuators B: Chem.* 13 (1), 155–158. doi:10.1016/0925-4005(93)85349-F

Lee, E., Yoon, Y. S., and Kim, D.-J. (2018). Two-Dimensional Transition Metal Dichalcogenides and Metal Oxide Hybrids for Gas Sensing. *ACS Sens.* 3 (10), 2045–2060. doi:10.1021/acssensors.8b01077

Li, L., Zhang, C., and Chen, W. (2015). Fabrication of SnO_2-SnO Nanocomposites with P-N Heterojunctions for the Low-Temperature Sensing of NO_2 Gas. *Nanoscale* 7 (28), 12133–12142. doi:10.1039/C5NR02334C

Liu, B., Tang, D., Zhou, Y., Yin, Y., Peng, Y., Zhou, W., et al. (2014). Electrical Characterization of H_2S Adsorption on Hexagonal WO_3 Nanowire at Room Temperature. *J. Appl. Phys.* 116 (16), 164310. doi:10.1063/1.4898127

Liu, T., Liu, J., Hao, Q., Liu, Q., Jing, X., Zhang, H., et al. (2016). Porous Tungsten Trioxide Nanolamellae with Uniform Structures for High-Performance Ethanol Sensing. *CrystEngComm* 18 (43), 8411–8418. doi:10.1039/C6CE01587E

Liu, W., Qu, Y., Li, H., Ji, F., Dong, H., Wu, M., et al. (2019). Nanostructure Bi_2WO_6: Surfactant-Assisted Hydrothermal Synthesis for High Sensitive and Selective Sensing of H_2S. *Sensors Actuators B: Chem.* 294, 224–230. doi:10.1016/j.snb.2019.05.042

Liu, X., Ma, T., Pinna, N., and Zhang, J. (2017). Two-Dimensional Nanostructured Materials for Gas Sensing. *Adv. Funct. Mater.* 27 (37), 1702168. doi:10.1002/adfm.201702168

Makarov, V. O., and Trontelj, M. (1996). Sintering and Electrical Conductivity of Doped WO_3. *J. Eur. Ceram. Soc.* 16 (7), 791–794. doi:10.1016/0955-2219(95)00204-9

Meng, Z., Fujii, A., Hashishin, T., Wada, N., Sanada, T., Tamaki, J., et al. (2015). Morphological and crystal Structural Control of Tungsten Trioxide for Highly Sensitive NO_2 Gas Sensors. *J. Mater. Chem. C* 3 (5), 1134–1141. doi:10.1039/C4TC02762K

Miao, N., Xu, B., Bristowe, N. C., Zhou, J., and Sun, Z. (2017). Tunable Magnetism and Extraordinary Sunlight Absorbance in Indium Triphosphide Monolayer. *J. Am. Chem. Soc.* 139 (32), 11125–11131. doi:10.1021/jacs.7b05133

Morrison, S. R. (1987a). Mechanism of Semiconductor Gas Sensor Operation. *Sensors and Actuators* 11 (3), 283–287. doi:10.1016/0250-6874(87)80007-0

Morrison, S. R. (1987b). Selectivity in Semiconductor Gas Sensors. *Sensors and Actuators* 12 (4), 425–440. doi:10.1016/0250-6874(87)80061-6

Nazemi, H., Joseph, A., Park, J., and Emadi, A. (2019). Advanced Micro- and Nano-Gas Sensor Technology: A Review. *Sensors* 19 (6), 1285. doi:10.3390/s19061285

Niklasson, G. A., Berggren, L., and Larsson, A.-L. (2004). Electrochromic Tungsten Oxide: the Role of Defects. *Solar Energ. Mater. Solar Cell* 84 (1), 315–328. doi:10.1016/j.solmat.2004.01.045

Novoselov, K. S., Geim, A. K., Morozov, S. V., Jiang, D., Zhang, Y., Dubonos, S. V., et al. (2004). Electric Field Effect in Atomically Thin Carbon Films. *Science* 306 (5696), 666–669. doi:10.1126/science.1102896

Oison, V., Saadi, L., Lambert-Mauriat, C., and Hayn, R. (2011). Mechanism of CO and O_3 Sensing on WO_3 Surfaces: First Principle Study. *Sensors Actuators B: Chem.* 160 (1), 505–510. doi:10.1016/j.snb.2011.08.018

Penza, M., Martucci, C., and Cassano, G. (1998). NO_x Gas Sensing Characteristics of WO_3 Thin Films Activated by noble Metals (Pd, Pt, Au) Layers. *Sensors Actuators B: Chem.* 50 (1), 52–59. doi:10.1016/S0925-4005(98)00156-7

Qin, Y., Hu, M., and Zhang, J. (2010). Microstructure Characterization and NO_2-Sensing Properties of Tungsten Oxide Nanostructures. *Sensors Actuators B: Chem.* 150 (1), 339–345. doi:10.1016/j.snb.2010.06.063

Roussel, P., Labbé, P., and Groult, D. (2000). Symmetry and Twins in the Monophosphate Tungsten Bronze Series $(PO_2)_4(WO_3)_{2m}$ ($2 \le M \le 14$). *Acta Crystallogr. Sect B* 56 (3), 377–391. doi:10.1107/S0108768199016195

Salje, E. K. H., Rehmann, S., Pobell, F., Morris, D., Knight, K. S., Herrmannsdörfer, T., et al. (1997). Crystal Structure and Paramagnetic Behaviour of. *J. Phys. Condens. Matter* 9 (31), 6563–6577. doi:10.1088/0953-8984/9/31/010

Salje, E., and Viswanathan, K. (1975). Physical Properties and Phase Transitions in WO_3. *Acta Cryst. Sect A.* 31 (3), 356–359. doi:10.1107/S0567739475000745

Seiyama, T., Kato, A., Fujiishi, K., and Nagatani, M. (1962). A New Detector for Gaseous Components Using Semiconductive Thin Films. *Anal. Chem.* 34 (11), 1502–1503. doi:10.1021/ac60191a001

Shi, J., Cheng, Z., Gao, L., Zhang, Y., Xu, J., and Zhao, H. (2016). Facile Synthesis of Reduced Graphene Oxide/hexagonal WO_3 Nanosheets Composites with Enhanced H2S Sensing Properties. *Sensors Actuators B: Chem.* 230, 736–745. doi:10.1016/j.snb.2016.02.134

Sone, B. T., Nkosi, S. S., Nkosi, M. M., Coetsee-Hugo, E., Swart, H. C., and Maaza, M. (2018). Self-assembled Micro-/nanostructured WO_3 Thin Films by Aqueous Chemical Growth and Their Applications in H_2 and CO_2 Sensing. *AIP Conf. Proc.* 1962 (1), 040003. doi:10.1063/1.5035541

Stankova, M., Vilanova, X., Calderer, J., Llobet, E., Ivanov, P., Gràcia, I., et al. (2004). Detection of SO_2 and H_2S in CO_2 Stream by Means of WO_3-Based Micro-hotplate Sensors. *Sensors Actuators B: Chem.* 102 (2), 219–225. doi:10.1016/j.snb.2004.04.030

Sun, W., Yeung, M. T., Lech, A. T., Lin, C.-W., Lee, C., Li, T., et al. (2015). High Surface Area Tunnels in Hexagonal WO_3. *Nano Lett.* 15 (7), 4834–4838. doi:10.1021/acs.nanolett.5b02013

Szilágyi, I. M., Saukko, S., Mizsei, J., Tóth, A. L., Madarász, J., and Pokol, G. (2010). Gas Sensing Selectivity of Hexagonal and Monoclinic WO_3 to H_2S. *Solid State. Sci.* 12 (11), 1857–1860. doi:10.1016/j.solidstatesciences.2010.01.019

Szilágyi, I. M., Wang, L., Gouma, P.-I., Balázsi, C., Madarász, J., and Pokol, G. (2009). Preparation of Hexagonal WO_3 from Hexagonal Ammonium Tungsten Bronze for Sensing NH_3. *Mater. Res. Bull.* 44 (3), 505–508. doi:10.1016/j.materresbull.2008.08.003

Tian, F. H., Gong, C., Peng, Y., and Xue, X. (2017). H_2 Sensing Mechanism under Different Oxygen Concentration on the Hexagonal WO_3 (001) Surface: A Density Functional Theory Study. *Sensors Actuators B: Chem.* 244, 655–663. doi:10.1016/j.snb.2016.12.035

Tian, F. H., Gong, C., Wu, R., and Liu, Z. (2018). Oxygen Density Dominated Gas Sensing Mechanism Originated from CO Adsorption on the Hexagonal WO_3 (001) Surface. *Mater. Today Chem.* 9, 28–33. doi:10.1016/j.mtchem.2018.04.004

Tian, F. H., Liu, Z., Tian, J., and Zhang, Y. (2020). Oxygen Vacancy O-Terminated Surface: The Most Exposed Surface of Hexagonal WO_3 (001) Surface. *Chin. Chem. Lett.* 31 (8), 2095–2098. doi:10.1016/j.cclet.2020.01.015

Tian, F., Zhao, L., Xue, X.-Y., Shen, Y., Jia, X., Chen, S., et al. (2014). DFT Study of CO Sensing Mechanism on Hexagonal WO_3 (001) Surface: The Role of Oxygen Vacancy. *Appl. Surf. Sci.* 311, 362–368. doi:10.1016/j.apsusc.2014.05.069

Tierney, M. J., and Kim, H. O. L. (1993). Electrochemical Gas Sensor with Extremely Fast Response Times. *Anal. Chem.* 65 (23), 3435–3440. doi:10.1021/ac00071a017

Trawka, M., Smulko, J., Hasse, L., Granqvist, C.-G., Annanouch, F. E., and Ionescu, R. (2016). Fluctuation Enhanced Gas Sensing with WO_3-Based Nanoparticle Gas Sensors Modulated by UV Light at Selected Wavelengths. *Sensors Actuators B: Chem.* 234, 453–461. doi:10.1016/j.snb.2016.05.032

Vogt, T., Woodward, P. M., and Hunter, B. A. (1999). The High-Temperature Phases of WO_3. *J. Solid State. Chem.* 144 (1), 209–215. doi:10.1006/jssc.1999.8173

Wang, L., Pfeifer, J., Balázsi, C., and Gouma, P. I. (2007). Synthesis and Sensing Properties to NH3of Hexagonal WO_3 Metastable Nanopowders. *Mater. Manufacturing Process.* 22 (6), 773–776. doi:10.1080/10426910701385440

Wei, S., Zhao, J., Hu, B., Wu, K., Du, W., and Zhou, M. (2017). Hydrothermal Synthesis and Gas Sensing Properties of Hexagonal and Orthorhombic WO_3 Nanostructures. *Ceramics Int.* 43 (2), 2579–2585. doi:10.1016/j.ceramint.2016.11.064

Wu, R., Tian, F., Liu, Z., Xue, X., Zhang, J., and Zu, J. (2019). CH_4 Activation and Sensing on Hexagonal WO_3 (001) and (110) Surfaces. *Appl. Surf. Sci.* 481, 1154–1159. doi:10.1016/j.apsusc.2019.03.094

Xu, Y., Tang, Z., Zhang, Z., Ji, Y., and Zhou, Z. (2008). Large-Scale Hydrothermal Synthesis of Tungsten Trioxide Nanowires and Their Gas Sensing Properties. *Sen Lett.* 6 (6), 938–941. doi:10.1166/sl.2008.534

Xu, Z., Vetelino, J. F., Lec, R., and Parker, D. C. (1990). Electrical Properties of Tungsten Trioxide Films. *J. Vacuum Sci. Technol. A: Vacuum, Surf. Films* 8 (4), 3634–3638. doi:10.1116/1.576517

Yamazoe, N., Sakai, G., and Shimanoe, K. (2003). Oxide Semiconductor Gas Sensors. *Catal. Surv. Asia* 7 (1), 63–75. doi:10.1023/A:1023436725457

Yang, S., Jiang, C., and Wei, S.-h. (2017). Gas Sensing in 2D Materials. *Appl. Phys. Rev.* 4 (2), 021304. doi:10.1063/1.4983310

Yang, W., Gan, L., Li, H., and Zhai, T. (2016). Two-dimensional Layered Nanomaterials for Gas-Sensing Applications. *Inorg. Chem. Front.* 3 (4), 433–451. doi:10.1039/C5QI00251F

Zee, F., and Judy, J. W. (2001). Micromachined Polymer-Based Chemical Gas Sensor Array. *Sensors Actuators B: Chem.* 72 (2), 120–128. doi:10.1016/S0925-4005(00)00638-9

Zhang, C., Debliquy, M., Boudiba, A., Liao, H., and Coddet, C. (2010). Sensing Properties of Atmospheric Plasma-Sprayed WO_3 Coating for Sub-ppm NO_2 Detection. *Sensors Actuators B: Chem.* 144 (1), 280–288. doi:10.1016/j.snb.2009.11.006

Zhang, H. (2015). Ultrathin Two-Dimensional Nanomaterials. *ACS Nano* 9 (10), 9451–9469. doi:10.1021/acsnano.5b05040

Zhang, W.-H., Ding, S.-J., Zhang, Q.-S., Yi, H., Liu, Z.-X., Shi, M.-L., et al. (2021). Rare Earth Element-Doped Porous In_2O_3 Nanosheets for Enhanced Gas-Sensing Performance. *Rare Met.* 40 (6), 1662–1668. doi:10.1007/s12598-020-01607-x

Zhang, Y., Zeng, W., and Li, Y. (2019). NO_2 and H_2 Sensing Properties for Urchin-like Hexagonal WO_3 Based on Experimental and First-Principle Investigations. *Ceramics Int.* 45 (5), 6043–6050. doi:10.1016/j.ceramint.2018.12.075

Zheng, H., Ou, J. Z., Strano, M. S., Kaner, R. B., Mitchell, A., and Kalantar-zadeh, K. (2011). Nanostructured Tungsten Oxide - Properties, Synthesis, and Applications. *Adv. Funct. Mater.* 21 (12), 2175–2196. doi:10.1002/adfm.201002477

Conflict of Interest: The authors declare that the research was conducted in the absence of any commercial or financial relationships that could be construed as a potential conflict of interest.

frontiers in Materials

ORIGINAL RESEARCH
published: 14 December 2021
doi: 10.3389/fmats.2021.806466

Theoretical Insight Into Diamond Doping and Its Possible Effect on Diamond Tool Wear During Cutting of Steel

Li Hao [1]*, Sergei Manzhos [2]* and Zhijun Zhang [3]

[1] *Country State Key Laboratory of Chem/Bio-Sensing and Chemometrics, College of Chemistry and Chemical Engineering, Hunan University Changsha, Changsha, China,* [2] *Ihara-Manzhos Laboratory, Meguro Yokohama Tamachi, Tokyo Institute of Technology, Tokyo, Japan,* [3] *Key Laboratory of Surface and Interface Science of Polymer Materials of Zhejiang Province, Department of Chemistry, Zhejiang Sci-Tech University, Hangzhou, China*

Natural diamond tools experience wear during cutting of steel. As reported in our previous work, Ga doping of diamond has an effect on suppressing graphitization of diamond which is a major route of wear. We investigate interstitial and substitutional dopants of different valence and different ionic radii (Ga, B, and He) to achieve a deeper understanding of inhibiting graphitization. In this study, *ab initio* calculations are used to explore the effects of three dopants that might affect the diamond wear. We consider mechanical effects *via* possible solution strengthening and electronic effects *via* dopant-induced modifications of the electronic structure. We find that the bulk modulus difference between pristine and doped diamond is clearly related to strain energies. Furthermore, boron doping makes the resulting graphite with stable sp2 hybridization more perfect than diamond, but Ga-doped diamond needs 2.49 eV to form the two graphene-like layers than only one layer, which would result in the suppressed graphitization and reduced chemical wear of the diamond tool.

Keywords: diamond tool wear, ab initio calculation, doping, mechanical properties, graphitization

OPEN ACCESS

Edited by:
Guangzhao Wang,
Yangtze Normal University, China

Reviewed by:
Liyuan Huai,
Ningbo Institute of Materials Technology and Engineering (CAS), China
Shuijian He,
Nanjing Forestry University, China

****Correspondence:***
Li Hao
haoli2018sg@gmail.com
Sergei Manzhos
sergei.manzhos@gmail.com

Specialty section:
This article was submitted to Computational Materials Science, a section of the journal Frontiers in Materials

Received: *31 October 2021*
Accepted: *29 November 2021*
Published: *14 December 2021*

Citation:
Hao L, Manzhos S and Zhang Z (2021) Theoretical Insight Into Diamond Doping and Its Possible Effect on Diamond Tool Wear During Cutting of Steel.
Front. Mater. 8:806466.
doi: 10.3389/fmats.2021.806466

INTRODUCTION

In the 21st century, miniaturization has gained rising importance owing to the increasing demand for higher precision and further downsizing of various devices. The ultra-precision processing technology has allowed for higher quality and reliability of products with complex shapes and micro-features. Natural single crystal diamond, said to be the hardest natural material on the Earth, is considered to be an excellent precision cutting tool in high-accuracy microscopic processing due to the excellent thermal conductivity, low thermal expansion, low coefficient of friction, and high wear resistance. It can be machined to form nanometric scale cutting edges and is widely used in ultra-precision machining of non-ferrous metals, optical components, molds, and other parts [Gao and Huang (2017), Wang et al. (2012), Zong et al. (2007), Uddin et al. (2007)].

However, single crystal diamond tools easily suffer excessive wear on their cutting edges when machining ferrous metals [Shimada et al. (2004); de Oliveira et al. (2007)]. Under the catalytic effect of ferrous metals and high interface temperatures, graphitization occurs and diamond in a metastable state transforms into stable layer graphite [Paul et al. (1996), Narulkar et al. (2009)]. Multiple

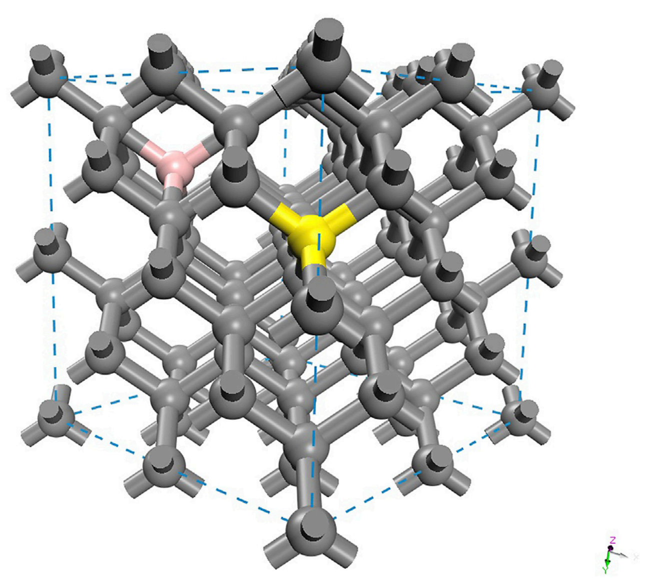

FIGURE 1 | Simulation cell of diamond (dark gray) showing interstitial (pink) and substitutional (golden) positions.

experimental tests were developed to reduce the chemical wear through tool modification techniques to alter the diamond tool properties and suppress the wear initiation process. We reported in a previous study that gallium doping reduced diamond tool wear when cutting steels [Lee et al. (2019)]. Boron-doped diamond, a semiconducting material, has attracted much attention in physics and electrochemistry [Zhao and Larsson (2014), The Anh et al. (2021), Garcia-Segura et al. (2015)]. However, the addition of boron, which in the same group and has a smaller ionic radius than gallium, makes the resulting graphite more perfect [Gu et al. (2016), Bagramov (2021)]. Therefore, it is necessary to have a further understanding of the effects of different dopants on diamond properties and the wear process. The doping effect can differ not only due to different dopant atoms but also due to different doping sites. For example, the same dopant atom can cause p-type doping in substitutional doping and n-type doping in an interstitial position. The smallest inert element He, which has been used to modify the structure and strength of diamond, was also studied as the interstitial dopant [Chen et al. (2020)]. In this study, we investigate *ab initio* calculations, using density functional theory, the effects of doping that might affect the diamond wear. We consider mechanical effects *via* possible solution strengthening and thermodynamic effects *via* dopant-induced modifications at the diamond surface. We compute the effect of interstitial and substitutional dopants of different valence and different ionic radii (Ga, B, and He) to help disambiguate mechanical and thermodynamic effects.

AB INITIO CALCULATIONS

To verify the implications of B-, Ga-, and He-doping in a diamond cutting tool, periodic *ab initio* simulations were performed on pristine and doped diamond materials. The mechanical and thermodynamic effects were assessed with interstitial (I) and substitutional (S) dopants in a cubic diamond cell with 64 C atoms, as shown in **Figure 1**.

B-, Ga-, and He-doped diamond materials were investigated by density functional theory (DFT) performed in the Vienna *ab initio* simulation package (VASP) [Kresse and Hafner (1993), Kresse and Furthmüller (1996), Kresse and Furthmüller (1996)] with the projector-augmented plane-wave method (PAW) [Blöchl (1994), Kresse and Joubert (1999)]. The Perdew–Burke–Ernzerhof (PBE) exchange–correlation functional [Perdew et al. (1996), Perdew et al. (1997)] was used, and a kinetic energy cutoff of 520 eV was selected for the plane wave basis set. Energy and force convergence criteria for electronic and structural relaxations (ion positions and cell vectors) were set at 1×10^{-6} eV and 0.01 eV/Å, respectively. Based on our past theoretical work [Lee et al. (2019)], the theoretical bulk lattice constant of diamond (3.573 A˚) was used, and the Brillouin zone is sampled using a 3 × 3×3Monkhorst–Pack k-point mesh in conventional standard cubic diamond cells (64 C atoms, 7.14 Å × 7.14 Å × 7.14Å). We computed the defect formation energies (E_f), strain energies (E_s), bulk moduli BM, and electronic structures.

For both I and S configurations, the energy required to dope the material is represented by E_f which is expressed as follows:

In the case of substitutional doping:

$$E_f = E(C_{63}M) - \frac{63}{64}E(C_{64}) - E(M). \tag{1}$$

In the case of interstitial doping:

$$E_f = E(C_{64}M) - E(C_{64}) - E(M), \tag{2}$$

where M represents the dopant (B, Ga, or He). E(M) is the energy per atom of M in its bulk He, B, or Ga. E (C_{64}) is the energy of the pure diamond cell with 64 atoms. E $(C_{64}M)$ and E $(C_{63}M)$ are the energies of I- and S-doped systems.

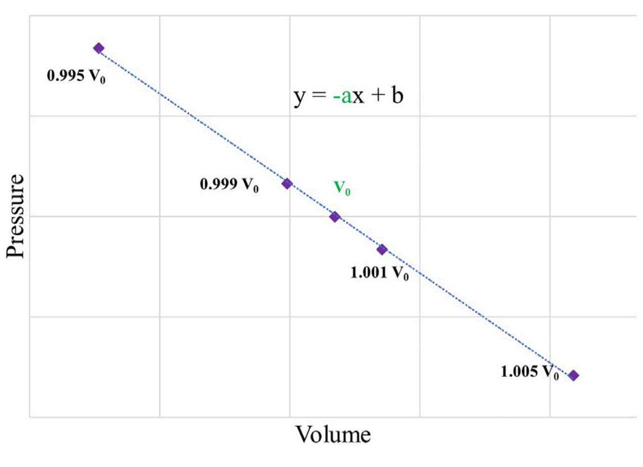

FIGURE 2 | A pressure–volume diagram with the isotropic compression and expansion by −0.5, −0.1, 0.1, and 0.5% of the volume.

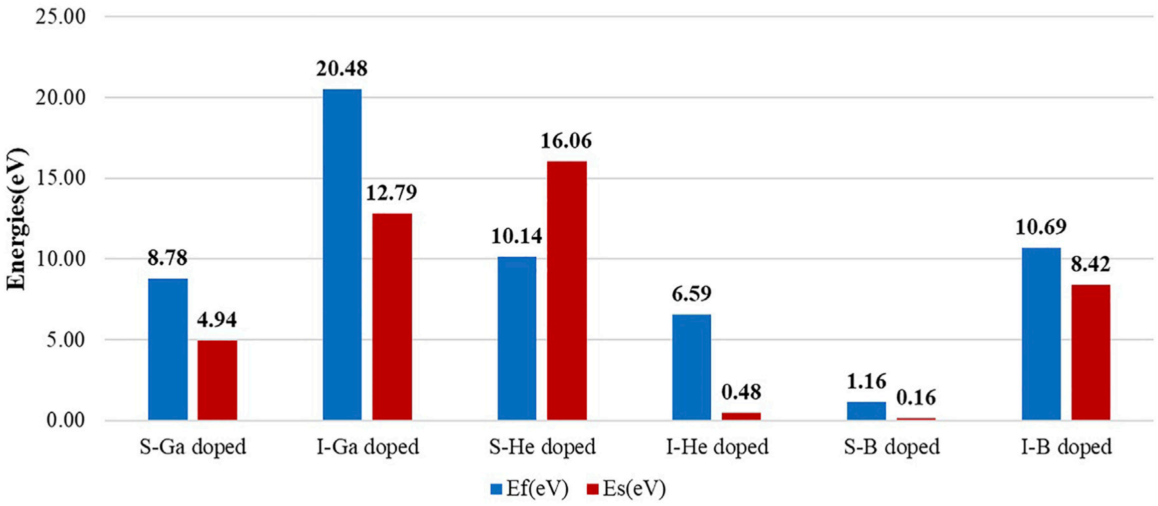

FIGURE 3 | Formation and strain energies for doped diamond materials.

TABLE 1 | The bulk modulus and strain energies of pristine and doped diamond materials. I and S are short for interstitial and substitutional positions. {*labeled results based on the previous theoretical work [Lee et al. (2019)]}.

Systems	B (GPa)	B-doped (Gpa)	Es (eV)
Pristine*	434.47		
Ga (S)*	415.74	429.53	4.94
Ga (I)*	398.30	421.68	12.79
He (S)	411.08	418.41	16.06
He (I)	427.88	433.99	0.48
B (S)	422.94	434.31	0.16
B (I)	410.33	426.05	8.42

The energy required to deform the diamond cell induced by the dopants can be estimated by E_s, where E (MC_{64}—M) is the energy of the distorted diamond material excluding the dopant atom, and E (C_{64}) is the energy of a fully relaxed pristine. In order to exclude the effect of a single vacancy defect on the strain energy, the dopant is replaced by a C atom with the same fractional coordinates in the case of S-doping, while the structure remains distorted.

$$E_s = E(MC_{64} - M) - E(C_{64}). \tag{3}$$

To assess the effects of dopants on the diamond mechanical properties, we also computed the bulk moduli BM. The value was obtained *via* a linear fitting equation with five data points, where P and V are the pressure and volume of a fully relaxed structure. The data points were computed by an isotropic compression and expansion of a simulation cell by −0.5, −0.1, 0.1, and 0.5% of the cell volume, as shown in **Figure 2**. The bulk modulus was computed as

$$BM = -VdP/dV, \tag{4}$$

where V and the derivative are taken at the optimized geometry (V_0 and -a of the linear equation, as marked in **Figure 2**).

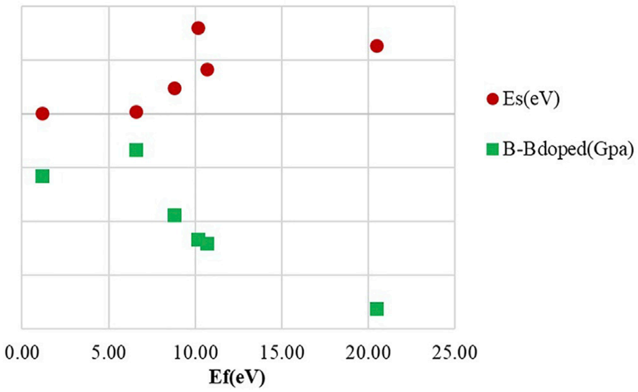

FIGURE 4 | Strain energies and the reduction of bulk modulus for diamond with different dopants.

We also studied the effect of doping on surface energy γ, where E^{hlk}_{slab} is the total energy of the slab structure, E^{hlk}_{bulk} is the energy of the oriented bulk, and A_{slab} is the surface area.

$$\gamma = \frac{E^{hlk}_{slab} - E^{hlk}_{bulk}}{2 \times A_{slab}}. \tag{5}$$

The effect of doping on the surface energy can be related to stability against exfoliation (graphitization) (Lee et al., 2019).

COMPUTATIONAL RESULTS

The defect formation energies of all dopants in interstitial sites are strongly positive, which means that doping is thermodynamically unfavored. Substitutional dopants are strongly energetically preferred to interstitials for both Ga

TABLE 2 | Surface energies for pristine and doped diamond systems with 64˚C atoms [Decreasing (%) is calculated by the formula: $\frac{E1-E2}{E1} \times 100\%$]. {*labeled results based on the previous theoretical work [Lee et al. (2019)]}.

Systems	Surface energies (Kcal*mol^{-1}*Å^{-2})				Decreasing (%)	
	E_1: Pristine*		E_2: Doped diamond			
	(110)	(111)	(110)	(111)	(110)	(111)
Ga doped*	6.85	8.12	6.20	7.85	−9.44%	−3.33%
He doped	6.85	8.12	6.42	7.38	−6.20%	−9.10%
B doped	6.85	8.12	6.55	7.57	−4.39%	−6.67%

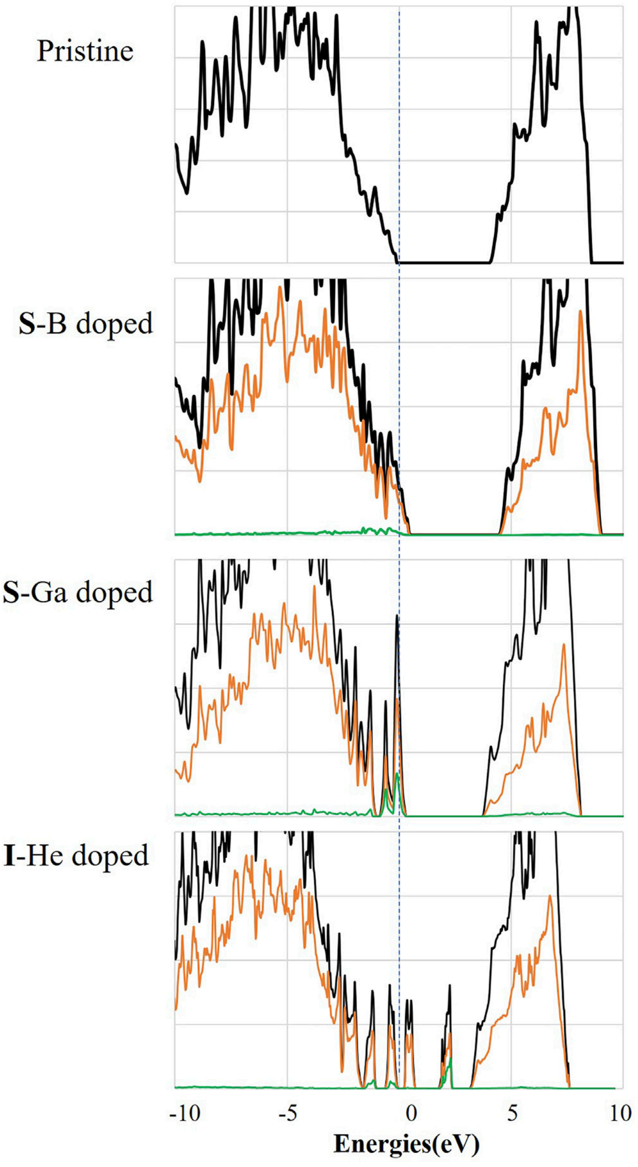

FIGURE 5 | Calculated density of states (DOS) of diamond with different dopants. (The black lines represent the total DOS; brown and green lines represent the PDOS of C atoms and the dopant).

and B dopants. The defect formation energy for a C vacancy in bulk diamond is 5.32 eV. For both substitutional and interstitial doping, the defect formation energies of He doping are strongly positive, 10.14 and 6.59 eV, as shown in **Figure 3**. There is an obvious difference in strain energies with He, 16.06 and 0.48 eV for substitutional and interstitial doping, respectively. The inert element is not chemically reactive and will not bond with other atoms, which results in significant displacements of surrounding C atoms for substitution and a very difficult way to insert but keeping the diamond crystal structure very well. But for B doping, it is obvious to see that the end state of substitution with a formation energy of 1.16 eV is much preferred to an interstitial position (10.69 eV).

The effects of dopants on the bulk modulus are summarized in **Table 1**. The bulk modulus of pristine diamond is computed to be 434 GPa, in good agreement with previously reported values [Brazhkin and Solozhenko (2019)]. The small size of B leads to less softening (422.94 GPa for substitution and 410.33 GPa for insertion) than Ga doping of diamond (415.74 GPa for substitution and 398.30 GPa for insertion) for the same doping position. For He and B dopants, we get close numbers as cross interstitial and substitutional positions. As shown in **Figure 4**, the bulk modulus difference between pristine and doped diamond is clearly related to strain energies. It can be deduced that the larger strain energies led to mechanical softening. Although the reduction in the bulk modulus is observed under the influence of a dopant and may promote wear, the mechanical property is still acceptable for machining purposes. Based on the above results, we will only discuss one favor configuration for each dopant in the following calculation, interstitial He and substitutional structures of B and Ga.

We compute the surface energy of pristine diamond for both (110) and (111) facets, as summarized in **Table 2**. The effects of dopants on the surface energy are summarized in **Table 2**. The surface energy decreasing (%) between pristine and doped diamond systems with 64 C atoms is calculated by the formula: $(\frac{E1-E2}{E1} \times 100\%)$.

Here, the decrease in surface energy is within 10% as compared with pure diamond but varies with that of different dopants. The surface energy of the (110) face decreases by 4.39 ~9.44%. The surface energy of the (111) face decreases by 3.33% for Ga doping, 9.10% for He doping, and 6.67% for B doping. This trend shows that the higher the concentration, the greater will be the decrease. The positive impact of the dopant comes with the lowering of the surface energy of the diamond. Dopants would reduce the surface energy and increase the surface stability of the diamond tool, which can reduce the interaction at the surface.

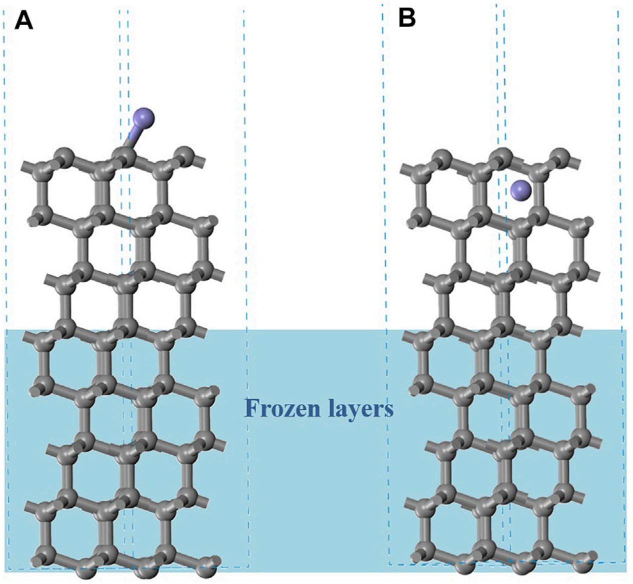

FIGURE 6 | The initial structures of diamond (111) surface with different Fe diffusion locations (purple marked Fe atom position). **(A)** Fe binding on diamond (111) surface, **(B)** Fe inserted into diamond.

The density of states of diamond with three different dopants is provided in **Figure 5**. The total DOS presents separated conduction bands (CB) and valence bands (VB). Partial DOS (PDOS) of B, Ga, and He is also presented as green lines. Compared to the DOS of pure diamond, the DOS is strongly influenced by dopants. Substitutional doping (B and Ga) in diamond moves the Fermi level downward with the reduced band gap. Additionally, interstitial doping (He) moves the Fermi level upward and introduces new energy states in the bandgap. Dopant-induced modifications would have effects on the band alignment at the diamond–iron interface and thereby on possible electrochemical reactions that might facilitate or inhibit the diamond wear.

The diamond cutting ability of ferrous materials is strongly limited due to its extreme affinity to iron; diffusion of Fe is reported into the diamond layer at higher temperatures (from 600°C) [Zenkin et al. (2018)]. In DSC (differential scanning calorimetry) curves, they observed inflection points about 890 °C corresponding to the transition temperature of the diamond graphitization reaction Lee et al., 2019. The {111} plane of diamond would graphitize preferentially, and graphitization occurs when the rings of the {111} plane are flattened [Liang et al. (2012)]. To assess effects of the three dopants on the graphitization process, a diamond (111) surface (5.05 Å × 5.05 Å, 64 C atoms) was constructed with a 15 Å vacuum layer, as shown in **Figure 6**.

In the diffusion process, the Fe atom will be absorbed on the diamond surface first, as shown in (A) of **Figure 6**. The energy required to remove the Fe atom from the diamond (111) surface can be estimated by the binding energy E_{bind}, where $E_{slab+Fe}$ is the total energy of the adsorption configuration. E_{slab} is the energy of the base fragment (diamond surface), and E_{cell} is the energy of unicell Fe in the face-centered cubic (fcc) arrangement with 2 Fe atoms ($n = 2$). The lower the bind energy, the weaker and harder is the Fe atom absorbed on the surface, and this is assumed to reduce the cutting tool wear.

$$E_{bind} = E_{slab+Fe} - E_{slab} - E_{cell}/n \tag{6}$$

According to **Figure 7**, there is no significant difference in the binding energy between He doping and pristine materials (6.81 and 6.78 eV). Ga doping gives a higher binding energy (7.04 eV), and B doping shows the biggest value (8.79 eV). The results indicate that the Fe atom should be much easier to bond to the diamond (111) surface after B doping. It also suggests that B doping might enhance cutting tool wear more than Ga and He doping.

As shown in **Figure 8**, adsorption configurations display that all systems retain the diamond structure very well. Most C-C bonds between different layers change less than 0.1 Å. The structure is distorted only near the doping site with the large size of the Ga atom. As Fe atoms diffuse into diamond, the graphitization process appears with the surface diamond (111) bilayer morphing into a graphene-like layer. Based on Bader charge analysis, the electrons localized in the Fe atoms are listed at

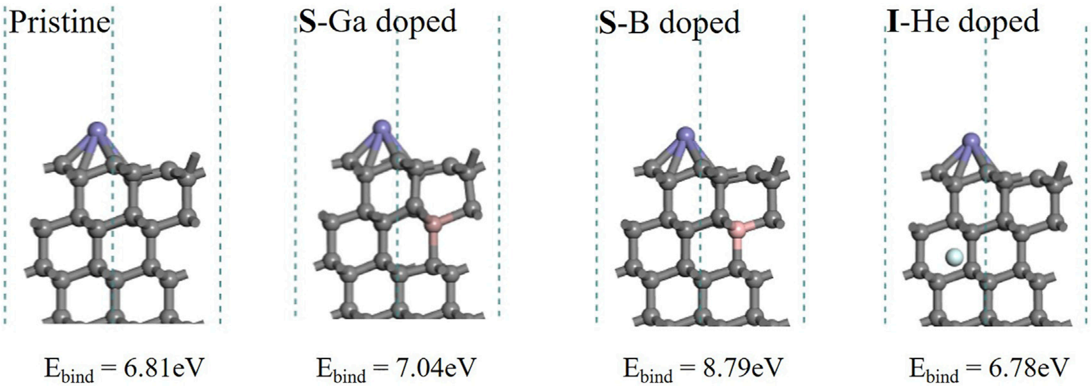

FIGURE 7 | Optimized structures of adsorption configurations with Fe atoms on pristine and doped diamond (111) surfaces.

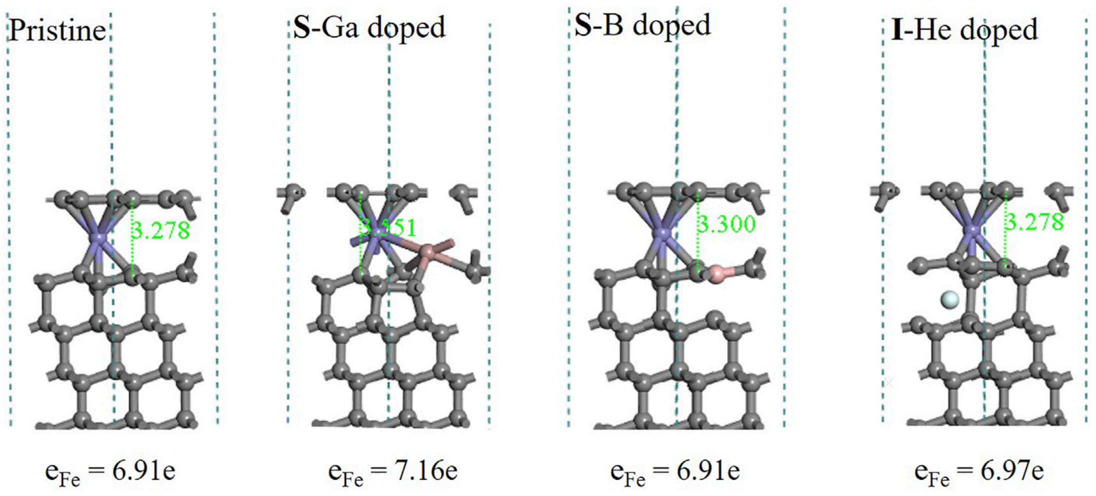

FIGURE 8 | Optimized structures of pristine and doped diamond (111) surfaces with Fe atoms diffused through the top bilayer.

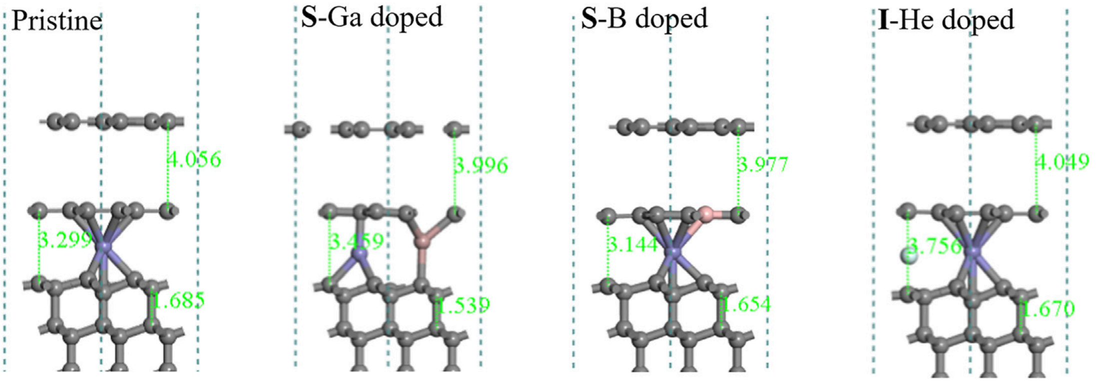

FIGURE 9 | Optimized structures of pristine and doped diamond (111) surfaces with Fe atoms diffused through the second bilayer.

the bottom. Compared to pristine (6.91e), Ga doping will reduce the charge transfer from the Fe atom to surrounding C atoms (7.16e). B and He doping resulted in the graphene-like structure around the doping site.

Figure 9 shows that there is a strong correlation between the degree of graphitization and the position of Fe sites. With Fe atoms diffusing into the diamond lattice, the deeper the Fe position, the more graphene-like layers are formed. The layers are sp^2 hybridized in the plane and weak π bonds to Fe atoms and the diamond substrate. It can be clearly seen that Ga doping makes a C-C bond in the substrate shorter (1.539 Å) than that in pristine diamond (1.685 Å).

Figure 10 reveals thermodynamic effects of different doping on graphitization as Fe atoms diffuse into the diamond lattice. After Fe atoms diffused through the first diamond (111) bilayer, all dopants make sp3-hybridized carbon atoms more susceptible to graphitization in thermodynamics. In the pristine system, there is only 2.42 eV released as one graphene-like layer is formed (3.08, 3.26 and even 9.06 eV released as B, He, and Ga doped). Furthermore, the different and interesting phenomenon occurred while Fe atoms diffused through the second C-C bilayer in the next step. The interstitial He atom is located in the same intermediate layer. He doping made reactants release more energy (5.06), and the exothermic reaction would be much more favorable. Compared to the pristine system, B atoms are given the same fundamental sp^2 hybridized bonds and are more stable than sp^3 hybridized atoms. Therefore, B doping demonstrated a similar phenomenon and may slightly accelerate the reaction. The larger ion radius of Ga results in a stronger interaction with the neighboring C atoms. Ga doping of diamond exhibited a completely opposite trend. It needs 2.49 eV to form another graphene-like layer. It is explained that the graphitization process is inhibited to some extent, with Ga dopants and the chemical wear of the diamond tool being reduced.

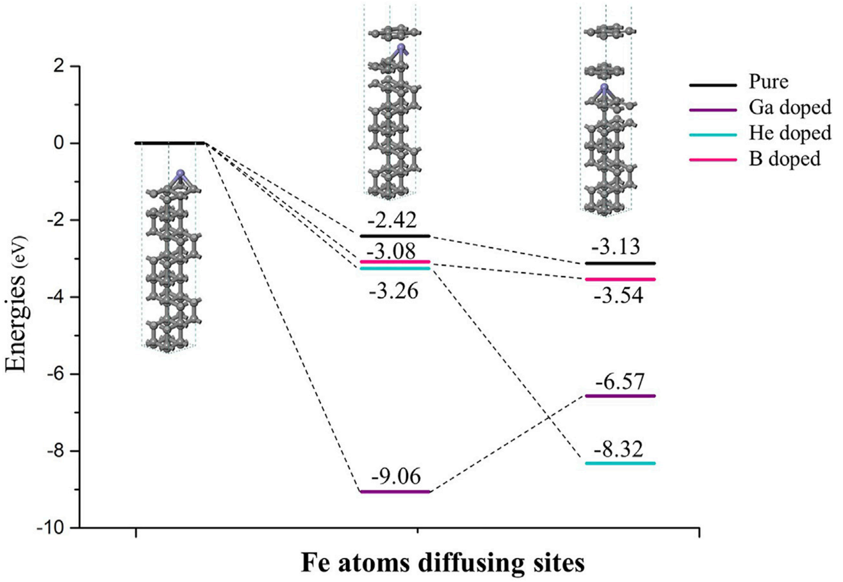

FIGURE 10 | As Fe atoms diffusing into the diamond lattice, thermodynamic effects of different doping on graphitization. The black lines represent the pristine systems without dopants; purple, sky blue and pink lines represent the Ga, He and B doped systems.

CONCLUSION

In this study, *ab initio* calculations are adopted to investigate the mechanical and thermodynamic effects of doping that might affect the diamond wear. We consider interstitial and substitutional dopants of different valence and different ionic radii (Ga, B, and He) to help identify the working principle. To summarize, some conclusions can be drawn.

1) The bulk modulus difference between pristine and the doped diamond is clearly related to strain energies. The larger strain energies led to mechanical softening.
2) All three dopants could reduce the surface energy and increase the surface stability of the diamond tool, which can reduce the interaction at the surface.
3) Three dopants make the diamond (111) surface more susceptible to graphitization in thermodynamics. It is especially favorable for the Ga-doped diamond, 9.06 eV released as the top graphene-like layer formed. The sp^2 hybridized B atoms demonstrated a similar phenomenon with the pristine system. The interstitial He atom was located in the same intermediate layer with diffused Fe atoms, which made the reaction much more favorable.

DATA AVAILABILITY STATEMENT

The original contributions presented in the study are included in the article/supplementary material; further inquiries can be directed to the corresponding authors.

AUTHOR CONTRIBUTIONS

LH carried out the formal analysis, investigation, data curation, writing of the original draft, and review and editing. SM was responsible for conceptualization, formal analysis, and revision. ZZ conducted the formal analysis, investigation, data curation, funding acquisition, and review and editing.

REFERENCES

Bagramov, R. H., Filonenko, V. P., Zibrov, I. P., Skryleva, E. A., Nikolaev, A. V., Pasternak, D. G., et al. (2021). Highly Boron-Doped Graphite and Diamond Synthesized from Adamantane and Ortho-Carborane under High Pressure. Available at: https://arxiv.org/abs/2108.04709.

Blöchl, P. E. (1994). Projector Augmented-Wave Method. *Phys. Rev. B* 50, 17953–17979. doi:10.1103/PhysRevB.50.17953

Brazhkin, V. V., and Solozhenko, V. L. (2019). Myths about New Ultrahard Phases: Why Materials that Are Significantly superior to diamond in Elastic Moduli and Hardness Are Impossible. *J. Appl. Phys.* 125, 130901. doi:10.1063/1.5082739

Chen, M., Best, J. P., Shorubalko, I., Michler, J., Spolenak, R., and Wheeler, J. M. (2020). Influence of Helium Ion Irradiation on the Structure and Strength of diamond. *Carbon* 158, 337–345. doi:10.1016/j.carbon.2019.10.078

de Oliveira, L. J., Bobrovnitchii, G. S., and Filgueira, M. (2007). Processing and Characterization of Impregnated diamond Cutting Tools Using a Ferrous Metal Matrix. *Int. J. Refractory Met. Hard Mater.* 25, 328–335. doi:10.1016/j.ijrmhm.2006.08.006

Gao, S., and Huang, H. (2017). Recent Advances in Micro- and Nano-Machining Technologies. *Front. Mech. Eng.* 12, 18–32. doi:10.1007/s11465-017-0410-9

Garcia-Segura, S., Vieira dos Santos, E., and Martínez-Huitle, C. A. (2015). Role of Sp3/sp2 Ratio on the Electrocatalytic Properties of boron-doped diamond Electrodes: A Mini Review. *Electrochemistry Commun.* 59, 52–55. doi:10.1016/j.elecom.2015.07.002

Gu, C., Li, W., Xu, J., Xu, S., Lu, C., Xu, L., et al. (2016). Graphene Grown Out of diamond. *Appl. Phys. Lett.* 109, 162105. doi:10.1063/1.4964710

Kresse, G., and Furthmüller, J. (1996). Efficiency of Ab-Initio Total Energy Calculations for Metals and Semiconductors Using a Plane-Wave Basis Set. *Comput. Mater. Sci.* 6, 15–50. doi:10.1016/0927-0256(96)00008-0

Kresse, G., and Furthmüller, J. (1996). Efficient Iterative Schemes Forab Initiototal-Energy Calculations Using a Plane-Wave Basis Set. *Phys. Rev. B* 54 (16), 11169–11186. doi:10.1103/physrevb.54.11169

Kresse, G., and Hafner, J. (1993). Ab Initiomolecular Dynamics for Liquid Metals. *Phys. Rev. B* 47, 558–561. doi:10.1103/physrevb.47.558

Kresse, G., and Joubert, D. (1999). From Ultrasoft Pseudopotentials to the Projector Augmented-Wave Method. *Phys. Rev. B* 59, 1758–1775. doi:10.1103/physrevb.59.1758

Lee, Y. J., Hao, L., Lüder, J., Chaudhari, A., Wang, S., Manzhos, S., et al. (2019). Micromachining of Ferrous Metal with an Ion Implanted diamond Cutting Tool. *Carbon* 152, 598–608. doi:10.1016/j.carbon.2019.06.043

Liang, Y. C., Wang, Z. G., Chen, M. J., and Chen, J. X. (2012). The Influence of Crystal Plane on Graphitization of Diamond by Structure Analysis. *Key Eng. Mater.* 522, 142–146. doi:10.4028/www.scientific.net/kem.522.142

Narulkar, R., Bukkapatnam, S., Raff, L. M., and Komanduri, R. (2009). Graphitization as a Precursor to Wear of diamond in Machining Pure Iron: A Molecular Dynamics Investigation. *Comput. Mater. Sci.* 45, 358–366. doi:10.1016/j.commatsci.2008.10.007

Paul, E., Evans, C. J., Mangamelli, A., McGlauflin, M. L., and Polvani, R. S. (1996). Chemical Aspects of Tool Wear in Single point diamond Turning. *Precision Eng.* 18, 4–19. doi:10.1016/0141-6359(95)00019-4

Perdew, J. P., Burke, K., and Ernzerhof, M. (1996). Generalized Gradient Approximation Made Simple. *Phys. Rev. Lett.* 77, 3865–3868. doi:10.1103/physrevlett.77.3865

Perdew, J. P., Burke, K., and Ernzerhof, M. (1997). Generalized Gradient Approximation Made Simple [Phys. Rev. Lett. 77, 3865 (1996)]. *Phys. Rev. Lett.* 78, 1396. doi:10.1103/physrevlett.78.1396

Shimada, S., Tanaka, H., Higuchi, M., Yamaguchi, T., Honda, S., and Obata, K. (2004). Thermo-Chemical Wear Mechanism of Diamond Tool in Machining of Ferrous Metals. *CIRP Ann.* 53, 57–60. doi:10.1016/S0007-8506(07)60644-1

The Anh, L., Catalan, F. C. I., Kim, Y., Einaga, Y., and Tateyama, Y. (2021). Boron Position-dependent Surface Reconstruction and Electronic States of boron-doped diamond(111) Surfaces: an Ab Initio Study. *Phys. Chem. Chem. Phys.* 23, 15628–15634. doi:10.1039/D1CP00689D

Uddin, M. S., Seah, K. H. W., Rahman, M., Li, X. P., and Liu, K. (2007). Performance of Single crystal diamond Tools in Ductile Mode Cutting of Silicon. *J. Mater. Process. Technol.* 185, 24–30. doi:10.1016/j.jmatprotec.2006.03.138

Wang, Z. Y., Dong, L. H., Wang, D. S., and Dong, Y. H. (2012). Study of HPHT Single crystal diamond as Precision Cutting Tool Material. *Precision Eng.* 36, 162–167. doi:10.1016/j.precisioneng.2011.07.009

Zenkin, S., Gaydaychuk, A., Okhotnikov, V., and Linnik, S. (2018). CVD Diamond Interaction with Fe at Elevated Temperatures. *Materials* 11, 2505. doi:10.3390/ma11122505

Zhao, S., and Larsson, K. (2014). Theoretical Study of the Energetic Stability and Geometry of Terminated and B-Doped Diamond (111) Surfaces. *J. Phys. Chem. C* 118, 1944–1957. doi:10.1021/jp409278x

Zong, W. J., Cheng, K., Li, D., Sun, T., and Liang, Y. C. (2007). The Ultimate Sharpness of Single-crystal diamond Cutting Tools-Part I: Theoretical Analyses and Predictions. *Int. J. Machine Tools Manufacture* 47, 852–863. doi:10.1016/j.ijmachtools.2006.04.001

Conflict of Interest: The authors declare that the research was conducted in the absence of any commercial or financial relationships that could be construed as a potential conflict of interest.

frontiers in Materials

ORIGINAL RESEARCH
published: 11 January 2022
doi: 10.3389/fmats.2021.816821

Controlled Growth of Indium Selenides by High-Pressure and High-Temperature Method

Yajie Dai[1], Shouxin Zhao[2], Hui Han[1], Yafei Yan[1], Wenhui Liu[1], Hua Zhu[1], Liang Li[1], Xi Tang[1], Yang Li[2], Hui Li[1]* and Changjin Zhang[1,3]

[1]Institute of Physical Science and Information Technology and Information Materials and Intelligent Sensing Laboratory of Anhui Province, Anhui University, Hefei, China, [2]School of Materials Science and Engineering, Harbin Institute of Technology, Harbin, China, [3]High Magnetic Field Laboratory of Anhui Province, Chinese Academy of Sciences, Hefei, China

The controlled growth of indium selenides has attracted considerable research interests in condensed matter physics and materials science yet remains a challenge due to the complexity of the indium–selenium phase diagram. Here, we demonstrate the successful growth of indium selenides in a controllable manner using the high-pressure and high-temperature growth technique. The γ-InSe and α-In_2Se_3 crystals with completely different stoichiometries and stacking manner of atomic layers have been controlled grown by subtle tuning growth temperature, duration time, and growth pressure. The as-grown γ-InSe crystal features a semiconducting property with a prominent photoluminescence peak of ~1.23 eV, while the α-In_2Se_3 crystal is ferroelectric. Our findings could lead to a surge of interest in the development of the controlled growth of high-quality van der Waal crystals using the high-pressure and high-temperature growth technique and will open perspectives for further investigation of fascinating properties and potential practical application of van der Waal crystals.

Keywords: indium selenides, controlled growth, high-pressure and high-temperature, photoluminescence, ferroelectricity

Edited by:
Zhaofu Zhang,
University of Cambridge,
United Kingdom

Reviewed by:
Hongchao Liu,
University of Macau, China
Kai Xu,
Zhejiang University, China

***Correspondence:**
Hui Li
huili@ahu.edu.cn

Specialty section:
This article was submitted to Computational Materials Science, a section of the journal Frontiers in Materials

Received: *17 November 2021*
Accepted: *02 December 2021*
Published: *11 January 2022*

Citation:
Dai Y, Zhao S, Han H, Yan Y, Liu W, Zhu H, Li L, Tang X, Li Y, Li H and Zhang C (2022) Controlled Growth of Indium Selenides by High-Pressure and High-Temperature Method. Front. Mater. 8:816821. doi: 10.3389/fmats.2021.816821

INTRODUCTION

Indium selenides (In_xSe_y) are group III–VI semiconductors with kinds of In and Se stoichiometries and several structural modifications, for example, InSe with β, ε, and γ phases, and In_2Se_3 with α, β, γ, and σ phases (Butler et al., 2013; Bandurin et al., 2017; Balakrishnan et al., 2018). The rich tapestry of stoichiometries and structures of indium selenides makes them the treasure trove for fascinating properties with prospects in both frontier fundamental research and electronic device design, such as exotic ferroelectricity in α-In_2Se_3, ultrahigh electron mobility ($>10^4$ cm^2 V^{-1} s^{-1} at low temperature) of γ-InSe, and excellent photoresponsivity in β-InSe (Lei et al., 2014; Milutinović et al., 2016; Ding et al., 2017; Tang et al., 2019; Guo et al., 2020; Li et al., 2020; Ding et al., 2021).

Among them, γ-InSe and α-In_2Se_3 are two promising materials that have achieved considerable attention. Both γ-InSe and α-In_2Se_3 are layered structures with the intralayer being covalent bonded and the interlayers being interacted by van der Waals force, as shown in the schematic drawing of crystal structures in **Figure 1**. The γ-InSe consists of quadruple Se-In-In-Se layers in the rhombohedral stacking behavior (**Figure 1A**), while the α-In_2Se_3 is composed of Se-In-Se-In-Se quintuple layers arranged in a rhombohedral ($R3m$) crystal structure (**Figure 1B**) (Butler et al., 2013; Bandurin et al., 2017; Balakrishnan et al., 2018; Tang et al., 2019). Such different stacking behaviors of

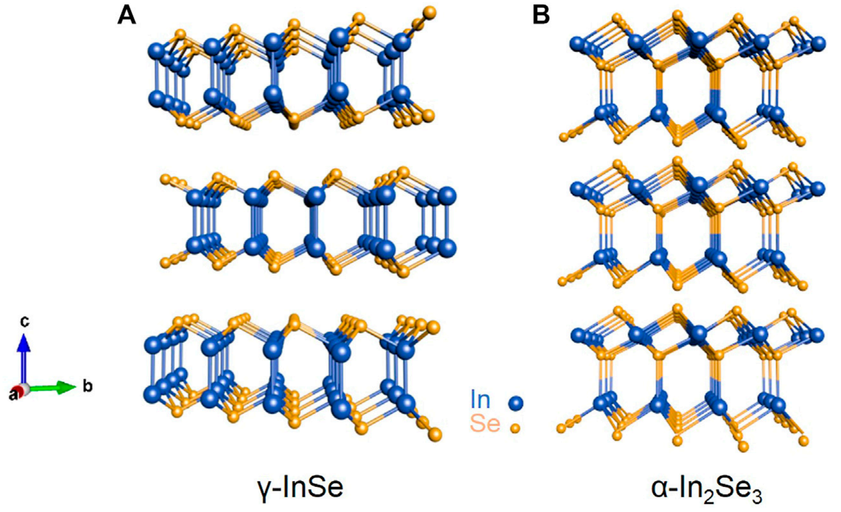

FIGURE 1 | Schematic rhombohedral crystal structure of γ-InSe consisting of quadruple Se-In-In-Se layers **(A)** and α-In_2Se_3 composed of Se-In-Se-In-Se quintuple layers **(B)** in 3D form.

In and Se atoms result in the γ-InSe and α-In_2Se_3 featuring distinct physical properties, which offers a new frontier of investigation on the relationship between the structures and properties. However, it is still a challenge to grow γ-InSe and α-In_2Se_3 in a controllable way because the energy difference between abundant structures of indium selenides is quite small.

Several approaches have been attempted to control grow γ-InSe and α-In_2Se_3, including chemical vapor deposition (CVD), chemical vapor transport (CVT), physical vapor deposition (PVD), pulse laser deposition (PLD), and the Bridgman method (Ishii, 1988; Zhou et al., 2016; Yang et al., 2017; Hu et al., 2018). Although substantial success has been achieved, the controlled growth of γ-InSe and α-In_2Se_3 still suffers from nonuniformity and time-consuming issues. Thus, the development of novel growth techniques is highly desirable. Recently, a few studies reported the utilization of the high-pressure and high-temperature (HPHT) growth method to grow the two-dimensional layered single crystals (Watanabe and Taniguchi, 2019). The high temperature and high pressure facilitate the crystallization and growth of crystals remarkably, which has provided an alternative and effective way toward the controlled growth of single crystals. However, the controlled growth of indium selenides using the HPHT technique has not been investigated. In this work, we systematically investigate the controlled growth of γ-InSe and α-In_2Se_3 using the HPHT growth technique by subtly adjusting the growth temperature, duration time, and the ratios of precursors. The photoluminescence (PL) of the as-grown γ-InSe and the ferroelectricity of the α-In_2Se_3 are further investigated.

RESULTS AND DISCUSSION

The controlled growth of In_xSe_y crystals with different stoichiometries was realized by the HPHT growth technique. **Figure 2** summarizes the controlled growth of In_xSe_y crystals with different stoichiometries by subtle tuning growth temperature, duration time, and the ratios of precursors (precursor In/Se ratio) with the growth pressure of 0.76 GPa. As shown in **Figure 2A**, the crystalline In_xSe_y with mixed stoichiometries of 2:3 and 1:1 is obtained at 250°C with duration time of 20 min and precursor In/Se ratio of 2.1:3. Such a mixing behavior might be due to the nonuniform reaction under the relatively low growth temperature of 250°C, which is very close to the melting points of In (156.6°C) and Se (221°C). Importantly, if we increase the reaction temperature, the mixing behavior could be completely eliminated. As can be seen from **Figure 2A**, crystalline InSe with a stoichiometry of 1:1 could be obtained at growth temperature of 300°C and 350°C, while the crystalline In_2Se_3 with a stoichiometry of 2:3 is eventually achieved as the growth temperature further increases to 400°C with other growth conditions unchanged. The present results are in principle consistent with the provisional equilibrium In-Se binary phase diagram (Lu et al., 1999), in which In_2Se_3 crystals are preferred to be formed at relatively high temperatures.

We further demonstrate that the stoichiometry of the obtained crystals could be effectively modulated by the growth duration time. As shown in **Figure 2B**, the stoichiometry of the obtained crystals changes from 2:3 (i.e., In_2Se_3) to 1:1 (i.e., InSe) with the growth duration time increasing from 10 to 30 min under 0.76 GPa and 400°C with precursor In/Se ratio of 2.1:3, indicating that the longer growth duration time is beneficial for the growth of InSe crystals. Further increasing duration time to 60 min does not change the stoichiometry of the obtained crystals.

In contrast to the growth temperature and duration time, the In/Se ratios of the precursors have no influence on the stoichiometry of the resultant crystals. The InSe crystals with a stoichiometry of 1:1 are obtained even with the precursor In/Se ratio changes in a wide range from 1.8:3 to 3:3 under the growth condition of 0.76 GPa, 400°C, and duration time of 30 min (**Figure 2C**).

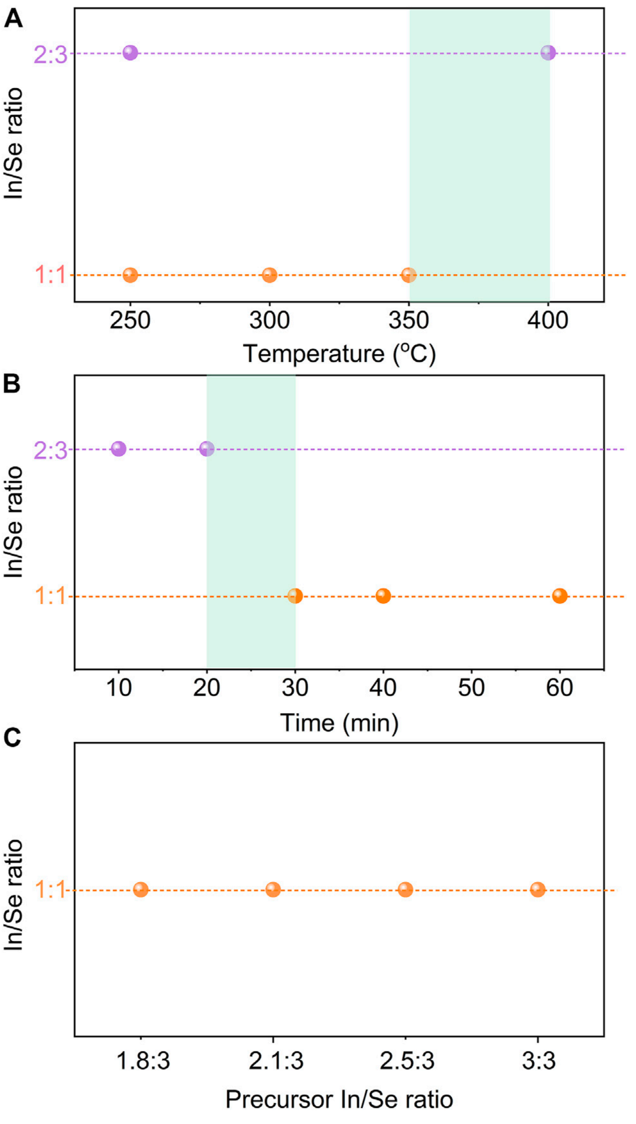

FIGURE 2 | Controlled growth of indium selenides using HPHT growth technique under 0.76 GPa. The growth temperature **(A)**, growth duration time **(B)**, and precursor ratio **(C)** dependence of the stoichiometry of final grown crystals. The shadow rectangle in **(A)** and **(B)** indicates the transition region. HPHT, high pressure and high temperature.

We perform a systematical investigation on the growth of In_xSe_y crystal with a controlled stoichiometry by adjusting the growth conditions, including growth pressure, duration time, and precursor ratios. As summarized in **Supplementary Table S1**, no bulk crystalline products were obtained under growth pressure above 2 GPa with various kinds of growth temperatures, growth duration time, and precursor In/Se ratio. This fact suggests that the high pressure above 2 GPa is not favorable in the growth of In_xSe_y crystals.

Figure 3 shows the optical images and scanning electron microscopy (SEM) images of the obtained crystals grown under 0.76 GPa and 400°C with In/Se precursor ratio of 2.1:3 for 30 and 10 min. The stoichiometry of the crystals is determined to be InSe (**Figure 3A**) and In_2Se_3 (**Figure 3B**) by the energy-dispersive X-ray spectroscopy (EDS) analysis, as shown in **Supplementary Figure S1**. The as-grown crystals are shiny with large sizes of about 5 × 1.6 mm for InSe (**Figure 3A**) and of about 1.7 × 1.3 mm for In_2Se_3 (**Figure 3B**). In addition, the resultant crystals exhibit clearly layered structures, as shown in the SEM images in **Figures 3C,D**.

Raman spectra were utilized to identify the phases of the InSe and In_2Se_3 crystals, as indicated in **Figure 4**. Four Raman modes, namely, A^1_{1g} at 114 cm^{-1}, E^1_{2g} at 177 cm^{-1}, A^1_{1g}(LO) at 198 cm^{-1}, and A^2_{1g} at 226 cm^{-1}, are clearly seen for InSe flakes, which suggests the as-grown InSe crystals are of γ-phase (**Figure 4A**) (Balakrishnan et al., 2018; Wu et al., 2019; Mudd et al., 2013). For In_2Se_3, three Raman peaks located at 103, 180, and 193 cm^{-1} are observed (**Figure 4B**), which can be ascribed to A_1(LO + TO), A_1(TO), and A_1(TO) phonon modes, respectively, of rhombohedral α-In_2Se_3 with space group of *R*3m, as indicated in **Figure 1B** (Lewandowska et al., 2001). Generally, *E* modes correspond to the in-plane vibration modes, while *A* modes correspond to the out-of-plane vibration modes. In α-In_2Se_3, only *A* modes are observed, which is probably due to the parallel measurement configuration of Raman measurement so that the wave vector of the exciting light is parallel to the *c*-axis of the α-In_2Se_3 (Lewandowska et al., 2001).

The crystal structures of the single crystals are further investigated by transmission electron microscopy (TEM). The thin γ-InSe and α-In_2Se_3 flakes were transferred on Cu grids by mechanical exfoliation and standard wet transfer method. **Figure 5A** shows the morphology of γ-InSe flakes. The selected area electron diffraction pattern (**Figure 5B**) measured in the marked area (red ellipse in **Figure 5A**) shows a six-fold symmetry, which suggests that the InSe crystals are of hexagonal structure. The high-resolution TEM image of the InSe flake clearly shows the hexagonal structure with the angle between the well-recognized *a* and *b* axes at 120° (**Figure 5C**). The lattice constant is determined to be about 0.4 nm, which is consistent with the lattice spacing of layered γ-InSe ($a = b = 4.005$ Å, $c = 24.96$ Å) (Chen et al., 2015). The same TEM investigations were also carried out on α-In_2Se_3 flakes, as shown in **Figures 5D–F**. The lattice constant is measured to be about 0.35 nm, which corresponds to *d*-spacing (100) lattice planes of α-In_2Se_3 (Ho et al., 2013; Zhou et al., 2015; Feng et al., 2016; Zhou et al., 2017; Tang et al., 2019).

Figure 6 shows the PL spectra of the γ-InSe flakes exfoliated from the as-grown crystals. A prominent peak at ~1.23 eV is observed for ~22-nm γ-InSe (**Figure 6A**). The thickness of γ-InSe flake is determined by the atomic force measurement, as shown in **Supplementary Figure S2**. By increasing the excitation laser power, the PL peak intensity increases. The excitation power dependence of the PL peak intensity follows the power law, $I \propto P^k$, in which *I*, *P*, and *k* are integrated peak intensity, excitation laser power, and power-law index, respectively. As shown in the log–log plot in **Figure 6B**, the value of *k* is fitted to be about 0.5. This suggests that the recombination is most likely originated from the localized electron–hole pairs in the γ-InSe, which is consistent with

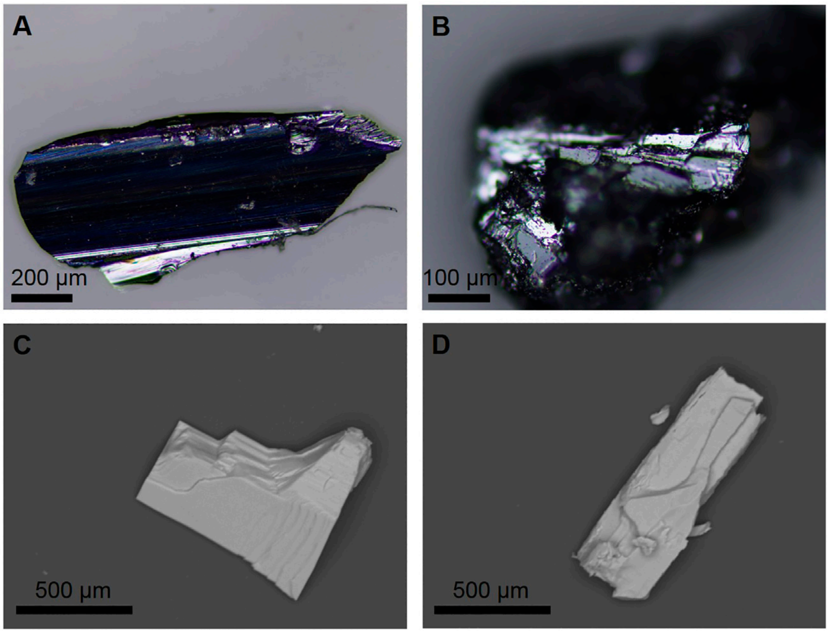

FIGURE 3 | Optical images of as-grown InSe crystal **(A)** and In_2Se_3 crystal **(B)**. SEM image of InSe crystal **(C)** and In_2Se_3 crystal **(D)** exfoliated on SiO_2 substrate. SEM, scanning electron microscopy.

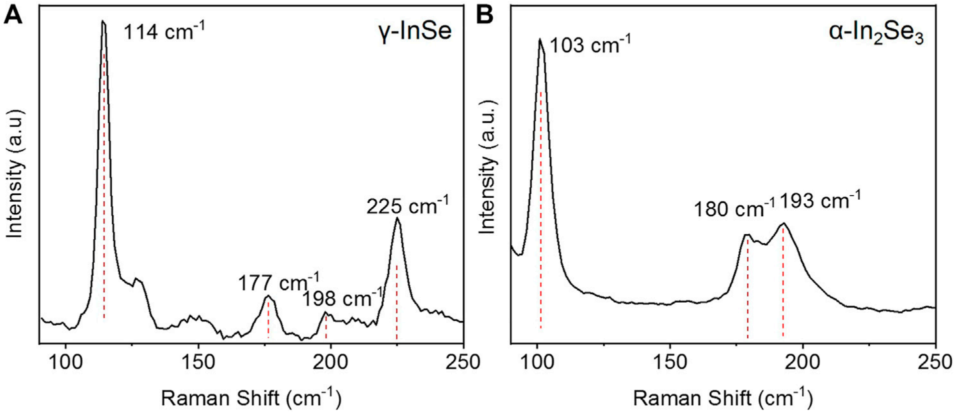

FIGURE 4 | Micro-Raman spectra of γ-InSe flake **(A)** and α-In_2Se_3 flake **(B)** with excitation laser wavelength of 532 nm.

the theoretical calculations for the phonon sideband emission process (Brener et al., 1992). A similar semiconducting property with a prominent PL peak at ~1.37 eV is also observed for α-In_2Se_3 flake, as shown in **Supplementary Figure S3**.

The piezoelectricity of the as-grown α-In_2Se_3 has been further investigated by the piezoresponse force microscopy (PFM) measurements. **Figure 7** shows the out-of-plane PFM amplitude (**Figure 7A**) and phase image (**Figure 7B**). The high and low amplitudes are clearly observed in the inner square and outer square, respectively, which corresponds to the opposite polarization states after writing with +7 V and −5 V, respectively. In addition, the domain wall between the oppositely polarized region is clear and does not coincide with the edges of the samples, which excludes the contribution of other artifact effects.

CONCLUSION

The controlled growth of indium selenide crystals was achieved successfully using the HPHT growth technique. The stoichiometry and structure of the indium selenides were well controlled by tuning the growth temperature and duration time at specific growth pressure of 0.76 GPa. The relatively low growth temperature and long duration time are beneficial for the growth of γ-InSe. On the contrary, α-In_2Se_3 crystals could be

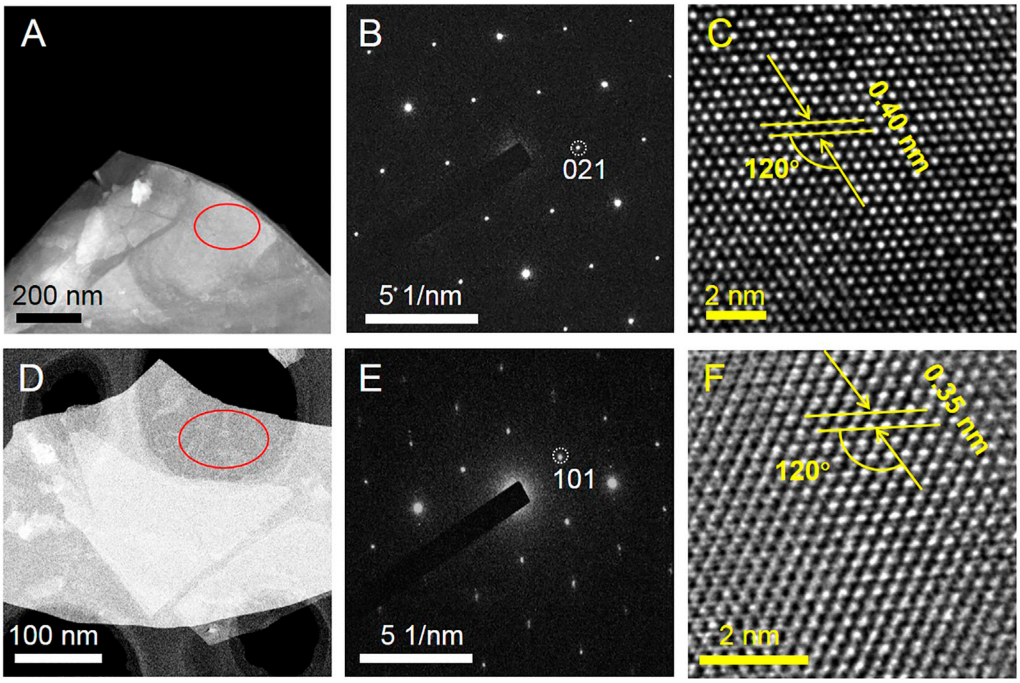

FIGURE 5 | (A) TEM image of γ-InSe flake. **(B)** SAED pattern and **(C)** HR-TEM image of γ-InSe flake collected in the marked area in **(A)**. **(D)** TEM image of α-In_2Se_3 flake. **(E)** SAED pattern and **(F)** HR-TEM image of α-In_2Se_3 flake collected in the marked area in **(D)**. TEM, transmission electron microscopy; SAED, selected area electron diffraction; HR-TEM, high-resolution TEM.

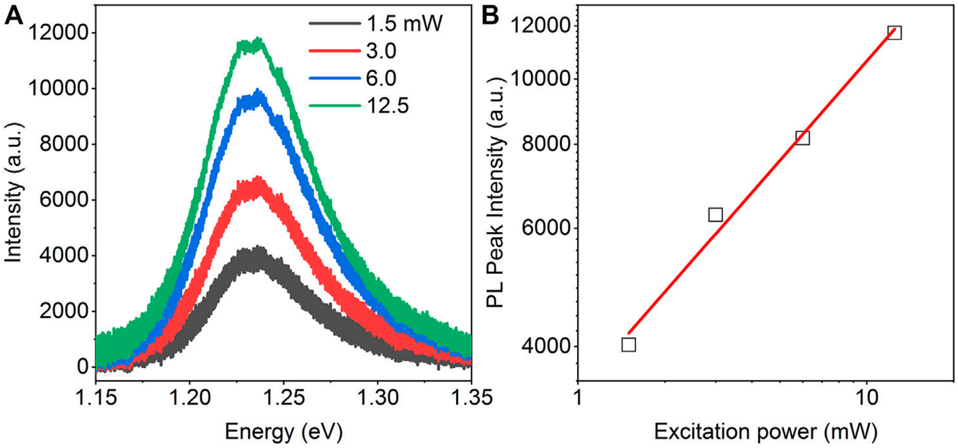

FIGURE 6 | (A) Photoluminescence (PL) spectra of the γ-InSe flake of about 22 nm at different incident laser power indicated. **(B)** Log–log plot of PL intensity as a function of the excitation power. The solid red line is the linear fitting curve with power-law index of ~0.5.

easily obtained at relatively high growth temperature and short growth duration time. Moreover, diverse physical properties were observed in the resultant crystals; i.e., γ-InSe shows a prominent PL peak at ~1.23 eV, and α-In_2Se_3 exhibits evident ferroelectricity, which holds promise for the potential applications in optoelectronics and ferroelectric memory devices. Our findings have provided an alternative strategy for crystals growth in a controlled manner and will stimulate further development of high-quality crystal growth with numerous fascinating physical properties and functional device applications.

METHODS

Characterization

Structural investigations and stoichiometry analyses of as-grown crystals were determined by EDS analysis through a field-emission

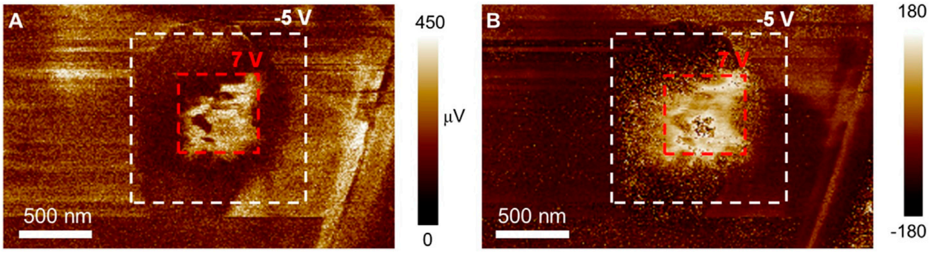

FIGURE 7 | The out-of-plane PFM amplitude **(A)** and phase **(B)** of as-grown α-In_2Se_3 flake exfoliated on SiO_2 substrate. The red and white dashed areas are polarized using different driving voltages of +7 V and −5 V, respectively. PFM, piezoresponse force microscopy.

SEM (JEOL-7100F, JEOL Ltd, Tokyo, Japan) at room temperature. The high-resolution images are measured by TEMs (JEM 2010; JEOL) with an acceleration voltage of 200 kV. The PL spectra were collected on micro-Raman/PL system (InVia, Renishaw, Wotton-under-Edge, UK) using an argon green laser at 514 nm. PFM measurements were performed in ambient conditions by using scanning probe microscopies (Bruker Dimension Icon-PT, Kontich, Belgium). Co/Cr tips (MESP, Bruker) were used for PFM measurements. An ac driving voltage of 0.5–1 V at a near resonance frequency of 280–400 kHz was applied to collect the PFM domain images (PFM phase and amplitude).

DATA AVAILABILITY STATEMENT

The raw data supporting the conclusion of this article will be made available by the authors, without undue reservation.

AUTHOR CONTRIBUTIONS

HL conceived the project. YD grew and characterized the crystals with support from HH, YL, WL, HZ, XT, SZ and YL. All authors contributed to the article and approved the submitted version.

FUNDING

This work was supported in part by the National Natural Science Foundation of China under Grant Nos. 11904001 and 51902069, the Joint Funds of the National Natural Science Foundation of China and the Chinese Academy of Sciences Large-Scale Scientific Facility under Grant No. U1932156, the Natural Science Foundation of Anhui Province under Grant No. 2008085QA29, and the Project of Science and Technology on Reliability Physics and Application Technology of Electronic Component Laboratory under Grant No. 61428060101.

SUPPLEMENTARY MATERIAL

The Supplementary Material for this article can be found online at: https://www.frontiersin.org/articles/10.3389/fmats.2021.816821/full#supplementary-material

REFERENCES

Balakrishnan, N., Steer, E. D., Smith, E. F., Kudrynskyi, Z. R., Kovalyuk, Z. D., Eaves, L., et al. (2018). Epitaxial Growth of γ -InSe and α , β , and γ -In 2 Se 3 on ε -GaSe. *2d Mater.* 5, 035026. doi:10.1088/2053-1583/aac479

Bandurin, D. A., Tyurnina, A. V., Yu, G. L., Mishchenko, A., Zólyomi, V., Morozov, S. V., et al. (2017). High Electron Mobility, Quantum Hall Effect and Anomalous Optical Response in Atomically Thin InSe. *Nat. Nanotech* 12, 223–227. doi:10.1038/nnano.2016.242

Brener, I., Olszakier, M., Cohen, E., Ehrenfreund, E., Ron, A., and Pfeiffer, L. (1992). Particle Localization and Phonon Sidebands in GaAs/AlxGa1−xAs Multiple Quantum wells. *Phys. Rev. B* 46, 7927–7930. doi:10.1103/physrevb.46.7927

Butler, S. Z., Hollen, S. M., Cao, L., Cui, Y., Gupta, J. A., Gutiérrez, H. R., et al. (2013). Progress, Challenges, and Opportunities in Two-Dimensional Materials beyond Graphene. *ACS Nano.* 7, 2898–2926. doi:10.1021/nn400280c

Chen, Z., Biscaras, J., and Shukla, A. (2015). A High Performance Graphene/few-Layer InSe Photo-Detector. *Nanoscale* 7, 5981–5986. doi:10.1039/c5nr00400d

Ding, J., Shao, D. F., Li, M., Wen, L. W., and Tsymbal, E. Y. (2021). Two-dimensional Antiferroelectric Tunnel junction. *Phys. Rev. Lett.* 126, 057601. doi:10.1103/PhysRevLett.126.057601

Ding, W., Zhu, J., Wang, Z., Gao, Y., Xiao, D., Gu, Y., et al. (2017). Prediction of intrinsic two-dimensional ferroelectrics in In2Se3 and other III2-VI3 van der Waals materials. *Nat. Commun.* 8, 14956. doi:10.1038/ncomms14956

Feng, W., Zheng, W., Gao, F., Chen, X., Liu, G., Hasan, T., et al. (2016). Sensitive Electronic-Skin Strain Sensor Array Based on the Patterned Two-Dimensional α-In2Se3. *Chem. Mater.* 28, 4278–4283. doi:10.1021/acs.chemmater.6b01073

Guo, H., Zhang, Z., Huang, B., Wang, X., Niu, H., Guo, Y., et al. (2020). Theoretical study on the photocatalytic properties of 2D InX(X = S, Se)/transition metal disulfide (MoS2 and WS2) van der Waals heterostructures. *Nanoscale* 12, 20025–20032. doi:10.1039/d0nr04725b

Ho, C.-H., Lin, C.-H., Wang, Y.-P., Chen, Y.-C., Chen, S.-H., and Huang, Y.-S. (2013). Surface Oxide Effect on Optical Sensing and Photoelectric Conversion of α-In2Se3 Hexagonal Microplates. *ACS Appl. Mater. Inter.* 5, 2269–2277. doi:10.1021/am400128e

Hu, Y., Feng, W., Dai, M., Yang, H., Chen, X., Liu, G., et al. (2018). Temperature-dependent Growth of Few Layer β-InSe and α-In2Se3 Single Crystals for Optoelectronic Device. *Semicond. Sci. Technol.* 33, 125002. doi:10.1088/1361-6641/aae629

Ishii, T. (1988). High Quality Single crystal Growth of Layered InSe Semiconductor by bridgman Technique. *J. Cryst. Growth* 89, 459–462. doi:10.1016/0022-0248(88)90206-0

Lei, S., Ge, L., Najmaei, S., George, A., Kappera, R., Lou, J., et al. (2014). Evolution of the Electronic Band Structure and Efficient Photo-Detection in Atomic Layers of InSe. *ACS Nano*. 8, 1263–1272. doi:10.1021/nn405036u

Lewandowska, R., Bacewicz, R., Filipowicz, J., and Paszkowicz, W. (2001). Raman Scattering in α-In2Se3 Crystals. *Mater. Res. Bull.* 36, 2577–2583. doi:10.1016/s0025-5408(01)00746-2

Li, Y.-H., Yu, C.-B., Li, Z., Jiang, P., Zhou, X.-Y., Gao, C.-F., et al. (2020). Layer-dependent and Light-Tunable Surface Potential of Two-Dimensional Indium Selenide (InSe) Flakes. *Rare Met.* 39, 1356–1363. doi:10.1007/s12598-020-01511-4

Lu, K., Sui, M. L., Perepezko, J. H., and Lanning, B. (1999). The Kinetics of Indium/amorphous-Selenium Multilayer Thin Film Reactions. *J. Mater. Res.* 14, 771–779. doi:10.1557/jmr.1999.0103

Milutinović, A., Lazarević, Z. Z., Jakovljević, M., Hadzić, B., Petrović, M., Petrović, M., et al. (2016). Optical Properties of Layered III-VI Semiconductor γ-InSe: M (M=Mn, Fe, Co, Ni). *J. Phys. Chem. Sol.* 86, 120–127.

Mudd, G. W., Svatek, S. A., Ren, T., Patanè, A., Makarovsky, O., Eaves, L., et al. (2013). Tuning the Bandgap of Exfoliated InSe Nanosheets by Quantum Confinement. *Adv. Mater.* 25, 5714–5718. doi:10.1002/adma.201302616

Tang, L., Teng, C., Luo, Y., Khan, U., Pan, H., Cai, Z., et al. (2019). Confined van der Waals Epitaxial Growth of Two-Dimensional Large Single-Crystal In2Se3 for Flexible Broadband Photodetectors. *Research* 2019, 1–10. doi:10.1155/2019/2763704

Watanabe, K., and Taniguchi, T. (2019). Far-UV Photoluminescence Microscope for Impurity Domain in hexagonal-boron-nitride Single Crystals by High-Pressure, High-Temperature Synthesis. *Npj 2d Mater. Appl.* 3, 40. doi:10.1038/s41699-019-0124-4

Wu, M., Xie, Q., Wu, Y., Zheng, J., Wang, W., He, L., et al. (2019). Crystal Structure and Optical Performance in Bulk γ-InSe Single Crystals. *AIP Adv.* 9, 025013. doi:10.1063/1.5086492

Yang, Z., Jie, W., Mak, C.-H., Lin, S., Lin, H., Yang, X., et al. (2017). Wafer-scale Synthesis of High-Quality Semiconducting Two-Dimensional Layered InSe with Broadband Photoresponse. *ACS Nano*. 11, 4225–4236. doi:10.1021/acsnano.7b01168

Zhou, J., Zeng, Q., Lv, D., Sun, L., Niu, L., Fu, W., et al. (2015). Controlled Synthesis of High-Quality Monolayered α-In2Se3 via Physical Vapor Deposition. *Nano. Lett.* 15, 6400–6405. doi:10.1021/acs.nanolett.5b01590

Zhou, S., Tao, X., and Gu, Y. (2016). Thickness-Dependent Thermal Conductivity of Suspended Two-Dimensional Single-Crystal In2Se3 Layers Grown by Chemical Vapor Deposition. *J. Phys. Chem. C* 120, 4753–4758. doi:10.1021/acs.jpcc.5b10905

Zhou, Y., Wu, D., Zhu, Y., Cho, Y., He, Q., Yang, X., et al. (2017). Out-of-Plane Piezoelectricity and Ferroelectricity in Layered α-In2Se3 Nanoflakes. *Nano. Lett.* 17, 5508–5513. doi:10.1021/acs.nanolett.7b02198

Conflict of Interest: The authors declare that the research was conducted in the absence of any commercial or financial relationships that could be construed as a potential conflict of interest.

frontiers
in Materials

ORIGINAL RESEARCH
published: 28 January 2022
doi: 10.3389/fmats.2022.838648

The Thermal and Electronic Properties of the Lateral Janus MoSSe/WSSe Heterostructure

Zhongliang Shen[1], **Kai Ren**[2], **Ruxing Zheng**[2], **Zhaoming Huang**[3]*, **Zhen Cui**[4], **Zijun Zheng**[1] **and Li Wang**[5]

[1]School of Mechatronic Engineering, Zhejiang Business Technology Institute, Ningbo, China, [2]School of Mechanical and Electronic Engineering, Nanjing Forestry University, Nanjing, China, [3]School of Mechanical Engineering, Wanjiang University of Technology, Maanshan, China, [4]School of Automation and Information Engineering, Xi'an University of Technology, Xi'an, China, [5]School of Electromechanical and Automotive Engineering, Xuancheng Vocational and Technical College, Xuancheng, China

Two-dimensional materials have opened up extensive applications for traditional materials. In particular, heterostructures can further create fantastic performances. In this investigation, the lateral heterostructure was constructed using Janus MoSSe and WSSe monolayers with armchair and zigzag interfaces. Performing first-principles calculations and molecular dynamics simulation method, the thermal stability and the semiconductor characteristics with the type-II band structure to separate the photogenerated charges of such Janus MoSSe/WSSe heterostructure are presented, which suggests the potential application of acting as a photocatalyst for water splitting. Importantly, the asymmetric interface of the Janus MoSSe/WSSe heterostructure can result in natural bending, which limits the heat flow transport. Smaller heat flow and the interfacial thermal resistance of the lateral MoSSe/WSSe heterostructure with a zigzag edge interface are mainly due to suppressed acoustic branches. These structural symmetry and interface-dependent properties show the future applications in photovoltaic and thermoelectric devices.

Keywords: two-dimensional material, type-II band structure, interfacial thermal resistance, lateral MoSSe/WSSe heterostructure, applications

Edited by:
Guangzhao Wang,
Yangtze Normal University, China

Reviewed by:
Hao Guo,
Hebei Normal University of Science and Technology, China
Kezhen Qi,
Shenyang Normal University, China

Correspondence:
Zhaoming Huang
jimmymacy@163.com

Specialty section:
This article was submitted to Computational Materials Science, a section of the journal Frontiers in Materials

Received: *18 December 2021*
Accepted: *07 January 2022*
Published: *28 January 2022*

Citation:
Shen Z, Ren K, Zheng R, Huang Z, Cui Z, Zheng Z and Wang L (2022) The Thermal and Electronic Properties of the Lateral Janus MoSSe/WSSe Heterostructure. Front. Mater. 9:838648. doi: 10.3389/fmats.2022.838648

INTRODUCTION

After graphene was discovered (Geim and Novoselov, 2010), it has frequently demonstrated some novel properties due to its very special monolayer structure (Butler et al., 2013; Kim et al., 2015; Xu et al., 2015; Wei et al., 2016; Gao et al., 2017; Zaminpayma et al., 2017; Zhang et al., 2018; Zhou et al., 2018; Sun and Schwingenschlögl, 2021a), which has attracted tremendous investigations to explore the other excellent characteristics and applications of two-dimensional (2D) materials (Li et al., 2014; Li et al., 2019; Li et al., 2021; Vahedi Fakhrabad et al., 2015; Keyte et al., 2019; Xu et al., 2020; Ren et al., 2021a; Ren et al., 2021b; Sun et al., 2021). For instance, biphenylene, a graphene-like material, was prepared, which is metallic, instead of dielectric (Fan et al., 2021). Biphenylene also possesses excellent electronic, mechanical, and catalytic properties (Luo et al., 2021). Two-dimensional $MoSi_2N_4$ was synthesized by chemical vapor deposition, suggesting a sandwiched structure; the exhibited semiconducting nature was also investigated, with a bandgap of about 1.94 eV (Hong et al., 2020). A novel 2D material of transition metal dichalcogenides (TMDs) has attracted considerable focus (Luo et al., 2019a; Luo et al., 2019b; Dongqi et al., 2021). For example, WSe_2 has been proved to

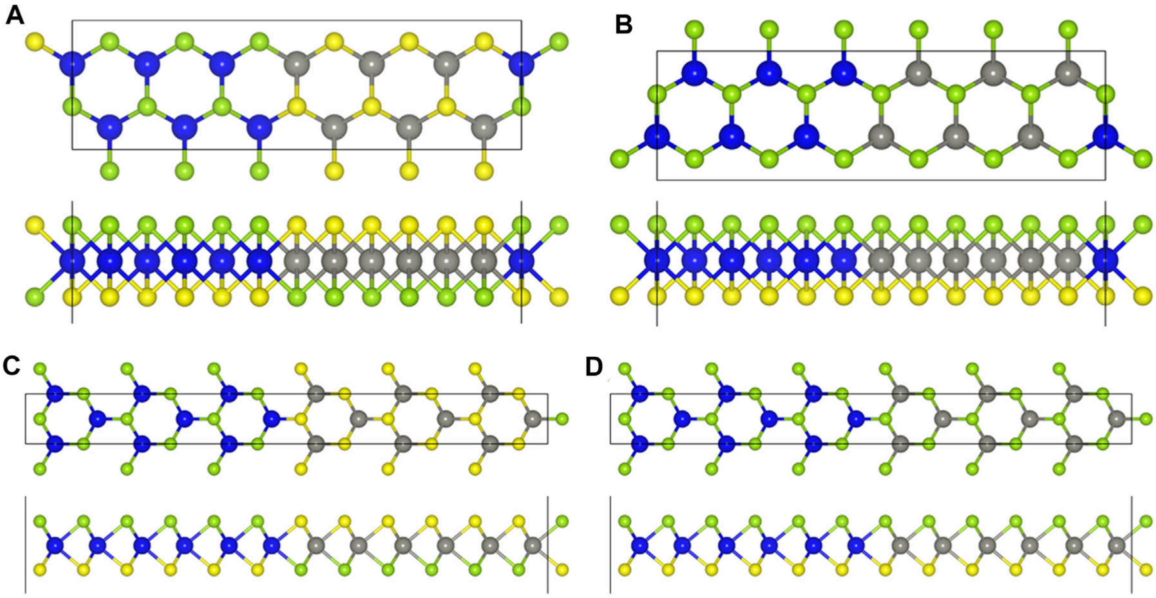

FIGURE 1 | Crystal structure of the **(A)** arm-1, **(B)** arm-2, **(C)** zig-1, and **(D)** zig-2 MoSSe/WSSe heterostructures; the blue, gray, cyan, and yellow are Mo, W, Se, and S atoms, respectively.

be a semiconductor material with indirect bandgap, high carrier mobility, remarkable optical properties, and the responsivity of the field effect transistor of this material in the visible wavelength range is of 10^{-1}–10^5A/W (Zhao et al., 2013; Allain and Kis, 2014; Jo et al., 2018). $MoSe_2$ is a layered material possessing a bandgap of 1.55 eV. It is found that $MoSe_2$ has strong light absorption capacity and photoelectric conversion efficiency (close to 10%) in the range of visible light and has a great application prospect in photovoltaic devices (Ma et al., 2011; Shi et al., 2013; Liu et al., 2016a). All these remarkable performances of the 2D materials present advanced applications in metal-ion batteries (Sun and Schwingenschlögl, 2020; Sun and Schwingenschlögl, 2021b), photocatalyst (Ong, 2017; Ren et al., 2019; Ren et al., 2021c; Sun et al., 2020; Agarwal et al., 2021), photodiode (Ouyang et al., 2021), light emitting devices (Ren et al., 2021d), etc.

Interestingly, these novel performances of the 2D materials can also be adjusted by suitable methods, such as external strain (Wang et al., 2019a; Shu, 2021; Zhao et al., 2021), electric field (Sun et al., 2017; Cui et al., 2021a), adsorption (Cui et al., 2021b), doping (Cui et al., 2021a), and defect (Sun et al., 2019). Recently, the synthesis of heterostructures demonstrates further properties and applications (Novoselov et al., 2016; Ang and Ang, 2019; Chen et al., 2020; Hidding and Guimarães, 2020). It is worth noting that a 2D heterostructure can be divided into a vertical heterostructure and a lateral heterostructure. The former can be obtained by artificial fixed-point transfer and chemical vapor deposition (CVD), and the latter is obtained by CVD epitaxial growth (Ding et al., 2018; Jiang, 2018). A vertical heterostructure is a structure that connects two or more layered materials through van der Waals (vdW) force, which can induce astonishing performances across the interface. For instance, the carrier mobility of a ZnO/BSe vertical heterostructure is as high as 2538.16 $cm^2{\cdot}v^{-1}{\cdot}s^{-1}$, which is higher than that of original ZnO (360.88 $cm^2{\cdot}v^{-1}{\cdot}s^{-1}$) and BSe (419.01 $cm^2{\cdot}v^{-1}{\cdot}s^{-1}$) (Ren et al., 2020a). The Z-Scheme photocatalytic mechanism was discovered in the $MoSe_2/HfS_2$ heterostructure and is used as an efficient photocatalyst for water splitting (Wang et al., 2019b). Nevertheless, due to the weak vdW force between layers, the vertical heterostructure will be unstable at high temperature and other extreme conductance; thus, Duan et al. synthesized $MoS_2/MoSe_2$ and WS_2/WSe_2 lateral heterostructures by using the CVD epitaxial growth method and proved that the lateral heterostructure can be formed with remarkable current rectification behavior (Duan et al., 2014). The MoS_2/WSe_2 lateral heterostructure was studied that the fracture strength was determined by the mechanical properties of MoS_2. When the temperature increases from 50 to 500 K, the fracture strength and strain of MoS_2/WSe_2 vdW heterostructure are reduced by about 35 and 36%, respectively (Qin et al., 2019). More recently, the TMD material with a Janus structure, MoSSe, was successfully prepared (Lu et al., 2017), which exhibits novel electronic and optical properties (Ren et al., 2020b). WSSe with a Janus structure also have unexpected properties (Lou et al., 2021). WSSe with an armchair edge nanotube has strong oxidation ability, resulting in high conversion efficiency of solar hydrogen production (Guo et al., 2020). Considering that both monolayers MoSSe and WSSe have outstanding properties, and the MoSSe/WSSe heterostructure was also recently prepared (Trivedi et al., 2020), the lateral MoSSe/WSSe heterostructure was selected to explore the interesting performances and potential applications.

In this investigation, the Janus MoSSe and WSSe monolayers are selected to construct lateral heterostructures by armchair and zigzag edges as interfaces. The stability of the Janus MoSSe/WSSe heterostructure is addressed by using the molecular dynamics

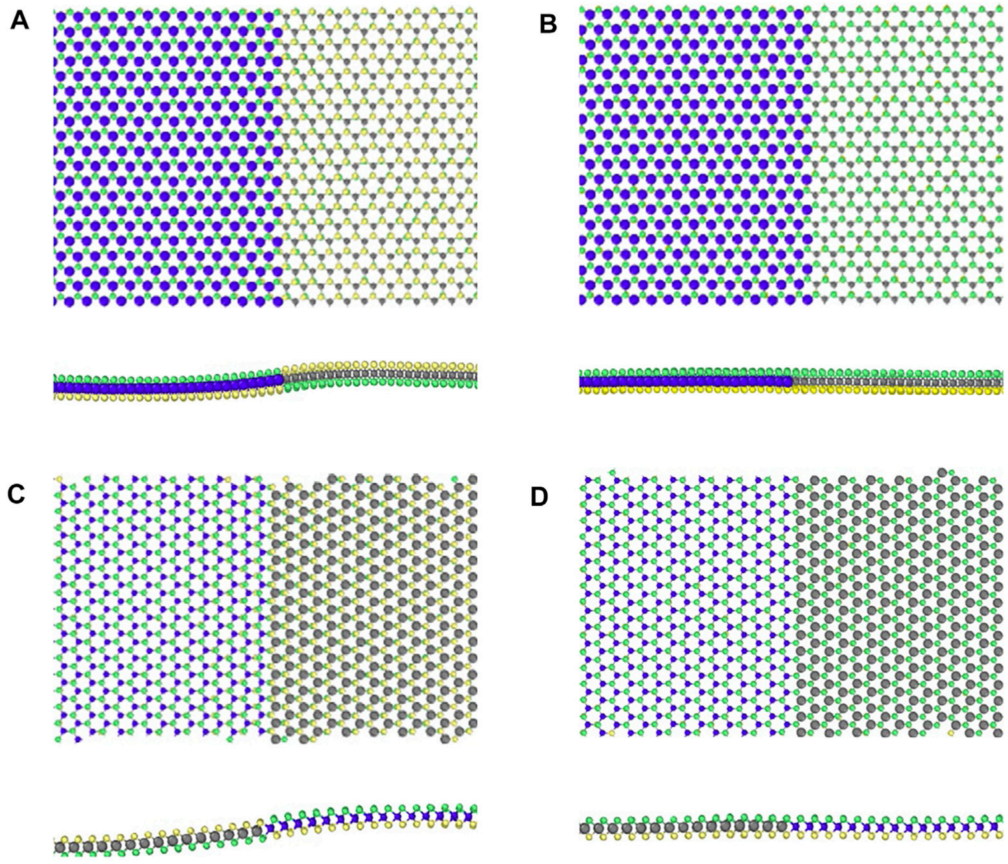

FIGURE 2 | MD snapshot for the structures of the **(A)** arm-1, **(B)** arm-2, **(C)** zig-1, and **(D)** zig-2 MoSSe/WSSe heterostructures at 300 K.

(MD) method. Then, electronic properties of the type-II band alignment of the MoSSe/WSSe heterostructure are obtained using first-principles calculations. Importantly, the structural symmetry and interface edge dependence for the thermal performance are further investigated.

COMPUTATIONAL METHODS

For the first-principles calculations, the simulations were conducted by the Vienna *ab initio* simulation package (VASP) based on density functional theory (DFT) (Capelle, 2006). The generalized gradient approximation (GGA) and the projector augmented wave potentials (PAW) were used by the Perdew–Burke–Ernzerhof (PBE) functional for the exchange correlation functional (Kresse and Furthmüller, 1996; Perdew et al., 1996; Kresse and Joubert, 1999). The energy cutoff and the Monkhorst–Pack *k*-point grids were considered to be 550 eV and $17 \times 17 \times 1$, respectively. The thickness of the vacuum energy level was employed by the 25 Å to prevent the interaction of the nearby layers. The studied heterostructures were fully relaxed by the Hellmann–Feynman force smaller than $0.01\ \mathrm{eV\ Å^{-1}}$ for each atom. Furthermore, the convergence of the energy for the systems was controlled within 1×10^{-5} eV. The density functional perturbation theory (DFPT) was used to obtain the phonon spectra of the investigated heterostructure by the PHONOPY code (Togo et al., 2008; Togo and Tanaka, 2015).

The MD calculations were performed by the LAMMPS package (Plimpton, 1995) in this work using parameterized Stillinger–Weber potential to demonstrate the covalent interaction between S, Se, Mo, and W atoms (Jiang, 2018). The time step of our MD simulation was set as 1 fs, and Newton's equations of atomic motion were considered in the velocity Verlet algorithm. First, the studied heterostructure was relaxed for 10 ps under 300 K by the NPT (isothermal and isobaric) ensemble, and then, NVT ensemble was used to further optimize the structure of the system by Nosé–Hoover temperature sustaining 2000 ps. Next, the Janus heterostructure was equilibrated by the NVE (isovolumetric and isoenergetic) (Ren et al., 2020c).

RESULTS AND DISCUSSION

The structure of the lateral MoSSe/WSSe heterostructure is constructed along two interfaces: armchair and zigzag edge. For the MoSSe/WSSe heterostructure with an armchair interface, asymmetric with a Janus structure, S and Se can be

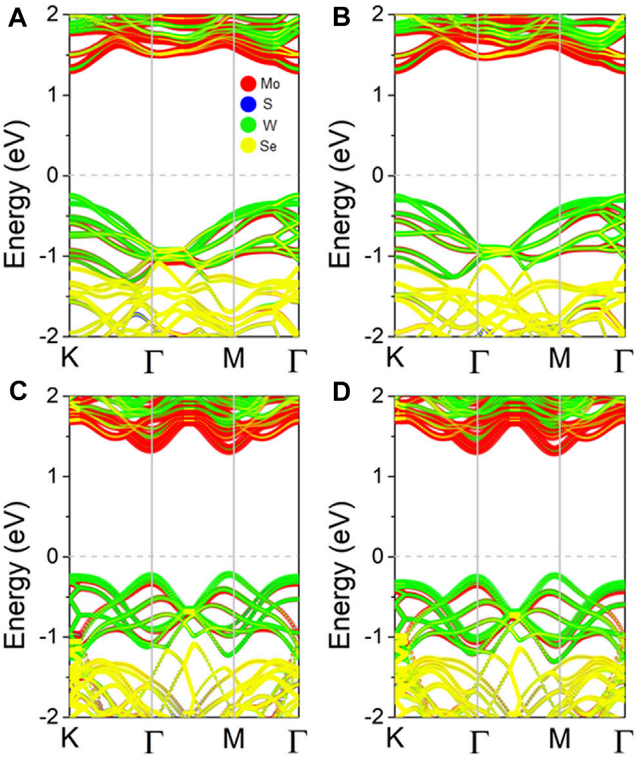

FIGURE 3 | Projected band structures of the **(A)** arm-1, **(B)** arm-2, **(C)** zig-1, and **(D)** zig-2 MoSSe/WSSe heterostructures.

arranged on both sides of Mo (or W) atoms and the same layer, namely, arm-1 and arm-2, as shown in **Figures 1A,B**, respectively. Similarly, the zig-1 and zig-2 are shown in **Figures 1C,D**, respectively. Besides, the MoSSe and WSSe monolayers are also optimized by the lattice constants of 3.23 and 3.27 Å, respectively. The obtained bond lengths of the Mo–S, Mo–Se, W–S, and W–Se in the optimized monolayered MoSSe and WSSe are 2.41, 2.53, 2.43 and 2.54 Å, respectively, which are agreement with the experimental work, 2.58 and 2.41 Å for Mo–Se and Mo–S, respectively (Lu et al., 2017). Thus, the lattice mismatch of the MoSSe/WSSe heterostructure with armchair and zigzag edges is 3.7 and 2.8%, respectively. Furthermore, the calculated formation energies of arm-1, arm-2, zig-1, and zig-2 MoSSe/WSSe heterostructures are 0.136, 0.095, 0.364, and 0.050 eV, respectively.

To assess the thermal stability of such a lateral MoSSe/WSSe heterostructure, molecular dynamics simulations were employed. After complete relaxation of the lateral MoSSe/WSSe heterostructure at a Nosé–Hoover temperature of 300 K, the structures of arm-1, arm-2, zig-1, and zig-2 lateral MoSSe/WSSe heterostructures are demonstrated in **Figures 2A–D**, respectively. The whole optimization process took about 4000 ps for the lateral MoSSe/WSSe heterostructure, and one can find that the structures of these heterostructures are still intact. Interestingly, at the interface of the arm-1 and zig-1 of the lateral MoSSe/WSSe heterostructure, a bending phenomenon occurred because of the asymmetric atomic arrangement pattern of the S and Se atoms. In detail, this natural folding phenomenon is also caused by the uneven stress of bonds at the interface.

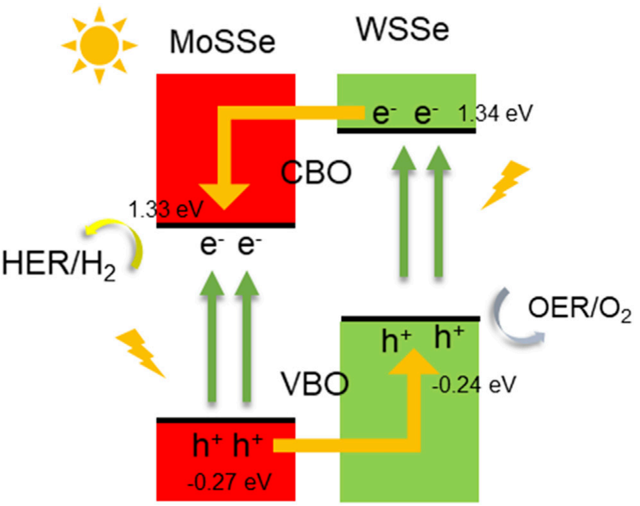

FIGURE 4 | Schematic of the exciton migration mode of the lateral MoSSe/WSSe heterostructure.

The projected band structure of arm-1, arm-2, zig-1, and zig-2 lateral MoSSe/WSSe heterostructures is shown in as **Figures 3A–D**, respectively. It can be seen that arm-1 and arm-2 lateral MoSSe/WSSe heterostructures possess similar band structures with the semiconductor characteristic with a direct bandgap of 1.57 and 1.58 eV, respectively, suggesting the conduction band minimum (CBM) and valence band maximum (VBM) located at K point. The zig-1 and zig-2 lateral MoSSe/WSSe heterostructures also have a direct bandgap of 1.56 and 1.56 eV, respectively, with the CBM and VBM at Γ point. Importantly, the red, blue, cyan, and yellow marks represent the band contributions of the Mo, S, W, and Se atoms, respectively, which show that these four Janus lateral heterostructures possess type-II band alignment and that the CBM and VBM resulted from MoSSe and WSSe layers, respectively. Besides, the obtained bandgaps are comparable with those of the reported MoSSe/WSSe heterostructure (about 1.53 eV) (Li et al., 2017).

The obtained type-II band structure of the lateral MoSSe/WSSe heterostructure provides the ability to separate the photogenerated electrons and holes continuously. As **Figure 4** shows, taking the arm-1 MoSSe/WSSe heterostructure as an example, the energy positions are also demonstrated. When the MoSSe/WSSe heterostructure is inspired by light, the photogenerated electrons of the MoSSe and WSSe layers can be stimulated to the conduction band (CB), and the photogenerated holes will result in the valence band (VB). Then, the photogenerated electrons at the CB of the WSSe layer and the photogenerated holes at the VB of the MoSSe layer transfer to the CB of the MoSSe layer and the VB of the WSSe layer by the power of the conduction band offset and valence band offset, named conduction band offset (CBO) and

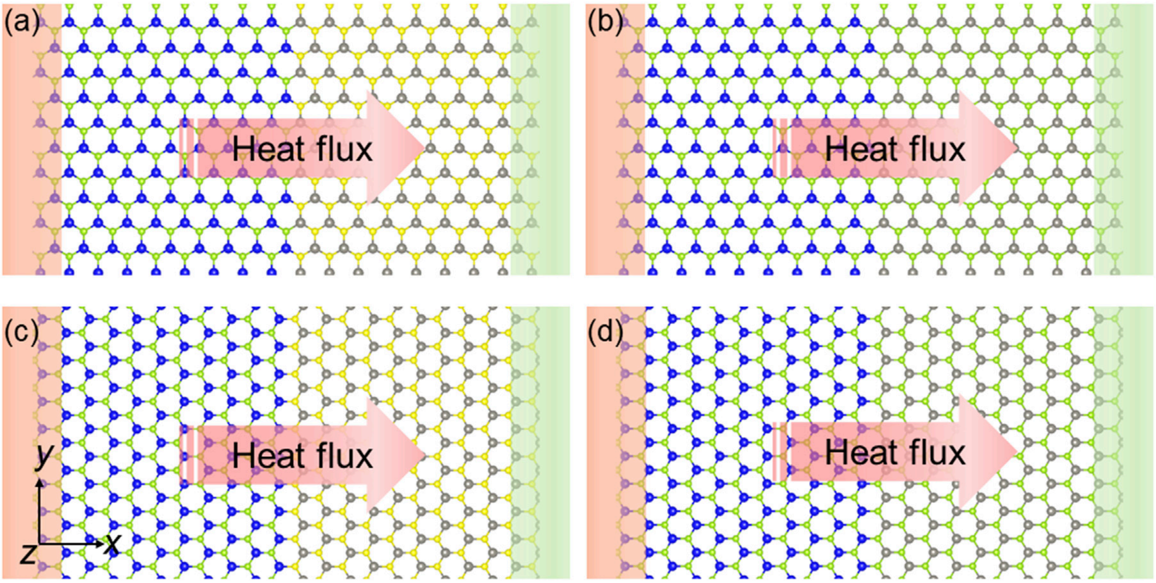

FIGURE 5 | Schematic of the heat transfer style of the **(A)** arm-1, **(B)** arm-2, **(C)** zig-1, and **(D)** zig-2 MoSSe/WSSe heterostructures for the NEMD simulations.

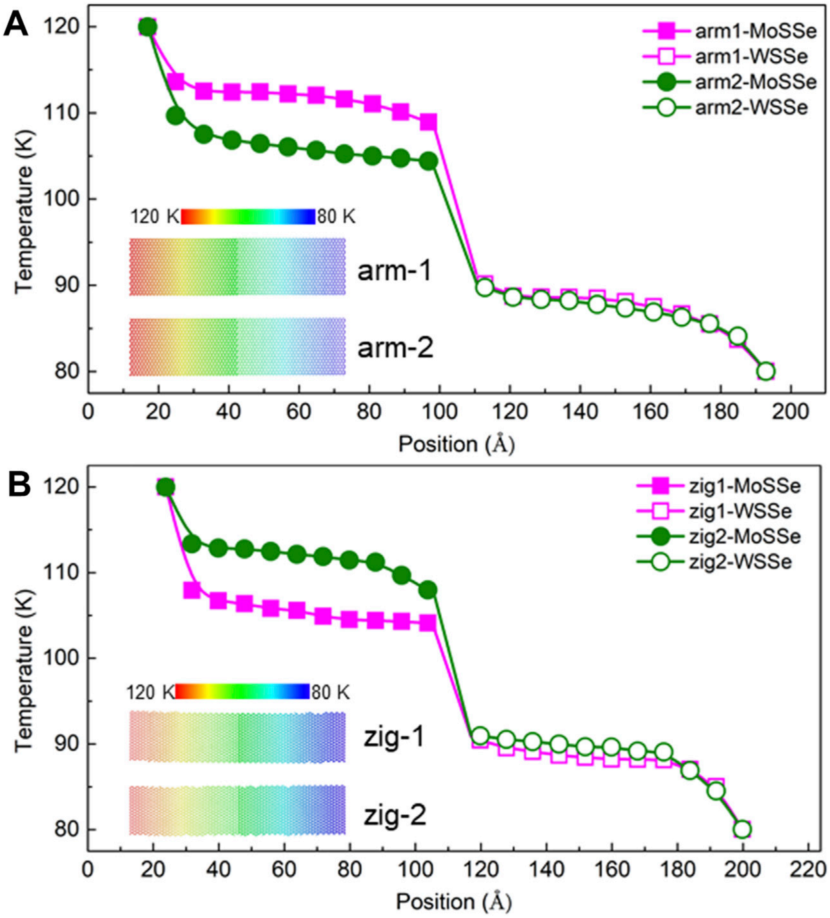

FIGURE 6 | Temperature profiles the **(A)** arm-1, **(B)** arm-2, **(C)** zig-1, and **(D)** zig-2 MoSSe/WSSe heterostructures.

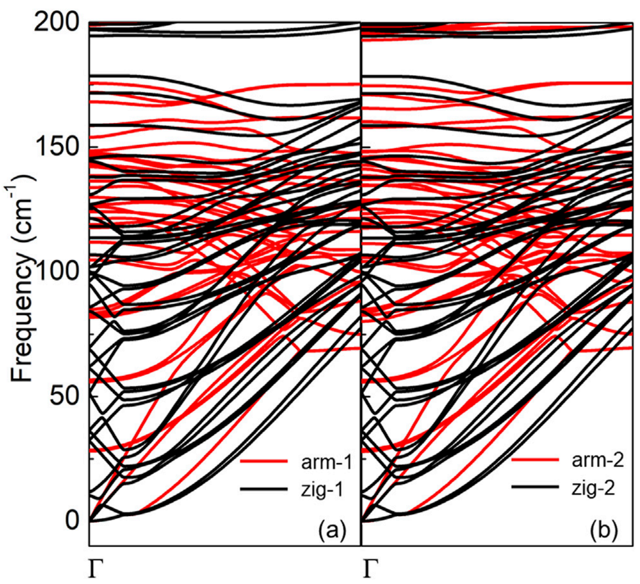

FIGURE 7 | Calculated phonon dispersion for MoSSe/WSSe heterostructure with **(A)** armchair and **(B)** zigzag interface.

valence band offset (VBO) in **Figure 4**, respectively. Thus, the separated photogenerated electrons at the CB of the MoSSe layer and holes at the VB of the WSSe layer can induce the hydrogen evolution reaction (HER) and oxygen evolution reaction (OER), respectively, suggesting these four lateral MoSSe/WSSe heterostructures can act as a potential photocatalyst for water splitting. In particular, if the photogenerated electrons at the CB of the MoSSe layer and the photogenerated holes at the VB of the WSSe layer develop recombination, the HER and the OER are induced at the CB of the WSSe layer and the VB of the MoSSe layer, respectively, and the Z-scheme photocatalytic mechanism is promoted (Xu et al., 2018; Ren et al., 2020d).

To investigate the heat conduction properties of the lateral MoSSe/WSSe heterostructure with different symmetries and interface edges, the non-equilibrium molecular dynamics (NEMD) method was adopted. A temperature gradient is constructed with MoSSe and WSSe acting as cold and hot baths, respectively. The schematic diagram of the temperature gradient of these four heterostructures arm-1, arm-2, zig-1, and zig-2 MoSSe/WSSe is shown in **Figures 5A–D**, respectively, suggesting heat flux flow from the MoSSe layer to the WSSe layer. Besides, NEMD simulations can explain the temperature interaction between atoms. The temperature distribution can also be demonstrated by NEMD calculations across the interface. In MD simulation work Nose–Hoover and Langevin are popular heat baths that can account for different experimental factors (Hu et al., 2020). The Nose–Hoover and Langevin can induce different temperature profiles, and in this NEMD investigation, the temperature jump across the interface of the MoSSe/WSSe heterostructure is critical. Therefore, the Nose–Hoover heat bath was selected. We fixed the ends of the MoSSe and WSSe and set the temperature at 80 and 100 K, respectively. We obtained the time-independent heat flux with enough relaxation time to build a non-equilibrium status. The heat flux (J) was calculated as follows:

$$J = \frac{1}{V}\left[\sum_{i}^{N}\varepsilon_i v_i + \frac{1}{2}\sum_{ij;i\neq j}^{N}\left(F_{ij}\cdot v_i\right)\mathbf{r}_{ij} + \frac{1}{6}\sum_{ijk,i\neq j\neq k}^{N}\left(F_{ijk}\cdot v_i\right)\left(\mathbf{r}_{ij}+\mathbf{r}_{ik}\right)\right], \tag{1}$$

where ε_i is the energy; v_i represents the velocity of an atom i; r_{ij} is the interatomic distance between atoms i and j; F_{ij} and F_{ijk} are two-body and three-body forces, respectively; and V represents the volume of the investigated MoSSe/WSSe heterostructure. Furthermore, the calculated thickness of MoSSe and WSSe is 3.243 and 3.230 Å, respectively.

After obtaining the steady state for the systems, the temperature profile of the lateral MoSSe/WSSe heterostructure with an armchair and zigzag interface edge is demonstrated in **Figures 6A,B**, respectively. Reflection, transmission, and mode conversion occur by phonons travelling across the interface of the MoSSe/WSSe heterostructure, suggesting a temperature jump, which can further result in interfacial thermal resistance. Linear fitting and extrapolation were explored to calculate a more reasonable temperature jump (Yu and Zhang, 2013). As **Figure 6** shows, a significant temperature jump (ΔT) is characterized at the interface of the lateral MoSSe/WSSe heterostructure. Such a temperature jump is also obtained by other reported heterostructures, such as graphene/h-BN (Liu et al., 2016b), phosphorene/graphene (Liu et al., 2018), and MoS_2/WSe_2 (Qin et al., 2019). The heat flux of the arm-1, arm-2, zig-1, zig-2 MoSSe/WSSe heterostructures is calculated as 5.48×10^9, 6.21×10^9, 3.70×10^9, and 4.28×10^9 W m^{-2}, respectively. Besides, the temperature jump of the arm-1, arm-2, zig-1, and zig-2 MoSSe/WSSe heterostructures is obtained at 18.77, 14.66, 17.43 and 13.67 K, respectively. The interfacial thermal resistance (ITC) of the lateral MoSSe/WSSe heterostructure was decided as follows:

$$\lambda = \frac{J}{\Delta T}. \tag{2}$$

Therefore, pronounced ITC across the interfaces of the arm-1, arm-2, zig-1, and zig-2 MoSSe/WSSe heterostructures is 2.92×10^8, 4.24×10^8, 2.12×10^8, and 3.13×10^8 W K^{-1}·m^{-2}, respectively, which is comparable with that of graphene/BP (2.5×10^8 W K^{-1}·m^{-2}) (Liu et al., 2018). More importantly, the obtained ITC, 4.24×10^8 W K^{-1}·m^{-2}, of the arm-2 MoSSe/WSSe heterostructure is also larger than lateral heterostructure MoS_2/WSe_2 (3.65×10^8 W K^{-1}·m^{-2} and 3.76×10^8 W K^{-1}·m^{-2} along armchair and zigzag directions) (Qin et al., 2019). It is worth noting that the heat flux of arm-2 (or zig-2) is larger than that of the arm-1 (zig-1) MoSSe/WSSe heterostructure, which is suppressed by the interface bending in arm-1 (or zig-1).

In particular, it is observed that the heat flux of the arm-1 (arm-2) heterostructure is also higher than that of the zig-1 (zig-2) heterostructure. The phonon scattering spectrums of lateral MoSSe/WSSe heterostructures with armchair and zigzag interfaces are demonstrated in **Figures 7A,B**, respectively, obtained by the density functional theory by the unit cell, as shown in **Figure 1**. It is worth noting that the slope of the acoustic branch in the arm-1 (or arm-2) heterostructure is steeper than that in the zig-1 (or zig-2) heterostructure in **Figure 7A** (or **Figure 7B**), which illustrates that the acoustic branches can be suppressed by the zigzag interface in the MoSSe/WSSe heterostructure, resulting in a lower group velocity. Thus, the heat flux in the MoSSe/WSSe heterostructure with an armchair interface is higher than that of the zigzag interface.

CONCLUSIONS

First-principles calculations and MD simulations were carried out to explore the electronic and thermal properties of the lateral Janus MoSSe/WSSe heterostructure. Four different structures of the Janus MoSSe/WSSe heterostructures were constructed by different symmetry and interface edges. These MoSSe/WSSe heterostructures possess direct type-II band structures, which can provide the ability to separate the photogenerated electrons and holes as a photocatalyst for water splitting. More interestingly, the asymmetric arrangement of S and Se in the Janus MoSSe/WSSe heterostructure can decrease the heat flux because of interface bending, while the lower heat flux and ITC of the Janus MoSSe/WSSe heterostructure with a zigzag interface is mainly due to the suppressed acoustic branches. The studied lateral Janus MoSSe/WSSe heterostructure in our work will provide theoretical guidance for the designing the 2D heterostructure to be used for future nano-devices.

DATA AVAILABILITY STATEMENT

The raw data supporting the conclusions of this article will be made available by the authors, without undue reservation.

AUTHOR CONTRIBUTIONS

All the authors listed have made a substantial, direct, and intellectual contribution to the work and approved it for publication.

FUNDING

The authors acknowledge the financial support for the research: Zhejiang Basic Public Welfare Research Program (Grant number: LGG20E050001), Academic Support Project for Top Talents of Subjects (majors) in Colleges and Universities (Grant number: gxbjZD63), Key Project of Natural Science Research of the Anhui Provincial Department of Education (Grant number: KJ 2019A1140), and School Level Scientific Research Promotion Plan Project (Grant number: ZXTS201801).

REFERENCES

Agarwal, A., Goverapet Srinivasan, S., and Rai, B. (2021). Data Driven Discovery of 2D Materials for Solar Water Splitting. *Front. Mater.* 8, 292. doi:10.3389/fmats.2021.679269

Allain, A., and Kis, A. (2014). Electron and Hole Mobilities in Single-Layer WSe2. *ACS Nano* 8, 7180–7185. doi:10.1021/nn5021538

Ang, Y. S., and Ang, L. K. (2019). Theory of Thermionic Carrier Injection in Graphene/organic Schottky Interface. *Front. Mater.* 6, 204. doi:10.3389/fmats.2019.00204

Butler, S. Z., Hollen, S. M., Cao, L., Cui, Y., Gupta, J. A., Gutiérrez, H. R., et al. (2013). Progress, Challenges, and Opportunities in Two-Dimensional Materials Beyond Graphene. *ACS Nano* 7, 2898–2926. doi:10.1021/nn400280c

Capelle, K. (2006). A Bird's-Eye View of Density-Functional Theory. *Braz. J. Phys.* 36, 1318–1343. doi:10.1590/s0103-97332006000700035

Chen, X.-K., Zeng, Y.-J., and Chen, K.-Q. (2020). Thermal Transport in Two-Dimensional Heterostructures. *Front. Mater.*, 427. doi:10.3389/fmats.2020.578791

Cui, Z., Luo, Y., Yu, J., and Xu, Y. (2021). Tuning the Electronic Properties of MoSi2N4 by Molecular Doping: A First Principles Investigation. *Physica E: Low-dimensional Syst. Nanostructures* 134, 114873. doi:10.1016/j.physe.2021.114873

Cui, Z., Lyu, N., Ding, Y., and Bai, K. (2021). Noncovalently Functionalization of Janus MoSSe Monolayer with Organic Molecules. *Physica E: Low-dimensional Syst. Nanostructures* 127, 114503. doi:10.1016/j.physe.2020.114503

Ding, G., He, J., Gao, G. Y., and Yao, K. (2018). Two-dimensional MoS_2-$MoSe_2$ Lateral Superlattice with Minimized Lattice Thermal Conductivity. *J. Appl. Phys.* 124. doi:10.1063/1.5051067

Dongqi, S., Xinjian, L., Ying, Z., Min, Z., and Xinyi, H. (2021). Structural and Transport Properties of 1T-VSe_2 Single crystal Under High Pressures. *Front. Mater.* 8, 710849. doi:10.3389/fmats.2021.710849

Duan, X., Wang, C., Shaw, J. C., Cheng, R., Chen, Y., Li, H., et al. (2014). Lateral Epitaxial Growth of Two-Dimensional Layered Semiconductor Heterojunctions. *Nat. Nanotech* 9, 1024–1030. doi:10.1038/nnano.2014.222

Fan, Q., Yan, L., Tripp, M. W., Krejčí, O., Dimosthenous, S., Kachel, S. R., et al. (2021). Biphenylene Network: A Nonbenzenoid Carbon Allotrope. *Science* 372, 852–856. doi:10.1126/science.abg4509

Gao, Y., Jing, Y., Liu, J., Li, X., and Meng, Q. (2017). Tunable Thermal Transport Properties of Graphene by Single-Vacancy Point Defect. *Appl. Therm. Eng.* 113, 1419–1425. doi:10.1016/j.applthermaleng.2016.11.160

Geim, A. K., and Novoselov, K. S. (2010). "The Rise of Graphene," in *Nanoscience and Technology: A Collection of Reviews from Nature Journals* (World Scientific), 11–19.

Guo, W., Ge, X., Sun, S., Xie, Y., and Ye, X. (2020). The Strain Effect on the Electronic Properties of the MoSSe/WSSe van der Waals Heterostructure: A First-principles Study. *Phys. Chem. Chem. Phys.* 22, 4946–4956. doi:10.1039/d0cp00403k

Hidding, J., and Guimarães, M. H. (2020). Spin-Orbit Torques in Transition Metal Dichalcogenides/Ferromagnet Heterostructures. *Front. Mater.* 7, 383. doi:10.3389/fmats.2020.594771

Hong, Y.-L., Liu, Z., Wang, L., Zhou, T., Ma, W., Xu, C., et al. (2020). Chemical Vapor Deposition of Layered Two-Dimensional MoSi 2 N 4 Materials. *Science* 369, 670–674. doi:10.1126/science.abb7023

Hu, Y., Feng, T., Gu, X., Fan, Z., Wang, X., Lundstrom, M., et al. (2020). Unification of Nonequilibrium Molecular Dynamics and the Mode-Resolved Phonon Boltzmann Equation for Thermal Transport Simulations. *Phys. Rev. B* 101, 155308. doi:10.1103/physrevb.101.155308

Jiang, J.-W. (2018). Misfit Strain-Induced Buckling for Transition-Metal Dichalcogenide Lateral Heterostructures: A Molecular Dynamics Study. *Acta Mech. Solida Sin.* 32, 17–28. doi:10.1007/s10338-018-0049-z

Jo, S.-H., Lee, H. W., Shim, J., Heo, K., Kim, M., Song, Y. J., et al. (2018). Highly Efficient Infrared Photodetection in a Gate-Controllable Van der Waals Heterojunction with Staggered Bandgap Alignment. *Adv. Sci.* 5, 1700423. doi:10.1002/advs.201700423

Keyte, J., Pancholi, K., and Njuguna, J. (2019). Recent Developments in Graphene Oxide/epoxy Carbon Fiber-Reinforced Composites. *Front. Mater.* 6, 224. doi:10.3389/fmats.2019.00224

Kim, D.-H., Kim, M.-S., and Kim, H.-D. (2015). Geometrical and Electronic Structures of Graphene Under Different Vacancy Density and Configuration. *Appl. Surf. Sci.* 359, 55–60. doi:10.1016/j.apsusc.2015.10.055

Kresse, G., and Furthmüller, J. (1996). Efficient Iterative Schemes Forab Initiototal-Energy Calculations Using a Plane-Wave Basis Set. *Phys. Rev. B* 54, 11169–11186. doi:10.1103/physrevb.54.11169

Kresse, G., and Joubert, D. (1999). From Ultrasoft Pseudopotentials to the Projector Augmented-Wave Method. *Phys. Rev. B* 59, 1758–1775. doi:10.1103/physrevb.59.1758

Li, F., Wei, W., Zhao, P., Huang, B., and Dai, Y. (2017). Electronic and Optical Properties of Pristine and Vertical and Lateral Heterostructures of Janus MoSSe and WSSe. *J. Phys. Chem. Lett.* 8, 5959–5965. doi:10.1021/acs.jpclett.7b02841

Li, J., Huang, Z., Ke, W., Yu, J., Ren, K., and Dong, Z. (2021). High Solar-to-hydrogen Efficiency in Arsenene/GaX (X = S, Se) van der Waals Heterostructure for Photocatalytic Water Splitting. *J. Alloys Comp.* 866, 158774. doi:10.1016/j.jallcom.2021.158774

Li, L., Yu, Y., Ye, G. J., Ge, Q., Ou, X., Wu, H., et al. (2014). Black Phosphorus Field-Effect Transistors. *Nat. Nanotech* 9, 372–377. doi:10.1038/nnano.2014.35

Li, L., Zhou, M., Jin, L., Liu, L., Mo, Y., Li, X., et al. (2019). Research Progress of the Liquid-phase Exfoliation and Stable Dispersion Mechanism and Method of Graphene. *Front. Mater.* 6, 325. doi:10.3389/fmats.2019.00325

Liu, X., Gao, J., Zhang, G., and Zhang, Y. W. (2018). Design of Phosphorene/graphene Heterojunctions for High and Tunable Interfacial Thermal Conductance. *Nanoscale* 10, 19854–19862. doi:10.1039/c8nr06110f

Liu, X., Zhang, G., and Zhang, Y.-W. (2016). Topological Defects at the Graphene/h-BN Interface Abnormally Enhance its Thermal Conductance. *Nano Lett.* 16, 4954–4959. doi:10.1021/acs.nanolett.6b01565

Liu, Y., Weiss, N. O., Duan, X., Cheng, H.-C., Huang, Y., and Duan, X. (2016). Van der Waals Heterostructures and Devices. *Nat. Rev. Mater.* 1, 16042. doi:10.1038/natrevmats.2016.42

Lou, J., Ren, K., Huang, Z., Huo, W., Zhu, Z., and Yu, J. (2021). Electronic and Optical Properties of Two-Dimensional Heterostructures Based on Janus XSSe (X = Mo, W) and Mg(OH)2: A First Principles Investigation. *RSC Adv.* 11, 29576–29584. doi:10.1039/d1ra05521f

Lu, A.-Y., Zhu, H., Xiao, J., Chuu, C.-P., Han, Y., Chiu, M.-H., et al. (2017). Janus Monolayers of Transition Metal Dichalcogenides. *Nat. Nanotech* 12, 744–749. doi:10.1038/nnano.2017.100

Luo, Y., Ren, C., Xu, Y., Yu, J., Wang, S., and Sun, M. (2021). A First Principles Investigation on the Structural, Mechanical, Electronic, and Catalytic Properties of Biphenylene. *Sci. Rep.* 11, 19008. doi:10.1038/s41598-021-98261-9

Luo, Y., Ren, K., Wang, S., Chou, J.-P., Yu, J., Sun, Z., et al. (2019). First-Principles Study on Transition-Metal Dichalcogenide/BSe van der Waals Heterostructures: A Promising Water-Splitting Photocatalyst. *J. Phys. Chem. C* 123, 22742–22751. doi:10.1021/acs.jpcc.9b05581

Luo, Y., Wang, S., Ren, K., Chou, J.-P., Yu, J., Sun, Z., et al. (2019). Transition-metal Dichalcogenides/Mg(OH)2 van der Waals Heterostructures as Promising Water-splitting Photocatalysts: A First-principles Study. *Phys. Chem. Chem. Phys.* 21, 1791–1796. doi:10.1039/c8cp06960c

Ma, Y., Dai, Y., Guo, M., Niu, C., Lu, J., and Huang, B. (2011). Electronic and Magnetic Properties of Perfect, Vacancy-Doped, and Nonmetal Adsorbed MoSe2, MoTe2 and WS2 Monolayers. *Phys. Chem. Chem. Phys.* 13, 15546–15553. doi:10.1039/c1cp21159e

Novoselov, K. S., Mishchenko, A., Carvalho, A., and Castro Neto, A. H. (2016). 2D Materials and van der Waals Heterostructures. *Science* 353, aac9439. doi:10.1126/science.aac9439

Ong, W.-J. (2017). 2D/2D Graphitic Carbon Nitride (G-C3n4) Heterojunction Nanocomposites for Photocatalysis: Why Does Face-To-Face Interface Matter. *Front. Mater.* 4, 11. doi:10.3389/fmats.2017.00011

Ouyang, T., Wang, X., Liu, S., Chen, H., and Deng, S. (2021). A Complete Two-Dimensional Avalanche Photodiode Based on $MoTe_2$–WS_2–$MoTe_2$ Heterojunctions with Ultralow Dark Current. *Front. Mater.* 8, 736180. doi:10.3389/fmats.2021.736180

Perdew, J. P., Burke, K., and Ernzerhof, M. (1996). Generalized Gradient Approximation Made Simple. *Phys. Rev. Lett.* 77, 3865–3868. doi:10.1103/physrevlett.77.3865

Plimpton, S. (1995). Fast Parallel Algorithms for Short-Range Molecular Dynamics. *J. Comput. Phys.* 117, 1–19. doi:10.1006/jcph.1995.1039

Qin, H., Pei, Q.-X., Liu, Y., and Zhang, Y.-W. (2019). The Mechanical and Thermal Properties of MoS2-WSe2 Lateral Heterostructures. *Phys. Chem. Chem. Phys.* 21, 15845–15853. doi:10.1039/c9cp02499a

Ren, K., Liu, X., Chen, S., Cheng, Y., Tang, W., and Zhang, G. (2020). Remarkable Reduction of Interfacial Thermal Resistance in Nanophononic Heterostructures. *Adv. Funct. Mater.* 30, 2004003. doi:10.1002/adfm.202004003

Ren, K., Shu, H., Huo, W., Cui, Z., Yu, J., and Xu, Y. (2021). Mechanical, Electronic and Optical Properties of a Novel B2P6 Monolayer: Ultrahigh Carrier Mobility and Strong Optical Absorption. *Phys. Chem. Chem. Phys.* 23, 24915–24921. doi:10.1039/d1cp03838a

Ren, K., Sun, M., Luo, Y., Wang, S., Yu, J., and Tang, W. (2019). First-principle Study of Electronic and Optical Properties of Two-Dimensional Materials-Based Heterostructures Based on Transition Metal Dichalcogenides and Boron Phosphide. *Appl. Surf. Sci.* 476, 70–75. doi:10.1016/j.apsusc.2019.01.005

Ren, K., Tang, W., Sun, M., Cai, Y., Cheng, Y., and Zhang, G. (2020). A Direct Z-scheme PtS2/arsenene van der Waals Heterostructure with High Photocatalytic Water Splitting Efficiency. *Nanoscale* 12, 17281–17289. doi:10.1039/d0nr02286a

Ren, K., Wang, S., Luo, Y., Chou, J.-P., Yu, J., Tang, W., et al. (2020). High-efficiency Photocatalyst for Water Splitting: A Janus MoSSe/XN (X = Ga, Al) van der Waals Heterostructure. *J. Phys. D: Appl. Phys.* 53, 185504. doi:10.1088/1361-6463/ab71ad

Ren, K., Yu, J., and Tang, W. (2020). Two-dimensional ZnO/BSe van der waals Heterostructure Used as a Promising Photocatalyst for Water Splitting: A DFT Study. *J. Alloys Comp.* 812, 152049. doi:10.1016/j.jallcom.2019.152049

Ren, K., Zheng, R., Lou, J., Yu, J., Sun, Q., and Li, J. (2021). Ab Initio Calculations for the Electronic, Interfacial and Optical Properties of Two-Dimensional AlN/Zr2CO2 Heterostructure. *Front. Chem.* 9, 796695. doi:10.3389/fchem.2021.796695

Ren, K., Zheng, R., Xu, P., Cheng, D., Huo, W., Yu, J., et al. (2021). Electronic and Optical Properties of Atomic-Scale Heterostructure Based on MXene and MN (M = Al, Ga): A DFT Investigation. *Nanomaterials* 11, 2236. doi:10.3390/nano11092236

Ren, K., Zheng, R., Yu, J., Sun, Q., and Li, J. (2021). Band Bending Mechanism in CdO/Arsenene Heterostructure: A Potential Direct Z-Scheme Photocatalyst. *Front. Chem.* 9, 788813. doi:10.3389/fchem.2021.788813

Shi, Y., Hua, C., Li, B., Fang, X., Yao, C., Zhang, Y., et al. (2013). Highly Ordered Mesoporous Crystalline MoSe2Material with Efficient Visible-Light-Driven Photocatalytic Activity and Enhanced Lithium Storage Performance. *Adv. Funct. Mater.* 23, 1832–1838. doi:10.1002/adfm.201202144

Shu, H. (2021). Adjustable Electro-Optical Properties of Novel Graphene-like SiC_2 via Strain Engineering. *Appl. Surf. Sci.* 559. doi:10.1016/j.apsusc.2021.149956

Sun, M., Chou, J.-P., Hu, A., and Schwingenschlögl, U. (2019). Point Defects in Blue Phosphorene. *Chem. Mater.* 31, 8129–8135. doi:10.1021/acs.chemmater.9b02871

Sun, M., Chou, J.-P., Ren, Q., Zhao, Y., Yu, J., and Tang, W. (2017). Tunable Schottky Barrier in van der Waals Heterostructures of Graphene and g-GaN. *Appl. Phys. Lett.* 110, 173105. doi:10.1063/1.4982690

Sun, M., Luo, Y., Yan, Y., and Schwingenschlögl, U. (2021). Ultrahigh Carrier Mobility in the Two-Dimensional Semiconductors B8Si4, B8Ge4, and B8Sn4. *Chem. Mater.* 33, 6475–6483. doi:10.1021/acs.chemmater.1c01824

Sun, M., and Schwingenschlögl, U. (2020). B2P6: A Two-Dimensional Anisotropic Janus Material with Potential in Photocatalytic Water Splitting and Metal-Ion Batteries. *Chem. Mater.* 32, 4795–4800. doi:10.1021/acs.chemmater.0c01536

Sun, M., and Schwingenschlögl, U. (2021). Structure Prototype Outperforming MXenes in Stability and Performance in Metal-Ion Batteries: A High Throughput Study. *Adv. Energ. Mater.* 11, 2003633. doi:10.1002/aenm.202003633

Sun, M., and Schwingenschlögl, U. (2021). Unique Omnidirectional Negative Poisson's Ratio in δ-Phase Carbon Monochalcogenides. *J. Phys. Chem. C* 125, 4133–4138. doi:10.1021/acs.jpcc.0c11555

Sun, M., Schwingenschlögl, U., and δ-, C. S. (2020). A Direct-Band-Gap Semiconductor Combining Auxeticity, Ferroelasticity, and Potential for High-Efficiency Solar Cells. *Phys. Rev. Appl.* 14, 044015. doi:10.1103/physrevapplied.14.044015

Togo, A., Oba, F., and Tanaka, I. (2008). First-principles Calculations of the Ferroelastic Transition Between Rutile-type and CaCl2-typeSiO2 at High Pressures. *Phys. Rev. B* 78, 134106. doi:10.1103/physrevb.78.134106

Togo, A., and Tanaka, I. (2015). First Principles Phonon Calculations in Materials Science. *Scripta Materialia* 108, 1–5. doi:10.1016/j.scriptamat.2015.07.021

Trivedi, D. B., Turgut, G., Qin, Y., Sayyad, M. Y., Hajra, D., Howell, M., et al. (2020). Room-Temperature Synthesis of 2D Janus Crystals and Their Heterostructures. *Adv. Mater.* 32, e2006320. doi:10.1002/adma.202006320

Vahedi Fakhrabad, D., Shahtahmasebi, N., and Ashhadi, M. (2015). Optical Excitations and Quasiparticle Energies in the AlN Monolayer Honeycomb Structure. *Superlattices and Microstructures* 79, 38–44. doi:10.1016/j.spmi.2014.12.012

Wang, B., Wang, X., Wang, P., Yang, T., Yuan, H., Wang, G., et al. (2019). Bilayer MoSe2/HfS2 Nanocomposite as a Potential Visible-Light-Driven Z-Scheme Photocatalyst. *Nanomaterials* 9, 1706. doi:10.3390/nano9121706

Wang, G., Zhang, L., Li, Y., Zhao, W., Kuang, A., Li, Y., et al. (2019). Biaxial Strain Tunable Photocatalytic Properties of 2D ZnO/GeC Heterostructure. *J. Phys. D: Appl. Phys.* 53, 015104. doi:10.1088/1361-6463/ab440e

Wei, N., Chen, Y., Cai, K., Zhao, J., Wang, H.-Q., and Zheng, J.-C. (2016). Thermal Conductivity of Graphene Kirigami: Ultralow and Strain Robustness. *Carbon* 104, 203–213. doi:10.1016/j.carbon.2016.03.043

Xu, Q., Zhang, L., Yu, J., Wageh, S., Al-Ghamdi, A. A., and Jaroniec, M. (2018). Direct Z-Scheme Photocatalysts: Principles, Synthesis, and Applications. *Mater. Today* 21, 1042–1063. doi:10.1016/j.mattod.2018.04.008

Xu, W., Zhang, G., and Li, B. (2015). Thermal Conductivity of Penta-Graphene from Molecular Dynamics Study. *J. Chem. Phys.* 143, 154703. doi:10.1063/1.4933311

Xu, Y., Lu, F., Liu, K., and Ma, C. (2020). Direct Graphene Synthesis on Lithium Niobate Substrate by Carbon Ion Implantation. *Front. Mater.* 7, 327. doi:10.3389/fmats.2020.572280

Yu, C., and Zhang, G. (2013). Impacts of Length and Geometry Deformation on thermal Conductivity of Graphene Nanoribbons. *J. Appl. Phys.* 113, 044306. doi:10.1063/1.4788813

Zaminpayma, E., Razavi, M. E., and Nayebi, P. (2017). Electronic Properties of Graphene with Single Vacancy and Stone-Wales Defects. *Appl. Surf. Sci.* 414, 101–106. doi:10.1016/j.apsusc.2017.04.065

Zhang, H., Chhowalla, M., and Liu, Z. (2018). 2D Nanomaterials: Graphene and Transition Metal Dichalcogenides. *Chem. Soc. Rev.* 47, 3015–3017. doi:10.1039/c8cs90048e

Zhao, H., Li, E., Liu, C., Shen, Y., Shen, P., Cui, Z., et al. (2021). DFT Computation of Two-dimensional CdO/GaS van der Waals Heterostructure: Tunable Absorption Spectra for Water Splitting Application. *Vacuum* 192, 110434. doi:10.1016/j.vacuum.2021.110434

Zhao, W., Ghorannevis, Z., Chu, L., Toh, M., Kloc, C., Tan, P.-H., et al. (2013). Evolution of Electronic Structure in Atomically Thin Sheets of WS2 and WSe2. *ACS Nano* 7, 791–797. doi:10.1021/nn305275h

Zhou, Q., Yong, Y., Su, X., Ju, W., Fu, Z., and Li, X. (2018). Adsorption Behavior of O2 on Vacancy-Defected Graphene with Transition-Metal Dopants: A Theoretical Study. *Int. J. Mod. Phys. B* 32, 1850304. doi:10.1142/s0217979218503046

Conflict of Interest: The authors declare that the research was conducted in the absence of any commercial or financial relationships that could be construed as a potential conflict of interest.

frontiers in Chemistry

ORIGINAL RESEARCH
published: 10 February 2022
doi: 10.3389/fchem.2021.832449

First-Principles Study on the Half-Metallicity of New MXene Materials Nd_2NT_2 (T = OH, O, S, F, Cl, and Br)

Kun Yang[1,2], Shuning Ren[2], Haishen Huang[1], Bo Wu[1]*, Guangxian Shen[2], Tingyan Zhou[1] and Xiaoying Liu[3]

[1]School of Physics and Electronic Science, Zunyi Normal University, Zunyi, China, [2]School of Physics and Electronic Science, Guizhou Normal University, Guiyang, China, [3]College of Teacher Education, Hainan Normal University, Haikou, China

This work systematically studied the structure, magnetic and electronic properties of the MXene materials Nd_2N and Nd_2NT_2 (T = OH, O, S, F, Cl, and Br) via first-principles calculations based on density functional theory. Results showed that Nd_2NT_2 (T = OH, O, S, F, Cl, and Br) have half-metallic characteristics whose half-metallic band gap width is higher than 1.70 eV. Its working function ranges from 1.83 to 6.50 eV. The effects of strain on its magnetic and electronic structures were evaluated. Results showed that the structure of Nd_2NT_2 (T = OH, O, S, and Br) transitions from a ferromagnetic half-metallic semiconductor to a ferromagnetic metallic and ferromagnetic semiconductor under different strains. By contrast, the structures of Nd_2NF_2 and Nd_2NS_2 were observed to transition from a half-metallic semiconductor to a ferromagnetic metallic semiconductor under different strains. Calculations of the electronic properties of different proportions of the surface functional groups of Nd_2NT_x (T = OH, O, and F; x = 0.5, 1(I, II), and 1.5) revealed that $Nd_2NO_{1.5}$ has the characteristics of semiconductors, whereas Nd_2NO(II) possesses the characteristics of half-metallic semiconductors. The other structures were observed to exhibit the characteristics of metallic semiconductors. Prediction of Nd_2NT_2 (T = OH, O, S, F, Cl, and Br) increases the types of lanthanide MXene materials. They are appropriate candidate materials for preparing spintronic devices.

Keywords: two-dimensional, MXene, Lanthanum series, half-metallic characteristics, spin polarization

Edited by:
Guangzhao Wang,
Yangtze Normal University, China

Reviewed by:
Xiaoming Zhang,
Hebei University of Technology, China
Hongkuan Yuan,
South University, United States

***Correspondence:**
Bo Wu
phywubo@163.com

Specialty section:
This article was submitted to Theoretical and Computational Chemistry, a section of the journal Frontiers in Chemistry

Received: *09 December 2021*
Accepted: *30 December 2021*
Published: *10 February 2022*

Citation:
Yang K, Ren S, Huang H, Wu B, Shen G, Zhou T and Liu X (2022) First-Principles Study on the Half-Metallicity of New MXene Materials Nd_2NT_2 (T = OH, O, S, F, Cl, and Br). Front. Chem. 9:832449. doi: 10.3389/fchem.2021.832449

1 INTRODUCTION

As candidate materials for preparing spintronic devices with a high-density, a high read/write speed, and an ultra-small volume, two-dimensional ferromagnetic half-metallic materials are the key to the development of spintronic devices (Wolf et al., 2001; Hu et al., 2014; Kent and Worledge, 2015; Wang et al., 2021a). Ferromagnetic half-metallic materials have 100% spin polarization. In a spin state, they have metallic properties at the Fermi level. In another spin state, they exhibit semiconductor or insulator properties at the Fermi level. Since 2004, graphene has been experimentally prepared successfully (Novoselov et al., 2004). Graphene is a semiconductor with a zero band gap, a feature limits its application in magnetic equipment (Novoselov et al., 2004; Geim and Novoselov, 2007). Graphene can be applied to spintronic devices by improving graphene or developing graphene-like materials. Extensive research on graphene-like materials, such as hexagonal boron nitride, silicon, phosphorus, transition-metal dichalcogenides and transition-metal carbon (nitrogen) compounds (MXenes), is being conducted (Denk et al., 1994; Sevik, 2013; Liu et al., 2014; Naguib et al., 2014; Kranthi Kumar et al., 2015). MXenes have received increased attention because they have abundant types.

Two-dimensional MXene materials have been developed using HF corrosion body phase material Ti_3AlC_2 to remove Al atom experimentally and obtain Ti_3C_2 materials with a few layers (Naguib et al., 2011). MXene materials are represented by the formula $M_{n+1}X_nT_x$ (n = 1, 2, 3), where M is a transition metal, X is either C or N, and T_x is a surface functional group. MXenes are becoming popular two-dimensional materials. Theoretical and experimental studies revealed that various MXene materials have intrinsic ferromagnetic half-metallicity, such as Cr_2C, Cr_2NO_2, Fe_2NO_2, Co_2NO_2, Ni_2NT_2 (T = O, F, OH), and Mn_2NT_2 (T = O, OH, F) (Si et al., 2015; Wang, 2016; Wang and Liao, 2017; Frey et al., 2018). External conditions can be applied to induce Ti_2NO_2, Cr_3C_2, and $Hf_2MnC_2O_2$ and obtain ferromagnetic half-metals (Chen et al., 2017; Zhang and Li, 2017; Siriwardane et al., 2019). However, several MXene materials have semiconductor properties, such as Sc_2CO_2, Ti_2CO_2, and Cr_2CT_2 (T = F, OH, O, Cl) (Lee et al., 2014; Si et al., 2015; Zhou et al., 2016). Therefore, MXenes have rich magnetic and electronic properties that must be harnessed.

Most MXene materials have different sensitivities to surface functional groups and external conditions. Therefore, MXene functional materials can be feasibly designed by exploiting functional groups or external conditions. However, current research on MXene materials mostly focuses on transition metals and largely ignores MXene materials with lanthanide elements. Tan et al. studied the strain piezoelectric coefficient of La_2CO_2, a lanthanide MXene material, under axial strain. They reported that strain piezoelectric coefficient of this material is up to 22.32 pm/V, which is substantially higher than that of other known piezoelectric materials, such as Sc_2CO_2, Y_2CO_2, BN, GaAs, and AlSb (Chen et al., 2021; Wang et al., 2021b). Bai et al. reported that the semiconductor MXene material Lu_2CT_2 (T = F, OH) has a low work function and a carrier mobility of about 105 cm^2/V at room temperature (Zhang et al., 2021). Therefore, lanthanide MXene materials have excellent properties with great application potential in sensors, electromagnetic interference and catalysis.

M_2N (M = Cr, Mo, W), which belongs to the VIB group in MXene materials (Hou et al., 2021), has excellent properties whose surface functional groups can induce Cr_2NO_2 to exhibit stable half-metallicity (Wang, 2016). On the basis of the semimetal properties of VIB MXene materials reported thus far, this work explored the structural and electromagnetic properties of the lanthanide MXene material Nd_2NT_2 (T = OH, O, S, F, Cl, and Br) to increase the known types of lanthanide MXene materials. This study provides theoretical guidance and direction to the preparation of related spintronic devices.

2 CALCULATION METHOD

First-principles calculations based on density functional theory were conducted using the CASTEP calculation package (Lin and Wang, 2017). Perdew–Burke–Ernzerhof exchange correlation function under the generalized gradient approximation was applied and ultrasoft pseudopotentials were selected to describe the interaction between electrons and ions in a two-dimensional system (Tan et al., 2019; Bai et al., 2020). In the process of geometric optimization of the structure of Nd_2NT_2 (T = OH, O, S, F, Cl, and Br), the two-dimensional structure preliminarily assumed was a ferromagnetic structure, and spin polarization calculations were performed. After testing the preliminary calculation parameters, the truncation energy chosen was 420 eV, the self-consistent convergence standard was set to 1×10^{-6} eV/atom, the sampling at k point was $10 \times 10 \times 1$, and the total energy convergence standard was set to 1×10^{-6} eV/atom. When the atomic structure was optimized, the force of each atom was not over 0.03 eV/Å, the maximum displacement of each atom was set to 0.001 Å, and the vacuum layer of the c axis was set to 20 Å.

The formation energy was calculated to describe the thermodynamic stability of two-dimensional MXene material systems with different surface functional groups by using the following formula (Bekaert et al., 2020):

$$E_F = E_{total}(Nd_2NT_2) - E_{total}(Nd_2N) - E_{total}(T_2) \tag{1}$$

where $E_{total}(Nd_2NT_2)$ is the total energy of Nd_2NT_2, $E_{total}(Nd_2N)$ is the total energy of Nd_2N, and $E_{total}(T_2)$ is the total energy of T_2 (T = OH, O, S, F, Cl, and Br) of functional groups.

3 RESULTS AND DISCUSSION

3.1 Surface Functional Groups of the Structure

The top and side views of Nd_2N after structural relaxation are shown in **Figures 1A, C**, respectively. The optimization results showed that Nd_2N is a hexagonal crystal structure composed of Nd atoms on both sides and N atoms in the middle. This structure is similar to that of materials reported in the literature (Si et al., 2015; Zhang et al., 2021). Different methods for preparing MXene materials inevitably result in the formation of certain functional groups on their surface. In this study, six different functional groups present T_2 (T = OH, O, S, F, Cl, and Br) in the optimized structure of Nd_2N were investigated (**Figures 1B, D**). According to previous studies, the functional groups on the surface may be found at three sites, namely, on the top of Nd, on the top of N, and on the top of Nd at the bottom of both sides. In this study, the functional groups were observed to be located on the top of Nd at the bottom of both sides, similar to that reported in the literature (Wang and Liao, 2017; Zhang et al., 2021).

The lattice constants of Nd_2N and Nd_2NT_2 and the bond lengths of Nd–N and Nd–T are listed in **Table 1**. The lattice constant of Nd_2NT_2 and the bond length of Nd–N are larger than those of Nd_2N, indicating that the functional groups on the

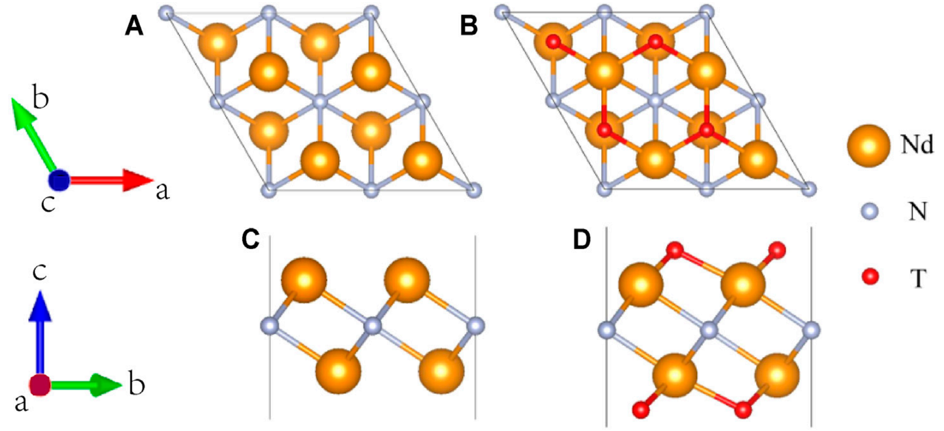

FIGURE 1 | Diagram of the structure of the 2 × 2×1 supercell of the two-dimensional MXene materials **(A,C)** Nd_2N and **(B,D)** Nd_2NT_2 (T = OH, O, S, F, Cl, and Br). **(A,B)** top views; **(C,D)** side views.

TABLE 1 | Lattice constants of the two-dimensional MXene materials Nd_2N and Nd_2NT_2 and bond lengths of Nd–N and Nd–T (T = OH, O, S, F, Cl, and Br).

Type	Nd_2N	$Nd_2N(OH)_2$	Nd_2NO_2	Nd_2NS_2	Nd_2NF_2	Nd_2NCl_2	Nd_2NBr_2
$a = b$/Å	3.743	3.785	3.755	4.232	3.796	3.911	3.971
$d_{\text{Nd-N}}$/Å	2.595	2.630	2.670	2.786	2.633	2.667	2.686
$d_{\text{Nd-N}}$/Å	—	2.541	2.280	2.738	2.457	2.857	3.015

TABLE 2 | Total atomic magnetic moment (M_{total}) and atomic resolution magnetic moment (M), and formation energy (E_F) of the two-dimensional MXene materials Nd_2N and Nd_2NT_2 (T = OH, O, S, F, Cl, and Br).

Structure	$M_{\text{Nd}}(\mu_B)$	$M_{\text{N}}(\mu_B)$	$M_{\text{T}}(\mu_B)$	$M_{\text{total}}(\mu_B)$	E_F(eV)
Nd_2N	9.04	−0.09	—	8.95	—
$Nd_2N(OH)_2$	7.24	−0.19	−0.04	7.01	−25.92
Nd_2NO_2	6.46	−0.88	−0.58	5.00	−16.98
Nd_2NS_2	6.76	−1.02	−0.76	4.98	−10.42
Nd_2NF_2	7.24	−0.19	−0.04	7.01	−14.75
Nd_2NCl_2	7.26	−0.20	−0.06	7.00	−10.47
Nd_2NBr_2	7.28	−0.20	−0.08	7.00	−9.016

surface can change the structure of Nd_2N. Nd_2NS_2 has the largest lattice constant (4.232 Å), whereas Nd_2NO_2 has the smallest lattice constant (3.755 Å). Moreover, the Nd–N and Nd–T bond lengths of Nd_2NS_2 are longer than those of Nd_2NO_2 because both O and S belong to the VIA family and have similar properties. The radius of the S atom is greater than that of the O atom. The lattice constants of Nd_2NF_2, Nd_2NCl_2, and Nd_2NBr_2 are 3.796, 3.911, and 3.971 Å, respectively. The lattice constants increase with the increase in the atomic radius of the VIIA family, and the bond lengths of Nd–N and Nd–T gradually increase. However, the bond length of Nd–T is quite different. Nd–Br has the maximum bond length (3.015 Å), whereas Nd–O has the minimum bond length (2.280 Å), indicating that the bonding intensity of Nd and O is greater than that of Nd–Br. However, the bond length of Nd–N is 2.62–2.69 Å, indicating that although the different surface functional groups have an effect on the structure of the monolayer Nd_2N, their effect on the bond length of this structure is less than that on its lattice constant.

3.2 Magnetic and Thermodynamic Stability

The atomic resolution magnetic moments and formation energies of Nd_2N and Nd_2NT_2 (T = OH, O, S, F, Cl, and Br) were calculated to assess their magnetic and thermodynamic stability (**Table 2**). The magnetic moments of monolayer Nd_2N (up to 8.95 μ_B) are higher than those of Nd_2NT_2 (T = OH, O, S, F, Cl, and Br). However, the magnetic moments of $Nd_2N(OH)_2$, Nd_2NF_2, Nd_2NCl_2, Nd_2NBr_2, Nd_2NO_2, and Nd_2NS_2 are 7.01, 7.01, 7.00, 7.00, 5.00, and 4.98 μ_B, respectively. The magnetic moment of Nd_2N mainly comes from two Nd atoms, and the contribution of the N atom to the total magnetic moment is small. The Nd atom is still the main contributor to the magnetic moment of $Nd_2N(OH)_2$. However, with the addition of –OH, the total magnetic moment is reduced to 7.01 μ_B. The magnetic moment of the nonmagnetic elements is also reduced because of the strengthening of hybridization between the atoms that strengthened the magnetic coupling effect and reduced the magnetic moment. In the structures of Nd_2NO_2 and Nd_2NS_2, the total magnetic moment is substantially reduced primarily because of the fact that the magnetic moment of the N atom of the Nd atom is remarkably smaller. Moreover, the magnetic moments of the nonmagnetic elements O and S in the induced surface functional groups are considerably smaller than those of the magnetic elements, indicating that the bonds between

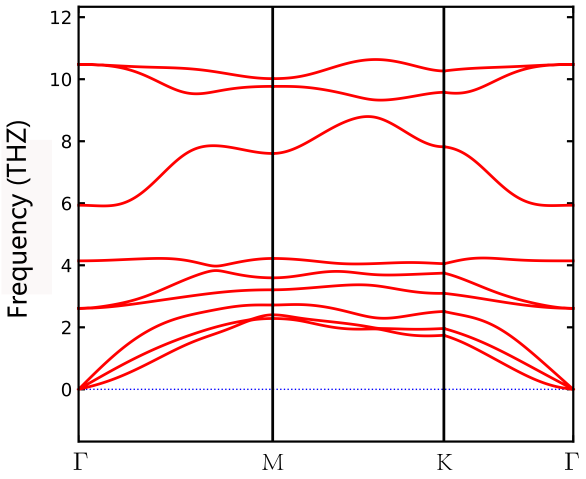

FIGURE 2 | Phonon spectrum of Nd_2N structure.

the O and S atoms and Nd atom are relatively intense, resulting in a sharp decrease in atomic localization. In addition, the total magnetic moment of the structures of Nd_2NF_2, Nd_2NCl_2, and Nd_2NBr_2 remains 7.00 μ_B. The increase in the amplitude of Nd and the F, Cl, and Br atoms is the same as that in the decrease in their amplitude. By comparison, the magnetic moment of the N atom remains low.

After the structural and magnetic properties of the materials were determined, the phonon spectrum of monolayer Nd_2N and the formation energy of Nd_2NT_2 (T = OH, O, S, F, Cl, and Br) were further calculated. According to the phonon spectrum of Nd_2N, it has good dynamic stability (**Figure 2**). **Equation 1** was also used to calculate the formation energy of Nd_2NT_2 (T = OH, O, S, F, Cl, and Br). $Nd_2N(OH)_2$ has the smallest formation energy of −25.92 eV, whereas Nd_2NBr_2 has the largest formation energy of −9.016 eV (**Table 2**), indicating an intense interaction between the metals and the surface functional groups. When the surface functional groups are F, Cl, and Br (VIIA group), the formation energy gradually decreases (**Table 2**). However, the surface functional groups O and S (VIA group) also show a similar rule. According to previous studies, on the surface functional groups of MXene structures, the formation energy can easily change from high to low under certain conditions. The formation energy of the –OH structure with surface functional groups is smaller than that of the O, S, F, Cl, and Br structures with surface functional groups (**Table 2**), suggesting that MXene materials with O, S, F, Cl, and Br as functional groups should not be washed or stored in H_2O during preparation to prevent them from being converted into –OH MXene materials (Perdew et al., 1996).

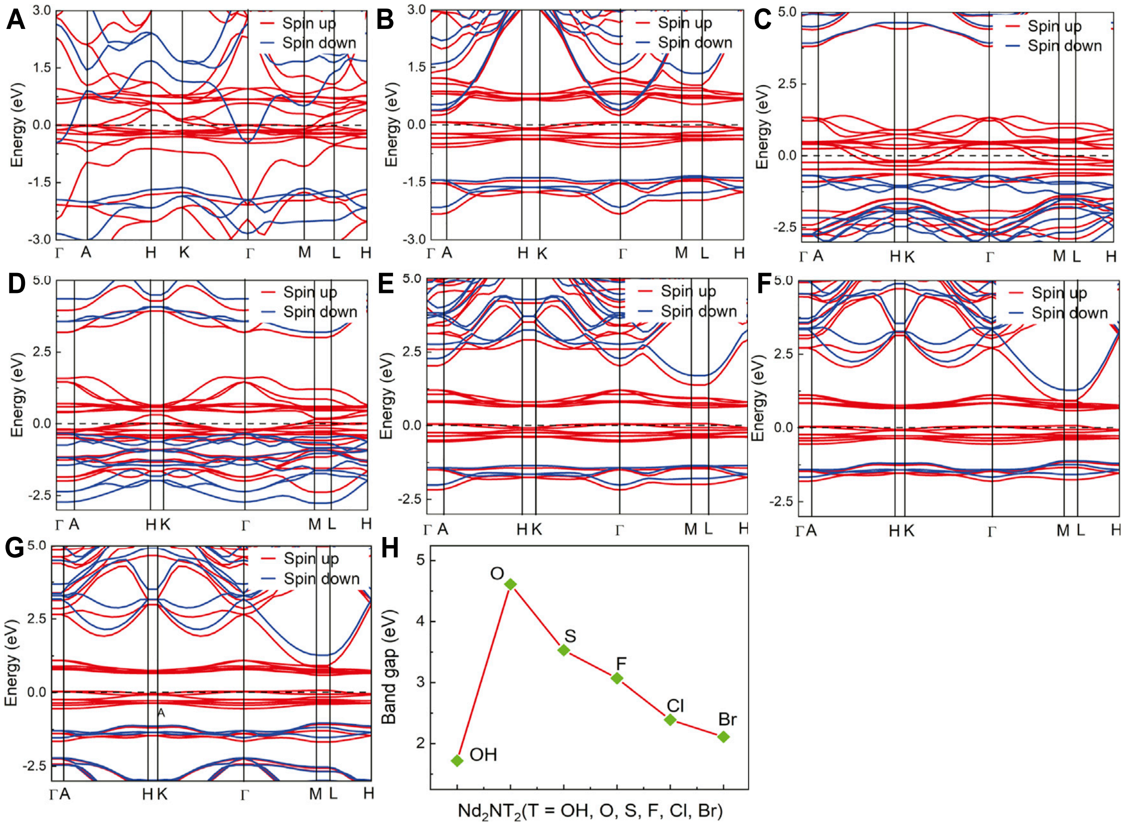

FIGURE 3 | Energy band structure and band gap width diagram of the two–dimensional MXene materials Nd_2N and Nd_2NT_2 (T = OH, O, S, F, Cl, and Br). **(A)** Nd_2N, **(B)** $Nd_2N(OH)_2$, **(C)** Nd_2NO_2, **(D)** Nd_2NS_2, **(E)** Nd_2NF_2, **(F)** Nd_2NCl_2, **(G)** Nd_2NBr_2, and **(H)** band gap width diagram.

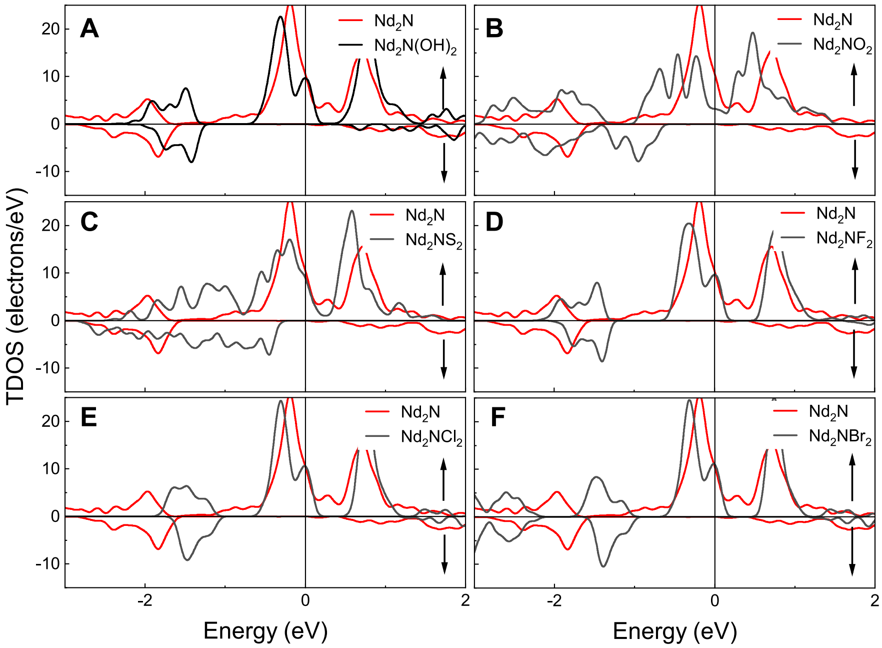

FIGURE 4 | Total density of states (TDOS) of Nd_2N and Nd_2NT_2 (T = OH, O, S, F, Cl, and Br). The red line represents Nd_2N, whereas the black line denotes is **(A)** $Nd_2N(OH)_2$, **(B)** Nd_2NO_2, **(C)** Nd_2NS_2, **(D)** Nd_2NF_2, **(E)** Nd_2NCl_2, **(F)** Nd_2NBr_2, respectively.

3.3 Electronic Properties

The electronic properties of Nd_2N and Nd_2NT_2 (T = OH, O, S, F, Cl, and Br) were evaluated by calculating and plotting the energy band structure diagram (**Figure 3**). The spin up and the spin down of the energy band structure of Nd_2N pass through the Fermi level, indicating that it has ferromagnetic characteristics. In the spin down channel, the energy band density near the Fermi level is relatively sparse, indicating that the energy band structure can be changed under certain conditions, which are described below.

1) In the energy band structure of Nd_2NT_2 (T = OH, F, Cl, and Br), the spin up energy band at the Fermi level passes through the Fermi level, whereas the spin down energy band has an energy band gap, indicating that it has semimetal characteristics. The spin up energy band has an energy band gap near the Fermi level, indicating that the structure may change from a semimetal to a semiconductor under certain conditions.
2) In the band structure of Nd_2NT_2 (T = O and S), the spin up band at the Fermi level passes through the Fermi level, suggesting that it has metal characteristics. However, the spin down band has an energy band gap at the Fermi level, reflecting the nature of a semiconductor. Therefore, there is 100% spin polarization at the Fermi level, indicating that it has semimetal characteristics. According to the energy band structure, the band gap width between the spin down valence band and the Fermi surface is approximately 0.2–0.6 eV, and the band gap width between the spin down conduction band and the Fermi surface is greater than 3 eV, indicating that the structure does not readily change from a half-metal to a metal. Theoretically, the half-metallicity remains stable under certain external conditions.
3) The spin down band gap width of the semimetal was counted. $Nd_2N(OH)_2$ has the smallest band gap width (1.72 eV), whereas Nd_2NO_2 has the largest band gap width (4.61 eV) (**Figure 3H**). Therefore, the half-metallicity can remain stable within a certain range.

The calculated total density of states (TDOS) of Nd_2N and Nd_2NT_2 (T = OH, O, S, F, Cl, and Br) are provided in **Figure 4**. As can be seen from the TDOS graphs, the polarization peak of $Nd_2N(OH)_2$ appears at 1.5 eV, but this phenomenon is not observed in Nd_2N. Moreover, the spin down band gaps of Nd_2NO_2 and Nd_2NS_2 move to the high energy region, and their band gap width increase. However, the spin down band gaps of Nd_2NF_2, Nd_2NCl_2, and Nd_2NBr_2 exhibit similar behavioral changes, and the only differences are in the energy range of spin polarization peaks, which gradually move to the high-energy region.

3.4 Work Functions of Nd_2NT_2 (T = OH, O, S, F, Cl, and Br)

Work function, as a reference for charge transfer, is a key parameter. The definition of work function (φ_{wf}) is as follows (Vanderbilt, 1990):

$$\varphi_{wf} = E_{vacuum} - E_F \tag{2}$$

where E_{vacuum} represents the energy of the surface electron energy level in the vacuum, and E_F is the Fermi level of the

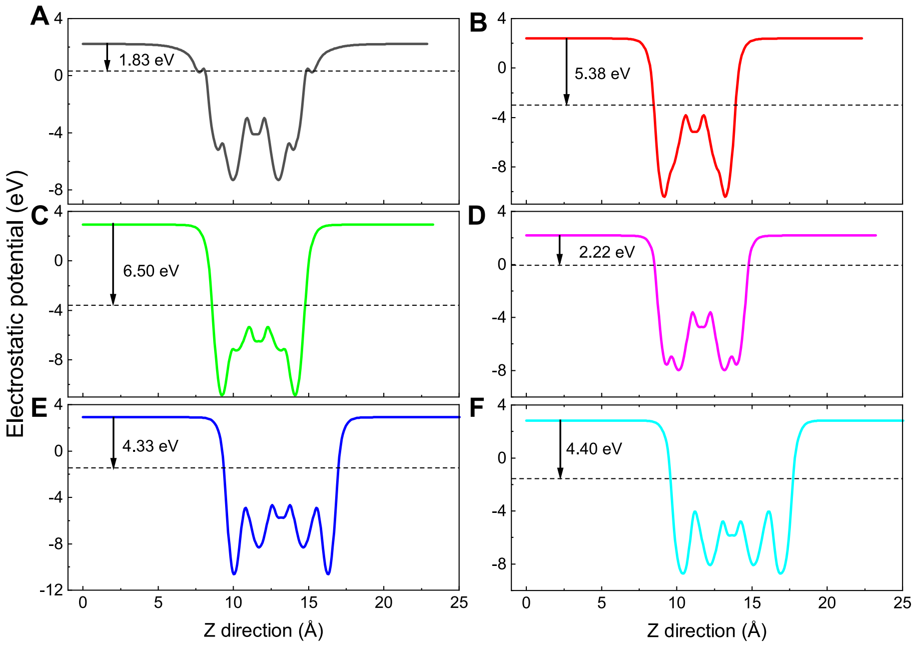

FIGURE 5 | Calculated electrostatic potentials along the *Z* direction of Nd_2NT_2 (T = OH, O, S, F, Cl, and Br), while **(A)** $Nd_2N(OH)_2$, **(B)** Nd_2NO_2, **(C)** Nd_2NS_2, **(D)** Nd_2NF_2, **(E)** Nd_2NCl_2, **(F)** Nd_2NBr_2, respectively. The black arrow indicates the difference from vacuum level to the Fermi level. The black dashed line denotes the Fermi level.

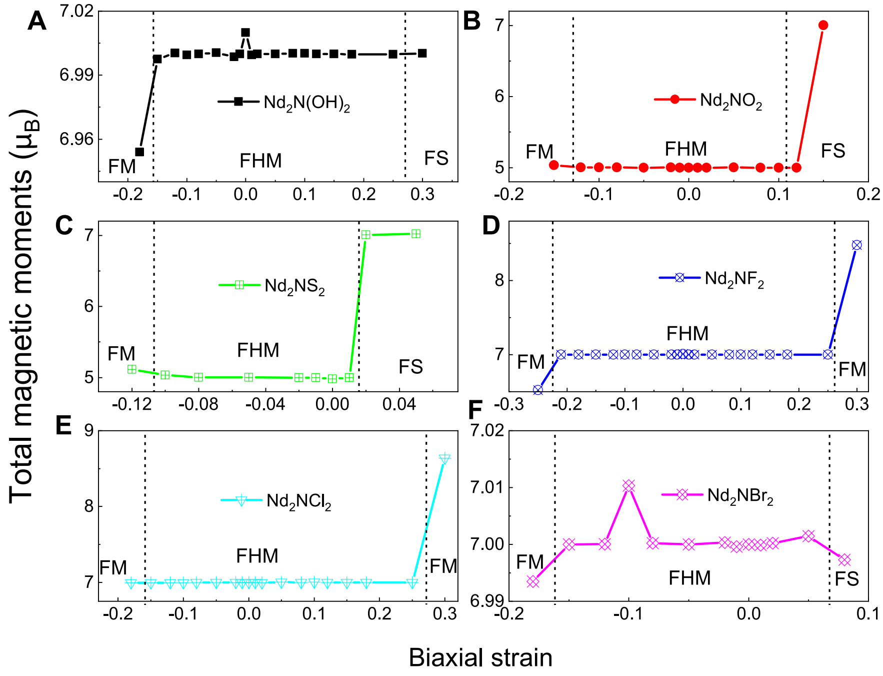

FIGURE 6 | Total magnetic moments of monolayer Nd_2NT_2 (T = OH, O, S, F, Cl, and Br) under biaxial strain. **(A)** $Nd_2N(OH)_2$, **(B)** Nd_2NO_2, **(C)** Nd_2NS_2, **(D)** Nd_2NF_2, **(E)** Nd_2NCl_2, **(F)** Nd_2NBr_2. FM, FHM, and FS denote ferromagnetic metallic, ferromagnetic half-metallic, and ferromagnetic semiconductor, respectively.

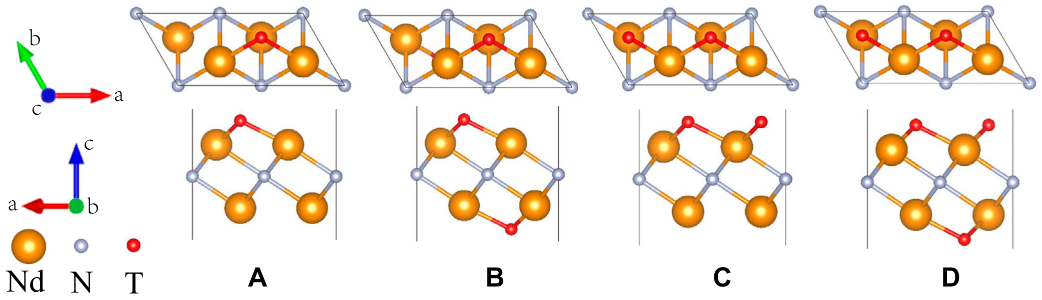

FIGURE 7 | Top and side views of the 2 × 1×1 supercell of the structure of the two-dimensional MXene material Nd_2NT_x (T = OH, O, F; x = 0.5, 1, and 1.5). **(A)** $Nd_2NT_{0.5}$ (T = OH, O, F), **(B)** Nd_2NT (T = OH, O, F)(I), **(C)** Nd_2NT (T = OH, O, F)(II), and **(D)** $Nd_2NT_{1.5}$ (T = OH, O, F).

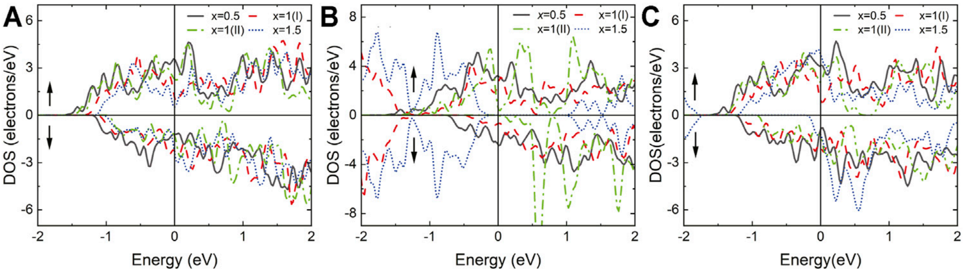

FIGURE 8 | Total density of state(DOS) of **(A)** $Nd_2N(OH)_x$, **(B)** Nd_2NO_x, and **(C)** Nd_2NF_x, where x = 0.5, 1(I), 1(II), and 1.5.

MXene material. The electrostatic potentials of Nd_2NT_2 (T = OH, O, S, F, Cl, and Br) are calculated using **Eq. 2** and plotted in **Figure 5**. The work function of Nd_2N is approximately 1.186 eV, whereas that of $Nd_2N(OH)_2$, Nd_2NO_2, Nd_2NS_2, Nd_2NF_2, Nd_2NCl_2, and Nd_2NBr_2 is 1.83, 5.38, 6.50, 2.22, 4.33, and 4.40 eV, respectively. The work function of –OH is 1.6–2.8 eV, similar to that reported in the literature (Khazaei et al., 2013). Moreover, the work function of Nd_2NT_2 (T = OH, F, Cl, and Br) increases as VIIA atoms are introduced. The work function of Nd_2NO_2 is evidently lower than that of Nd_2NS_2. The work functions indicate that lanthanide MXene materials have potential applications in spintronic devices.

3.5 Strain Effect

The effects of strain on the magnetic and electronic structure of monolayer Nd_2NT_2 (T = OH, O, S, F, Cl, and Br) were evaluated by calculating the magnetic moment under different biaxial strains (**Figure 6**). Theoretical studies indicated that the electronic and magnetic properties of the monolayer MXenes Ti_2C and Ti_2N are tunable by strain (Clark et al., 2005; Sternik and Wdowik, 2018). Thus, biaxial strain was applied to monolayer Nd_2NT_2 (T = OH, O, S, F, Cl, and Br) by using the following formula:

$$\varepsilon = \frac{L - L_0}{L_0} \tag{3}$$

where L and L_0 are the lattice constants of strain and the equilibrium, respectively. Positive and negative ε values correspond to tensile and compressive strain, respectively. Under different strains, both Nd_2NF_2 and Nd_2NCl_2 transition from a ferromagnetic half-metallic structure to a ferromagnetic metallic structure (**Figure 6**), and their total magnetic moment is maintained is from 6.5 to 9.0 μ_B. By comparison, $Nd_2N(OH)_2$, Nd_2NO_2, Nd_2NS_2, and Nd_2NBr_2 transition from a ferromagnetic half-metallic structure to a ferromagnetic metallic structure and a ferromagnetic semiconductor under different strains. Notably, the total magnetic moments of the transition of Nd_2NO_2 and Nd_2NS_2 range from 5 to 7 $\mu_B$under strain.

3.6 Electronic Properties of Different Proportions of the Surface Functional Groups of Nd_2NT_x (T = OH, O, F; x = 0.5, 1(I, II), and 1.5)

Surface functional groups have a great influence on the electronic properties of MXene materials (Xie et al., 2014). The influence of different proportions of the surface functional groups of the Nd_2NT_x materials on their electronic properties was assessed at proportions of x = 0.5, 1, and 1.5 (**Figure 7**). x = 1 has two types; in type I, the functional groups are distributed on both sides, whereas in type II, the functional groups are distributed on one side only. After geometry optimization, TDOS was calculated (**Figure 8**).

The structures of $Nd_2N(OH)_x$ and Nd_2NF_x exhibit metal characteristics because of the asymmetry of their surface functional groups. When the surface functional group is 100%, the material has half-metallic characteristics. This result provides a direction for detecting the richness of surface functional groups experimentally.

When $x = 0.5$ and 1 (type I), the structure of Nd_2NO_x exhibits metal characteristics. However, when $x = 1$ (type II), an obvious band gap is observed in the spin downward at the Fermi level, indicating that it has half-metal characteristics. Unexpectedly, when $x = 1.5$, both spin up and spin down have a symmetric band gap width at the Fermi level, indicating that it has the characteristics of a semiconductor. This result provides a reliable direction for the regulation of electronic properties by controlling the richness of surface functional groups experimentally.

4 DISCUSSION

The structural, magnetic, and electronic properties of Nd_2N and Nd_2NT_2 (T = OH, O, S, F, Cl, and Br) were evaluated via first-principles calculations based on density functional theory. According to the calculated phonon spectrum and formation energies, Nd_2N and Nd_2NT_2 (T = OH, O, S, F, Cl, and Br) are stable. Owing to the effects of surface functional groups on the electronic properties of Nd_2NT_2 (T = OH, O, S, F, Cl, and Br), it exhibits the characteristics of a half-metal, and its band gap width is higher than 1.70 eV. The work function ranges from 1.83 to 6.50 eV, indicating that lanthanide MXene materials have potential applications in spintronic devices. Under different strains, Nd_2NT_2 (T = OH, O, S, and Br) transition from a ferromagnetic half-metallic structure to a ferromagnetic metallic structure and a ferromagnetic semiconductor. However, the structures of Nd_2NF_2 and Nd_2NS_2 transition from a half-metallic structure to a ferromagnetic metallic structure under different strains. Calculation of the electronic properties of different proportions of the surface functional groups of Nd_2NT_x (T = OH, O, F; $x = 0.5$, 1(I, II), and 1.5) revealed that $Nd_2NO_{1.5}$ has the characteristics of a semiconductors, whereas Nd_2NO(II) has the characteristics of a half-metal. The other structures show the characteristics of a metal. This study demonstrated that new lanthanide MXene materials have a high application potential in spintronic devices.

DATA AVAILABILITY STATEMENT

The original contributions presented in the study are included in the article/Supplementary Material, further inquiries can be directed to the corresponding author.

AUTHOR CONTRIBUTIONS

Methodology, KY and BW; software, TZ and KY; data curation, SR; XL and KY; writing-original draft preparation, KY and HH; writing-review and editing, GS; BW and KY. All authors have read and agreed to the published version of the manuscript.

FUNDING

This work was financially supported by the Graduate Research Fund of Guizhou Province (YJSCXJH(2019)042), Major Research Projects for Innovative Groups of Guizhou Education Department (QJHKY(2020)025), Natural Science Foundation of Hainan Province (121MS032), Guizhou Science and Technology Plan Project (QKHJC-ZK(2021)029), Zunyi Science and Technology Plan Project (ZSKHHZ(2021)211), Key Laboratory of Clean Energy Materials and Devices in Guizhou Province (QJHKY(2019)055).

REFERENCES

Bai, X., Zha, X.-H., Qiao, Y., Qiu, N., Zhang, Y., Luo, K., et al. (2020). Two-dimensional Semiconducting Lu2CT2(T = F, OH) MXene with Low Work Function and High Carrier Mobility. *Nanoscale* 12, 3795–3802. doi:10.1039/C9NR10806H

Bekaert, J., Sevik, C., and Milošević, M. V. (2020). First-principles Exploration of Superconductivity in Mxenes. *Nanoscale* 12, 17354–17361. doi:10.1039/D0NR03875J

Chen, Q. D., Yuan, S. F., Dai, J. H., and Song, Y. (2021). Functionalized M2TiC2Tx MXenes (M = Cr and Mo; T = F, O, and OH) as High Performance Electrode Materials for Sodium Ion Batteries. *Phys. Chem. Chem. Phys.* 23, 1038–1049. doi:10.1039/D0CP01846E

Chen, W., Li, H.-F., Shi, X., and Pan, H. (2017). Tension-Tailored Electronic and Magnetic Switching of 2D Ti2NO2. *J. Phys. Chem. C* 121, 25729–25735. doi:10.1021/acs.jpcc.7b08496

Clark, S. J., Segall, M. D., Pickard, C. J., Hasnip, P. J., Probert, M. I. J., Refson, K., et al. (2005). First Principles Methods Using CASTEP. *Z. Kristallogr. Krist.* 220, 567–570. doi:10.1524/zkri.220.5.567.65075

Denk, M., Lennon, R., Hayashi, R., West, R., Belyakov, A. V., Verne, H. P., et al. (1994). Synthesis and Structure of a Stable Silylene. *J. Am. Chem. Soc.* 116, 2691–2692. doi:10.1021/ja00085a088

Frey, N. C., Kumar, H., Anasori, B., Gogotsi, Y., and Shenoy, V. B. (2018). Tuning Noncollinear Spin Structure and Anisotropy in Ferromagnetic Nitride Mxenes. *ACS Nano* 12, 6319–6325. doi:10.1021/acsnano.8b03472

Geim, A. K., and Novoselov, K. S. (2007). The Rise of Graphene. *Nat. Mater* 6, 183–191. doi:10.1038/nmat1849

Hou, H., Shao, G., and Yang, W. (2021). Recent Advances in G-C3n4-Based Photocatalysts Incorporated by MXenes and Their Derivatives. *J. Mater. Chem. A.* 9, 13722–13745. doi:10.1039/D1TA02527A

Hu, H., Wang, Z., and Liu, F. (2014). Half Metal in Two-Dimensional Hexagonal Organometallic Framework. *Nanoscale. Res. Lett.* 9, 690. doi:10.1186/1556-276X-9-690

Kent, A. D., and Worledge, D. C. (2015). A New Spin on Magnetic Memories. *Nat. Nanotech* 10, 187–191. doi:10.1038/nnano.2015.24

Khazaei, M., Arai, M., Sasaki, T., Chung, C.-Y., Venkataramanan, N. S., Estili, M., et al. (2013). Novel Electronic and Magnetic Properties of Two-Dimensional Transition Metal Carbides and Nitrides. *Adv. Funct. Mater.* 23, 2185–2192. doi:10.1002/adfm.201202502

Kranthi Kumar, V., Dhar, S., Choudhury, T. H., Shivashankar, S. A., and Raghavan, S. (2015). A Predictive Approach to CVD of Crystalline Layers of TMDs: the Case of MoS2. *Nanoscale* 7, 7802–7810. doi:10.1039/C4NR07080A

Lee, Y., Cho, S. B., and Chung, Y.-C. (2014). Tunable Indirect to Direct Band Gap Transition of Monolayer Sc2CO2 by the Strain Effect. *ACS Appl. Mater. Inter.* 6, 14724–14728. doi:10.1021/am504233d

Lin, X., and Wang, J. (2017). Research Progress on Preparation and Application of Two-Dimensional Transition Metal Dichalcogenides Nanomaterials. *Acta Chim. Sinica* 75, 979. doi:10.6023/A17060282

Liu, H., Neal, A. T., Zhu, Z., Luo, Z., Xu, X., Tománek, D., et al. (2014). Phosphorene: An Unexplored 2D Semiconductor with a High Hole Mobility. *ACS Nano* 8, 4033–4041. doi:10.1021/nn501226z

Naguib, M., Kurtoglu, M., Presser, V., Lu, J., Niu, J., Heon, M., et al. (2011). Two-Dimensional Nanocrystals Produced by Exfoliation of Ti3AlC2. *Adv. Mater.* 23, 4248–4253. doi:10.1002/adma.201102306

Naguib, M., Mochalin, V. N., Barsoum, M. W., and Gogotsi, Y. (2014). 25th Anniversary Article: Mxenes: A New Family of Two-Dimensional Materials. *Adv. Mater.* 26, 992–1005. doi:10.1002/adma.201304138

Novoselov, K. S., Geim, A. K., Morozov, S. V., Jiang, D., Zhang, Y., Dubonos, S. V., et al. (2004). Electric Field Effect in Atomically Thin Carbon Films. *Science* 306, 666–669. doi:10.1126/science.1102896

Perdew, J. P., Burke, K., and Ernzerhof, M. (1996). Generalized Gradient Approximation Made Simple. *Phys. Rev. Lett.* 77, 3865–3868. doi:10.1103/PhysRevLett.77.3865

Sevik, C. (2013). Assessment on Lattice thermal Properties of Two-Dimensional Honeycomb Structures: Graphene,h-BN,h-MoS2, Andh-MoSe2. *Phys. Rev. B* 89. doi:10.1103/PhysRevB.89.035422

Si, C., Zhou, J., and Sun, Z. (2015). Half-Metallic Ferromagnetism and Surface Functionalization-Induced Metal-Insulator Transition in Graphene-like Two-Dimensional Cr2C Crystals. *ACS Appl. Mater. Inter.* 7, 17510–17515. doi:10.1021/acsami.5b05401

Siriwardane, E. M. D., Karki, P., Loh, Y. L., and Çakır, D. (2019). Strain-Spintronics: Modulating Electronic and Magnetic Properties of Hf2MnC2O2 MXene by Uniaxial Strain. *J. Phys. Chem. C* 123, 12451–12459. doi:10.1021/acs.jpcc.9b00594

Sternik, M., and Wdowik, U. D. (2018). Probing the Impact of Magnetic Interactions on the Lattice Dynamics of Two-Dimensional Ti2X (X = C, N) MXenes. *Phys. Chem. Chem. Phys.* 20, 7754–7763. doi:10.1039/c7cp08270c

Tan, J., Wang, Y., Wang, Z., He, X., Liu, Y., Wang, B., et al. (2019). Large Out-of-Plane Piezoelectricity of Oxygen Functionalized Mxenes for Ultrathin Piezoelectric Cantilevers and Diaphragms. *Nano Energy* 65, 104058. doi:10.1016/j.nanoen.2019.104058

Vanderbilt, D. (1990). Soft Self-Consistent Pseudopotentials in a Generalized Eigenvalue Formalism. *Phys. Rev. B* 41, 7892–7895. doi:10.1103/PhysRevB.41.7892

Wang, G., and Liao, Y. (2017). Theoretical Prediction of Robust and Intrinsic Half-Metallicity in Ni 2 N MXene with Different Types of Surface Terminations. *Appl. Surf. Sci.* 426, 804–811. doi:10.1016/j.apsusc.2017.07.249

Wang, G., Qin, W., Wang, S., Teketel, B. S., Yu, W., Luo, T., et al. (2021). CrI3/Y2CH2 Heterointerface-Induced Stable Half-Metallicity of Two-Dimensional CrI3 Monolayer Ferromagnets. *ACS Appl. Mater. Inter.* 13, 16694–16703. doi:10.1021/acsami.1c01768

Wang, G. (2016). Theoretical Prediction of the Intrinsic Half-Metallicity in Surface-Oxygen-Passivated Cr2N MXene. *J. Phys. Chem. C* 120, 18850–18857. doi:10.1021/acs.jpcc.6b05224

Wang, Z., Yu, K., Gong, S., Mao, H., Huang, R., and Zhu, Z. (2021). Cu3BiS3/MXenes with Excellent Solar-Thermal Conversion for Continuous and Efficient Seawater Desalination. *ACS Appl. Mater. Inter.* 13, 16246–16258. doi:10.1021/acsami.0c22761

Wolf, S. A., Awschalom, D. D., Buhrman, R. A., Daughton, J. M., von Molna´r, S., Roukes, M. L., et al. (2001). Spintronics: A Spin-Based Electronics Vision for the Future. *Science* 294, 1488–1495. doi:10.1126/science.1065389

Xie, Y., Naguib, M., Mochalin, V. N., Barsoum, M. W., Gogotsi, Y., Yu, X., et al. (2014). Role of Surface Structure on Li-Ion Energy Storage Capacity of Two-Dimensional Transition-Metal Carbides. *J. Am. Chem. Soc.* 136, 6385–6394. doi:10.1021/ja501520b

Zhang, Y., and Li, F. (2017). Robust Half-Metallic Ferromagnetism in Cr 3 C 2 MXene. *J. Magnet. Magn. Mater.* 433, 222–226. doi:10.1016/j.jmmm.2017.03.031

Zhang, Y., Sa, B., Miao, N., Zhou, J., and Sun, Z. (2021). Computational Mining of Janus Sc2C-Based MXenes for Spintronic, Photocatalytic, and Solar Cell Applications. *J. Mater. Chem. A.* 9, 10882–10892. doi:10.1039/d1ta00614b

Zhou, Y., Luo, K., Zha, X., Liu, Z., Bai, X., Huang, Q., et al. (2016). Electronic and Transport Properties of Ti2CO2 MXene Nanoribbons. *J. Phys. Chem. C* 120, 17143–17152. doi:10.1021/acs.jpcc.6b06426

Conflict of Interest: The authors declare that the research was conducted in the absence of any commercial or financial relationships that could be construed as a potential conflict of interest.

frontiers in Chemistry

ORIGINAL RESEARCH
published: 14 February 2022
doi: 10.3389/fchem.2022.847319

Two-Dimensional $PtS_2/MoTe_2$ van der Waals Heterostructure: An Efficient Potential Photocatalyst for Water Splitting

Changqing Shao[1], Kai Ren[2], Zhaoming Huang[3]*, Jingjiang Yang[4] and Zhen Cui[5]*

[1]School of Applied Engineering, Zhejiang Institute of Economics and Trade, Hangzhou, China, [2]School of Mechanical and Electronic Engineering, Nanjing Forestry University, Nanjing, China, [3]School of Mechanical Engineering, Wanjiang University of Technology, Ma'anshan, China, [4]School of Geely Automobile, Hangzhou Vocational and Technical College, Hangzhou, China, [5]School of Automation and Information Engineering, Xi'an University of Technology, Xi'an, China

Recently, the energy shortage has become increasingly prominent, and hydrogen (H_2) energy has attracted extensive attention as a clean resource. Two-dimensional (2D) materials show excellent physical and chemical properties, which demonstrates considerable advantages in the application of photocatalysis compared with traditional materials. In this investigation, based on first-principles methods, 2D PtS_2 and $MoTe_2$ are selected to combine a heterostructure using van der Waals (vdW) forces, which suggests a type-II band structure to prevent the recombination of the photogenerated charges. Then, the calculated band edge positions reveal the decent ability to develop the redox reaction for water splitting at pH 0. Besides, the potential drop between the $PtS_2/MoTe_2$ vdW heterostructure interface also can separate the photogenerated electrons and holes induced by the charge density difference of the PtS_2 and $MoTe_2$ layers. Moreover, the fantastic optical performances of the $PtS_2/MoTe_2$ vdW heterostructure further explain the promising advanced usage for photocatalytic decomposition of water.

Keywords: two-dimensional, heterostructure, photocatalyst, type-II band structure, water splitting

Edited by:
Guangzhao Wang,
Yangtze Normal University, China

Reviewed by:
Shuyuan Xiao,
Nanchang University, China
Junli Chang,
Southwest University, China

****Correspondence:***
Kai Ren
kairen@njfu.edu.cn
Zhaoming Huang
jimmymacy@163.com

Specialty section:
This article was submitted to Theoretical and Computational Chemistry, a section of the journal Frontiers in Chemistry

Received: *02 January 2022*
Accepted: *10 January 2022*
Published: *14 February 2022*

Citation:
Shao C, Ren K, Huang Z, Yang J and Cui Z (2022) Two-Dimensional $PtS_2/MoTe_2$ van der Waals Heterostructure: An Efficient Potential Photocatalyst for Water Splitting. Front. Chem. 10:847319. doi: 10.3389/fchem.2022.847319

INTRODUCTION

Energy shortage and environmental problems have been widely concerning, which also urges new generation of green and efficient resources. Hydrogen (H_2) has always been considered as a renewable and clean energy because of the environmentally friendly combustion product, H_2O (Hernández-Alonso et al., 2009). Tremendous efforts have been explored to develop H_2 (Ni et al., 2007; Carmo et al., 2013; Dincer and Acar, 2015), and the photocatalytic decomposition of water is very popular (Moniz et al., 2015), after the investigation the TiO_2 was used as an electrode for splitting water via desirable light and temperature proposed by Fujishima and Honda (1972).

When the semiconductor acts as photocatalyst, the hydrogen evolution reaction (HER) can be induced by the higher potential of conduction band minimum (CBM) than −4.44 eV, while the lower potential of valence band maximum (VBM) than −5.67 eV can develop the oxygen evolution reaction (OER) (Wang et al., 2018a). Recently, two-dimensional (2D) materials have attracted abundant focus because of the discovery of fantastic physical and chemical performances (Geim and Novoselov, 2007; Sun et al., 2019, 2021; Ren et al., 2021a; Sun and Schwingenschlögl, 2021), which suggests advanced applications, such as photovoltaic (Long et al., 2016) and photocatalytic (Peng et al., 2018) devices, transistors (Tan et al., 2016), solar cells (Tsai et al., 2014), batteries (Sun and Schwingenschlögl, 2020) and thermoelectrics (Ren et al., 2020a), etc. Using 2D photocatalyst for water splitting is advantageous by the large specific surface area for the catalytic active site (Stoller et al., 2008). More importantly, the heterostructure with type-II band alignment can further provide prolonged lifetime of the photogenerated charges (Wang et al., 2014, 2020a, 2020b). Therefore, the investigations of nanostructured heterostructures are conducted such as boron nitride/cadmium sulfide (Wang et al., 2020c), CdO/arsenene (Ren et al., 2021b), ZnO/GeC (Wang et al., 2020d), transition metal dichalcogenides (TMDs)/BP (Ren et al., 2019), etc. Besides, type-I heterostructures also show considerable optical performances as photocatalysts (Ren et al., 2021c, 2021d; Zhu et al., 2021). Recently, TMD materials are widely studied because of their intriguing electronic (Shen et al., 2022), thermal (Ren et al., 2022), and optical (Luo et al., 2019) properties. The TMD materials also can be prepared by chemical vapor deposition (CVD) growth method (Wang et al., 2015; Tan et al., 2016). Especially, PtS_2 monolayer has been synthesized by CVD (Zhao et al., 2019) and investigated to possess potential application as Z-scheme photocatalyst when stacking with the arsenene (Ren et al., 2020b) for water splitting. Furthermore, another TMD, $MoTe_2$, has also been prepared by magnetron co-sputtering, and the Seebeck coefficient was obtained by $\times 2.89\ 10^4$ S/m (Shi et al., 2017). Besides, as a semiconductor (Conan et al., 1984), the monolayered $MoTe_2$ shows tunable mobility (Qu et al., 2017). Therefore, both PtS_2 and $MoTe_2$ monolayers have promising electronic nature as a heterostructure photocatalyst together with the same hexagonal structure.

In this research, performing first-principles simulations, the electronic characteristic of the $PtS_2/MoTe_2$ heterostructure is investigated by a type-II band structure. Then, the photocatalytic mechanism is addressed by such decent band structure and band edge positions for water splitting. The potential drop and the charge density of the $PtS_2/MoTe_2$ heterostructure interface are also calculated. Finally, the optical performances of the monolayered PtS_2, $MoTe_2$, and $PtS_2/MoTe_2$ heterostructure are investigated.

Computational Methods

In this investigation, we used the Vienna *ab initio* simulation package (VASP) to explore the first-principles calculation by the density functional theory (DFT) (Kresse and Furthmüller, 1996; Capelle, 2006). The projector augmented wave potential (PAW) (Kresse and Joubert, 1999) was used by generalized gradient approximation (GGA) (Perdew et al., 1996) and the Perdew–Burke–Ernzerhof (PBE) method was also considered in this work. The DFT-D3 function was conducted for the weak dispersion forces. To obtain the more real electronic and optical properties of the materials in the work, the Heyd–Scuseria–Ernzerhof hybrid method was employed (Heyd et al., 2005). Furthermore, the energy cut-off and the Monkhorst–Pack *k*-point grids were obtained by 500 eV and $15 \times 15 \times 1$, respectively. To eliminate atomic interference between adjacent layers, vacuum thickness was set as 25 Å. Besides, the convergences were implemented by the force within 0.01 eV $Å^{-1}$ and the energy limited in 0.01 meV. The binding energy (E_B) was calculated using:

$$E_B = E(PtS_2/MoTe_2) - E(PtS_2) - E(MoTe_2), \tag{1}$$

where $E(PtS_2/MoTe_2)$, $E(PtS_2)$, and $E(MoTe_2)$ represent the energy of the $PtS_2/MoTe_2$ system, monolayered PtS_2, and $MoTe_2$, respectively. The charge difference between the $PtS_2/MoTe_2$ interface is obtained by:

$$\Delta\rho = \rho(PtS_2/MoTe_2) - \rho(PtS_2) - \rho(MoTe_2), \tag{2}$$

where $\rho(PtS_2/MoTe_2)$, $\rho(PtS_2)$ and $\rho(MoTe_2)$ are total charge density of the $PtS_2/MoTe_2$ heterostructure, primitive PtS_2, and $MoTe_2$ monolayers, respectively. The light absorption spectrum of the studied materials in this work is decided by:

$$\alpha(\omega) = \frac{\sqrt{2}\omega}{c}\left\{\left[\varepsilon_1^2(\omega) + \varepsilon_2^2(\omega)\right]^{1/2} - \varepsilon_1(\omega)\right\}^{1/2}, \tag{3}$$

where $\varepsilon_1(\omega)$ and $\varepsilon_2(\omega)$ represent the dielectric constant for real and imaginary parameters, respectively. The speed of light, absorption coefficient, and the angular frequency are described by c, α, and ω, respectively.

RESULTS AND DISCUSSION

The PtS_2 and $MoTe_2$ monolayers possess hexagonal honeycomb structure, shown in **Figures 1A,B**, respectively. And the structures of the PtS_2 and $MoTe_2$ monolayers are optimized, first, by the lattice parameters of 3.564 and 3.529 Å, respectively. Besides, the band structure of the PtS_2 and $MoTe_2$ monolayers are also calculated by HSE06 method, demonstrated in **Figures 1C,D**, respectively, suggesting both layered materials are semiconductors. The PtS_2 monolayer possesses an indirect bandgap of 2.60 eV with the CBM and VBM located between the Γ and M points. Furthermore, the $MoTe_2$ monolayer has a direct bandgap calculated to be 1.22 eV by the CBM and VBM at K point. The obtained lattice parameters and bandgaps of the monolayered PtS_2 and $MoTe_2$ are in good agreement with other investigations (Nguyen et al., 2019; Wang et al., 2021). Besides, the optimized bond length of the Pt–S and Mo–Te are 2.40 and 2.74 Å, respectively.

The $PtS_2/MoTe_2$ heterostructure can be constructed by six different configurations considering the high symmetry, named PM-1, PM-2, PM-3, PM-4, PM-5, and PM-6 styles. To decide the most stable staking structure, the binding energy of these different configurations are calculated, and the lowest binding energy is about −28.10 meV $Å^{-2}$ for PM-6 stacking style, suggesting the van der Waals (vdW) forces between the interface of the $PtS_2/MoTe_2$ heterostructure (Chen et al., 2013). The obtained bond length of the Pt–S and Mo–Te in the $PtS_2/MoTe_2$ heterostructure are 2.39 and 2.73 Å, which is almost the same as that of the original single-layer material, further demonstrating the vdW interaction. Moreover, the interlayer height (H_i) shown in **Figure 2A** of the $PtS_2/MoTe_2$ vdW heterostructure with PM-6 stacking style is calculated by 2.87 Å. Besides, the following obtained works are based on such PM-6 stacking style.

The projected band structure of the $PtS_2/MoTe_2$ vdW heterostructure are calculated in **Figure 3A**, which shows that the

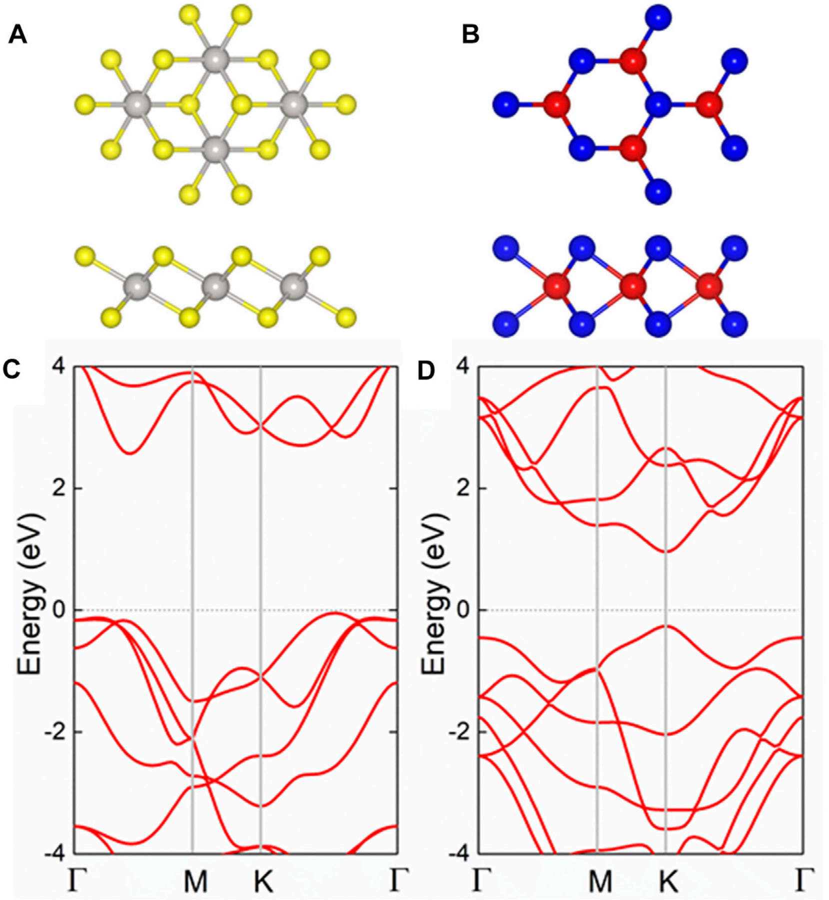

FIGURE 1 | The **(A,B)** geometric and **(C,D)** band structures of the pristine **(A,C)** PtS_2 and **(B,D)** $MoTe_2$ monolayers; the yellow, gray, red, and blue balls represent S, Pt, Mo, and Te atoms, respectively; the Fermi level is expressed as 0 using gray dash line.

CBM and the VBM of the heterostructure are contributed by the PtS_2 and $MoTe_2$ monolayers, respectively, suggesting an intrinsic type-II band structure. One can see that the PtS_2/$MoTe_2$ vdW heterostructure also is a semiconductor by an indirect bandgap of 1.26 eV that the CBM is located between the Γ and M points, while the CBM exists at K point. Besides, the obtained band-resolved charge densities, explained by **Figure 3B**, of the PtS_2/$MoTe_2$ vdW heterostructure can further demonstrate the different layered contribution to CBM and VBM.

The type-II band structure of the PtS_2/$MoTe_2$ vdW heterostructure can provide the ability to separate the photogenerated electrons (PE) and the holes used as a photocatalyst for water splitting. As shown in **Figure 4A**, the PtS_2/$MoTe_2$ vdW heterostructure takes in the energy of the photon larger than the bandgap of the PtS_2 and $MoTe_2$ layers; the PE are excited by the CB of the PtS_2 and $MoTe_2$ layers, and thus, the photogenerated holes (PH) stay at the VB at the same time. Then, the PE at the CB of the $MoTe_2$ layer will move to the CB of the PtS_2 layer because of the promoting of the conduction band offset, named CBO in **Figure 4A**. Similarly, the PH at the PtS_2 layer also can transfer to the VB of the $MoTe_2$ layer by the development of the valence band offset, denoted by VBO in **Figure 4A**. Therefore, the PEs are continuously promoted from the CB of the $MoTe_2$ layer to PtS_2 layer, while the PHs keep moving from the VB of the PtS_2 layer to the $MoTe_2$ layer under continuous solar photodynamic, which induces a PE and PH circulating flow (Wang et al., 2018b).

Furthermore, the band edge positions of the PtS_2/$MoTe_2$ vdW heterostructure is also calculated in **Figure 4B** to investigate the photocatalytic driving potential for water splitting. At pH 0, the standard potential energy of the HER and the OER are −4.44 and −5.67 eV, respectively (Wang et al., 2018a). The obtained band alignment of the monolayered PtS_2, $MoTe_2$, and the PtS_2/$MoTe_2$ vdW heterostructure is demonstrated by **Figure 4B**, which shows that the monolayered PtS_2 and the PtS_2/$MoTe_2$ vdW heterostructure have suitable band edge positions to induce the HER and OER at pH 0. However, the PtS_2 cannot separate the PE and PH compared with the type-II band structure in the PtS_2/$MoTe_2$ vdW heterostructure. Thus, the PtS_2/$MoTe_2$ vdW heterostructure can be considered as a potential photocatalyst to decompose the water.

The interfacial performances of the PtS_2/$MoTe_2$ vdW heterostructure are assessed by charge density difference ($\Delta\rho$) and the potential. The charge density difference is calculated by Bader charge analysis (Tang et al., 2009; Henkelman et al., 2006), shown in the inset of **Figure 5**; the cyan and yellow marks denote the taking and giving of electrons, suggesting that the PtS_2 and $MoTe_2$ monolayers act as receivers and donors, respectively. Besides, the obtained charge transfer between the PtS_2 and $MoTe_2$ vdW heterostructure is 0.047

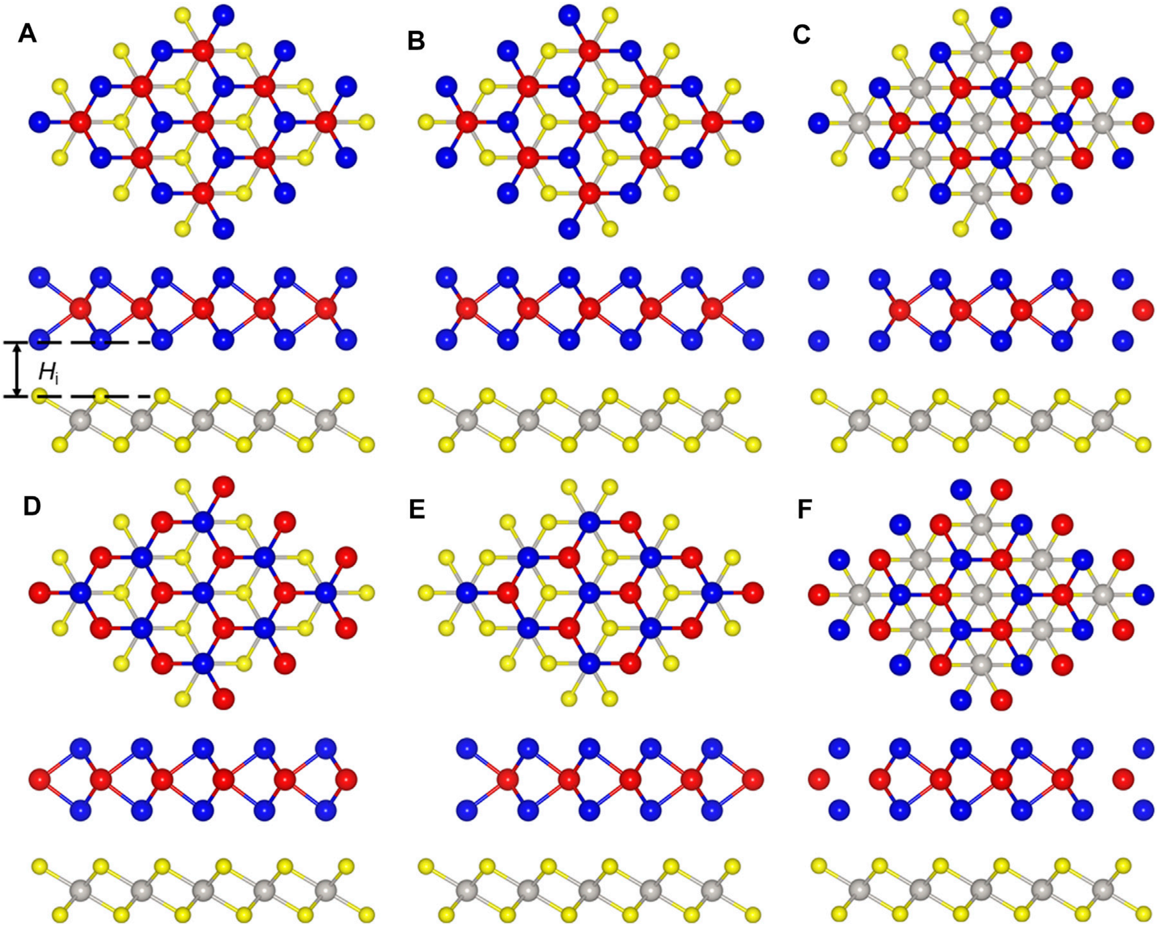

FIGURE 2 | The stacking styles of the $PtS_2/MoTe_2$ heterostructure constructed by **(A)** PM-1, **(B)** PM-2, **(C)** PM-3, **(D)** PM-4, **(E)** PM-5, and **(F)** PM-6, respectively.

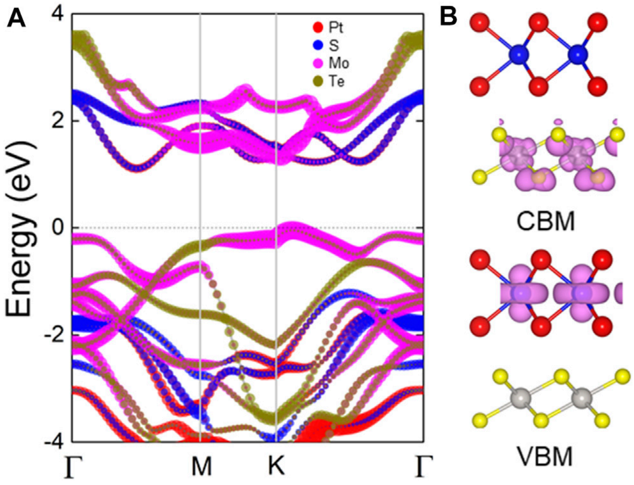

FIGURE 3 | (A) The HSE method obtained projected band structure and the **(B)** band-resolved charge densities of the PtS_2/ $MoTe_2$ vdW heterostructure; the Fermi level is expressed as 0 using gray dash line.

electrons. Furthermore, such charge transfer also can induce a potential drop (ΔV) across the $PtS_2/MoTe_2$ vdW heterostructure interface, explained by **Figure 5**. From the PtS_2 layer to the $MoTe_2$ layer, the potential decreases by 4.672 eV, which is higher than that in arsenene/GaS (4.215 eV) (Li et al., 2021), AlN/Zr_2CO_2 (0.663 eV) (Ren et al., 2021c), and Hf_2CO_2/GaN (3.752 eV) (Ren et al., 2021d) heterostructures. It is worth noting that the potential drop also can provide decent assistance in the process of the separation of photogenerated charges (Wang et al., 2018b).

Used as a photocatalyst for water splitting, light absorption capacity also has a vital role. The light absorption properties of the monolayered PtS_2, $MoTe_2$, and the $PtS_2/MoTe_2$ vdW heterostructure are evaluated and shown in **Figure 6**. The PtS_2/ $MoTe_2$ vdW heterostructure obviously can improve the optical ability of the monolayered PtS_2, $MoTe_2$ in ultraviolet and visible regions. In the visible wavelength range, the absorption peaks of the PtS_2 and $MoTe_2$ monolayers and the $PtS_2/MoTe_2$ vdW heterostructure are obtained at 4.70×10^5, 2.90×10^5, and 2.57×10^5 cm^{-1} with wavelengths of 384, 505, and 531 nm, respectively. It is worth noting that $MoTe_2$ monolayer and the tS_2/ $MoTe_2$ vdW heterostructure possess another absorption peak at 1.53×10^5 and 6.82×10^5 cm^{-1} with wavelengths of 650 and

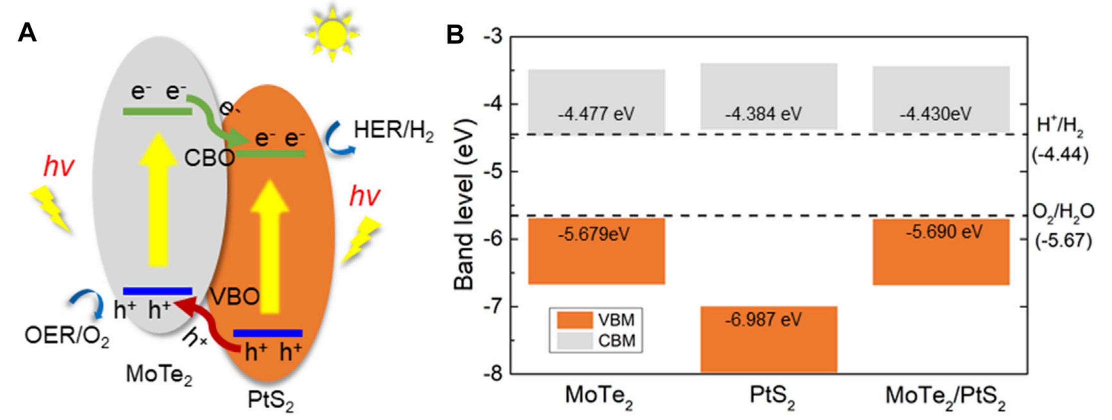

FIGURE 4 | **(A)** The photogenerated charges migration path and **(B)** the band alignment of the $PtS_2/MoTe_2$ vdW heterostructure.

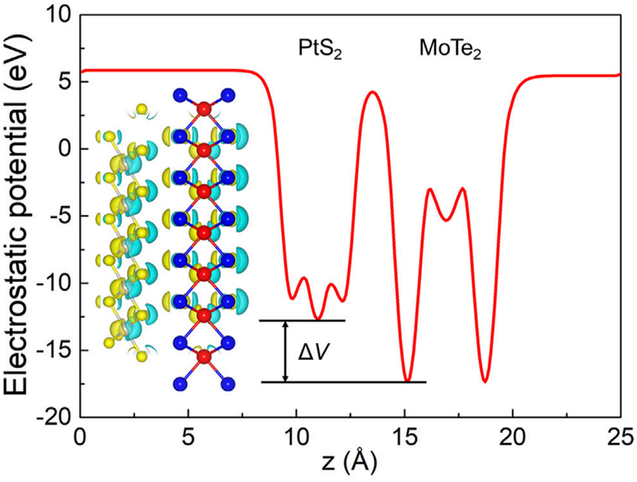

FIGURE 5 | The potential drop between the interface of the $PtS_2/MoTe_2$ vdW heterostructure; the inset represents the charge density. The isosurface lever was set at 0.015|e|.

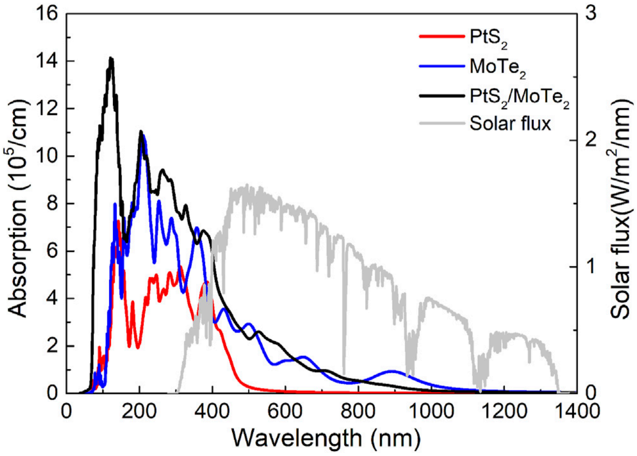

FIGURE 6 | The calculated optical absorption spectrum of the monolayered PtS_2, $MoTe_2$, and $PtS_2/MoTe_2$ vdW heterostructure.

380 nm, respectively. The results show that the PtS_2 and $MoTe_2$ monolayers and the $PtS_2/MoTe_2$ vdW heterostructure have excellent optical performances, which is higher than other reported 2D heterostructures, such as WSSe/Mg(OH)$_2$ (4.295×10^5 cm^{-1}) (Lou et al., 2021), arsenene/GaSe (5.868×10^5 cm^{-1}) (Li et al., 2021), etc.

CONCLUSIONS

Using DFT calculations, the structural and electronic nature of the monolayered PtS_2 and $MoTe_2$ are investigated as semiconductors. Then, the $PtS_2/MoTe_2$ heterostructure is constructed by vdW interactions, also showing a type-II band alignment to prevent the PE and PH from recombining. More importantly, the $PtS_2/MoTe_2$ vdW heterostructure possesses desirable band edge positions to boost the HER and OER in the PtS_2 and $MoTe_2$ layers, respectively. In the $PtS_2/MoTe_2$ vdW heterostructure, the PtS_2 layer obtains 0.047 electrons from the $MoTe_2$ layer, which induces a 4.672 eV potential drop. Furthermore, all these monolayered PtS_2 and $MoTe_2$ and the $PtS_2/MoTe_2$ vdW heterostructure show excellent optical properties; particularly, the $PtS_2/MoTe_2$ vdW heterostructure suggests a novel light absorption performance in the visible range, revealing the potential application such as new energy vehicle fuel cell photocatalyst.

DATA AVAILABILITY STATEMENT

The raw data supporting the conclusions of this article will be made available by the authors, without undue reservation.

AUTHOR CONTRIBUTIONS

All authors listed have made a substantial, direct, and intellectual contribution to the work and approved it for publication.

ACKNOWLEDGMENTS

The authors thank the Natural Science Foundation Project of Science and Technology Department of Zhejiang Province (Grant No.LZY21E060002), Scientific Research Project of Education Department of Zhejiang Province (Grant No.Y201840751), and Basic Research Fund Project of Colleges and Universities in Zhejiang Province (Grant No.19YQ24).

REFERENCES

Capelle, K. (2006). A Bird's-Eye View of Density-Functional Theory. *Braz. J. Phys.* 36, 1318–1343. doi:10.1590/s0103-97332006000700035

Carmo, M., Fritz, D. L., Mergel, J., and Stolten, D. (2013). A Comprehensive Review on PEM Water Electrolysis. *Int. J. Hydrogen Energ.* 38, 4901–4934. doi:10.1016/j.ijhydene.2013.01.151

Chen, X., Tian, F., Persson, C., Duan, W., and Chen, N.-X. (2013). Interlayer Interactions in Graphites. *Sci. Rep.* 3, 3046. doi:10.1038/srep03046

Conan, A., Bonnet, A., Amrouche, A., and Spiesser, M. (1984). Semiconducting Properties and Band Structure of MoTe2 Single Crystals. *J. Phys. France* 45, 459–465. doi:10.1051/jphys:01984004503045900

Dincer, I., and Acar, C. (2015). Review and Evaluation of Hydrogen Production Methods for Better Sustainability. *Int. J. Hydrogen Energ.* 40, 11094–11111. doi:10.1016/j.ijhydene.2014.12.035

Fujishima, A., and Honda, K. (1972). Electrochemical Photolysis of Water at a Semiconductor Electrode. *Nature* 238, 37–38. doi:10.1038/238037a0

Geim, A. K., and Novoselov, K. S. (2007). The Rise of Graphene. *Nat. Mater* 6, 183–191. doi:10.1038/nmat1849

Henkelman, G., Arnaldsson, A., and Jónsson, H. (2006). A Fast and Robust Algorithm for Bader Decomposition of Charge Density. *Comput. Mater. Sci.* 36, 354–360. doi:10.1016/j.commatsci.2005.04.010

Hernández-Alonso, M. D., Fresno, F., Suárez, S., and Coronado, J. M. (2009). Development of Alternative Photocatalysts to TiO_2: Challenges and Opportunities. *Energ. Environ. Sci.* 2, 1231. doi:10.1039/b907933e

Heyd, J., Peralta, J. E., Scuseria, G. E., and Martin, R. L. (2005). Energy Band Gaps and Lattice Parameters Evaluated with the Heyd-Scuseria-Ernzerhof Screened Hybrid Functional. *J. Chem. Phys.* 123, 174101. doi:10.1063/1.2085170

Kresse, G., and Furthmüller, J. (1996). Efficient Iterative Schemes Forab Initiototal-Energy Calculations Using a Plane-Wave Basis Set. *Phys. Rev. B* 54, 11169–11186. doi:10.1103/physrevb.54.11169

Kresse, G., and Joubert, D. (1999). From Ultrasoft Pseudopotentials to the Projector Augmented-Wave Method. *Phys. Rev. B* 59, 1758–1775. doi:10.1103/physrevb.59.1758

Li, J., Huang, Z., Ke, W., Yu, J., Ren, K., and Dong, Z. (2021). High solar-to-hydrogen efficiency in Arsenene/GaX (X = S, Se) van der Waals heterostructure for photocatalytic water splitting. *J. Alloys Compd.* 866, 158774. doi:10.1016/j.jallcom.2021.158774

Long, M., Liu, E., Wang, P., Gao, A., Xia, H., Luo, W., et al. (2016). Broadband Photovoltaic Detectors Based on an Atomically Thin Heterostructure. *Nano Lett.* 16, 2254–2259. doi:10.1021/acs.nanolett.5b04538

Lou, J., Ren, K., Huang, Z., Huo, W., Zhu, Z., and Yu, J. (2021). Electronic and Optical Properties of Two-Dimensional Heterostructures Based on Janus XSSe (X = Mo, W) and Mg(OH)2: a First Principles Investigation. *RSC Adv.* 11, 29576–29584. doi:10.1039/d1ra05521f

Luo, Y., Wang, S., Ren, K., Chou, J.-P., Yu, J., Sun, Z., et al. (2019). Transition-metal dichalcogenides/Mg(OH)2 van der Waals heterostructures as promising water-splitting photocatalysts: a first-principles study. *Phys. Chem. Chem. Phys.* 21, 1791–1796. doi:10.1039/c8cp06960c

Moniz, S. J. A., Shevlin, S. A., Martin, D. J., Guo, Z.-X., and Tang, J. (2015). Visible-light Driven Heterojunction Photocatalysts for Water Splitting - a Critical Review. *Energy Environ. Sci.* 8, 731–759. doi:10.1039/c4ee03271c

Nguyen, C. V., Bui, H. D., Nguyen, T. D., and Pham, K. D. (2019). Controlling electronic properties of PtS2/InSe van der Waals heterostructure via external electric field and vertical strain. *Chem. Phys. Lett.* 724, 1–7. doi:10.1016/j.cplett.2019.03.048

Ni, M., Leung, D. Y. C., and Leung, M. K. H. (2007). A Review on Reforming Bio-Ethanol for Hydrogen Production. *Int. J. Hydrogen Energ.* 32, 3238–3247. doi:10.1016/j.ijhydene.2007.04.038

Peng, C., Wei, P., Li, X., Liu, Y., Cao, Y., Wang, H., et al. (2018). High Efficiency Photocatalytic Hydrogen Production over Ternary Cu/TiO2@Ti3C2Tx Enabled by Low-Work-Function 2D Titanium Carbide. *Nano Energy* 53, 97–107. doi:10.1016/j.nanoen.2018.08.040

Perdew, J. P., Burke, K., and Ernzerhof, M. (1996). Generalized Gradient Approximation Made Simple. *Phys. Rev. Lett.* 77, 3865–3868. doi:10.1103/physrevlett.77.3865

Qu, D., Liu, X., Huang, M., Lee, C., Ahmed, F., Kim, H., et al. (2017). Carrier-Type Modulation and Mobility Improvement of Thin MoTe2. *Adv. Mater.* 29, 1606433. doi:10.1002/adma.201606433

Ren, K., Zheng, R., Yu, J., Sun, Q., and Li, J. (2021). Band Bending Mechanism in CdO/Arsenene Heterostructure: A Potential Direct Z-Scheme Photocatalyst. *Front. Chem.* 9, 788813. doi:10.3389/fchem.2021.788813

Ren, K., Liu, X., Chen, S., Cheng, Y., Tang, W., and Zhang, G. (2020). Remarkable Reduction of Interfacial Thermal Resistance in Nanophononic Heterostructures. *Adv. Funct. Mater.* 30, 2004003. doi:10.1002/adfm.202004003

Ren, K., Shu, H., Huo, W., Cui, Z., Yu, J., and Xu, Y. (2021). Mechanical, Electronic and Optical Properties of a Novel B2P6 Monolayer: Ultrahigh Carrier Mobility and strong Optical Absorption. *Phys. Chem. Chem. Phys.* 23, 24915–24921. doi:10.1039/d1cp03838a

Ren, K., Sun, M., Luo, Y., Wang, S., Yu, J., and Tang, W. (2019). First-principle Study of Electronic and Optical Properties of Two-Dimensional Materials-Based Heterostructures Based on Transition Metal Dichalcogenides and boron Phosphide. *Appl. Surf. Sci.* 476, 70–75. doi:10.1016/j.apsusc.2019.01.005

Ren, K., Tang, W., Sun, M., Cai, Y., Cheng, Y., and Zhang, G. (2020). A direct Z-scheme PtS2/arsenene van der Waals heterostructure with high photocatalytic water splitting efficiency. *Nanoscale* 12, 17281–17289. doi:10.1039/d0nr02286a

Ren, K., Zheng, R., Lou, J., Yu, J., Sun, Q., and Li, J. (2021). Ab Initio Calculations for the Electronic, Interfacial and Optical Properties of Two-Dimensional AlN/Zr2CO2 Heterostructure. *Front. Chem.* 9, 796695. doi:10.3389/fchem.2021.796695

Ren, K., Zheng, R., Xu, P., Cheng, D., Huo, W., Yu, J., et al. (2021). Electronic and Optical Properties of Atomic-Scale Heterostructure Based on MXene and MN (M = Al, Ga): A DFT Investigation. *Nanomaterials* 11, 2236. doi:10.3390/nano11092236

Ren, K., Qin, H., Liu, H., Chen, Y., Liu, X., Zhang, G., et al. (2022). Manipulating Interfacial Thermal Conduction of 2D Janus Heterostructure via a Thermo-Mechanical Coupling. *Adv. Funct. Mater.* 105, 2110846. doi:10.1002/adfm.202110846

Shen, Z., Ren, K., Zheng, R., Huang, Z., Cui, Z., Zheng, Z., et al. (2022). The Thermal and Electronic Properties of the Lateral Janus MoSSe/WSSe Heterostructure. *Front. Mater.* 9, 838648. doi:10.3389/fmats.2022.838648

Shi, D., Wang, G., Li, C., Shen, X., and Nie, Q. (2017). Preparation and Thermoelectric Properties of MoTe 2 Thin Films by Magnetron Co-sputtering. *Vacuum* 138, 101–104. doi:10.1016/j.vacuum.2017.01.030

Stoller, M. D., Park, S., Zhu, Y., An, J., and Ruoff, R. S. (2008). Graphene-based Ultracapacitors. *Nano Lett.* 8, 3498–3502. doi:10.1021/nl802558y

Sun, M., Chou, J.-P., Hu, A., and Schwingenschlögl, U. (2019). Point Defects in Blue Phosphorene. *Chem. Mater.* 31, 8129–8135. doi:10.1021/acs.chemmater.9b02871

Sun, M., Luo, Y., Yan, Y., and Schwingenschlögl, U. (2021). Ultrahigh Carrier Mobility in the Two-Dimensional Semiconductors B8Si4, B8Ge4, and B8Sn4. *Chem. Mater.* 33, 6475–6483. doi:10.1021/acs.chemmater.1c01824

Sun, M., and Schwingenschlögl, U. (2020). B2P6: A Two-Dimensional Anisotropic Janus Material with Potential in Photocatalytic Water Splitting and Metal-Ion Batteries. *Chem. Mater.* 32, 4795–4800. doi:10.1021/acs.chemmater.0c01536

Sun, M., and Schwingenschlögl, U. (2021). Structure Prototype Outperforming MXenes in Stability and Performance in Metal-Ion Batteries: A High

Throughput Study. *Adv. Energ. Mater.* 11, 2003633. doi:10.1002/aenm.202003633

Tan, H., Fan, Y., Rong, Y., Porter, B., Lau, C. S., Zhou, Y., et al. (2016). Doping Graphene Transistors Using Vertical Stacked Monolayer WS2 Heterostructures Grown by Chemical Vapor Deposition. *ACS Appl. Mater. Inter.* 8, 1644–1652. doi:10.1021/acsami.5b08295

Tang, W., Sanville, E., and Henkelman, G. (2009). A Grid-Based Bader Analysis Algorithm without Lattice Bias. *J. Phys. Condens. Matter* 21, 084204. doi:10.1088/0953-8984/21/8/084204

Tsai, M.-L., Su, S.-H., Chang, J.-K., Tsai, D.-S., Chen, C.-H., Wu, C.-I., et al. (2014). Monolayer MoS2 Heterojunction Solar Cells. *ACS nano* 8, 8317–8322. doi:10.1021/nn502776h

Wang, B.-J., Li, X.-H., Cai, X.-L., Yu, W.-Y., Zhang, L.-W., Zhao, R.-Q., et al. (2018). Blue Phosphorus/Mg(OH)2 van der Waals Heterostructures as Promising Visible-Light Photocatalysts for Water Splitting. *J. Phys. Chem. C* 122, 7075–7080. doi:10.1021/acs.jpcc.7b12408

Wang, B., Wang, X., Wang, P., Kuang, A., Zhou, T., Yuan, H., et al. (2021). Bilayer $MoTe_2/XS_2$ (X = Hf,Sn,Zr) Heterostructures with Efficient Carrier Separation and Light Absorption for Photocatalytic Water Splitting into Hydrogen. *Appl. Surf. Sci.* 544. doi:10.1016/j.apsusc.2020.148842

Wang, G., Gong, L., Li, Z., Wang, B., Zhang, W., Yuan, B., et al. (2020). A Two-Dimensional CdO/CdS Heterostructure Used for Visible Light Photocatalysis. *Phys. Chem. Chem. Phys.* 22, 9587–9592. doi:10.1039/d0cp00876a

Wang, G., Li, Z., Wu, W., Guo, H., Chen, C., Yuan, H., et al. (2020). A Two-Dimensional H-Bn/c2n Heterostructure as a Promising Metal-free Photocatalyst for Overall Water-Splitting. *Phys. Chem. Chem. Phys.* 22, 24446–24454. doi:10.1039/d0cp03925j

Wang, G., Zhang, L., Li, Y., Zhao, W., Kuang, A., Li, Y., et al. (2020). Biaxial Strain Tunable Photocatalytic Properties of 2D ZnO/GeC Heterostructure. *J. Phys. D: Appl. Phys.* 53, 015104. doi:10.1088/1361-6463/ab440e

Wang, G., Zhi, Y., Bo, M., Xiao, S., Li, Y., Zhao, W., et al. (2020). 2D Hexagonal Boron Nitride/Cadmium Sulfide Heterostructure as a Promising Water-Splitting Photocatalyst. *Phys. Status Solidi B* 257, 1900431. doi:10.1002/pssb.201900431

Wang, H., Zhang, L., Chen, Z., Hu, J., Li, S., Wang, Z., et al. (2014). Semiconductor Heterojunction Photocatalysts: Design, Construction, and Photocatalytic Performances. *Chem. Soc. Rev.* 43, 5234–5244. doi:10.1039/c4cs00126e

Wang, S., Tian, H., Ren, C., Yu, J., and Sun, M. (2018). Electronic and Optical Properties of Heterostructures Based on Transition Metal Dichalcogenides and Graphene-like Zinc Oxide. *Sci. Rep.* 8, 12009. doi:10.1038/s41598-018-30614-3

Wang, S., Wang, X., and Warner, J. H. (2015). All Chemical Vapor Deposition Growth of MoS2:h-BN Vertical van der Waals Heterostructures. *ACS nano* 9, 5246–5254. doi:10.1021/acsnano.5b00655

Zhao, D., Xie, S., Wang, Y., Zhu, H., Chen, L., Sun, Q., et al. (2019). Synthesis of Large-Scale Few-Layer PtS2 Films by Chemical Vapor Deposition. *AIP Adv.* 9, 025225. doi:10.1063/1.5086447

Zhu, Z., Ren, K., Shu, H., Cui, Z., Huang, Z., Yu, J., et al. (2021). First-Principles Study of Electronic and Optical Properties of Two-Dimensional WSSe/BSe van der Waals Heterostructure with High Solar-to-Hydrogen Efficiency. *Catalysts* 11, 991. doi:10.3390/catal11080991

Conflict of Interest: The authors declare that the research was conducted in the absence of any commercial or financial relationships that could be construed as a potential conflict of interest.

Advantages of publishing in Frontiers

OPEN ACCESS
Articles are free to read for greatest visibility and readership

FAST PUBLICATION
Around 90 days from submission to decision

HIGH QUALITY PEER-REVIEW
Rigorous, collaborative, and constructive peer-review

TRANSPARENT PEER-REVIEW
Editors and reviewers acknowledged by name on published articles

Frontiers
Avenue du Tribunal-Fédéral 34
1005 Lausanne | Switzerland

Visit us: www.frontiersin.org
Contact us: frontiersin.org/about/contact

REPRODUCIBILITY OF RESEARCH
Support open data and methods to enhance research reproducibility

DIGITAL PUBLISHING
Articles designed for optimal readership across devices

FOLLOW US
@frontiersin

IMPACT METRICS
Advanced article metrics track visibility across digital media

EXTENSIVE PROMOTION
Marketing and promotion of impactful research

LOOP RESEARCH NETWORK
Our network increases your article's readership